Efficiency and characterisation comparison between various compositions of conventionally sintered PZT ceramics for piezoelectric energy harvesting.

Veronica Lizeth Garcia Caballero

Submitted in fulfilment of the requirements of the Degree of Doctor of Philosophy.

School of Engineering, College of Science and Engineering

University of Glasgow

March 2024

ABSTRACT

Amongst the available kinetic energy harvesting methods, piezoelectric devices have gained popularity due to their prolonged service life, as well as their reduced maintenance, weight and size. Lead zirconate titanate, also known as PZT, is one of the most common piezoelectric ceramics used worldwide. When left undoped, changing the proportions of TiO_2 and ZrO_2 in the material will result in different proximities to the morphotropic phase boundary (MPB), which is thought to be where the best piezoelectric properties are exhibited. Additionally, the purity of the parent oxides used in the preparation of PZT has been found to have a direct effect not only on its properties but also on its fabrication cost.

To identify the effects of varying these properties, this dissertation presents and discusses the work done to compare the efficiency and characteristics of ten different compositions of PZT disks sintered through a two-stage conventional ceramic method. The disks were fabricated using two grades of purity for the parent oxides, and three different chemical compositions. Six of the sets were made using the same grade of purity for the main PZT disk and the lead zirconate (PZ) atmosphere that was used to compensate the PbO loss that occurs near ~888°C. The other four were sintered using the opposite grade of purity for the PZ atmosphere. Three of these were for the high-purity compositions and one for the samples made with the lowest concentration of TiO_2 and lower-grade starting powders.

The ten sets were physically characterised using their densities, Scanning Electron Microscopy (SEM), X-ray diffraction (XRD), and Energy Dispersion Analysis (EDS). The samples were processed to achieve smooth parallel surfaces and functionally characterised after applying silver electrodes on their faces. The disks were poled along their thickness using 4kV/mm for 15min at ~100°C, prior to measuring their piezoelectric constants, electromechanical coupling factor, mechanical quality factor and acoustic impedance. The lower purity (LP) PZT samples registered higher densities and seemingly behaved as hard ceramics, resisting polarization and exhibiting lower permittivities and Curie points.

Although the highest piezoelectric coefficients ($d_{33} > 310pC/N$) were measured from the higher purity (HP) PZT samples, the highest coupling factors ($k_p > 54\%$) were obtained from compositions that were made with the LP chemicals or used LP PZ disks, suggesting that the presence of the LP components had a positive effect in the energy conversion.

After coupling the samples as energy harvesters, controlled impact tests were done at two different frequencies for approximately 12s each to obtain their I-V curves. The highest average output power density was achieved by the samples with the highest TiO_2 made with LP PZT and PZ (43.7µW/cm^3 at ~6 hits/s and ~28.4µW/cm^3 at 14 hits/s). This further supports the positive effects the LP chemicals can have, not only offering similar properties as the HP counterparts but also implicating major cost reductions when fabricated in bulk for large-scale commercial use, whilst their higher densities anticipate a better response to the expected conditions associated with their use.

TABLE OF CONTENTS

LIST OF FIGURES

LIST OF TABLES

ACKNOWLEDGEMENTS

I dedicate this work to all the people who kept pushing me and never stopped believing in me.

AUTHOR'S DECLARATION

I declare that this thesis represents entirely my own work, except when mentioned or acknowledged to others. I declare that the present work does not include any sections already submitted for any other degree at the University of Glasgow or any other institution.

Veronica Lizeth Garcia Caballero

Date: 18-09-2023

ABBREVIATIONS/NOMENCLATURE

Symbol/Abbreviation	Meaning
#	Number
°	Degrees
°C	Degrees Celsius
$(c^p_{11})^D$	Elastic stiffness at constant dielectric displacement (GN/m^2)
$(c^p_{11})^E$	Elastic stiffness at constant electric field (GN/m^2)
µm	micro metres/ microns (10^{-6} m)
$µC/cm^2$	10^{-6} Coulombs per centimetre
A	Ampere
A	Surface Area (mm^2)
Å	Angstrom (10^{-10} m)
a.u.	Arbitrary units
AC	Alternating Current (Amperes)
atm	atmosphere
B	Susceptance
$BaTiO_3$	Barium Titanate
C	Capacitance (Farads)
C_0	Static Capacitance (Farads)
c_j	Sound speed or velocity (m/s)
CNT	Carbon Nanotubes
c^p_{11}	Elastic stiffness (F/m)
D	Dielectric displacement
d	Diameter
d_{31}	Piezoelectric charge coefficient perpendicular to poling (pC/N)
d_{33}	Piezoelectric charge coefficient parallel to the poling (pC/N)
DC	Direct Current
DI	Deionised water
DMF	Dimethylformamide
E	Electric field (V)
E	Energy (J)
E_c	Coercive field (kV/mm)
EDS/EDS/EDAX	Energy Dispersive X-ray Analysis
Eq.	Equation
eV	Electron-volt
f	Frequency
f_a	Antiresonance frequency
F	Force
FOM	Figures of Merit
f_r	Resonance frequency
g	grams
G	Conductance
GN/m^2	10^9 Newtons per square metre

g_{33}	Piezoelectric voltage constant parallel to poling (Vm/N)
g_{31}	Piezoelectric voltage constant perpendicular to poling (Vm/N)
GSM	Global System for Mobile
h	Thickness (mm)
h	Hour
HAWT	Horizontal Axis Wind Turbine
HP	Higher/High Purity
HP/HP	High purity PZT with High Purity PbO Compensation
HP/LP	High purity PZT with Low Purity PbO Compensation
IEA	International Energy Agency
IR	Infrared
J	Current density
K	Relative dielectric constant
k_{ij}	Coupling factor of for an electric field in direction i and longitudinal vibrations in direction j
k_p	Coupling factor for an electric field parallel to poling direction and perpendicular radial vibrations
kHz	kilohertz
kV/mm	kilovolts per millimetre
LP	Lower/Low Purity
LP/HP	Low purity PZT with High Purity PbO Compensation
LP/LP	Low purity PZT with Low Purity PbO Compensation
m	Mass (g)
MEMS	Micro-Electro-Mechanical Systems
min	minutes
mL	millilitre
MPB	Morphotropic Phase Boundary
mW/cm^2	milliwatt per square centimetre
NA	Not available
NaCl	Sodium Chloride
nF	10^{-9} Farads
Ns/m^2	Newton second per square metre or Rayls
P	Polarization
P	Power (W)
Pb	Lead
PbO	Lead Oxide
pC/N	10^{-12} Coulombs per Newton
pm^2/N	10^{-12} square metres per Newton
PDMS	Polydimethylsiloxane, dimethylpolysiloxane or dimethicone
PEG	Pyroelectric Electric Generator
P_r	Remanent polarization ($\mu C/cm^2$)
P_s	Saturation or Spontaneous Polarization
PT	Lead Titanate ($PbTiO_3$)
PVA	Polyvinyl Alcohol
PVDF	Polyvinylidene Fluoride

PVDF-HFP	Polyvinylidene fluoride-co-hexafluoropropylene
PZT	Lead Zirconate Titanate ($PbZr_{(1-x)}Ti_{(x)}O_3$)
Q_m	Mechanical Quality Factor
r	Radius (mm)
R	Resistance (Ω)
Rayls	Unit of Acoustic Impedance or N·s/m^2
RES	Renewable Energy Supply
RF	Radio Frequency
rpm	Revolutions per minute
S	Strain
s	Elastic compliance ($\times 10^{-12}$ m^2/N)
s^E_{ij}	Elastic compliance for stress in direction i and strain in direction j, under constant electric field (pm^2/N)
s^D_{ij}	Elastic compliance for stress in direction i and strain in direction j, under constant displacement (pm^2/N)
SEM	Scanning Electron Microscopy
T	Stress
tan δ	Dielectric Loss
T_C	Curie Temperature
TEG	Thermoelectric Generators
THF	Tetrahydrofuran or oxolane
TiO_2	Titanium Dioxide
T_R	Room Temperature (°C)
V	Volume (m^3)
V	Voltage (V)
V	Volts
Vm/N	Voltmeter per Newton
w/V%	Weight per volume percentage
w	Weight
W	Watt
wt%	Percentage by weight
X	Reactance
XRD	X-ray Diffraction
Y	Electrical Admittance (Ω)
Z	Electrical Impedance (Ω)
Z_c	Acoustic Impedance (Ns/m^2)
ZrO_2	Zirconium Dioxide
Δ	Absolute error
ε	Dielectric permittivity
ε_r	Dielectric constant or relative permittivity
ε^T_{33}	Permittivity under constant stress parallel to poling
Ω	Ohm
ρ	Density (g/cm^3)
σ	Standard deviation
σ^p	Poisson's Planar Ratio

Chapter 1. INTRODUCTION

In a day and age where technology has become a necessity and a key part of people's lives, the electricity demand has significantly increased to keep up with this new lifestyle. With the exponentially growing world population and the constant appearance of new technological innovations, a continuous increment of energy demand seems unavoidable. Decades ago, the carbon-based fuel sources that were heavily relied on in the past, were identified as a finite solution to this problem, not only because of their non-renewable nature but also due to the harmful environmental effects that derive from their processing and usage.

Consequently, new, and better alternative sources, generally in the form of renewable energy, started being researched and developed in the last few decades in an attempt to reduce the need for fossil fuels and offer sustainable solutions to energy security problems. Renewable energy technologies like solar, wind and wave have become some of the most successful and widely known sources; nevertheless, several other renewable sources have become the focus of many researchers. Amongst this group, a particular type of kinetic energy harvester, known as piezoelectrics, has been identified and studied since the 1880s and continues to be of interest due to its promising potential.

Despite having some disadvantages, amongst which limited power generation and complex manufacturing can be identified, piezoelectrics have been found to offer lighter and more compact systems with prolonged service lives that require less maintenance and are not weather-dependent. Due to this, piezoelectric harvesters were chosen as the main focus of this research, specifically the development, analysis and testing of multiple compositions of lead-based piezoelectric ceramics for energy harvesting purposes.

1.1 Aim and layout of the thesis

The aim of this thesis is to measure and analyse the physical, functional, and monetary effects of varying the chemical composition, grade of purity of the parent oxides, and the sintering arrangements involved in the fabrication of ten different compositions of pure lead zirconate titanate (PZT) ceramic disks intended for energy harvesting.

This thesis is composed of six chapters, including this chapter, which is considered Chapter 1 and covers a brief introduction to the thesis and its main subject as well as its aims and layout followed by the proposed objectives and posed research questions.

Chapter 2 covers the literature review related to the area of research, starting from the current energy crisis and moving to the concept of energy harvesting and the diverse types of energy harvesters available. The chapter then focuses on the types of piezoelectric materials and their applications, explaining the diverse methods to obtain piezoelectric ceramics, the stages involved in the most commonly used processes, and the details of the functional and physical characterisation needed to understand the behaviour and capabilities of the material as well as its potential to be modified for specific technological applications.

Chapter 3 explains in detail the processes followed for the sintering of pure lead-based bulk piezoelectric ceramics through a two-stage conventional ceramic method. The chapter includes subsections for the mixture, drying, shaping and actual two-stage sintering process followed to obtain the PZT samples chosen to be the main focus of study of this research, as well as covering possible issues and areas to pay particular attention to in order to guarantee a significant reduction of defects in the material and improve their performance as potential kinetic energy harvesters.

Chapter 4 describes the physical characterisation performed on the resulting sintered pellets. Its contents provide a framework of the densities, microstructure, phase formation, and composition of the samples, through scanning electron microscopy (SEM), X-ray diffraction (XRD) and energy dispersion (EDS). The data obtained through these analyses is compared and correlated throughout the chapter, in addition to making several connections to the parameters used during the sintering method explained in Chapter 3. This discussion aided in the selection of the best samples from each composition to be processed and studied in Chapter 5, before being tested as energy harvesters in Chapter 6.

Chapter 5 focuses on the steps that were followed to prepare the chosen samples for their functional characterisation, including lapping and electrode placement. Additionally, the associated figures of merit (FOM) were measured after poling saturation was reached in each sample, where the piezoelectric constants and the planar coupling coefficients were determined, as well as the quality factors, acoustic impedance, and dielectric properties, where the Curie point of each PZT composition was estimated from the acquired plots.

Chapter 6 covers the electronic adaptation of the samples and their potential as energy harvesters. The measured impedance and associated resistance of each chosen PZT sample are included in the first section of this chapter followed by their classification as either soft or hard ceramics based on the characteristics previously discussed.

Additionally, the voltage and current (I-V) curves are presented, as well as the resulting average and peak output powers and energies calculated from these. The relative power and energy densities per unit area and unit volume are also listed and discussed, enabling an easy comparison with the reference values presented in Chapter 2. Furthermore, a cost analysis is shown, describing the outcome of this project from an economic point of view, which highlights the major financial differences between the HP and LP materials when considering the bulk preparation that would be required for commercial purposes.

Lastly, Chapter 7 presents a summary of this work, along with the derived conclusions from each of the experimental chapters (Chapters 3 to 6). This chapter also includes the limitations met through this project, and thus, the final recommendations associated with these. Furthermore, some of the related research done after this project is mentioned to exemplify possible areas for future study where interdisciplinary work is expected and encouraged. The appendices, related works and references follow this chapter.

1.2   Research Questions

- What is the best process, regarding the conventional ceramic method, to obtain the best piezoelectric effect in pure PZT thin disks?
- What are the setbacks or difficulties when working with lead-based piezoceramics?
- What is the best way to compensate for the PbO loss that occurs during PZT sintering?
- What are the effects on the properties and cost implications of using lower-grade purities for the sintering of pure PZT piezoceramics?
- Are higher purities needed to obtain the best piezoelectric characteristics and performance from sintered PZT ceramics?
- What is the best chemical composition and sintering arrangement to use when creating piezoelectric PZT ceramics for energy harvesting purposes?
- Do the calculated theoretical values match the experimental values obtained for the sintered PZT compositions regarding mechanical to electrical conversion efficiencies?
- How much energy and power can be generated by the PZT ceramics when adapted as piezoelectric energy harvesters?
- How can the piezoelectric properties presented in ceramics be improved or maximised?

1.3 Objectives

The following are the objectives that were set for this work:

- Study and design a two-stage conventional ceramic method for sintering bulk PZT piezoelectric ceramics for energy harvesting purposes.

- Identify possible sources of error or areas of opportunity in the sintering method to improve the piezoelectric properties of the ceramic material.

- Obtain the physical characterisation of the sintered samples, including the calculation of their density, and the analysis of their microstructure, phase formation, and composition.

- Prepare the sintered pellets for energy harvesting by lapping the material, applying electrodes to the faces of the disks, and aligning its dipoles through the poling process.

- Generate and analyse the hysteresis loops for each different chosen composition of PZT.

- Determine the figures of merit (FOM) of the sintered piezoelectric ceramics, including their piezoelectric charge constant d_{ij}, piezoelectric voltage constant g_{ij}, planar coupling factor k_p, quality mechanical factor Q_m and acoustic impedance Z_c.

- Measure the dielectric properties of the processed PZT samples, including their relative permittivities and dielectric losses as well as their capacitance.

- Analyse the measured impedance and associated resistance through both the radial and the thickness resonance achieved on each poled PZT disk.

- Determine the possible nature of the PZT disks, classifying them as either a "hard" or "soft" piezoelectric ceramic.

- Test each composition regarding their outputs and efficiencies as energy harvesters by coupling the researched piezoelectric materials and creating a controlled impact test to evaluate their performance.

- Perform a cost analysis to determine which purity and composition are the best for the desired applications.

1.4 Innovation and originality of this thesis

The innovation and originality of this work lies on four main aspects covered by the research presented throughout Chapters 3 to 6. The first idea focuses on the introduction of lower purity starting powders as an opportunity to reduce fabrication costs of bulk PZT ceramic disks for energy harvesting purposes without compromising their performance. This would represent a major advantage when looking into manufacturing piezoelectric energy harvesters at a large scale for commercial purposes and defied the idea that higher grades of chemical purity meant better performance from the coupled devices.

To explore and test this idea, the PZT samples were prepared using two different grades of purity for the three parent oxides required for the fabrication of PZT. The detailed description of this process is described in Chapter 3.

This was linked to the second innovative idea that was explored in this project, which proposed testing different concentrations of TiO_2 in the samples to evaluate the effect in their piezoelectric properties and associated energy conversion efficiency. The three compositions chosen were based on their proximity to the assumed morphotropic phase boundary ($x = 0.47$) reported in the literature and were meant to test the applicability of this value when changing the grade of purity of the initial oxides. The full functional analysis and physical characterisation that was completed to evaluate the capabilities and associated parameters of each chosen PZT composition, is included in Chapters 4, 5 and 6.

The sintering arrangement used and described in Chapter 3 became the third original contribution of this thesis as became a new system that could be employed since it was not possible to follow the typical ceramic method, which involves pressing the PZT mixes into a single cylinder for both stages of the process and cutting the final product into the necessary thin disks after discarding the top and bottom layers of the cylinder. In this case, the sintering stage was conducted after pressing individual disks from the PZT mixture and placing them in an intercalated arrangement with the non-stoichiometric PZ atmosphere disks, starting with a PZ disk at the bottom of the crucible. This intercalated arrangement proved to be the best possible system to reduce the amount of PbO that escaped from the samples during the second heat treatment, whilst also preventing the PZT disks from sticking to each other or the bottom of the alumina crucible. Both being known issues encountered when fabricating lead-based piezoelectric ceramics.

Finally, the last innovative idea that was included in this work involved the fabrication of PZT samples that were made with the opposite grade of purity for the PZ atmosphere disks, as it was initially thought that if the best performance was expected from the higher purity PZT samples, it was probable that some monetary savings could be achieved if the PbO compensation was made with the lower purity chemicals, with minimal effects on the anticipated electrical responses from the material. This resulted in novel behaviours from the samples, where enhancements were seen throughout some of the weak or poor performing areas of the higher purity PZT disks when using the lower purity PZ instead of the higher purity compensation, including higher electromechanical coupling factors, higher permittivities, lower impedances and higher mechanical quality factors.

Chapter 2.   LITERATURE REVIEW

2.1   Energy crisis: Background and solutions currently being developed

In a fast-growing world, where the transportation and industry sectors are responsible for an exponential increase in the global energy demand over the last ~200 years, and with the current fossil fuel reserves nearing exhaustion whilst severely polluting our environment, we, as a society, are facing an energy and environmental crisis. Based on the current rate of consumption of the fuels that make up over 80% of the global supply (IEA, 2022), the existing reserves of conventional oil are said to last ~50 more years, while natural gas could be gone in less than 70 years, and coal in another 200 (Solar Impulse Foundation, 2020).

The International Energy Agency (IEA) predicts that without any adequate public policies regarding this issue, the total energy demand could rise by more than half by 2030 (IEA, 2022). According to Martin Hoffert, a professor of physics at the New York University, this number could triple within the next century, leaving us in desperate need of alternative and innovative solutions (Parfit, 2020).

Overconsumption, overpopulation, outdated infrastructure and energy wastage can be identified as four of the major contributing factors that need to be addressed regarding the energy crisis (Conserve Energy Future, 2017). Nevertheless, it is imperative that not only the demand is met by any means possible but also doing so taking into consideration the close relationship between the energy and the environmental crisis and the current climate change effects. It is because of this, that an energy transition to renewable energy sources is required and that unlike fossil fuels, these do not continue deteriorating our environment by emitting greenhouse gases.

Amongst the group of environmentally friendly and sustainable alternative energy sources, natural resources such as solar, wind and water can be found along with thermal, biological, chemical, and kinetic. These solutions, combined with the modernisation and improvement of our current infrastructure and power generating equipment, and the exchange of old devices for highly efficient ones, have been proven to be a viable solution with great potential to slow down and hopefully put an end to the energy crisis in the coming decades. This chapter addresses various state-of-the-art energy harvesters using different energy sources.

2.2 Energy Harvesting

Energy harvesting is one of the processes being exploited to deal with the ongoing energy crisis as it involves capturing energy from our environment and converting it into electricity that could be used to power devices such as wireless sensor nodes, consumer electronics and vehicles (IDTechEx, 2015; Richards, et al., 2004). The energy that could be captured would otherwise be lost as heat, light, sound, vibration or movement (IOP Institute of Physics., 2012; Jung, et al., 2009).

Besides not being harmful to the environment and providing access to new technology, energy harvesting helps reduce costs and improve efficiency, enabling battery-free, maintenance-free devices (IOP Institute of Physics., 2012). Furthermore, industries are using energy harvesting in areas such as consumer electronics, transport, healthcare, construction, mobility, aerospace and military, and agriculture, amongst others (IDTechEx, 2015). The sources vary from a vast range of alternatives, including the human body, vehicles, structures, industrial or mechanical devices, and the environment. Table 2-1 lists various examples of these sources (Chang, et al., 2010; Priya, 2007).

Table 2-1 Various sources of energy available in our surroundings. (Priya, 2007)

Human body	Vehicles	Structures	Industrial	Environment
• Breathing • Blood pressure • Body heat • Walking • Body motion • Jogging • Eating • Talking	• Aircrafts • Helicopters • Cars & trains • Tyres, tracks & brakes • Shock absorbers • Turbines	• Bridges • Roads • Tunnels • Farmhouse structures • Ducts	• Motors • Compressors • Chillers • Pumps • Fans • Conveyors • Vibrating machinery	• Wind • Solar • Temperature gradients • Ocean currents • Acoustic & EM waves • RF signal

2.2.1 Advantages and Disadvantages

Amongst the advantages of energy harvesting, the most straightforward one is the usage of the energy that is already found in our surroundings without detrimental or damaging effects. This method recovers energy that is already being generated, either naturally or synthetically from our human activities, which would otherwise be wasted if not collected for conversion. Nevertheless, while energy harvesting can collect any available wasted energy, converting it into electrical energy will never be 100% efficient as it will still suffer dissipation during the process, where some heat will be produced (Orfei, 2019).

Furthermore, energy harvesters do not tend to have a constant flux of energy and require some sort of energy storage and voltage regulator besides the converter system. Because of this, using them as the sole energy source of a system requires very efficient energy management as well as an improvement in their current cost and performance. Consequently, this often makes it somewhat difficult to keep the systems small while still providing a useful amount of energy, especially considering that the size of the generator is proportional to its efficiency (Orfei, 2019).

Although these systems could initially be more complex and costly, their significantly longer working life provides a valuable advantage over the alternatives. This is not only because most of them operate with renewable sources but also due to the minimal maintenance they require, being energetically autonomous, light, and capable of wireless communications (Orfei, 2019), which allows for the operation of electronic systems in secluded, dangerous or difficult-to-access scenarios.

2.2.2 Power Density and Efficiency

Power density (W/cm^2) is one of the characteristics that can measure the efficiency of an energy harvester. It describes the amount of power in a system or region of space per unit volume or area. Efficiency is generally the quotient of the output power over the input power and must always be equal to or less than one. Improving power density, as well as cost, maximum number of charging cycles and energy density, has been and continues to be a major field of research (Machado, et al., 2023). Table 2-2 shows some of the main alternative energy harvesting sources with their efficiencies and output power.

Table 2-2 Main energy harvesting sources, their efficiencies and power densities (Adu-Manu, et al., 2018).

Energy Source		Source Characteristic	Conversion Efficiency	Harvested Power
Light	Indoor	0.1 mW/cm^2	15-20%	$<10 \, \mu\text{W/cm}^2$
	Outdoor	100 mW/cm^2		15 mW/cm^2
Vibration	Human	$0.5\text{m} @ 1\text{Hz} \, \& \, 1\text{m/s}^2 @ 50\text{Hz}$	Source dependent	$4 \, \mu\text{W/cm}^2$
	Industrial	$1\text{m} @ 5\text{Hz} \, \& \, 10\text{m/s}^2 @ 1\text{kHz}$		$100 \, \mu\text{W/cm}^2$
Thermal	Human	20 mW/cm^2	0.2%	$40 \, \mu\text{W/cm}^2$
	Industrial	100 mW/cm^2	Source dependent	$1\text{-}10 \text{ mW/cm}^2$
RF(GSM)	900MHz	$0.3 \, \mu\text{W/cm}^2$	50%	$0.1 \, \mu\text{W/cm}^2$
	1800MHz	$0.1 \, \mu\text{W/cm}^2$		

2.3   Types of Energy Harvesters

To be able to choose the correct energy source for the desired application amongst the numerous types available in our surroundings, it is necessary to not only understand the potential or expected output power from the converter but also the requirements of the device in terms of location and expected performance. The following sections include an overview of the most common, widely available, and currently researched energy harvesters.

2.3.1 Light Energy Harvesters (Solar)

Most commonly known as solar cells or panels, these relatively low-cost energy harvesters use the photovoltaic effect to convert light into electricity. Although solar is the most successful renewable technology so far, exhibiting the highest power densities at ~12 mW/cm^2 (RF Wireless World, 2012), it requires some form of energy storage and overcharge protection in the harvester due to the source being unpredictable. The basic principle involves the light being collected and the material absorbing the photons with energies larger than the band gap of the material and generating electron-hole pairs, which are then separated by the electric field, which creates a current proportional to the irradiated light (Falin, 2013).

These devices include indoor and outdoor harvesting of luminous sources, with indoor light being less efficient due to the low-intensity sources. The most common types available include amorphous silicon-based, crystalline-based, and dye-sensitized, which are flexible and can be moulded into various shapes and sizes. Most commercial panels have efficiencies of up to 20%, with researchers nearing 50% in the most recent photovoltaic cells (Center for Sustainable Systems, 2022).

2.3.2 Thermal Energy Harvesters

Considered the second most successful energy harvesters after solar, thermal harvesters gather energy from heat sources such as the human body, appliances, and machines, as well as from ambient conditions, and convert it into electrical energy.

i.   Thermoelectric harvesters

These devices exhibit what is known as the Seebeck effect using structures called thermocouples, where a temperature gradient in the material allows free electrons and holes to move and generate a current flow in the closed circuit (Falin, 2013). Thermoelectric generators (TEG) are highly reliable devices that can generate up to a few mW/cm^2, they are quiet and can be scalable to convert large amounts of energy if required and can operate at temperatures up to 250°C (Enescu, 2019).

ii. **Pyroelectric harvesters**

Pyroelectric electric generators (PEGs) are made of unique materials that possess the ability to sense and respond to external stimuli, in this case, temperature. These materials become electrically polarized when they experience a temperature difference and are characterised by this coupled effect of generating an electric displacement due to a temperature change. PEGs can convert most of the electromagnetic spectrum, including ultraviolet, IR, microwave and X-ray sources into electricity, but unlike thermoelectric, the materials used in these harvesters have the advantage of remaining stable at much higher temperatures ($\geq 1200°C$), increasing their thermodynamic efficiency to over 40% and widening the range of usable sources (Batra & Aggarwal, 2013).

2.3.3 Biological and Chemical energy harvesters

Biochemical energy harvesters include bio-fuel cells that use the chemical energy of elements like glucose and oxygen. Although this represents the advantage of having a constantly available source and being implantable in the human body, they are not available commercially and have a limited working life (RF Wireless World, 2012). These devices can currently generate between 0.1 and 1 mW/cm^2 (Tuna & Güngör, 2015) but research is fast moving into attempting the extraction of power directly from biological cells and its potential use in wireless communications (Catacuzzeno, et al., 2019).

2.3.4 Wind Energy Harvesters

Wind power generation has shown rapid growth during the past two decades due to its appeal as a "free", renewable and environmentally friendly alternative, but similar to solar power, these devices are dependent on their sources being present or active for their harvesting. Because of this, they provide an unsteady output and require strategic placement to maximise their efficiency, often located in secluded areas with no traditional power grids. Traditionally, wind power is achieved by using a wind turbine that relies on the air density and airflow speed, transforming wind into movement and the latter into electrical energy (Tong, 2010), technically making it part of the family of kinetic energy harvesters.

There are two classifications for wind turbines depending on their axis of rotation: the horizontal and vertical axis wind turbines. The first have their axis of rotation horizontal to the ground and are almost parallel to the wind direction, while the second ones are nearly perpendicular to it. Horizontal Axis Wind Turbines are the most commercially available when used for electricity generation due to their energy conversion efficiencies being higher than the vertical-axis alternative (Zhao, et al., 2019).

2.3.5 Water Harvesters

Like wind harvesters, water energy harvesters use their respective source to generate movement, which will then be converted into electrical energy by employing the principles described in section 2.3.6. Hydrokinetic energy relies on an abundant, clean, and renewable source that covers almost 70% of our planet. These harvesters can find supply not only from big bodies of water but also from any natural currents, as well as flowing water in pipes. Unlike wind or solar, hydropower is less dependent on the weather and can be used to store energy for when it is needed on demand (Bai, et al., 2018).

2.3.6 Kinetic Energy Harvesters

As their name suggests, kinetic or mechanical energy harvesters, use vibration or movement as their source to generate electricity. There are three main types of kinetic energy harvesters, which are electromagnetic, electrostatic, and piezoelectric.

This type of harvesting has led to the development of devices such as a capacitive vibration energy harvester, also known as an electrostatic transducer (Basset, et al., 2014; Le & Halvorsen, 2012), a magnetic levitation energy harvester that converts walking and running into useful electric energy (Berdy, et al., 2015), a hand-held electromagnetic device that harvests human body motion (Zhang, et al., 2014), and multiple piezoelectric devices that can found listed in section 2.6.

i. Electromagnetic harvesters

Electromagnetism occurs when a current is briefly induced through a wire due to its relative interaction with a magnetic field, as seen in Figure 2-1 (Pollock, 2014). This principle was demonstrated by Michael Faraday in 1831, known as Faraday's Law, and relates the amount of output voltage to the number of loops in the coil and the rate of change of the magnetic flux (Woodford, 2015). Fleming's right-hand rule is used to determine the direction in which the current flows, while its magnitude can be measured by an ammeter.
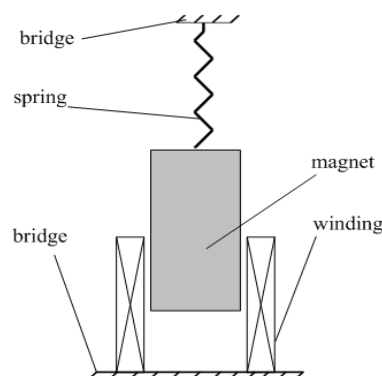
Figure 2-1 Electromagnetic energy harvester (Sazonov, 2004)

These devices present a relatively simple construction, typically based on a spring-mass-damper system, with either a moving magnet or moving coil configuration. Unfortunately, since most of these harvesters produce an alternating current (AC), external components are required to convert this into a direct current (DC) that can be used by the circuit. Additionally, their functionality is typically limited to low frequencies, although their working bandwidths and efficiencies have been improved through advances in fabrication technologies and materials (Muscat, et al., 2022).

ii. Electrostatic harvesters

On the other hand, the electrostatic technique requires two opposite-charged plates to be mechanically forced against one another to generate a charge or voltage (Pollock, 2014), as illustrated below in Figure 2-2. Due to the opposite charges on the plates, an electrostatic force will produce work against the motion, which will then be transformed into electrical energy and stored in a capacitor (Kiziroglou & Yeatman, 2012).
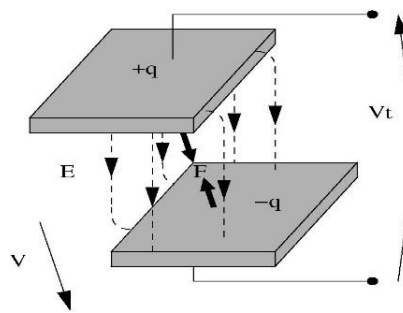
Figure 2-2 Electrostatic harvester (Mitcheson & Yeatman, 2008).

iii. Piezoelectric harvesters

The piezoelectric effect (Figure 2-3) was first discovered by the Curie brothers, Jacques and Pierre, in 1880 (Curie & Curie, 1880). The word "piezoelectricity" comes from the ancient Greek word "piezo", which means stress or pressure (Measurement Specialties, Inc., 1999). When mechanical stress is applied to a piezoelectric material, electrical charges appear between its two opposite sides (direct effect), when an electrical field is applied to this material a mechanical strain is generated (converse effect) (Ueberschlag, 2001).
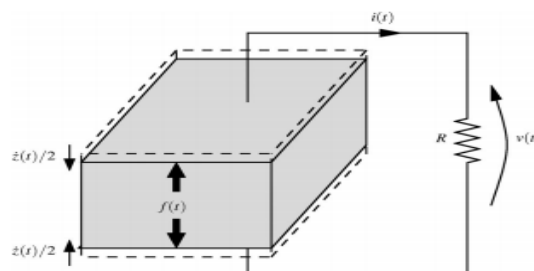
Figure 2-3 Piezoelectric harvester (Mitcheson, et al., 2008).

2.4   Piezoelectricity from a crystallographic approach

As defined in the previous section, piezoelectricity is the charge that accumulates in certain solid materials in response to an applied mechanical strain (IOP Institute of Physics, 2012). Achieving piezoelectricity in these materials is determined by multiple factors, one of them being the specific internal structure and a lack of symmetry within the crystal arrangement (Miclea, 2012). In crystallography, the chemical composition of any solid material is built by the unique position of the different ions that find themselves repeating over and over in the three dimensions throughout space. The smallest repeating arrangement of these ions is known as the unit cell, which with its size, shape and symmetry, will result in a specific orderly stacked structure with translational invariance called *lattice* and will determine the possibility of that crystal exhibiting piezoelectric properties (Miclea, 2012).

Besides the lack of cell symmetry, a characteristic that influences a material's ability to exhibit its piezoelectric properties, is the Curie point or temperature, T_C. This value is where certain materials undergo a sharp change in their magnetic/ferroelectric properties, as going above the T_C will disrupt the atomic arrangements, as illustrated in Figure 2-4, making the material lose its piezoelectricity whilst becoming paramagnetic/paraelectric (Encyclopaedia Britannica, 2022).
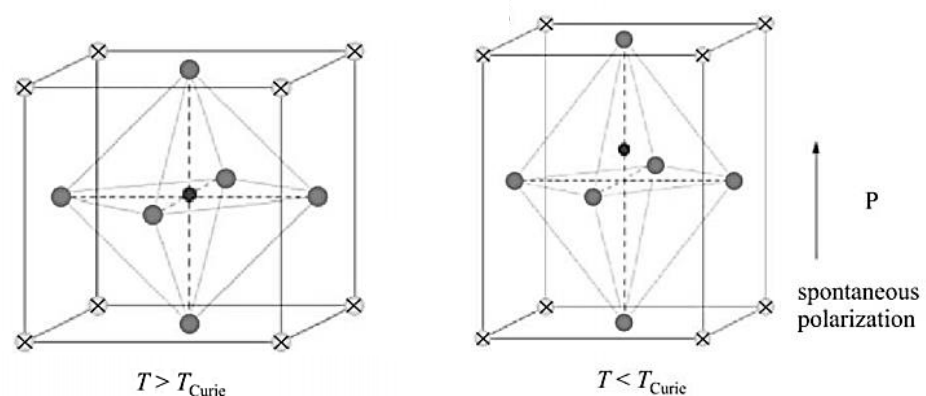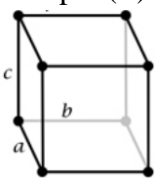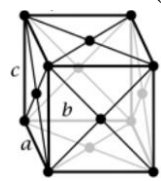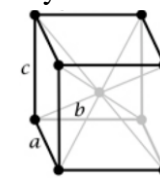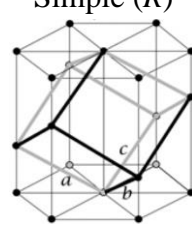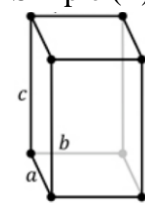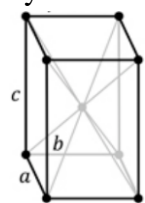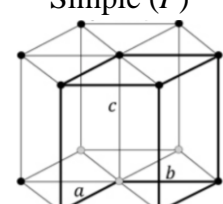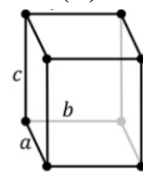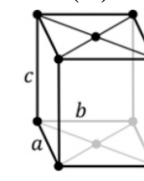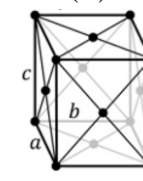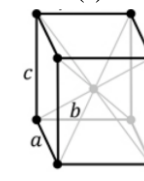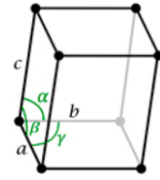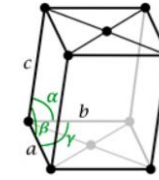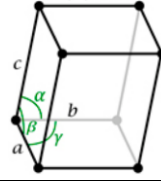
Figure 2-4 Crystal structure above (left) and below (right) the Curie temperature (Cacopardo, 2018).

Out of the 32-point groups in which crystals can be categorised according to the layout of their unit cell, twenty were identified and published in 1910 in Woldemar Voigt's *Lehrbuch Der Kristallphysik* as being piezoelectric (Mends, 2019). Although there are seven main systems into which the unit cell falls, including cubic, rhombohedral, tetragonal, hexagonal, orthorhombic, monoclinic, and triclinic, fourteen subcategories, known as Bravais lattices, are created from these systems depending on the location of the atoms in the cell (Landaua, et al., 1967) and included in Table 2-3.

Table 2-3 Bravais Lattices (Martínez Ripoll, 2002).

Crystal System	Axial Dimensions	Lattice Name (Symbol) & Shape			
Cubic	$a = b = c$ $\alpha = \beta = \gamma = 90°$	Simple (*P*)	Face-centred (*F*)	Body-centred (*I*)	
Trigonal / Rhombohedral	$a = b = c$ $\alpha = \beta = \gamma \neq 90°$	Simple (*R*)			
Tetragonal	$a = b \neq c$ $\alpha = \beta = \gamma = 90°$	Simple (*P*)	Body-centred (*I*)		
Hexagonal	$a = b \neq c$ $\alpha = \beta = 90°$ $\gamma = 120°$	Simple (*P*)			
Orthorhombic	$a \neq b \neq c$ $\alpha = \beta = \gamma = 90°$	Simple (*P*)	Base-centred (*C*)	Face-centred (*F*)	Body-centred (*I*)
Monoclinic	$a \neq b \neq c$ $\alpha = \gamma = 90° \neq \beta$	Simple (*P*)	Base-centred (*C*)		
Triclinic	$a \neq b \neq c$ $\alpha \neq \beta \neq \gamma \neq 90°$	Simple (*P*)			

Based on their cell structure, piezoelectric materials can be classified as tungsten-bronze, bismuth-layered, or perovskites. While tungsten-bronze materials have corner-linked oxygen octahedra with an AB_2O_6 formula, bismuth-layered piezoelectrics have a $Bi_2A_{x-1}B_xO_{3x+3}$ structure consisting of perovskites and $Bi_2O_2^{2+}$, where x is the number of units in the perovskite layer (Miclea, 2012). Finally, perovskites have a cubic lattice, where the ABO_3 formula establishes A^{2+} or A^{1+} cations on the corners, a smaller B^{4+} or B^{5+} cation centred on the body, and O^{2-} anions in the centre of the faces. Amongst piezoelectrics, the best performance is shown by perovskites, making them the main focus of research worldwide (Sezer & Koç, 2021).

2.5   Types of Piezoelectric Materials

There are several types of piezoelectric materials, some are naturally occurring, like bone, wood, tendon, collagen, silk, enamel, quartz, sucrose, topaz, and Rochelle salt, and some are man-made quartz analogous crystals, like gallium orthophosphate and langasite (Mends, 2019). Nevertheless, the most commonly used materials for energy harvesting are polycrystalline ceramics, electrostrictive polymers, piezoelectric single crystals, and thick and thin films (Pollock, 2014). Piezoelectric composites are a booming interest in this field due to their improved properties and reduced flaws, for example, by using different ceramics, one reinforcing the other, or submerging the ceramic in an electrically passive matrix (Wenzheng, et al., 2023).

2.5.1 Piezoelectric Ceramics

Piezoelectric ceramics include perovskites like $PbTiO_3$, $BaTiO_3$, and $SrTiO_3$, which have been of constant interest due to their ferroelectric behaviour and structural phase transitions (Jona & Shirane, 1962). In particular, lead titanate ($PbTiO_3$, PT) is highly important due to its high Curie temperature (T_C), high pyroelectric coefficient, low dielectric constant, and high spontaneous polarization. When combined with other oxides, PT can become the main component in capacitors, ultrasonic transducers, thermistors, and optoelectronics (Migoni, et al., 1976; Wongmaneerung, et al., 2007; Chaudhari & Bichile, 2013). It has also been extensively used in a range of piezoelectric applications, becoming a key part of significant ferroelectric perovskites such as PZT (Chaudhari & Bichile, 2013).

PZT ceramics are said to possess the best piezoelectric, pyroelectric and ferroelectric properties when their composition is near the morphotropic phase boundary (MPB) located between the Ti-rich tetragonal and Zr-rich rhombohedral phases (Benam, 2013), as illustrated in the phase diagram included in Figure 2-5.
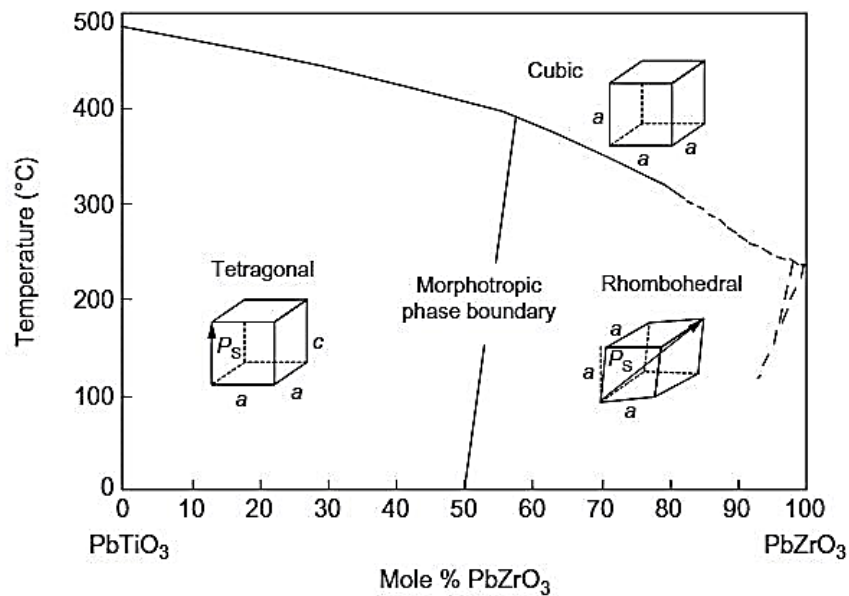
Figure 2-5 Phase diagram of Lead Zirconate Titanate (PZT) (Uchino, 2000).

These materials can be categorised as "soft" or "hard" ceramics. Amongst the two, soft ceramics are characterised by having larger or higher piezoelectric and dielectric constants, permittivity, dielectric losses, electromechanical coupling factors and electrical resistance as well as being easier to polarize or depolarize, while hard ceramics have higher mechanical quality factors and coercive fields as well as better linearity. Although able to produce larger displacements and wider signal bandwidths, soft ceramics are mainly used in sensors rather than power applications due to their relatively lower Curie points ($\leq 300°C$) and difficulty dealing with high-frequency inputs (>10MHz) (APC International, Ltd, 2016).

Unfortunately, these materials pose some challenges due to the required high processing temperatures, polar reorientation, and high manufacturing costs, as well as the potential toxicity of lead-based materials like PZT (Tadigadapa & Materi, 2009). To overcome this, lead-free ceramics like sodium potassium niobate ($NaKNbO_3$), bismuth ferrite ($BiFeO_3$) and sodium niobate ($NaNbO_3$) are being explored (Mends, 2019), as well as developing new polymeric materials in the MEMS field (Liu, 2007) as an alternative.

2.5.2 Piezoelectric Polymers

In 1961, polyvinylidene fluoride (PVDF) was invented, becoming the most cited and commonly used piezoelectric polymer in electromechanical devices, due to its large piezoelectric coefficient compared to other bulk polymers and the strongest piezoelectric response of any commercially available polymer (Liu & Wang, 2023). In 1969, Kawai found out that PVDF becomes strongly ferroelectric after having been subject to the effects of both mechanical stretching and the application of an electrical field (Ueberschlag, 2001).

PVDF belongs to the group of semi-crystalline piezoelectric polymers with a typical crystallinity of 50% that operate similar to inorganic piezoelectric materials (Vinogradov, et al., 2004). The solid polymer films, which are a subcategory of bulk piezoelectric polymers, obtain their piezoelectric properties through their molecular structure and its arrangement (Ramadan, et al., 2014), and range in thickness from 10 to 760µm (Vinogradov, et al., 2004).

PVDF thin films are considered valuable for actuating and sensing applications that piezoceramics cannot achieve (Ueberschlag, 2001). When used in micro-fabricated devices, they have the advantage of mechanical flexibility, dimensional stability, biocompatibility, high dielectric constant and mechanical resistance, lower fabrication cost, faster processing compared to silicon-based polymers, and can be directly used as an active material in transducers (Ramadan, et al., 2014; Ueberschlag, 2001).

Despite their low density, excellent sensitivity, mechanical toughness, and compliance 10 times greater than that of ceramics, they are relatively weak electromechanical transmitters, particularly at resonance and in low-frequency applications (Measurement Specialties, Inc., 1999).

2.6 Applications for piezoelectric materials

Piezoelectrics are often used for medical ultrasounds, acting as a receiver and a transmitter (Lee, et al., 2012), but are also found in gas cooker ignition switches, electric guitar pick-ups, inkjet printers, and mobile phone speakers (IOP Institute of Physics, 2012; Lerch, 1990). Researchers and industries are keen on these materials due to their potential as power sources for micro-electro-mechanical systems (MEMS) since they are lighter, smaller, and more practical to implement in a range of technologies (Shuvo, et al., 2022). Furthermore, the energy density that could be achieved could surpass the values obtained from the electrostatic and electromagnetic alternatives (Richards, et al., 2004).

More complex applications include piezoelectric pumps (Sager & Matice, 1998); converting mechanical vibrations of railway vehicles into electrical power, (De Pasquale, et al., 2011); a piezoelectric generator for converting acoustic energy (Kolm & Kolm, 1984); a one-dimensional thermoacoustic piezoelectric resonator to convert solar or waste heat energy (Smoker, et al., 2012); energy harvesting from the firing acceleration as well as the vibratory motion and spinning of munitions during their flight (Rastegar, et al., 2006).

Despite being very brittle and encountering PbO volatilization and high porosity during its sintering, as seen with PT (Wongmaneerung, et al., 2007), PZT is widely used for energy harvesting due to their good coupling coefficient (Pollock, 2014) and demonstrating efficiencies above 80% (Flynn & Sanders, 2002). Some of the applications include PZT being used to generate electricity from human movement by integrating it beneath a standard running shoe's removable insole (Paradiso & Starner, 2005), as well as being placed in a shoe heel inside a holder that directs the pressure from walking towards the middle point of the harvester while protecting it from excessive pressure (Leinonen, et al., 2014).

Alternatively, amongst its applications, PVDF was proposed as the base for a power supply that could be surgically implanted in an animal to convert its breathing into electrical power (Hausler & Stein, 1984). Energy harvesting systems that employ piezoelectric polymers also include the energy harvesting eel, using the energy from oceans and rivers as a source (Taylor, et al., 2001), and mounting piezoelectric polymers in windmills to harvest the wind (Schmidt, 1992). Even though PVDF has been widely used as films and bulk materials, creating fibres from granules by continuous melt extrusion and in-line poling has become an alternative morphology for e-textile applications (Wan, et al., 2023).

2.7   Methods for synthesising piezoelectric ceramics

The are several available methods can be employed to prepare piezoelectric ceramics. Two of the most popular are presented below, one physical and one non-physical. The physical technique was the one chosen to synthesize the material studied in this project.

2.7.1 Sol-gel Method

Amongst the non-physical routes, sol-gel, coprecipitation and hydrothermal are the most relevant. The reaction in all these methods takes place at the molecular level. The sol-gel method starts with a silicate solution that goes through a hydrolysis and polycondensation process to form a sol, which will then be transformed into a gel through gelation. After going through ageing, drying, densification, and crystallization, the latter will become a porous 3D network of silica in the form of a dry gel (Neacşu, et al., 2016).

This method benefits from producing a wide range of morphologies such as films, powders, fibres and monoliths, with a high degree of homogeneity and potential control over the texture and surface, otherwise difficult with the physical alternatives (Miclea, 2012). Additionally, it has low production costs and can be used at room temperature, offering an ample variety of novel and functional materials (Aguilar, 2018).

Nevertheless, due to the slow deposition rate and high level of stress experienced by the material during processing, the sol-gel method is not suitable for the production of high-quality films that are a few microns in thickness, which are highly desirable for ultrasonic applications with ultra-high operating frequencies (>100 MHz) (Liu, et al., 2013).

2.7.2 Conventional Ceramic Method

Regarding the physical routes for synthesising these materials, the conventional ceramic method involves the weighing and mixing of the stoichiometric amounts of the starting chemicals, usually employing high-speed ball milling, followed by the calcination of the mixture at high temperatures, where the sought solid-state reaction is reached (Miclea, 2012). Although the temperatures to achieve this may vary depending on the composition, calcination usually takes place below 1000°C (Miclea, 2012). Alternatively, the mechanochemical synthesis has particulate collisions that occur during milling being responsible for inducing the chemical reaction, and since no calcination is needed, a more structurally and chemically homogenous product is produced (Miclea, 2012).

When the ceramic method is carried out as a two-stage process, the calcined material is put through a second grinding, where binders can be added to aid the cohesion of the particles and help reduce brittleness and other associated defects by improving the ceramic's mechanical strength (Sangawar, et al., 2001). The most popular binders for piezoceramics include organic materials like polyvinyl alcohol (PVA), starches, methylcellulose and derivatives, polyethylene glycol, paraffins and polyacrylates (Sangawar, et al., 2001).

A mould or die set is typically used to shape the mixture using a hydraulic or mechanical press. The amount of force, pressing speed, die design and pressing technology will vary on the amount, consistency, and composition of the material. Within the press technologies, the uniaxial pressing of single or dual action is the most common due to its flexibility, cost-effectiveness, short cycle time and control over its compression rate (APC International, Ltd., 2015).

Once finished, the resulting product is placed under a second high-temperature treatment, known as sintering. Whilst calcination is commonly used at temperatures below the melting point of the material and is related to changing the phase of a sample without particularly affecting the particle size (CM Furnaces Inc., 2015), sintering is achieved at even higher temperatures (>1000°C) that will cause densification by changing the particle size and cohesion of the material but without surpassing its melting point (Basheer, 2014).

2.8 PbO volatilisation and methods of compensation in the conventional ceramic method

One of the drawbacks associated with the preparation of lead-based piezoelectric ceramics like PZT through the conventional ceramic method is the lead loss that can occur due to the volatilisation of PbO at temperatures near or above 887°C (Haynes, 2015). If left uncompensated, this will affect the final composition of the material along with the phase formations, degrading its piezoelectric properties and performance, increasing the associated porosity and likelihood of microcracking caused by the cooling-induced stress, which could lead to spontaneous fracture (Wongmaneerung, et al., 2007; Chaudhari & Bichile, 2013).

Many groups report that the loss of lead may be minimized by sintering the compacted powders in a surrounding lead-based powder or a PbO vapour atmosphere, although this may lead to a Pb gradient in the final sintered product (Hong & Wei, 2000). The porosity issue caused by this has also been largely addressed through particle size control of the starting powder, which can potentially be improved by choosing a better method or parameters for milling, higher quality starting oxides and the use of binders.

2.9 Density of piezoelectric ceramics

One of the physical characteristics that reflects the quality and therefore, the success of the sintering process in piezoceramics, is their density. Densification is an important property since it not only relates to the grain size growth in crystalline materials like PZT (Yeheskel, 2018), but it is also a key factor for energy harvesting as the materials employed need to be dense enough to withstand the constant strain from the motion or vibration being harnessed without breaking. Denser ceramics lead to a reduced number and size of pores, thus making them the best option for this process as they will be less prone to cracks when being subjected to compression. In general, ceramics are considered of medium density, exhibiting higher values than polymers but less than metals (Bayne & Thompson, n.d.).

Density refers to the level of compactness of a material and is usually defined as the quotient of the mass per unit volume. While the mass can be obtained using a high-precision scale, the volume is typically found through the dimensions of the element. Nevertheless, the morphology of the material might not allow direct measurements to be taken, in which case, the law of buoyancy can be used by fully submerging the object in a fluid and measuring the displaced volume (Molland, 2008).

It is worth noting that the concept of crystallographic density differs from the true density of a material, as it refers to the mass per unit volume of the unit cell. As previously mentioned, the unit cell is a three-dimensional structure containing the smallest repeating group of atoms that provides the overall symmetry of a crystal and will define its system and lattice depending on its arrangement (BYJU, 2020). As with any other 3D structure, its volume can be determined using the dimensions of the cell, while its mass equals the sum of the mass of each atom inside, which can be obtained by dividing its molar mass by Avogadro's number ($N_A = 6.02214076 \times 10^{23}$ mol^{-1}).

2.10 Lapping

Lapping is a finishing process reserved for products that demand highly precise levels of flatness, parallelism or thickness, in which a loose micron-sized abrasive, usually diamond, aluminium oxide or silicon carbide, is used to carefully produce the desired surface roughness and accuracy by using an oil or water-based carrier vehicle and gradually removing layers through a rolling or sliding motion (Lapmaster Wolters, 1998). The process can be done through the use of a machine, as depicted in Figure 2-6, or can be done manually.
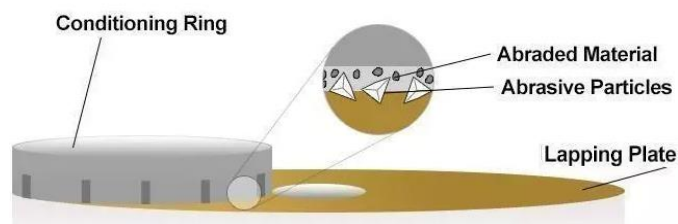
Figure 2-6 Machine lapping and labelled components (Kermet International Ltd, 2019).

Machine lapping involves placing the material under a holder or conditioning ring on top of a moving lapping plate while the abrasive is fed as a slurry, slowly modifying the workpiece by detaching microscopic chips of the material until the desired amount (between 5 and 500 microns) is removed from each side (Kermet International Ltd, 2019). When a lapping machine is not available, completing the process by hand involves performing the sliding motion by manually applying a small amount of pressure on the sample holder whilst moving it around the lapping plate coated with the abrasive and the liquid vehicle.

Multiple factors need to be considered during the lapping process including the type of workpiece and its required pressure, the speed, material, temperature and flatness of the lapping plate, the size and type of abrasive, the vehicle used and its ratio with the abrasive, and the feed system being employed (Lapmaster Wolters, 1998).

Before electrodes can be applied, piezoceramics need to be lapped and cleaned to reach the desired dimensions and achieve a smooth surface after eradicating superficial defects or contaminants. After lapping has been completed and prior to the electrode placement, the surface can be polished with a micron-sized aluminium oxide abrasive to either produce a reflective appearance, improve the electrical contact or optical qualities of the material, or obtain an optimum sealing surface (Kermet International Ltd, 2019).

2.11 Electrode Placement

Electrodes are solid electric conductors, usually metal, placed on the surface of non-metallic materials, gases, plasmas, or vacuums to carry electric currents (Dingle, 2021). The positive electrode is called the anode and is the one responsible for receiving the electrons, while the negative or cathode is where they emerge. Electrodes are a central aspect of the poling process for piezoelectric materials, as they are responsible for allowing the piezoelectric properties to be enabled by providing a contact surface where the external electric field can be applied evenly so the internal dipoles of the material can be aligned.

Furthermore, electrode placement is also a vital part of the piezoelectric harvester design since it is the only way of conducting the electric response the piezoelectric element generates when compressed, to the load circuit (Fu, et al., 2018). Since their placement can improve or worsen the material properties depending on their type and quality, it is imperative to choose the right ones for the intended material and purpose.

Additionally, it is also important to select a material that can withstand the temperatures the device will be exposed to, whether that is through preparation processes like curing, quenching, or poling, or the electronic adaptation and intended functional testing conditions of the final harvesting device. They can be made of gold, silver, and platinum, amongst other metals, like chromium or nickel, and they can be applied manually or through different automated processes, like sputtering. Fired on silver, heat-cured silver epoxy and nickel platting can be found amongst the most standard electrodes, where most wires can be soldered or bonded with similar silver epoxies (APC International, Ltd, 2016).

Although nickel can withstand extreme environments, silver electrodes are cost-effective and easy to work with. They can be used as a solid plate or be painted or deposited and cured directly on the material, which is the most common choice for piezoelectric elements due to the wide variety of morphologies (APC International, Ltd, 2016).

Even though this offers the advantage of adapting to any surface shape and better contact with the material, it can also create a short circuit if the paint filters through any pores or cracks.

2.12 Polarization in piezoelectric materials

Piezoelectrics are a special type of anisotropic dielectric, which means that certain physical properties will change depending on the direction they are measured. An electric dipole is an electrically neutral unit where the positive and negative charges do not coincide and are located at a certain distance from each other (Cacopardo, 2018). Piezoelectrics can exhibit electrical dipoles when loaded electrically, although there are certain materials within the piezoelectric family, known as ferroelectrics, which can exhibit spontaneous polarization and electric dipoles even without applying an electric field. It should be noted that every ferroelectric material is piezoelectric but not vice versa (Esterly, 2002).

Piezoelectricity in a ferroelectric material, such as PZT, is achieved when the internal dipoles of the material, formed from its asymmetric atomic structure, are reoriented and aligned in a single direction by the application of an external electric field while below its Curie temperature (T_C). When the field is removed, a remanent polarization, P_r, that also changes with the applied stress, is left, locking most of the dipoles in position (Setter, et al., 2006; Cacopardo, 2018). Polarization is the result of the total dipole moment per unit volume (Cacopardo, 2018). As stated in section 2.4, if the Curie point is exceeded, the piezoelectric properties in a material will disappear as there is no dipole moment when the atomic structure changes to a symmetrical one. The polarization process can be appreciated in Figure 2-7.
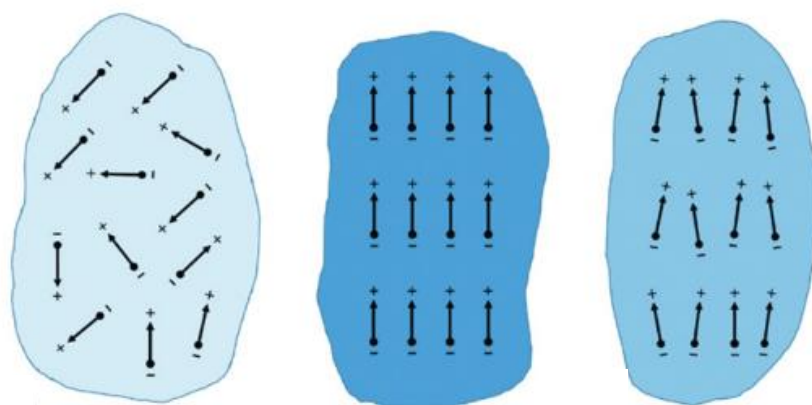
Figure 2-7 Dipoles before (left), during (centre) and after (right) poling (Priya, et al., 2017).

Throughout the process, the material experiences compression in the direction perpendicular to the poling axis, while also slightly expanding in the direction parallel to it.

The resulting properties will be highly linked with the final alignment in the material, which, although never truly complete, will be determined by the strength of the applied field in combination with the chosen temperature (Haertling, 1999). A similar poling process is followed to get an effective piezoelectric response from bulk semi-crystalline polymers, like PVDF. Untreated PVDF can have several crystalline phases and must be mechanically stretched and electrically poled to obtain the necessary phase for exhibiting piezoelectricity (Chang, et al., 2010). In both piezoelectric ceramic and polymer poling, elevating the material's temperature will reduce the required electric field (Ramadan, et al., 2014).

2.13 Dielectric Hysteresis Loops

Originally, the many domains associated with the grains in a polycrystalline material will be randomly distributed creating a zero net macroscopic polarization. When external factors, such as stress, electric or magnetic fields, and temperature changes are applied to the material, these domains will have a direct response and redistribute themselves until a macroscopic polarization is induced (Jin, et al., 2014).

Hysteresis loops (Figure 2-8) are the result of these internal domains spontaneously breaking symmetry and slowly aligning themselves in the direction of the applied field. They represent the polarizing response, *P,* of a material, in relation to the applied external electric field *E.*
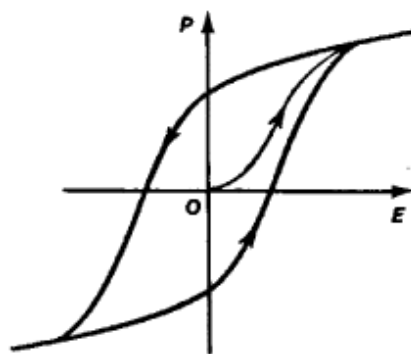
Figure 2-8 Dielectric hysteresis loop showing the polarization P against the applied electric field E
(The Great Soviet Encyclopedia, 2010)

This plotted behaviour can help determine characteristic parameters like spontaneous or saturation polarization (P_s), remanent polarization (P_r), and coercive field (E_c) (Jin, et al., 2014). The shape variations are associated with the poling saturation that occurs at the high field ends, where the material behaves as a linear dielectric, and with the domain switching that occurs near the coercive field, where polarization reversal takes place.

Although these loops should ideally be symmetric, with equal values for the negative and positive P_r and E_c, these are typically influenced by the sample thickness, composition, thermal treatments, and any mechanical stresses or charged defects (Jin, et al., 2014). Ferroelectrics can also present a piezoelectric hysteresis, illustrated in Figure 2-9, where the reverse effect associates the deformation U of the material with the electric field E, but this is not included in the scope of this research.
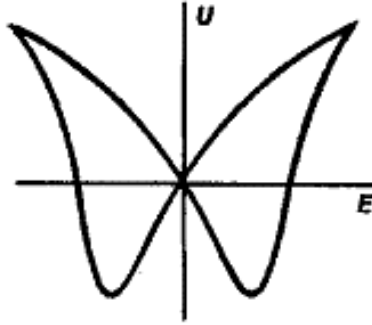
Figure 2-9 Piezoelectric hysteresis loops (The Great Soviet Encyclopedia, 2010)

2.14 Figures of merit (FOM)

A figure of merit or FOM is a numerical quantity that represents the performance, or effectiveness of a material or device based on one or more of its characteristics (Merriam-Webster, 2017). Piezoelectrics have five major figures of merit that can be used to evaluate their energy conversion efficiency, including the piezoelectric charge constant d_{ij}, the piezoelectric voltage constant g_{ij}, the electromechanical coupling factor k_{ij}, the mechanical quality factor Q_m, and the acoustic impedance Z_c (Uchino, 2003).

2.14.1 Piezoelectric strain/charge constant d_{ij}

The strain constant d_{ij} represents the polarization generated per unit of mechanical stress, expressed as $\times 10^{-12}$ C/N (pC/N), or the strain experienced due to an electric field, denoted as $\times 10^{-12}$ m/V (pm/V). Vibrational devices, such as sonar and sounders, benefit from high charge coefficients (Haertling, 1999). The polarization direction or that of the applied field strength can be found in subscript i, while subscript j represents the direction of the applied stress or induced strain (APC International Ltd, 2016). Equations 2-1 & 2-2 relate the stress (T) and strain (S) in the material with the electric field (E) and displacement (D), where d is the piezoelectric charge constant, s is the elastic compliance and ε is the dielectric constant (Miclea, 2012).

$$D = dT + \varepsilon^T E \tag{2-1}$$

$$S = s^E T + dE \tag{2-2}$$

2.14.2 Piezoelectric voltage constant g_{ij}

Similar to the charge constant, the piezoelectric voltage constant g_{ij} represents the ratio between the electric field produced to the mechanical stress (Vm/N), or the mechanical strain experienced per unit of electric displacement applied (m^2/C) (Sensor Technology Ltd, 2019). While the second subscript is the same as above, the first indicates the direction of E, or the direction of the applied electric displacement (APC International Ltd, 2016).

The ability of piezoelectric ceramics to generate high voltages per unit of input stress is also reflected in these coefficients and allows us to evaluate their suitability. This value is related to the charge constant d through equation (2-3), where ε_{ij} is the dielectric permittivity, and ε_0 the permittivity of free space (8.854×10^{-12} F/m).

A high voltage constant in a ceramic usually indicates that a material will present some difficulty or opposition to being polarized, known as a hard ceramic, whilst also presenting a lower dielectric constant (Haertling, 1999).

$$g_{ij} = \frac{d_{ij}}{K\varepsilon_0} = \frac{d_{ij}}{\varepsilon_{ij}} \tag{2-3}$$

2.14.3 Electromechanical coupling factor k_{ij}

The coupling coefficient k represents the effectiveness of converting mechanical energy into electrical, or vice versa (Sensor Technology Ltd, 2019). It is typically found as either the total electrical output divided by the total mechanical input in the direct effect, or the reciprocal of this for the converse effect (Haertling, 1999). Typically, piezoceramics can exhibit 30 to 75% effectiveness depending on their composition and treatment. For example, values can range from $k = 0.35$ for $BaTiO_3$ to 0.72 for materials like PLZT, where higher values are the most desirable and sought (Haertling, 1999). Besides better energy conversion, high coupling will improve the bandwidth and sensitivity of the device (Lee, et al., 2012).

There are different expressions for this factor depending on the morphology of the sample, such as k_p, k_{33} and k_{31}. The values of k_{31} and k_{33} refer to the conversion efficiencies of ceramic rods, where the electric field is parallel to the direction in which the material was polarized, and vibrations are measured longitudinally, perpendicular to the polarization for k_{31} and parallel for k_{33}. For this project, the focus was on the planar coupling coefficient, k_p, as it relates to a thin disk with an electric field applied parallel to the direction of polarization and radial vibrations that are perpendicular to it (APC International Ltd, 2016).

2.14.4 Mechanical quality factor Q_m

This figure of merit represents the ratio of the reactance to the resistance in a piezoelectric resonator while being related to the sharpness of the resonance frequency. It measures the energy decay rate in each cycle of vibrations. (Sensor Technology Ltd, 2019) Q_m can be determined by using the following equation (2-4):

$$Q_m = \frac{1}{2\pi f_r Z_r C_0} \left(\frac{f_a^2}{f_a^2 - f_r^2} \right) \tag{2-4}$$

Where f_r is the resonance frequency (Hz), f_a the anti-resonance frequency (Hz), Z_r is the impedance at f_r (Ω), and C_0 is the static capacitance (Farads)

2.14.5 Acoustic impedance Z_c

Similar to electrical impedance, the acoustic impedance Z_c measures the resistance met by the acoustic flow as it passes through the material (Weerakkody & Morgan, 2005). Defined as the product of a material's density ρ and the sound speed c_j, this FOM is important in piezoelectrics as it reflects the coupling efficiency between a transducer and its application (Bui, et al., 1988). Low acoustic impedance is essential to guarantee the best coupling between the acoustic energy of the device and a low-impedance mechanical energy source.

While piezoceramics tend to have very high values of Z_c even with low k_p, piezopolymers like PVDF offer very low acoustic impedances but would be unsuitable for ultrasonic transducers due to their low coupling factor, low dielectric constant and high dielectric losses; thus, making composites the best alternative to achieve a low impedance device with high coupling factor and low Q_m (Bui, et al., 1988).

The longitudinal sound speed c_j, where the subscript j refers to the direction in which resonance was achieved, can be obtained through equation (2-5), where f_{aj} corresponds to the antiresonance frequency in the open circuit condition and can be taken as the frequency where the maximum electrical impedance is registered (Bui, et al., 1988).

$$c_j = 2(\text{thickness})*f_{aj} \tag{2-5}$$

When looking for the acoustic impedance in a material that has been analysed through radial resonance, the transverse sound speed should be used instead, replacing the thickness with the length or diameter of the chosen sample, depending on its shape.

2.15 Permittivity, relative dielectric constant, and dielectric loss

The dielectric permittivity, ε, is defined as the amount of dielectric displacement experienced by piezoelectric materials per unit of electric field (APC International Ltd, 2016). It can be found through equation (2-6), by measuring the material's capacitance, C, surface area, A, and thickness, h, under an electric field E.

$$\varepsilon = C*h/A \qquad (2\text{-}6)$$

When a superscript is included in this value, it indicates the measurement has been taken under a constant parameter. As with the charge and voltage constants, the subscripts refer to the direction of the components involved in this characteristic, the first indicating the direction of the displacement and the second the direction of the electric field. For example, ε^T_{11} would indicate the permittivity with D and E in the direction perpendicular to the poling direction under constant stress, while ε^S_{11} would represent the value under constant strain in the direction parallel to the one used for poling.

The relative permittivity or dielectric constant, ε_r or K, refers to the ratio between the material's permittivity, ε, and the permittivity of vacuum, ε_0 (APC International Ltd, 2016). The dielectric dissipation factor, *tan δ*, reflects the relationship between the effective conductance, G, and the effective susceptance, B, in a parallel circuit. It is the tangent of the dielectric loss angle, and it is typically measured at 1kHz (APC International Ltd, 2016).

2.16 Chapter 2 Summary

This chapter presented and explored the most relevant information to introduce the field of energy harvesters as a mean to help tackle the current energy crisis being faced in our society. Additionally, a particular focus was given to piezoelectric energy harvesters as the chosen area of study for this dissertation, detailing the various types, their characteristics, advantages and disadvantages, as well as the available fabrication and processing methods. The content is then shifted to define the most important physical and functional properties in piezoelectric ceramics, including the main figures of merit and their dielectric response.

To provide a point of reference or comparison for the data included in the next chapters of this project, various compositions of typical ferroelectric ceramics along with some of their main piezoelectric properties are presented in Table 2-4. This also highlights the range of values that different materials can present based on their composition.

Table 2-4 Compositions and properties of typical ferroelectric ceramics (Haertling, 1999).

Composition	ρ (g/cm^3)	T_C (°C)	K	tan δ (%)	k_p	d_{33} (pC/N)	d_{31} (pC/N)	g_{33} ($\times 10^{-3}$V·m/N)	s_{11}^E ($\times 10^{-12}$m^2/N)
BaTiO$_3$	5.7	115	1700	0.5	0.36	190	-78	11.4	9.1
PZT-4	7.5	328	1300	0.4	0.58	289	-123	26.1	12.3
PZT-5A	7.8	365	1700	2.0	0.60	374	-171	24.8	16.4
PZT-5H	7.5	193	3400	4.0	0.65	593	-274	23.1	16.5
PMN-PT (65/35)	7.6	185	3640	NA	0.58	563	-241	30.1	15.2
PbNb$_2$O$_6$	6.0	570	225	1.0	0.07	85	-9	43.1	25.4
PLZT 12/40/60	7.7	145	1300	1.3	0.47	235	NA	12.0	7.5
PLZT 8/65/35	7.8	110	3400	3.0	0.65	682	NA	20.0	12.4

Amongst the materials included in Table 2-4, different variations of undoped PZT are included, as well as barium titanate (BaTiO$_3$), lead metaniobate (PbNb$_2$O$_6$), lead magnesium niobate-lead titanate (PMN-PT) and a couple of lanthanum doped PZT (PLZT). Although only the undoped PZT can be used for direct comparison with the samples prepared in this work, the other ferroelectrics included show some of the alternatives used for piezoelectric ceramics and illustrate the difference in the main properties of the material.

Chapter 3.   Sintering of Bulk Piezoelectric Ceramic PZT Through a Two-Stage Conventional Ceramic Method

Lead zirconate titanate ($PbZr_{1-x}Ti_xO_3$ or PZT) ceramic disks were sintered following a two-stage method that was created by complementing the procedure mentioned in section 2.7.2 with the teachings of Dr Abel Fundora from the University of Havana, Cuba.

This procedure followed closely the process mentioned by Wongmaneerung, Yimnirun, and Ananta (Wongmaneerung, et al., 2007), which carried out the two stages depicted in Figure 3-1 for the sintering of PT ceramics. The first stage involved heating the material, using a heating ramp of 1°C/min, from room temperature to a temperature T_1 (900°C in Wongmaneerung's research and 800°C for this project), where the sample was left for 2h before cooling it back to T_R using the same ramp rate. In their research, Wongmaneerung included a stop at 600°C for 1h before continuing the process and reaching T_1. This was not followed when sintering the PZT studied in this dissertation, as T_1 was set under PbO's evaporation point (~888°C). The second stage involved a similar process, reaching a set temperature T_2 (1200°C) in one single step.
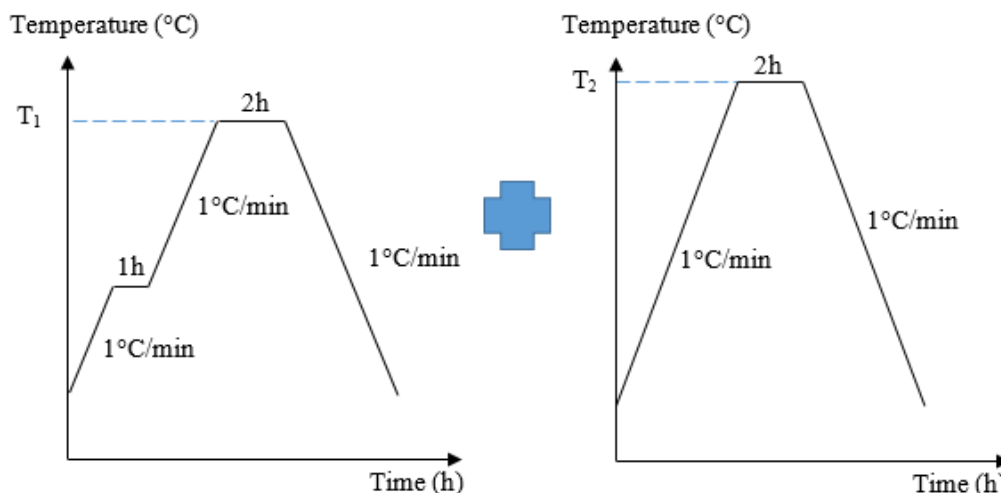
Figure 3-1 Two-stage ceramic method used in (Wongmaneerung, et al., 2007).

The sintering of the samples was accomplished thanks to the combined provision of equipment, materials and guidance obtained from the Autonomous University of Nuevo Leon (UANL), Mexico; the University of Havana, Cuba; and the School of Chemistry in the University of Glasgow, UK; which are acknowledged at the beginning of this thesis, and their specific contributions, recognised. The steps followed, as well as the materials and equipment used, are presented, and described in the following sections.

3.1 Weighing of parent materials/oxides

To understand the effects chemical purity can have on the piezoelectric properties of PZT ceramics and thus any significant cost implications for larger-scale production, two different grades of purity were used for the required parent oxides in their powder presentation. Lead (II) oxide (PbO) at 99% (Jalmek, 1317-36-8), zirconium (IV) oxide (ZrO_2) at 99% (Sigma-Aldrich, 1314-23-4) and titanium dioxide (rutile) (TiO_2) at 97% (DuPont Ti-Pure R-104, 13463-67-7), were used to sinter the "Low Purity" (LP) samples. PbO at 99.9% (Aldrich, 1317-36-8), ZrO_2 at 99.8% (Koch-Light Laboratories, 8869h) and TiO_2 at 99.99% (Sigma-Aldrich, 1317-80-2) were used to sinter the "High Purity" (HP) ones. The atomic weights of the elements involved are presented in Table 3-1.

Table 3-1 Atomic weights of elements involved (IUPAC Commission on Isotopic Abundances and Atomic Weights., 2021).

Element	Atomic Weight
O	15.9994
Pb	207.2000
Ti	47.8800
Zr	91.2240

Due to the nature of the chemicals involved in the preparation of the samples, particularly considering the hazards associated with lead oxide and its potential toxicity, it was imperative that personal protective equipment (PPE) was worn at all times when handling any of the oxides throughout the steps described in this and the following sections. The PPE included the use of nitrile gloves, disposable face masks, and safety glasses, as well as wearing appropriate work clothing that would cover the majority of any exposed skin. Furthermore, adequate ventilation in the laboratory and containment of the chemicals was necessary to reduce the risk of cross-contamination, inhalation, ingestion, or contact.

Contaminated gloves and face coverings were disposed of after each use per applicable laws and good laboratory practices. Additionally, before and after wearing the PPE, hands were washed and dried thoroughly. It is worth mentioning that none of these powders should be discharged into the environment or allowed to enter the drains as their effects would be harmful and deteriorating. Sections of the safety data sheet (SDS) for PbO, identifying all its hazards, are presented in Appendix A. Although TiO_2 and ZrO_2 are not considered hazardous compounds, their complete handling instructions can be found in their SDS. (Merck Life Science UK Limited, 2019; Merck Life Science UK Limited, 2019)

Before any chemical equations were established, it was necessary to decide which value of x in the PbZr$_{1-x}$Ti$_x$O$_3$ formula was best. From the information presented in the literature review (section 2.7.2), it was identified that piezoelectric and dielectric properties have shown particularly sharp maximums (d_{33}~300pC/N and K~1300) when the composition for PZT is chosen near the morphotropic phase boundary (MPB), a region that experiences a phase coexistence between the Ti-rich tetragonal and Zr-rich rhombohedral phases (Noheda, 2002; Sundar, et al., 2018). Although the exact value of the MPB can vary from sample to sample, amongst research aiming to obtain the best piezoelectric properties from PZT ceramics, $x = 0.47$ has been widely used.

Because of this, three values were chosen close to the assumed MPB ($x = 0.47$) and used in the equations for both degrees of purity employed. These values were set as *0.46, 0.47* and *0.48*, and represent the percentage of TiO$_2$ present in the B cation located in the centre of the unit cell, which is shared with ZrO$_2$. The chemicals were weighed following the stoichiometry included in section 3.1.1, using a FA1204B Electronic Balance (China) for the LP chemicals (Figure 3-2), and an A&D GR-300 Analytical Scale (Japan) for the HP ones (Figure 3-3), both with a 0.1mg precision.

Figure 3-2 Analytical scale FA1204B weighing low purity ZrO$_2$ (left) and PbO (right).
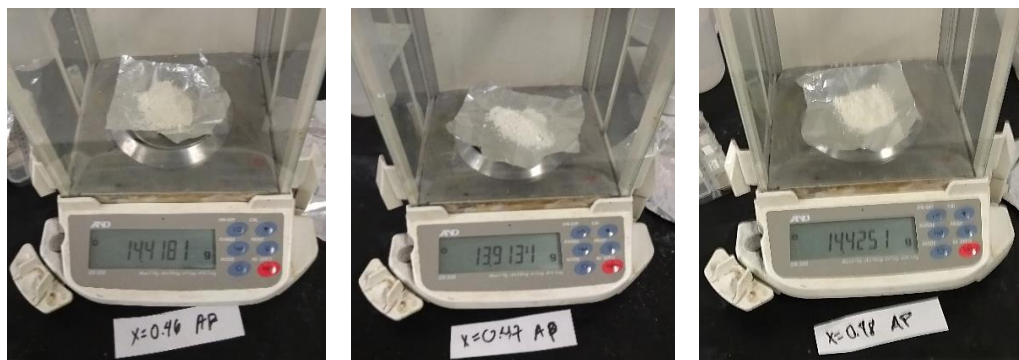
Figure 3-3 A&D GR-300 Analytical scale weighing high purity PZT chemicals for compositions 0.46 (left), 0.47(centre) and 0.48 (right).

3.1.1 Stoichiometric amounts for synthesising low and high-purity PZT

   Tables 3-2 to 3-4 show the stoichiometric equations used to obtain the desired amount of the low and high-purity PZT starting mix for the three different chosen compositions, i.e., $x = 0.46, 0.47, 0.48$. Each table first presents the total atomic weight of each parent oxide and the final PZT mix based on the specific value of x and their chemical formula, followed by the adjusted amounts needed to produce 15g of each composition, which is then adjusted to consider the purity of each chemical, thus presenting the final amounts required for the LP and HP PZT mixes.

Table 3-2 Stoichiometry for 15g of low and high purity PZT with x = 0.46.

Stoichiometric formula	PbO	+	(1-x) ZrO$_2$	+	xTiO$_2$	=	Pb(Zr$_{1-x}$Ti$_x$)O$_3$
Equation with *x = 0.46*	223.1994	+	66.5403	+	36.7442	=	326.4840
Equation for 15g	10.2547	+	3.0571	+	1.6882	=	15
Adjusted to LP oxides	10.3583	+	3.0880	+	1.7404	=	15.1867
Adjusted to HP oxides	10.2650	+	3.0633	+	1.6883	=	15.0166

Table 3-3 Stoichiometry for 15g of low and high purity PZT with x = 0.47.

Stoichiometric formula	PbO	+	(1-x) ZrO$_2$	+	xTiO$_2$	=	Pb(Zr$_{1-x}$Ti$_x$)O$_3$
Equation with *x = 0.47*	223.1994	+	65.3081	+	37.5430	=	326.0505
Equation for 15g	10.2683	+	3.0045	+	1.7272	=	15
Adjusted to LP oxides	10.3720	+	3.0349	+	1.7806	=	15.1875
Adjusted to HP oxides	10.2786	+	3.0105	+	1.7273	=	15.0165

Table 3-4 Stoichiometry for 15g of low and high purity PZT with x = 0.48.

Stoichiometric formula	PbO	+	(1-x) ZrO$_2$	+	xTiO$_2$	=	Pb(Zr$_{1-x}$Ti$_x$)O$_3$
Equation with *x = 0.48*	223.1994	+	64.0759	+	38.3418	=	325.6171
Equation for 15g	10.2820	+	2.9517	+	1.7663	=	15
Adjusted to LP oxides	10.3858	+	2.9816	+	1.8209	=	15.1883
Adjusted to HP oxides	10.2923	+	2.9577	+	1.7664	=	15.0164

3.1.2 Non-stoichiometric amounts of PbZrO$_3$ (PZ) for lead compensation

   As mentioned in section 2.8, creating a PbO-rich atmosphere is necessary to help the PZT samples maintain their composition during the sintering process, where they tend to experience PbO losses due to high temperatures. To aid with this issue, non-stoichiometric PZ disks of both purities were prepared, and the calculated necessary amounts are presented in Table 3-5. These calculations need to be non-stoichiometric so the bond between the PbO and ZrO$_2$ remains unstable, thus easily liberating lead oxide into the environment when reaching the required temperatures.

Non-stoichiometric formula	0.8PbO	+	ZrO_2	=	$PbZrO_3$
Non-stoichiometric equation	178.5595	+	123.2228	=	301.7823
Equation for 30g of LP PZ	17.9298	+	12.3732	=	30.3030
Equation for 25g of HP PZ	14.8069	+	10.2284	=	25.0353

Since the amount of PZ required to compensate each sample is half of its corresponding PZT weight, at least 22.5g of PZ is needed to cover all three compositions within each purity. The amounts made exceeded this to account for any powder loss during handling and for potential tests with PZT samples of the opposite purity. A bit more LP atmosphere was made compared to the HP one due to its lower cost regarding parent oxides.

3.2 The mixture of the weighed parent oxides

After being weighed, each of the three compositions for both purities of PZT and PZ were individually ground in a planetary ball mill. The mixes were made into a slurry for this process by adding a non-reactive liquid, such as pure ethanol or 90% isopropyl alcohol, as it has been found to help achieve a higher degree of homogeneity. Since both liquids evaporate when left to dry, leaving the raw starting mix unaltered, they are considered entirely interchangeable and/or substitutable. An exact measurement of these solvents is not required, although adding too much can cause the mix to overflow or escape the container during the process due to the high speeds and will make the drying process much slower. Regardless of the planetary ball mill used, the container should always be left with one-third of the space empty to allow the centrifugal action to be effective (Fritsch GmbH, 1987).

The high-purity PZT and PZ atmosphere powders were placed in separate agate containers along with a sufficient amount of pure ethanol to keep the mix wet and 20 small agate balls, as shown in Figure 3-4, which were then securely clamped in the Restch© planetary ball mill PM 100 (Germany) depicted in Figure 3-5, for 1h at 250rpm.

Figure 3-4 Ball mill agate container with HP PZT wet mix and twenty 1 cm agate balls.

Figure 3-5 Retsch® planetary ball mill PM 100 and inner container holder with counterweight.

The agate balls used were each 1cm in diameter and weighed 25g altogether, giving a ratio of ~1.67g of agate/g of HP mix or ~0.7 cm^3/g. The container was checked after 30min to make sure the mix was still wet, then placed back into the machine to finish the process.

The lower purity PZT and PZ compositions were ground with 90% alcohol in an agate container with three and five agate balls, respectively, inside the Fritsch® pulverisette 5 planetary mill (Germany) shown in Figure 3-6. The agate balls were 1.9cm in diameter and weighed 9.89g each. The resulting ratio was ~1.93g of agate/g of LP PZT mix or ~0.72cm^3/g considering the total volume of the balls. The LP PZT was ground for 2h at ~260rpm (speed 8 in the rotatory knob), while its PZ atmosphere was left for only 1h. The rest of the process was identical to the HP samples, aiming to achieve a similar homogeneity and particle size in the final product.

Figure 3-6 Fritsch® pulverisette 5 planetary ball mill and inner container holder with counterweight.

The differences between the ball milling done with the HP and LP samples were due to the available equipment at the time of preparation. While the HP samples were made in Prof Duncan Gregory's laboratory in the School of Chemistry at the University of Glasgow, the LP ones were prepared under the supervision of Dr Abel Fundora in the Material Science and Technology Institute at the University of Havana, Cuba.

Although the rotational speed, agate balls to mix ratio, and grinding time were tried to be kept as close as possible in the two processes, there was still a slight difference in the total weight of the balls used and the speed chosen, as well as the total duration of the wet ball milling. Nevertheless, it is believed that these minor differences did not affect the characteristics of the powders since having a slightly higher ratio and speed in addition to double the duration for the LP mixes, helped compensate for the fact that employing larger balls would have left the final product with a bigger particle size. This is further explored as part of the microstructure analysis included in Chapter 4 section 4.2.1.

Ratios and particle size of the PZ powders were not as important since the material is only intended as a sacrificial element in the sintering process, but the parameters used were still accounted for as specified in the previous paragraphs.

A possible low-cost alternative to ball milling, used on piezoelectric samples that are not discussed in this project, includes hand grinding the powders with an agate pestle and mortar for 2h at room temperature (T_R) while keeping the mixture wet with ethanol or other non-reacting liquid (Figure 3-7). This process should be carried out inside an extraction chamber, following the proper safety guidelines to prevent inhalation and contamination. Like planetary ball milling, this process is done using agate materials since the PbO in the mixture cannot abrade it, thus preventing any potential contamination.

Figure 3-7 Wet hand grinding of PZT done with previous samples.

Finally, to allow for the most accurate conclusions to be drawn from the analysis and tests performed on the samples and included in the following chapters, it should be noted that another batch of PZT disks from composition 0.46 LP had to be made due to accidental cross-contamination of the first powder mix that was made in Cuba. These samples followed the same process as the one done for all three HP compositions, using 20 agate balls in the Restch© planetary ball mill for 1h at 250rpm. The original LP PZ mix was not affected.

3.3   Drying the wet mixture of oxides

Once the ball milling was done, the resulting low-purity mixtures, including the second attempt of composition 0.46, were dried inside a fume cupboard or extraction chamber by placing the open agate container inside, covered with a piece of paraffin film or commercially available aluminium sheets to avoid any contamination from external foreign particles. Any product on the lid was scrapped off with a stainless-steel spatula and added to the rest of the mixture before drying or was left to dry next to the container whilst also being covered. Depending on the wetness of the mixture, this process could take between 24 and 48 hours, but it could be reduced to ~2h by using a heat lamp on the uncovered container, which was implemented for LP compositions.

A faster alternative was used on the HP mixtures, which were placed in their agate containers next to their lids inside a drying oven (Genlab MINO/100, UK) for 2h between 120 to 125°C from T_R, with no specific heating or cooling ramp required. Although this process is faster, it is also more costly and has more risks if the oven or furnace used is shared or malfunctions, which could damage the agate container and alter the mixed material or its composition by starting a premature solid-state reaction.

3.4   Shaping mixture into disks by using a hydraulic press

After the LP and HP mixtures for the PZT and PZ were dried, a stainless-steel spatula was used to scrape off the material from the agate balls and container to try to salvage as much powder as possible and stored in labelled glass vials. The total amount gathered from both PZT purities was then lightly pressed under 1Ton using a manually operated hydraulic press (Figure 3-8 Specac Manual Hydraulic Press GS15011, UK) and a uniaxial 20mm diameter die (Figure 3-9 Across International 20mm Diameter ID Dry Pressing Die Set SDS20, USA). The resulting pressed samples can be seen in Figure 3-10.

Figure 3-8 Specac manual hydraulic press.

Figure 3-9 20mm dry pellet pressing die set.
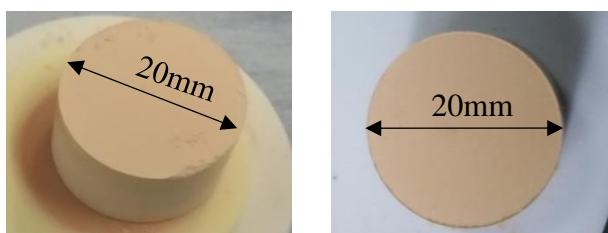
Figure 3-10 Lightly pressed LP PZT mix on alumina bases with a 20mm diameter.

3.5   Calcination of the lightly compressed dry mixture of oxides

The first part of the two-stage ceramic method followed in this project involves the calcination of all the lightly compressed PZT mixed oxide powders at 800°C (T_1) in air. This process starts changing the phase structure of the ceramic but without affecting its density, allowing the perovskite structure to be obtained in the material.

The pellets are placed in closed alumina crucibles inside a high-temperature furnace (Figure 3-11), until T_1 is reached from room temperature (T_R ~22°C), with a 1°C/min heating ramp. After 2h at 800°C, the samples are cooled down to T_R at 1°C/min. The specified ramp rates must be followed to achieve the proper solid-state reaction over the samples' volume.

Figure 3-11 Sealed HP PZT pressed compositions placed inside a Lenton Furnace before calcination.

A Vecstar LF3 Chamber Muffle Furnace with Eurotherm temperature controller 2416 (Figure 3-12, UK) was used for the LP samples, while a Lenton Laboratory Chamber Furnace with Eurotherm temperature controller 3216 (Figure 3-13, UK) was employed for the HP ones. Since calcination occurs below the melting point of PbO (~887°C), it does not require a fume or extraction chamber, although it is still recommended as a safety measure.

Figure 3-12 Vecstar chamber muffle furnace with Eurotherm 2416 controller.

Figure 3-13 Lenton Chamber Furnace with Eurotherm 3216 controller.

After calcination was completed, the distinctive orange colour that is characteristic of lead-based starting powders, which can be observed in some of the images in sections 3.2 and 3.4 of this chapter, as well as the left image in Figure 3-14 below, changed to a very light pale yellow, as shown on the right image of the same figure.

Since the calcination temperatures (800°C) are kept under the evaporation point of PbO (~888°C), lead volatilisation would not be expected to happen during this stage. Therefore, this physical change exhibited by the resulting samples and exemplified in Figure 3-15, would have no relationship with any PbO loss and instead would indicate that an internal transformation has occurred in the material and that the desired solid-state reaction has taken place. In this case, the starting PbO powder has changed from litharge, with a tetragonal structure, to massicot, with an orthorhombic lattice after surpassing ~500°C (Pavlov, 2011).

Figure 3-14 LP 0.47 PZT compressed pellet before (left) and after (right) calcination at 800°C.

Figure 3-15 Resulting pressed pellets of high purity PZT compositions 0.46 (left), 0.47 (centre) and 0.48 after calcination at 800°C.

3.6   Second ball milling and drying of calcined PZT samples

Before the second stage of the ceramic process, the calcined compressed PZT was roughly ground with an agate pestle and mortar before putting it through a second wet ball milling process. The resulting slurries from each purity mix inside agate containers are shown in Figure 3-16. This second ball milling followed the same specifications as the ones indicated in section 3.2.

Figure 3-16 Wet LP (left) and HP (right) PZT mix after second ball milling.

Afterwards, each PZT mixture was dried as described in section 3.3 and then stored in glass vials after gathering the material with a stainless-steel spatula. Figure 3-17 shows the open agate container with LP PZT mix left to dry overnight after the second ball milling.

Figure 3-17 Drying LP PZT mixture overnight at T_R after second ball milling.

3.7 Addition of a binder before sintering of bulk PZT ceramics

As indicated in the literature review, the use of a binder before sintering can be quite useful to improve the piezoelectric properties of ceramics and reduce the possible defects that might occur due to the porous and brittle nature of these materials. Although a 5% binder is usually employed during this process, a 3% Polyvinyl Alcohol (PVA) binder was chosen for this project as this is a water-soluble synthetic polymer that will evaporate at ~500°C during the sintering process, leaving fewer gaps in the material.

3.7.1 3% PVA binder incorporation to PZT dried calcined mixture

A 3% PVA binder was prepared in a weight-volume (w/V) dissolution by adding 600mg of PVA powder (Sigma-Aldrich, 98% CAS: 9002-85-5) into a 20mL solution made with ethanol and deionized water (50/50). The mix was placed in a beaker on a stirring hot plate (Figure 3-18 Thermo Fisher Scientific SP142025Q Cimarec, USA) and stirred at 700rpm (speed 7) while being heated at 125°C until turning completely transparent, as seen in Figure 3-19.

Figure 3-18 Stirring hot plate used to prepare polyvinyl alcohol (PVA).

Figure 3-19 Polyvinyl alcohol (PVA) binder at 3%.

Although there is no standard specified, as this varies depending on the material and desired properties, Dr Abel Fundora indicated that one drop of the resulting PVA solution should be added as a binder per gram of each of the dry calcined PZT powders and incorporated through a 30min manual grinding in an agate mortar at T_R (Figure 3-20). The consistency sought is that of a loose powder that would stick in a clump to the bottom of the agate pestle when pressed against the sides of the mortar in a sliding motion and then lifted.

Figure 3-20 Agate pestle and mortar used to incorporate PVA binder to calcined PZT powders.

3.8   Pressing of PZT ceramic pellets for sintering

The resulting PZT mixtures and the saved PZ atmosphere powder were pressed into 20mm wide disks employing the same equipment and tools as described in section 3.4. Unlike the previous shaping, where all the powder was compressed under 1Ton into a single cylinder, each PZT composition was divided into several thin disks and pressed under 4Tons per disk. For each PZT disk, there was a PZ one made to be used as a PbO compensator during the sintering process. Each non-stoichiometric atmosphere disk weighed approximately half of its corresponding PZT counterparts.

Since compositions 0.47 and 0.48 LP were the first to be made, the original 15g that were prepared for each PZT composition was expected to be divided into 5 samples, each weighing less than ~3g, due to the anticipated loss of material between steps of the ceramic process. Although composition 0.47 was pressed into five disks, each weighing ~2.84 ± 0.05g, it was found that composition 0.48 had lost more material along the process and only four disks could be pressed, with three of them weighing ~2.88 ± 0.07g and the last one weighing only 2.48g.

Following a similar process, the 0.47 HP mix was pressed into 5 disks, each weighing ~2.76 ± 0.02g. On the other hand, compositions 0.46 and 0.48 HP only had three disks originally made per composition to reduce the total shaping time, each weighing 2.86g. Nevertheless, a few weeks later, three more samples were pressed for these compositions for additional alternative tests, along with five disks for composition 0.46 LP. These final samples were each made with less than 2g of the material, as it was observed that the disks resulting from the previous pressings were too thick and required a lot more processing to reach the sought ratio between their diameter and thickness ($h < d/16$), which is further explained in section 5.1 of Chapter 5.

Two instances were registered where the disks proved more challenging to press, this was the case for samples 0.46 LP and 0.47 HP. These PZT mixes required multiple attempts to be pressed before obtaining the disks, which might have affected their particle size.

The weight of each sample and their corresponding atmosphere are presented in Table 3-6 below. The identifier that was given to each resulting pellet was merely based on their storage location (box# - cell#) after being sintered and can be found in the last column of the table.

Table 3-6 Weights of each PZT disk and their corresponding PZ atmospheres before sintering.

Composition	PZT (g) ± 0.00005g	PZ (g) ± 0.00005g	PZT disk identifier
0.46 LP	1.9862	0.9930	6-4
	1.9918	0.9959	6-11
	1.9908	0.9954	6-12
	1.9570	0.9785	6-9
	1.9574	0.9787	6-10
0.47 LP	2.7911	1.3870	4-8
	2.8929	1.4519	4-9
	2.8557	1.4278	4-10
	2.7803	1.3949	4-11
	2.8616	1.4394	4-12
0.48 LP	2.8233	1.4075	4-1
	2.4792	1.2308	4-2
	2.8510	1.4102	4-3
	2.9644	1.4784	4-4
0.46 HP	2.8605	1.4301	5-7
	2.8604	1.4311	5-8
	2.8601	1.4301	5-9
	1.9171	0.9586	6-6
	1.9169	0.9586	6-7
	1.9069	0.9536	6-8
0.47 HP	2.7801	1.4102	5-1
	2.7809	1.4108	5-2
	2.7801	1.4110	5-3
	2.7545	1.3773	6-1
	2.7457	1.3728	4-7
0.48 HP	2.8591	1.4301	5-4
	2.8604	1.4301	5-5
	2.8605	1.4301	5-6
	1.9270	0.9638	6-3
	1.9060	0.9531	4-5
	1.9262	0.9634	4-6

3.9   Sintering of PZT piezoelectric ceramic disks

The second and final part of the conventional ceramic method employed to obtain the PZT ceramic disks involves putting the pressed material at 1200°C (T_2) for 2h with the same heating/cooling ramp used during calcination (1°C/min). The elevated temperature sinters the ceramic and alters the particle/grain size causing densification and a reduction of volume. As done through the first stage, the disks are enclosed in sealed alumina crucibles inside high-temperature furnaces located in extraction chambers. The Vecstar LF3 Chamber Furnace (UK) was used to sinter the LP samples, and an Elite Chamber Furnace BCF 13/12 (Figure 3-21, UK) for the HP samples.

Figure 3-21 Elite Chamber Furnace used for HP sample sintering.

3.9.1 Lead compensation during sintering of the bulk PZT ceramic disks

The high temperature required for sintering ($T_2 = 1200$°C), will cause the PZT samples to experience lead oxide volatilisation as it surpasses its evaporation point (~887°C), which, as previously discussed, will change their compositions, and modify the material's piezoelectric properties and performance if it is not compensated. To counteract the PbO loss suffered by the samples, a PbO-rich environment must be created surrounding the pellets that allow them to maintain their stoichiometric compositions and thus, the quality of the sought properties.

To achieve this, the non-stoichiometric PZ disks that were prepared and pressed through the previous steps need to be placed inside the crucibles along with their corresponding PZT samples. From previous piezoelectric ceramic sample preparation not included in this work, it was concluded that the arrangement that resulted in fewer defects on the samples had the PZ and PZT disks in an intercalated vertical layout, starting with a PZ disk at the base of the arrangement, as seen in the images presented in Figure 3-22.

This structure provides the most efficient and evenly spaced PbO compensation, as well as preventing the pellets from sticking to each other or the crucible.
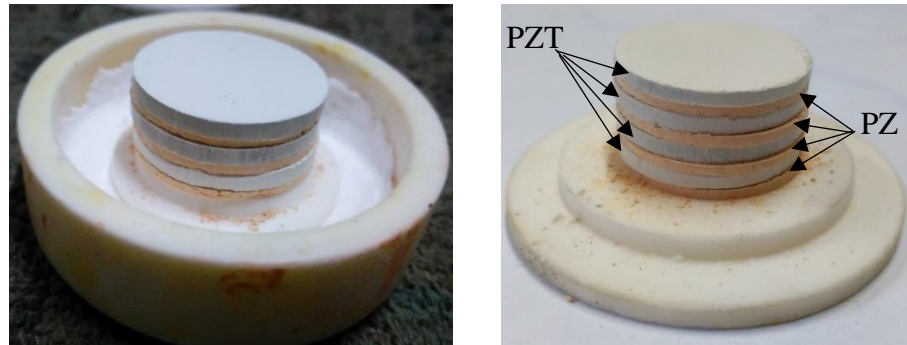
Figure 3-22 LP PZT compositions 0.47 (left) and 0.48 (right) pressed disks in the intercalated layout with their PZ atmospheres before sintering.

Furthermore, it was also established that the best presentation for this method was disks made with the same force and die as the PZT powders but with only half their mass. A powder form of the non-stoichiometric PZ was assessed in previous experiments, and it was found inefficient since it would make the sample stick to the bottom of the crucible, making it too difficult to remove without breaking the pellet. Pure PbO, in any presentation, was also found to be an unsuitable option since it would melt entirely after passing 887°C and would irreparably damage the PZT samples and the container.

A tight seal needs to be created between the crucible and its lid to prevent any PbO from escaping the crucible. Figure 3-23 shows the tightly packed layer of alumina powder that was pressed around the external circumference of the crucible where it met with the lid, using a stainless-steel spatula. The prepared crucibles containing the intercalated arrangement were then placed inside the Elite Chamber Furnace, as shown in Figure 3-24.

Figure 3-23 Alumina crucible being sealed with alumina powder before calcination at 800°C.

Figure 3-24 Sealed alumina crucibles inside the Elite Chamber Furnace before sintering.

It was observed that the compositions that had at least three intercalated PZT disks, had the one located at the top of the arrangement presenting some degree of deformation or curvature on the edges. To minimise this, it is suggested that the structure should finish with a PZ atmosphere disk on top to prevent PbO loss from above. Since the design also needs to start with a PZ atmosphere, an extra PZ disk is required. This extra disk could be made from the non-stoichiometric mixture or from redistributing the initial weighed material before pressing.

Just as with the calcination process, after undergoing this stage, the PZT pellets of both purities experienced several physical changes, including a change in colour from the light pale yellow observed after calcination to a matte grey, and a slight reduction in their dimensions, which is further explored in the next chapter alongside their densities. The PZ disks transitioned from the distinctive PbO orange colour to a stained off-white and became very brittle. This change reflected the PbO loss that was purposely induced in the non-stoichiometric atmospheres and confirmed that the lead-rich atmosphere that was sought to help the PZT samples keep their original composition to achieve optimal performance, had successfully been created. Figure 3-25 shows the resulting PZT and PZ samples for LP composition 0.48 after sintering was complete to illustrate these changes.
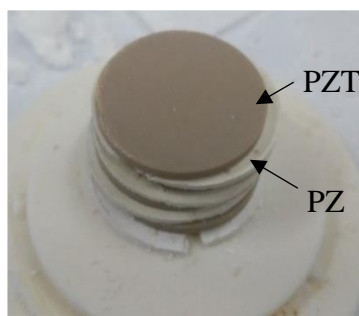
Figure 3-25 LP PZT composition 0.48 (right) after the sintering process

Although the main arrangement for the samples sintered in this study paired the PZT disks with a PZ atmosphere of the same purity, a few samples were made using the opposite grade to identify potential benefits from combining them during the final stage of the process, including associated physical effects and cost implications. For the three HP PZT compositions, PZ disks made from LP chemicals were used to sinter HP/LP sets, while only one set of LP/HP samples was sintered for LP composition 0.46 using HP atmospheres due to time constraints. Priority was given to the HP samples as a better performance was expected from the higher purity chemicals, presenting the biggest economic advantage with the highest efficiency. Figure 3-26 shows the resulting pellets from the 0.47 HP/LP set.
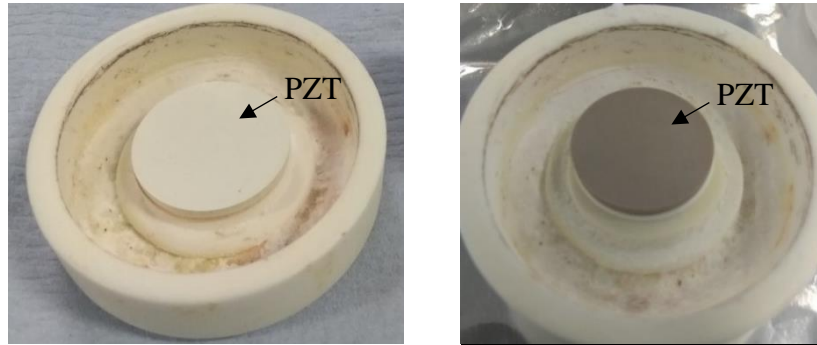
Figure 3-26 0.47 HP/LP PZT/PZ arrangement before (left) and after (right) the sintering process.

3.10 Chapter 3 Summary

The desired material was sintered using a two-stage conventional ceramic method, which required multiple stages of grinding the combined starting powders after these were weighed according to the stoichiometric calculations completed to produce ~15g of each of the chosen compositions of PZT, and two separate heat treatments (800°C for the 1st stage and 1200°C for the second), whilst placing the pressed material inside alumina crucibles that were additionally sealed with alumina powder.

Although the rotational speed, agate balls-to-mix ratio and grinding time were tried to be kept as close as possible during the high-speed ball milling that was performed on all the samples during this process, there was still a slight difference in the total weight of the balls used and the speed chosen for the HP and LP samples, as well as leaving the LP mix for twice the amount of time to compensate for the larger dimensions of the agate balls used.

While it was believed that these minor differences would not affect the characteristics of the resulting PZT pellets in a significant manner, it was later found that the second iteration of the 0.46 LP/LP samples, which underwent the same conditions as the HP pellets, showed smaller grain sizes when compared to the other two compositions in the LP/LP group, suggesting that the increased ball milling times on LP PZT powders, as well as the higher ratios used between the agate and the mix, might not have been enough to match the other parameters employed or the capability of the smaller agate balls to generate a more refined powder mix.

Additionally, it was found that pressing the dried ground powder mix into the desired shape should be done as soon as possible after the PVA binder has been added and combined with the mixture, as this prevents the additive from evaporating and making the sample more

fragile, reducing chances of it breaking during the shaping process. Moreover, the additional hand-grinding that was required every time a sample could not be properly pressed was also identified as being an influencing factor in the amount of PVA left in the mix and should be avoided to reduce any possible modifications to the composition. Less PVA would mean less material evaporates during sintering, leaving fewer gaps and in theory, a denser material.

From the available morphologies, it was concluded that the best presentation for the non-stoichiometric PZ disks was to use half of the PZT mass, pressed with the same dimensions as the PZT pellets but with the grinding and shaping conditions being more lenient than with the main PZT mixtures. This is because the intended purpose of the PZ disks is to release their PbO inside the alumina crucible to create a PbO-rich environment, but the mixture cannot be placed directly on the PZT disks as loose powder as it was discovered this would melt at the high temperatures used for sintering and end up damaging both the crucible and the PZT samples. Therefore, a light pressing is needed to keep the disks together for the process but still allow them to saturate the atmosphere to reduce the PbO volatilisation known to occur in lead-based ceramics.

On top of this, to guarantee the released PbO was kept as much as possible inside the crucible, alumina powder was used to tightly seal the sides of the crucibles after these were placed on their corresponding bases or upside down on their lids, encasing the entire intercalated PZT-PZ arrangement.

A detailed physical and functional characterisation of the resulting sintered disks from each composition is included and discussed in Chapters 4 and 5, respectively.

Chapter 4. PHYSICAL CHARACTERISATION OF THE PZT PIEZOELECTRIC CERAMICS

Ten different sets of samples were sintered through the two-stage conventional ceramic method, as described in Chapter 3. Six sets came from the LP/LP and HP/HP arrangements, three were obtained from the HP PZT with LP PZ, and the final set was for the 0.46 LP PZT with HP PZ. Although ten variations were sintered, due to time constraints and equipment availability, some sections of this chapter involve only the main six sets, pertaining to the compositions where the PZT and PZ were made from the same purity.

The samples' physical characteristics, including their density, microstructure, phase formation and chemical composition are presented and discussed throughout the next sections. Additionally, possible relationships between the results and the conditions that were set and followed through the sintering process in the previous chapter are explored.

4.1 Density of the sintered PZT disks

Following their sintering at 1200°C, the samples were weighed using the A&D GR-300 analytical balance (Japan) with 0.1mg precision, shown in Figure 3-3, while their thickness (mm) and diameter (mm) were measured using a 150mm digital calliper with 0.01mm precision. Being originally pressed with a 20mm diameter mould, the disks showed an average reduction of 2.55mm; which, in addition to the colour variation mentioned in Chapter 3, exemplifies the reactions taking place inside the material and suggests a more compact and less porous material, thus improving its suitability for energy harvesting.

Furthermore, when comparing the weights of each sample before and after sintering, it was noticed that an overall average of 0.0461g of material was lost per sample. The average amounts in mg missing per composition are shown in Table 4-1 along with the values relative to the weights before the samples were sintered (W_0), shown in Table 3-6 in section 3.8.

Table 4-1 Average absolute and relative weight differences of PZT samples after sintering.

Composition	0.46				0.47			0.48		
PZT Purity	HP		LP		HP		LP	HP		LP
PZ Purity	HP	LP	LP	HP	HP	LP	LP	HP	LP	LP
Average ΔW (mg)	36.9	34.4	31.6	27.7	54.7	46.1	91.2	32.9	34.8	35.2
Average ΔW/W₀ (%)	1.4	1.8	1.6	1.4	2.0	1.7	3.2	1.3	1.8	1.3

It can be observed that although the samples lost a maximum of 3.2% of their original mass, confirming a successful PbO compensation, composition 0.47 of both sets made with the same degree of purity for the PZT disks and their PZ atmospheres had the highest relative losses, with the 0.48 sets from the same groups being the ones with the lowest losses after sintering. To analyse this further, the volume of each sample and its absolute error were calculated through equation 4-1, while their density ρ and corresponding absolute error $\Delta\rho$ were determined through equation 4-2. The rules of error propagation were followed, with the instrument errors taken as half of their smallest division. The measured dimensions, calculated values, and uncertainties of each disk can be found in Appendices B & C.

$$V = \pi r^2 * \text{thickness} \quad \rightarrow \quad \Delta V = \left(2* \frac{\Delta r}{r} + \frac{\Delta\text{thickness}}{\text{thickness}}\right) *V \qquad (4\text{-}1)$$

$$\rho = \frac{m}{V} \quad \rightarrow \quad \Delta\rho = \left(\frac{\Delta m}{m} + \frac{\Delta V}{V}\right) *\rho \qquad (4\text{-}2)$$

Tables 4-2 to 4-5 show the absolute density of each pellet with their mean absolute error, which was taken as the average value calculated from all the sintered samples. The identifiers used to differentiate each pellet according to their storage location are included in the second column of each table, while the accuracy percentage when compared to the standard value known for PZT, $\rho_{reference} = 7.50\text{g/cm}^3$ (Sakakibara, et al., 1994), appears on the last column as a relative density. The values from the six main sets, corresponding to the samples made with the same degree of purity for the PZT and their PbO compensation, are presented in Tables 4-2 and 4-3.

Table 4-2 Absolute and relative densities of LP/LP PZT pellets after sintering at 1200°C.

Composition	Pellet identifier	Density (g/cm³) (± 0.03)	Relative Density (%) ($\rho/\rho_{\text{reference}}$ *100)
0.46	6-11	6.50	86.61
	6-12	7.18	95.72
	6-4	7.39	98.48
0.47	4-8	7.22	96.31
	4-9	6.68	89.11
	4-10	7.26	96.85
	4-11	7.23	96.39
	4-12	7.30	97.38
0.48	4-1	7.08	94.40
	4-2	7.05	93.98
	4-3	7.38	98.37
	4-4	7.23	96.40

Table 4-3 Absolute and relative densities of HP/HP PZT pellets after sintering at 1200°C.

Composition	Pellet identifier	Density (g/cm³) (± 0.03)	Relative Density (%) ($\rho/\rho_{reference}$ *100)
0.46	5-7	6.55	87.36
	5-8	6.30	83.98
	5-9	6.40	85.36
	6-6	6.89	91.87
0.47	5-1	6.82	90.99
	5-2	6.75	90.05
	5-3	6.74	89.92
	6-1	6.45	86.06
0.48	5-4	6.60	87.99
	5-5	6.25	83.35
	5-6	6.73	89.75
	6-3	6.55	87.32

Table 4-4 and Table 4-5 present the values obtained from the samples made using the opposite chemical purity as PbO compensation during the sintering of the sets.

Table 4-4 Absolute and relative densities of HP/LP PZT pellets after sintering at 1200°C.

Composition	Pellet identifier	Density (g/cm³) (± 0.03)	Relative Density (%) ($\rho/\rho_{reference}$ *100)
0.46	6-7	7.10	94.64
	6-8	6.85	91.36
0.47	4-7	6.04	80.49
0.48	4-5	6.73	89.72
	4-6	6.19	82.59

Table 4-5 Absolute and relative densities of LP/HP PZT pellets after sintering at 1200°C.

Composition	Pellet identifier	Density (g/cm³) (± 0.03)	Relative Density (%) ($\rho/\rho_{reference}$ *100)
0.46	6-9	6.56	87.53
	6-10	6.99	93.21

Below, Table 4-6 includes a summary of the average absolute and relative densities calculated for each of the ten sintered sets. As described previously, the relative values were taken as the quotient between the experimental density and the standard found in the literature for PZT piezoelectric ceramics. It can be seen that the low-purity compositions made with low-purity PZ have the highest densities, with composition 0.47 being the one with the highest accuracy when compared to the standard.

Table 4-6 Average absolute and relative densities for each composition set.

Composition	0.46				0.47			0.48		
PZT Purity	HP		LP		HP		LP	HP		LP
PZ Purity	HP	LP	LP	HP	HP	LP	LP	HP	LP	LP
Average Absolute Density (g/cm³)	6.65	6.97	7.02	6.78	6.61	6.04	7.26	6.54	6.46	7.18
Average Relative Density (%) ($\rho/\rho_{reference} *100$)	88.7	93.0	93.6	90.4	88.2	80.5	96.6	87.2	86.2	95.8

Nevertheless, when comparing the individual values, the highest density is found to be from pellet 6-4 (0.46 LP/LP), followed by pellet 4-3 (0.48 LP/LP), and finally, pellet 4-12 (0.47 LP/LP). Amongst the HP/HP compositions, composition 0.46 has the highest average absolute and relative densities, with compositions 0.47 and 0.48 being slightly less dense. This tendency is also observed when comparing the individual values in Table 4-3, where the highest density was obtained for pellet 6-6 (0.46 HP/HP).

Additionally, although composition 0.46 for HP PZT did show an increment in the average density when sintered with an LP PZ atmosphere, the mean of the other two compositions appeared to have decreased. It is believed that because there were only one or two samples inside the crucibles for these compositions, these experienced higher losses of PbO and therefore ended with a lower ρ. If the same number of samples had been sintered, the average could have increased for all the high-purity compositions when paired with low-purity PbO compensations, since the individual values shown in Table 4-4 demonstrate the potential for higher densities.

On the other hand, the 0.46 LP PZT composition made with HP PZ disks had both sintered samples showing similar or slightly lower values than the ones sintered with LP atmospheres. This would suggest that higher purity materials do not compensate the PZT samples as well as their counterparts.

Therefore, it was concluded that HP PZT samples would benefit from having LP PbO compensation, which would represent a major economic advantage in terms of the amount of parent oxides used and their market price. This is further discussed in Chapter 6. These results need to be correlated with their functional characteristics to find the best compositions for energy harvesting.

4.2   Microstructure analysis of the PZT ceramic disks

A scanning electron microscope uses a high-energy electron beam to show a high-resolution magnified two-dimensional image of a scanned solid sample. It is usually employed to carry out a microanalysis or failure analysis in a material, as well as to allow the precise measurement of very small objects or dimensions, and can expose texture, and orientation and help with chemical characterisation (Laboratory Testing Inc., 2020). For this project, SEM (Hitachi S4700, Japan) was used to characterise and examine the microstructure of the PZT sets, randomly selecting one disk from each group for the analysis.

Unfortunately, due to the intermittent access to the machine and the limited number of samples in the sets with opposite lead compensation, only the images obtained from the main sets are included in this section. The remaining sets presented altered surfaces that impeded a clear visualisation of the crystals as SEM could only be carried out after they had already been prepared for the electrode placement. The machine was accessed in the James Watt Nanofabrication Centre at the University of Glasgow, UK.

The SEM images present different areas of interest and magnifications for each sample, making it possible to observe their varying grain sizes, as well as gaps and other material defects or contaminants on the surfaces. Each caption indicates the composition depicted, including the sample's identifier. Furthermore, each image presents the parameters used for each measurement, including the accelerating voltage (20kV), working distance (between 12.1 and 12.4mm), magnification and scale.

Starting with composition 0.46 LP/LP, Figure 4-1 shows a tightly packed microstructure, where crystals of various sizes can be seen. The specific crystal structure is explored in section 4.3. Figure 4-1 (a) also shows a semi-crushed pair of crystals (yellow circle) that could indicate potential defects in the sample but were more likely a minor superficial imperfection since no others were found throughout the scanning process. Dark areas can be observed on some of the crystals shown in Figure 4-1 (a), (b), (c) and (d) (red circles), which could be related to PbO losses but would require further analysis through the study of the sample's composition, which is included and discussed in section 4.4 of this chapter. Additionally, although the last four images show dark areas between grains (blue circles), indicating possible gaps or grain fusions, proper sintering of this composition can be confirmed since these were only found sparsely.
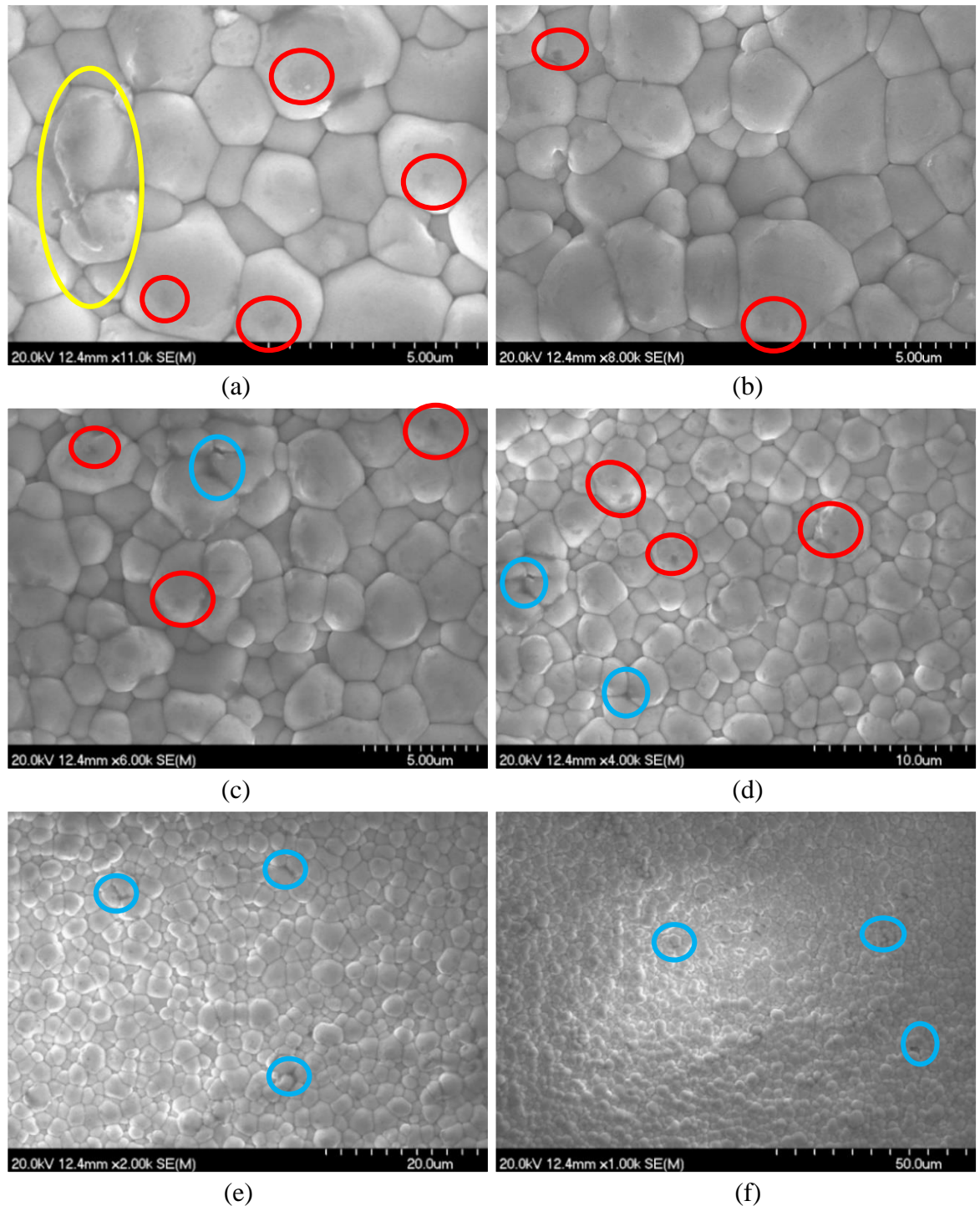
Figure 4-1 SEM images from PZT pellet 6-12 (0.46 LP/LP) after sintering at 1200°C with magnifications of (a) x11.0k, (b) x8.00k, (c) x6.00k, (d) x4.00k, (e) x2.00k and (f) x1.00k.

Although Figure 4-2 shows the expected microstructure for composition 0.47 LP/LP, the dark spots circled in red in (a), (b) & (d) appear to be bigger and more frequent than those spotted in the last figure, with grain boundaries appearing more fused. Crushed crystals (yellow), unknown particles (orange) and a small gap (green) are also seen in this sample. The most likely explanation for this is that the SEM was performed after using silicon carbide paper and distilled water to smooth the sample's surface during the lapping process.
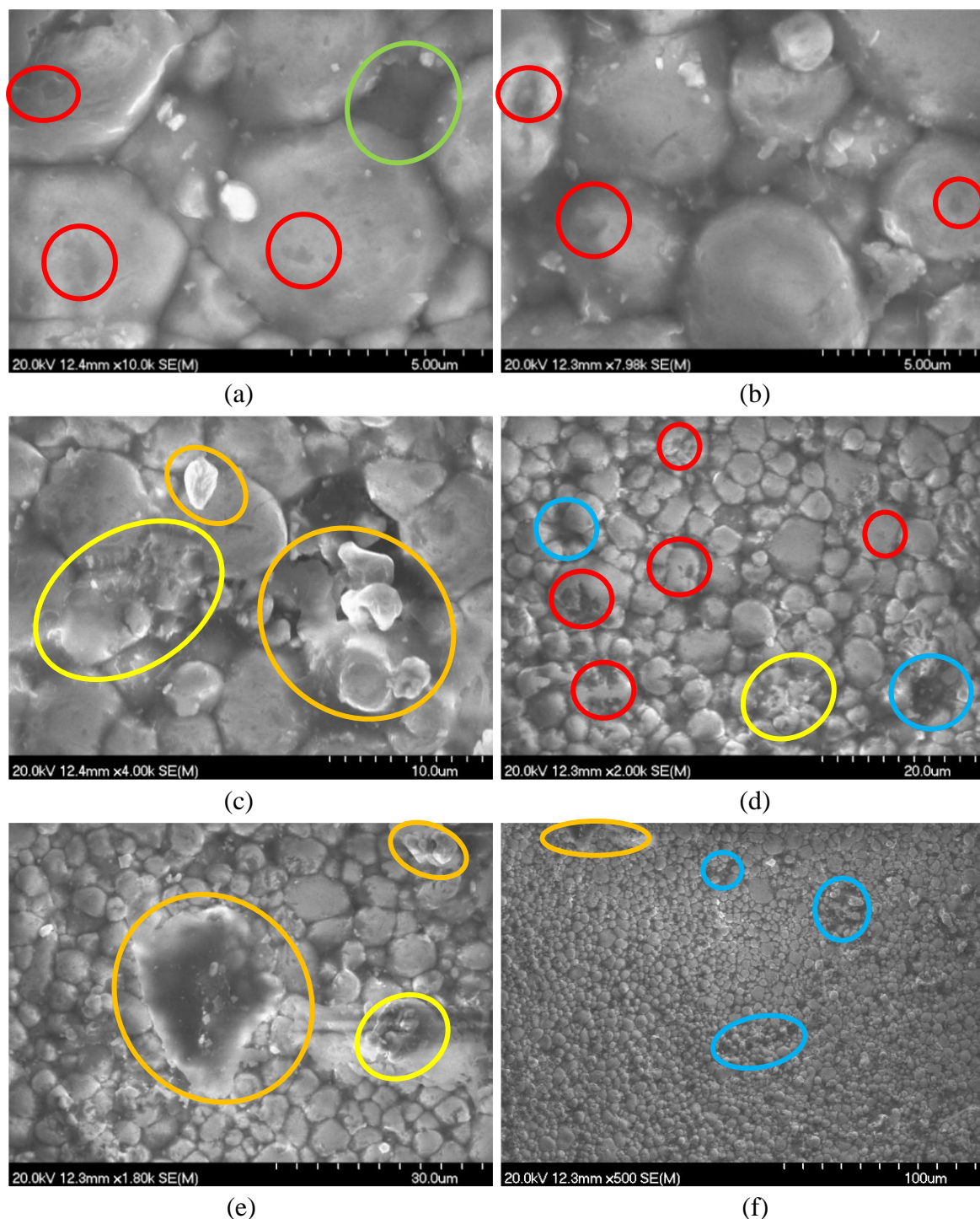
Figure 4-2 SEM images from PZT pellet 4-12 (0.47 LP/LP) after sintering at 1200°C with magnifications of (a) x10.0k, (b) x7.98k, (c) x4.00k, (d) x2.00k, (e) x1.80k and (f) x500.

Regarding composition 0.48 LP/LP, Figure 4-3 shows a similar superficial texture with darker grain boundaries (blue) as with 0.47, which was not seen in the 0.46 LP/LP disk. Despite this similarity, images from the 0.47 sample show more crushed crystals and contaminants (orange circles) than the 0.48 ones, which is coherent with the 0.47 disk being lapped before analysing it. Nevertheless, Figure 4-3 (a) does present a pore with visible smaller crystals inside (green circle), which was not spotted in the previous compositions.
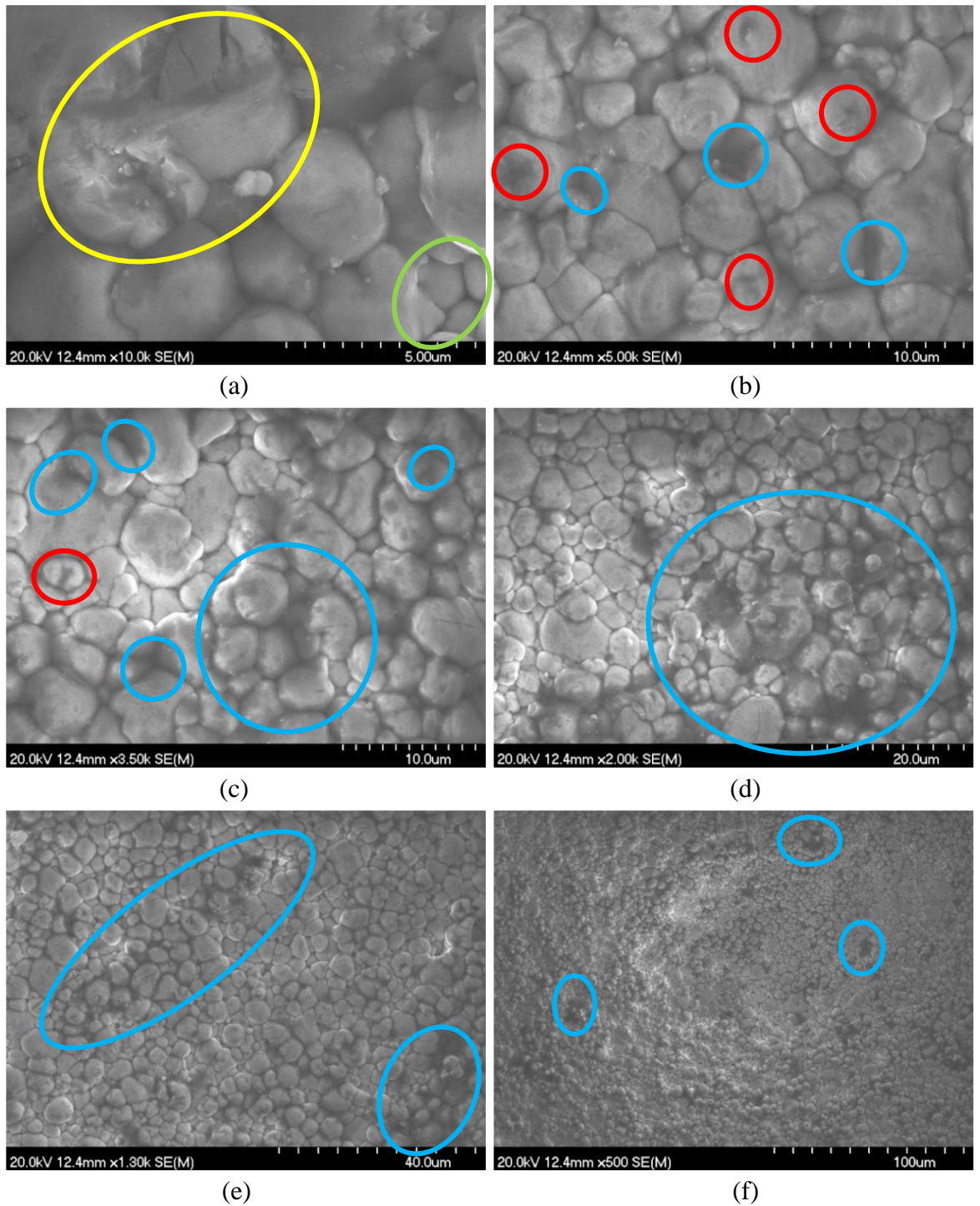
Figure 4-3 SEM images from PZT pellet 4-3 (0.48 LP/LP) after sintering at 1200°C with magnifications of (a) x10.0k, (b) x5.00k, (c) x3.50k, (d) x2.00k, (e) x1.30k and (f) x500.

Figure 4-3 also appears to exhibit a lot more obscured areas (blue circles) compared to the previous figures, as seen in images (c), (d) and (e), although when comparing image (f) from this and Figure 4-2, the amount observed at a relatively low magnification (x500) is very similar. The displayed microstructure remains consistent despite presenting a wider variety of shapes on the crystal areas from the surface.

Sample 0.46 HP/HP in Figure 4-4 presents grain boundaries with a texture between that seen in the 0.46 and 0.47 LP/LP samples, with easily outlined crystals but slightly fused boundaries. Like in the LP/LP compositions, dark spots are seen on the material's surface (red circles), with the difference of having faint concentric lines that appear to be expanding from the corners of the crystals. This fingerprint-like pattern can be observed in images (a) and (b) of the HP/HP figures, which were not lapped or polished prior to the analysis.

(a)

(b)

(c)

(d)

(e)

(f)
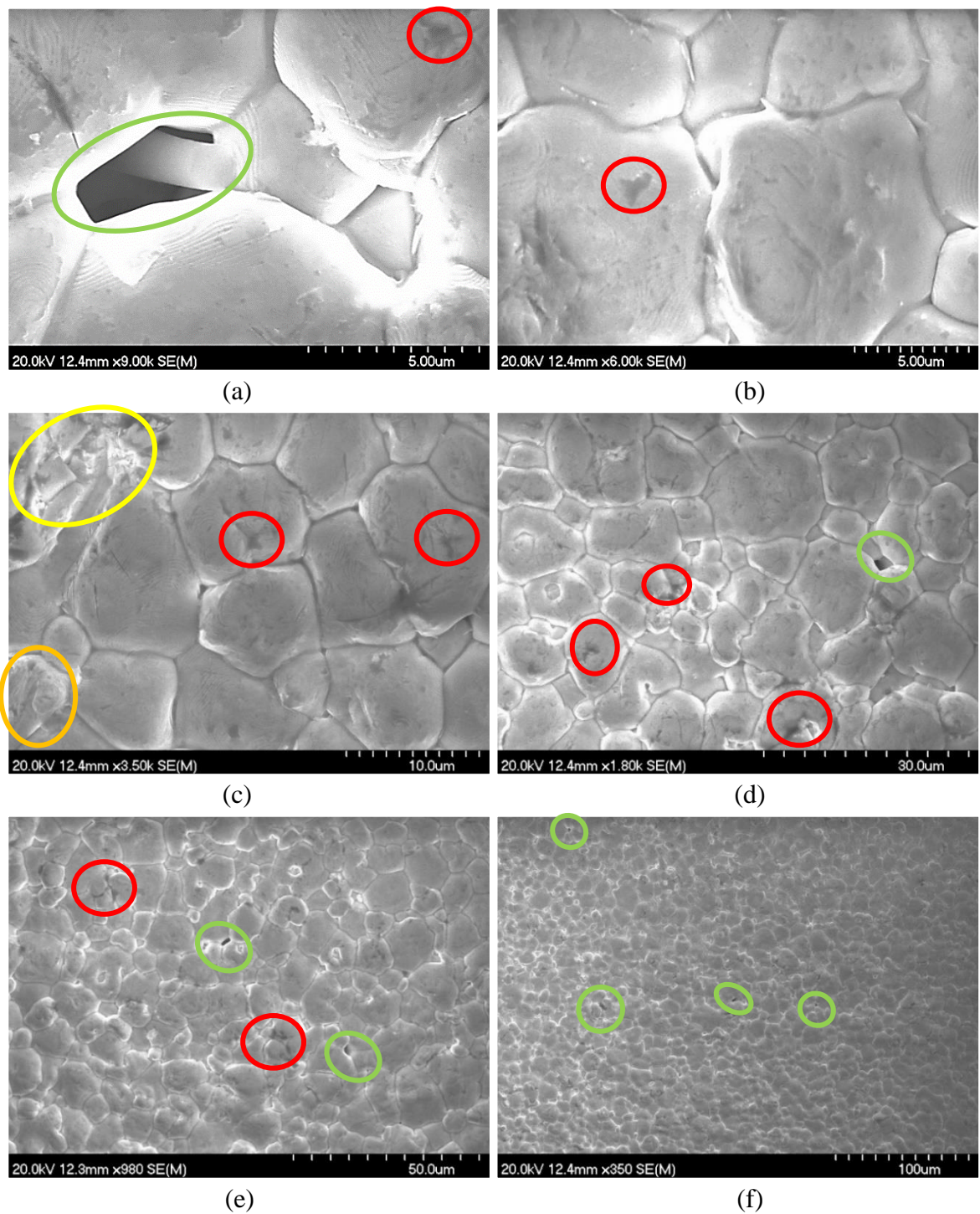
Figure 4-4 SEM images from PZT pellet 5-7 (0.46 HP/HP) after sintering at 1200°C with magnifications of (a) x9.00k, (b) x6.00k, (c) x3.50k, (d) x1.80k, (e) x980 and (f) x350.

Figure 4-4 (a) also showed a small rod of about 2µm inside a pore, which remained unidentified and would require further analysis through EDS to study its composition. For pellet 0.47 HP/HP, depicted in Figure 4-5, a similar texture and structure can be seen, but the surface marks appear more prominent than those previously observed. Additionally, the number of gaps (green), contaminants (orange) and amorphous particles (yellow) appears to have increased compared to previous figures.
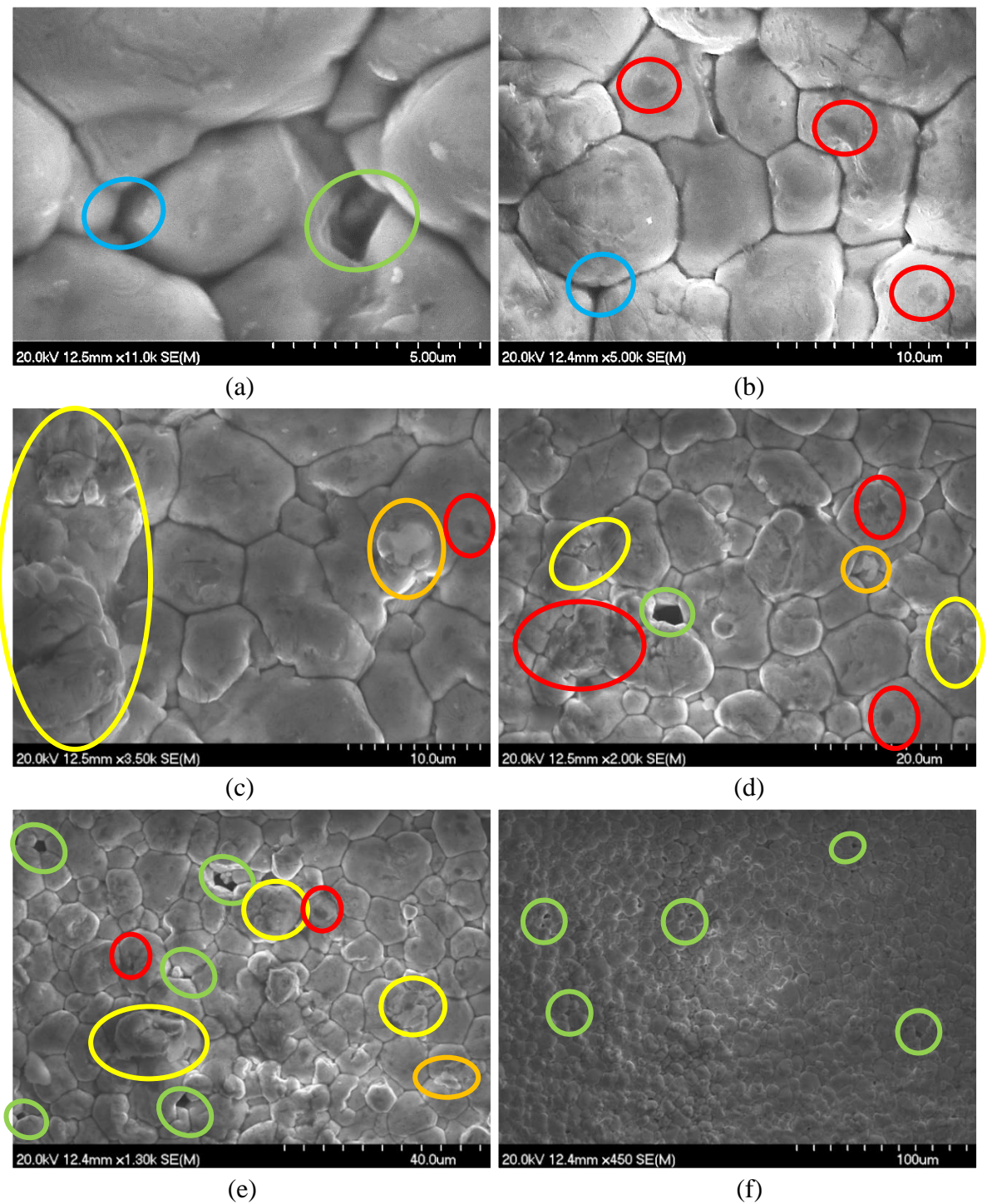
Figure 4-5 SEM images from PZT pellet 5-2 (0.47 HP/HP) after sintering at 1200°C with magnifications of (a) x11.0k, (b) x5.00k, (c) x3.50k, (d) x2.00k, (e) x1.30k and (f) x450.

Figure 4-6 below shows a comparable texture to the other HP/HP samples, with darker spots on the surface of the grains, but also presents the slightly fused and darker grain boundaries seen in the images from LP/LP compositions 0.47 and 0.48. Furthermore, the concentric pattern that was identified in the other HP/HP disks can be spotted on the crystals seen on the scans' surface as well as on the ones found inside the pores captured in images (a) and (b) of this figure.
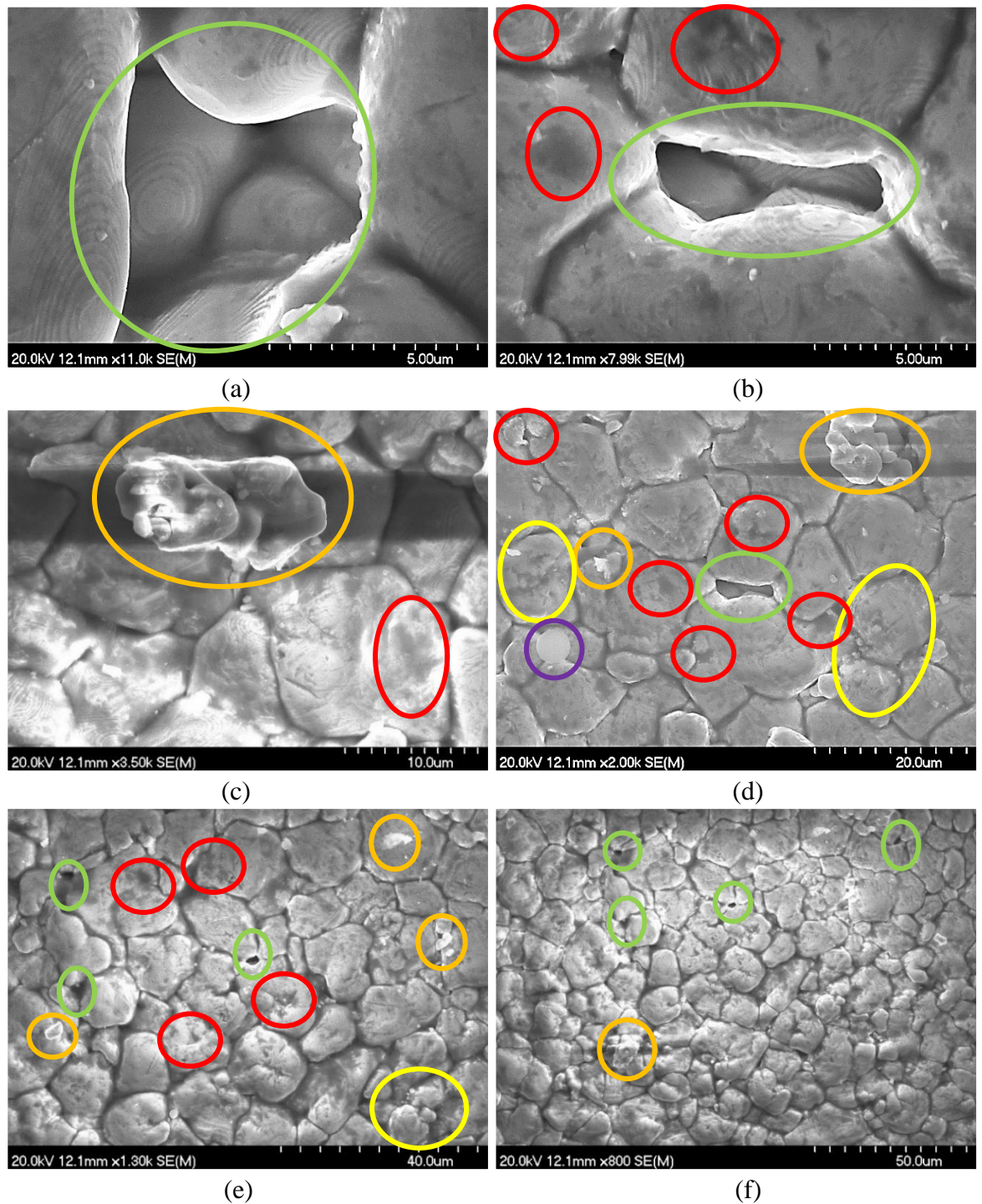
Figure 4-6 SEM images from PZT pellet 5-6 (0.48 HP/HP) after sintering at 1200°C with magnifications of (a) x11.0k, (b) x7.99k, (c) x3.50k, (d) x2.00k, (e) x1.30k and (f) x800.

A seemingly higher number of pores is seen on the HP/HP samples compared to their LP/LP counterparts. These can be observed in images (a), (d), (e) and (f) of the HP/HP figures, and in Figure 4-6 (b). Unlike the LP/LP samples, where pores were rarely seen, the HP/HP disks show more pores as the magnification is lowered, covering a wider area, indicating it is a common occurrence for these compositions.

Crushed crystals and amorphous clusters can also be seen in the images belonging to the HP/HP compositions, primarily in scans (c), (d) and (e) of Figures 4-5 and 4-6, as well as Figure 4-4 (c). Although some of these defects were also spotted in a few LP/LP scans, they appear to be more common on the HP/HP, even when they did not experience any prior processing. An unknown element can be spotted in Figure 4-6 (d) (purple), resembling the rod seen in 4-4 (a). Additional analysis would be required to identify the unknown particles.

To allow for direct comparison amongst the disks, the scan taken at ~ ×2k from each of the previous compositions is shown in Figure 4-7. Compositions 0.46 are included at the top, 0.47 in the middle, and 0.48 at the bottom, with the LP on the left and HP on the right.

(a) (b)

(c) (d)

(e)   (f)
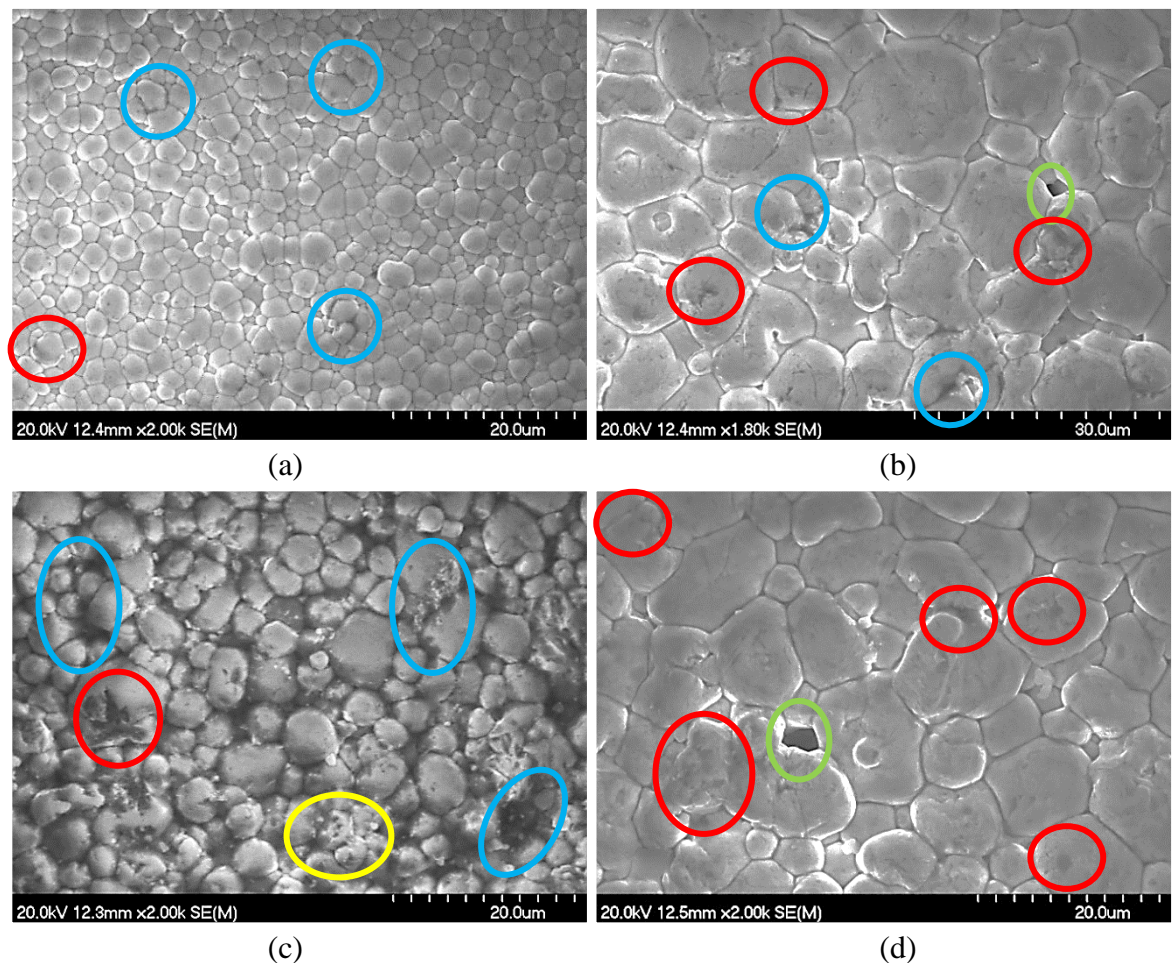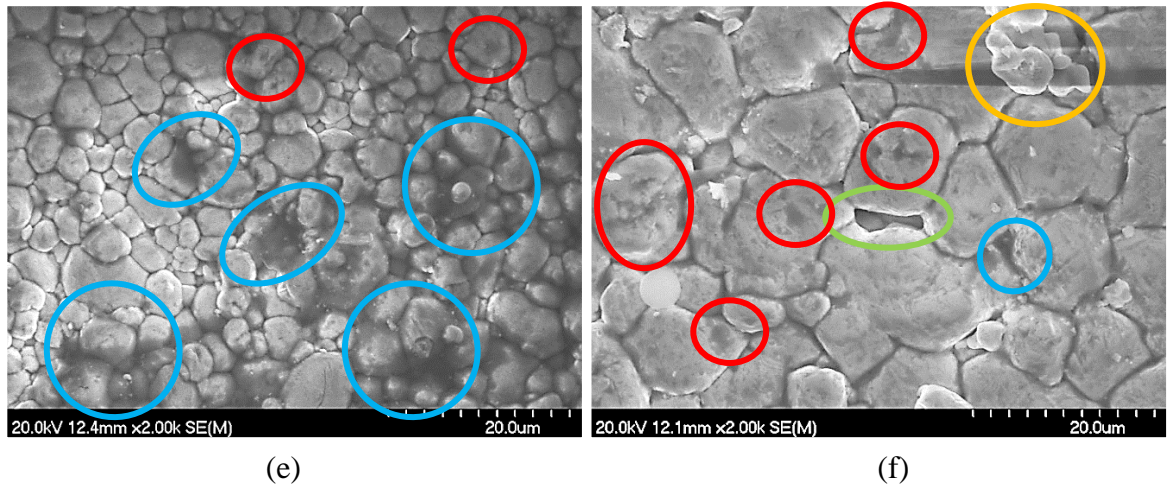
Figure 4-7 SEM images from (a) 0.46 LP/LP (pellet 6-12), (b) 0.46 HP/HP (pellet 5-7), (c) 0.47 LP/LP (pellet 4-12), (d) 0.47 HP/HP (pellet 5-2), (e) 0.48 LP/LP (pellet 4-3), and (f) 0.48 HP/HP (pellet 5-6), at ~2.00k magnification.

At first glance, all six compositions show a similar structure with a wide range of grain sizes and a tightly packed arrangement. Although the LP disks seem the most consistent, it is difficult to fully appreciate this in the images provided by the SEM due to the compactness of the material and lack of isolated crystals. The images in this figure also confirm the increased number of pores in the HP/HP disks, which were not found on the LP/LP pellets, even when more surface area was covered.

Additionally, from an initial visual comparison of these scans, it can be observed that the grains in the HP samples appear bigger than the LP ones in the same magnification. Composition 0.46 (a) appears to present the smallest grain size amongst the LP samples, while compositions 0.47 (c) and 0.48 (e), appear very close in dimensions and would require further studies. Regarding HP/HP compositions, although there is no immediate differentiation, upon closer inspection, composition 0.47 (d) potentially shows the smallest crystals, followed by 0.46 (b) and finally, 0.48 (f). These assumptions are examined further in section 4.2.1 and detailed in Table 4-8 below.

The gaps, pores and cracks found on the surface and between grain boundaries were identified as being linked to the PbO loss that can occur at high temperatures, and for which the PZ atmosphere disks were used. Additionally, the unknown particles and amorphous crystals that were observed tend to be associated with the processing of the PZT samples before the SEM analysis, and/or the presence of a pyrochlore phase (Qian, et al., 2013), which is one of the possible cell structures for piezoelectric materials.

Since the only sample that experienced any processing before being analysed was composition 0.47 LP/LP, it can be assumed that the rest of these defects suggest the existence of pyrochlore in the material, which is explored further in section 4.3.1 of the phase formation analysis. Therefore, the pyrochlore phase and its associated defects, just like the gaps, pores, and cracks, are said to be a consequence of PbO volatilisation during sintering.

The increased occurrence and magnitude of these defects in the HP/HP compositions would indicate that these suffered from a greater PbO loss, which further supports the statement made in the previous section, where the individual densities suggest that the HP/HP pellets had lower values due to lower concentration of PbO after sintering.

On the other hand, after studying the dark spots that were seen on the samples' surface, highlighted with the red and blue circles, it was concluded that these were associated with a higher concentration of PbO in the material in those areas. The red circles show the vacancies left by the lead evaporation, while the blue emphasizes the PbO located between grain boundaries.

Shared grain boundaries are observed in all the scanned samples, except when encountering a gap or pore between the crystals. This characteristic indicates a proper change in densification through the sintering process, modifying the grain size and enhancing the contact between crystals, reducing the possibility of the pellets short-circuiting while evaluating them as energy harvesters. A loose arrangement of the grains could also make the grain boundaries appear more obscure, as the crystals become less tight and allow the electrons being bombarded on the surface to be absorbed more easily, thus explaining the dark edges seen between the grain boundaries of some of the compositions in Figure 4-8.

Contrastingly, some of these images show very bright areas between the grains, which occurred when pausing on them for a relatively lengthy period to study and take an image using the SEM machine. This effect is related to the conductivity of the material, where the brightness is a response to the charging effect caused by electrons that did not penetrate the ceramic. This means that the material has a higher resistance to the electron bombardment done by the SEM and consequently, lower electric conductivity. To correct this, contrast levels were adjusted but some of the brightness can still be appreciated, particularly on the HP samples.

4.2.1 Grain size and crystal density

As well as visually showing the microstructure of the crystals and possible defects present in the samples at various magnifications, the SEM images were used to calculate the average grain size for each composition by employing the scale presented at the bottom right of each image in Figure 4-7 and measuring an average of around 130 lengths throughout them. This process was accomplished by using the ImageJ 1.46r software, which is a public-domain image processing and analysis program.

This software was also employed to count the number of crystals in three different images from each set, including SEM scans not presented in this thesis but belonging to the same sample previously discussed. It is worth mentioning that the concept of crystal density employed here refers to the number of crystals, grains, or particles per unit area (μm^2) and not the true theoretical density of the grains, which would involve their mass and cell volume.

The scale provided was used to measure the area shown in the images, and thus calculate the crystal density in the material. The specifications of the images used are presented in Table 4-7. Despite the magnifications varying amongst the images chosen from each sample, the key features that were sought during the selection process, were presenting a clear scan with well-defined crystals and a big enough scale that allowed for individual measurements to be easily made with the ImageJ 1.46r software.

Table 4-7 Magnification of the images used for the calculation of the average crystal density of the six main PZT compositions sintered.

PZT Composition	PZT/PZ Purity	Pellet ID	Magnification of the images used for the crystal density
0.46		6-12	x11.0k, x6.00k & x2.00k
0.47	**LP/LP**	4-12	x7.98, x5.01 & x2.00
0.48		4-3	x5.00k, x3.5k & x2.00k
0.46		5-7	x1.80k, x1.00k & x980
0.47	**HP/HP**	5-2	x5.00k, x2.00k & x1.30k
0.48		5-6	x2.5k, x1.3k & x800

The average grain size and crystal densities found for each of the six main PZT compositions, along with their respective absolute errors, have been included in Table 4-8.

The standard error for the mean grain size was calculated as the quotient of the standard deviation (σ) and the square root of the total number of measurements ($\sqrt{N} = \sqrt{\sim}130$), while the uncertainty for the average crystal density was calculated as the quotient of the difference between the maximum and minimum densities found and the square root of the total number of measurements ($\sqrt{N} = \sqrt{3}$). Both calculations were obtained following the rules for the statistical analysis of small and large data sets described by (Penn University - Department of Physics & Astronomy, 2020).

Table 4-8 Average grain size and crystal density of the six main PZT compositions sintered along with their absolute errors.

PZT Composition	PZT/PZ Purity	Pellet ID	Average Grain Size (μm)	Average Crystal Density (grains or crystals/μm²)
0.46		6-12	3.364 ± 0.694	0.373 ± 0.038
0.47	**LP/LP**	4-12	5.338 ± 0.134	0.105 ± 0.024
0.48		4-3	5.320 ± 0.132	0.117 ± 0.012
0.46		5-7	10.696 ± 0.225	0.019 ± 0.002
0.47	**HP/HP**	5-2	8.733 ± 0.237	0.030 ± 0.005
0.48		5-6	13.187 ± 0.365	0.010 ± 0.001

Table 4-8 confirms the grain size assumptions that were made from the images in Figure 4-7, putting sample 0.46 LP/LP with the highest crystal density and the smallest average grain size, while composition 0.48 HP/HP showed the lowest crystal density and the biggest average grain size. Though the pellets were treated similarly and put through the same two-stage ceramic process, it can be appreciated the variations in compositions and purities used, made significant changes in the final outcome, which is further supported by the observations made in Figure 4-1 through 4-7 and the values presented in Table 4-8.

According to (Qian, et al., 2013), the grain size decreases as the proximity with the MPB increases, suggesting that the composition with the smallest grains would be the one closest to the MPB, thus exhibiting better piezoelectric characteristics. In this case, this would mean that amongst the lower purity sets, composition 0.46 appears to be closest to the MPB, suggesting that for this group, the MPB is slightly displaced from the assumed value mentioned in section 3.1 (*x = 0.47*). On the other hand, composition 0.47 HP/HP would be the most proximal to the MPB for the higher purity sets, which is consistent with the previously mentioned value. These assumptions are further explored in section 4.3.

PZT ceramics with reduced grain size are said to have displayed higher mechanical strength and retain their electromechanical properties even at frequencies above 50MHz, making them ideal for high-frequency ultrasound transducers (Lee, et al., 2012). Nevertheless, this can only be confirmed after conducting the full functional characterisation of the disks, presented in Chapter 5. It is also imperative to keep in mind that the scans presented might not reflect all the samples in their sets and that composition 0.46 LP/LP had variations in the parameters used for the ball milling process compared to the other two LP/LP compositions.

4.3   Phase formation analysis of the PZT ceramic disks

X-ray diffraction (XRD) was performed on one randomly chosen sample from each of the ten sintered sets, using a powder diffractometer to identify and compare their phase formation. X-ray diffraction is a non-destructive method in which a material is irradiated from multiple directions to determine its solid-state structure. The rays impact the crystals as if they were formed by equally distanced parallel planes and reflect on them at the same angle of incidence, creating a unique pattern from the constructive interference that arises when reflection occurs in successive planes (Gamba, 2009). The intensities and positions of the resulting peaks are compared to reference patterns from a database to identify the phase formation and chemical composition of the material (Speakman, 2014).

The intensity of the peaks is established by the specific chemistry and position of the atoms, and their location is determined by the interatomic distances. The number of plane families in a crystal, with their different orientations and spacing, is reflected in the number of points found in the pattern. To aid in the identification of the microstructure of the material, these planes are identified by a set of numbers known as Miller Indices, which correspond to the reciprocal axial intercepts of a plane with the unit cell and are written as integers in the format *(h k l)*, where an overbar denotes a negative integer (Speakman, 2014).

The graphs included in this section were created through the OriginPro 8.5 Program by plotting the data obtained from the Highscore Plus software linked to the XRD machines employed for this study. The X'Pert[3] model (PANalytical, UK) was used to study five of the six main sets in Mexico, while the X'Pert Pro was used in Glasgow for the 0.46 LP sample and the four sets that had opposite purity used as PbO compensation. Both machines operated with Cu K_α radiation and covered a scattering angle (2θ) from $20°$ to $90°$, with a step size of $\sim 0.02°$. The complete machine specifications are included in Appendices D and E.

A reference pattern from the ICSD database (Nan, et al., 2011) is included in Figure 4-10, which shows ten peaks found in a PZT sample with a 50/50 Ti/Zr composition, exhibiting cubic phase. Since this phase is the simplest of all the crystal systems, generating the least number of peaks, this was used as a base to identify the position, relative intensity, and associated planes within the samples' patterns, as well as to study the phase transitions linked to any splitting or changes that occur when shifts in the direction and parameters of the structure take place depending on the sample composition and purity.
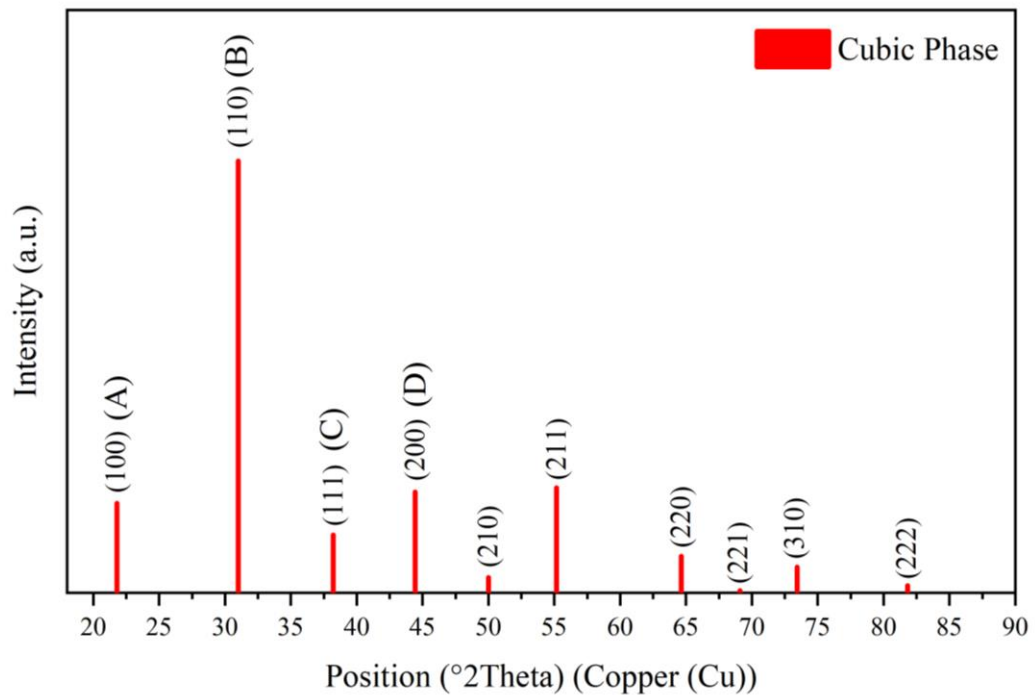
Figure 4-8 XRD reference pattern 01-080-7943 for 50/50 PZT exhibiting cubic phase, with emphasis on peaks (100) (A), (110) (B), (111) (C) and (200) (D).

Although all the peaks have been labelled with their corresponding Miller index, the first four peaks have also been assigned a letter to make further comparisons later in the discussion due to being considered the most important peaks in a perovskite, this is because their behaviour can help determine the presence of the tetragonal and rhombohedral phases based on their shape (Plane (100) = (A), (110) =(B), (111) = (C) and (200) = (D)). If the material presents a tetragonal phase, the deformation of the crystal structure will be reflected on peaks (A) and (D), which will unfold into two peaks (doublet) of about half the height of the original. On the other hand, if the structure is rhombohedral, the diagonal deformation will cause the splitting in the peaks (C) and (D). Since this deformation is generally small, the observed doublet can be subtle but can become more pronounced as the rhombohedral phase increases. The splitting in both cases is caused by crystal phase transitions (Bokhimi, 2016).

Since the PZT compositions were chosen due to their proximity to the previously mentioned assumed MPB (*x = 0.47*), where the material exhibits the best piezoelectric properties, the obtained diffractograms are expected to include a mixture of the Ti-rich tetragonal and Zr-rich rhombohedral phases that coexist in this region, as illustrated in Figure 2-5. The following deductions regarding the presence of each of these two phases are made by studying the variations observed in the obtained diagrams for each sample and comparing them against the anticipated behaviours that were gathered from several ICSD reference patterns obtained from the Highscore Plus software belonging to PZT ceramics exhibiting these two phases and with similar compositions as the ones chosen for this work (Tetragonal, ICSD: 90478, Rhombohedral, ICSD: 90700).

Figures 4-9 to 4-11 show the full-range patterns of the three LP/LP samples. After comparing the XRD pattern of pellet 6-12 with composition 0.46 LP/LP, presented in Figure 4-9, against the base pattern included in Figure 4-8, it can be observed that peaks (100) and (200) remain as a singlet, while peaks (110) and (111) split into doublets, indicating the clear presence of a rhombohedral phase. Additionally, although less prominent, peaks (211), (220) and (221), at 55°, 64°, and 68°, respectively, also present the splitting linked to the rhombohedral phase, while a slight displacement or broadening can be subtly spotted on peaks (200) and (210), indicating low traces of the tetragonal phase.
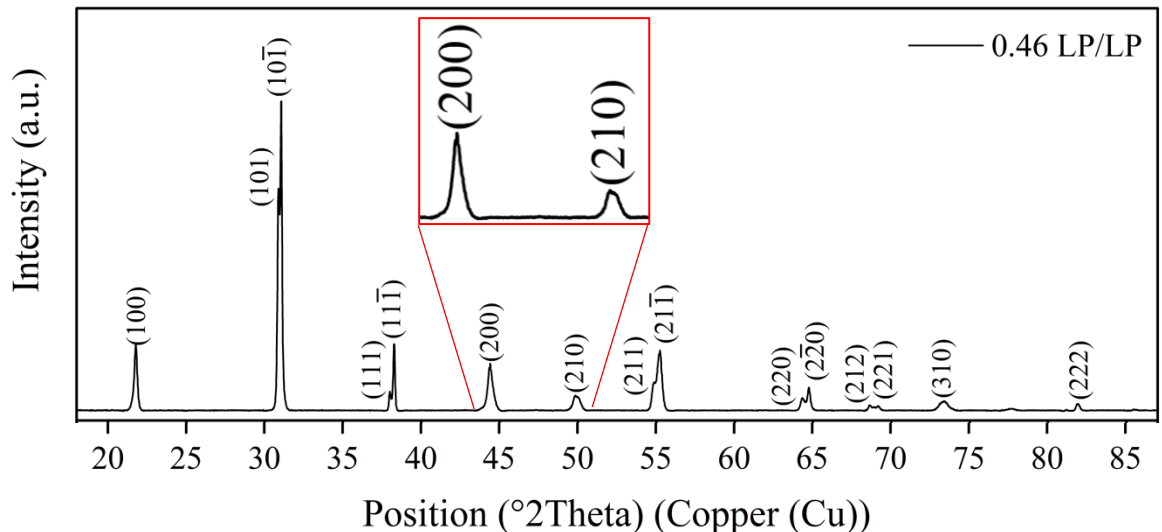
Figure 4-9 Full XRD pattern from composition 0.46 LP/LP PZT (pellet 6-12), after sintering at 1200°C.

Regarding composition 0.47 LP/LP in Figure 4-10, a splitting of the majority of the peaks can be seen in the pattern, with the exception of peaks (310) and (222). Besides the unfolding of some of these peaks into the expected doublets, peak (200) can also be initially seen splitting into a triplet. This behaviour suggests a coexistence of the two expected

phases, tetragonal (P4mm) and rhombohedral (R3m), although a closer examination would be required to explore their proportion in the sample. The indexing shown uses the phases and space groups mentioned, with the rhombohedral reflections using a rhombohedral base.
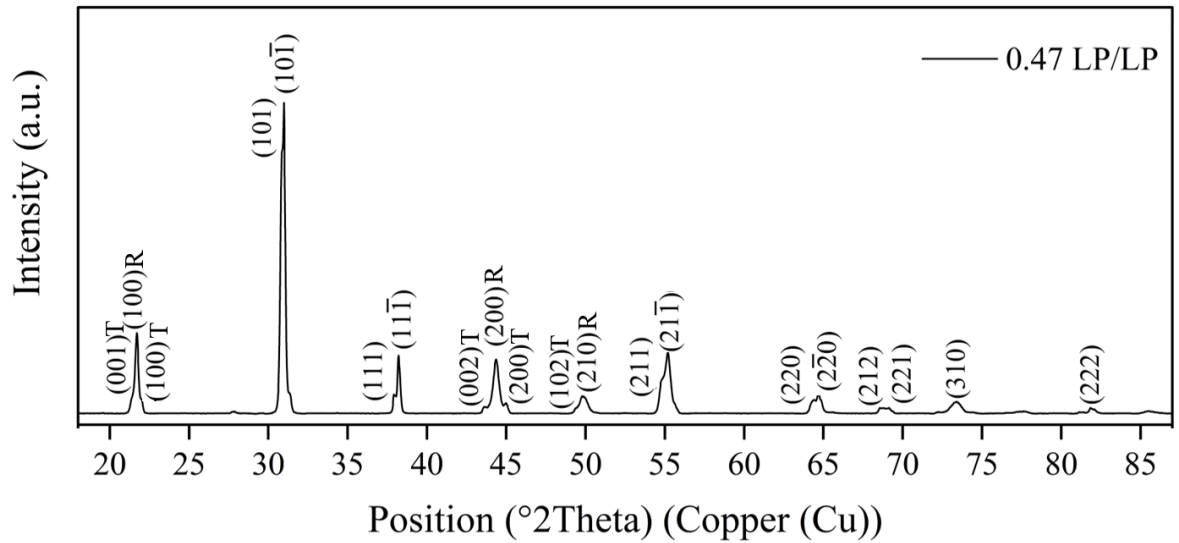
Figure 4-10 Full XRD pattern from composition 0.47 LP/LP PZT (pellet 4-8), after sintering at 1200°C.

Finally, Figure 4-11 shows the diffractogram of pellet 4- 1 belonging to composition 0.48 LP/LP. This pattern presents multiple peaks widening and subtle splitting as seen in the previous diagram, but unlike pellet 0.47 LP/LP, no overlapping of the two phases can be spotted at this scale. Nevertheless, it can be seen that the unfolding of peaks (110) and (111) has decreased, indicating that the percentage of the rhombohedral phase in the sample has also decreased, which would agree with the amount of TiO_2 used in the sample, reflected in the higher value of x.
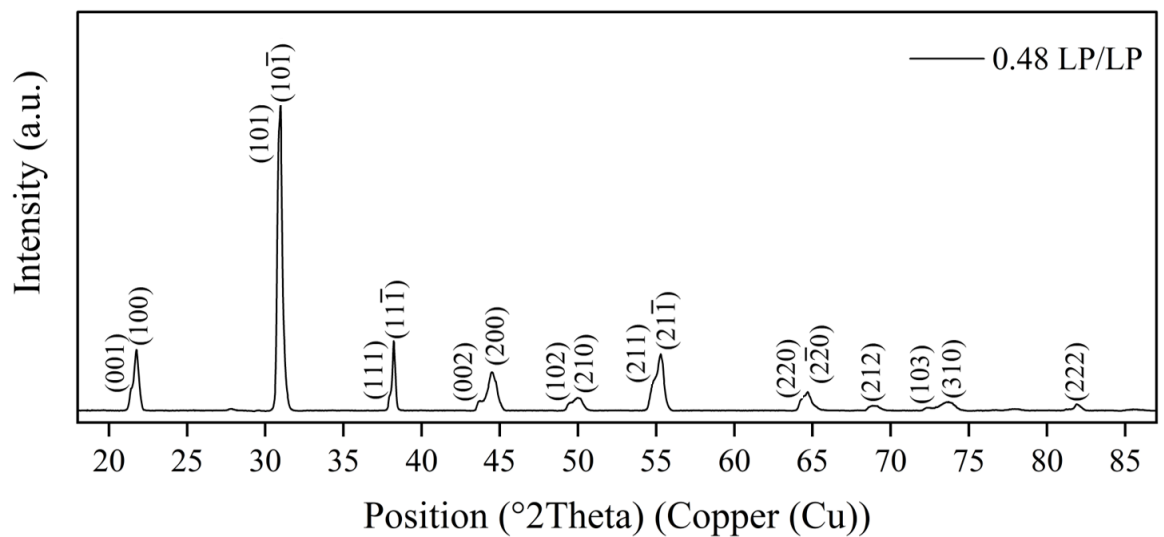
Figure 4-11 Full XRD pattern from composition 0.48 LP/LP PZT (pellet 4-1), after sintering at 1200°C.

91

A closer comparison of the four main peaks from the three LP/LP patterns, belonging to planes (100), (110), (111) and (200), is presented in Figure 4-12.
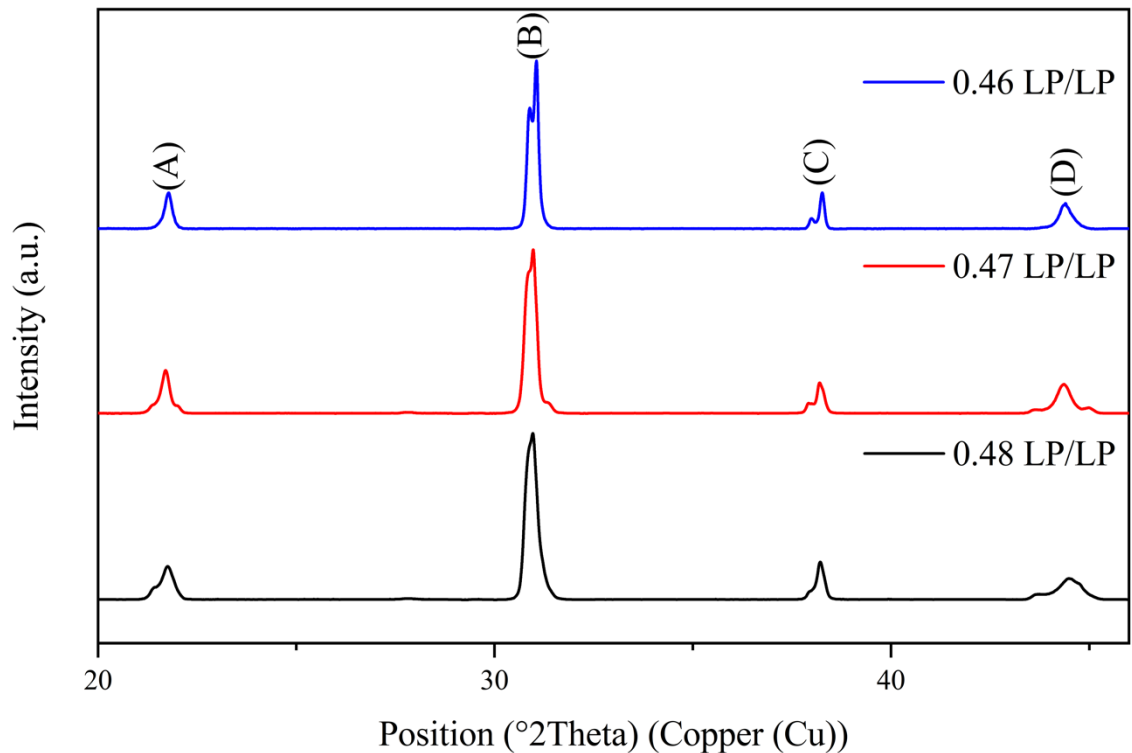
Figure 4-12 Comparison of XRD peaks (100) (A), (110) (B), (111) (C) and (200) (D) from the PZT compositions 0.46 LP/LP pellet 6-12 (top), 0.47 LP/LP pellet 4-8 (middle) and 0.48 LP/LP pellet 4-1 (bottom) after sintering at 1200°C.

Upon further inspecting the 0.47 LP/LP pattern above, all four peaks can be seen unfolding, with peaks (A), (B) and (D) transforming into a triplet. To determine which of the two coexisting phases dominates, the relative intensity of their associated peaks needs to be compared. In this case, peaks (A) and (D), show the initial stages of the tetragonal splitting, while peaks (B) and (C) display reduced rhombohedral features. Since the sharpness of the rhombohedral single peaks is still clearly present and surpassing the intensity of the tetragonal splitting in (A) and (D), it can be assumed that the dominant phase in this composition is rhombohedral, but maintaining an evident proximity to the MPB.

When compared to the other two compositions in this group, a progression of the phases encountered can be identified. Composition 0.46 LP/LP present the highest degree of the rhombohedral phase with only a small percentage of the tetragonal structure, while composition 0.48 LP/LP demonstrates the opposite, a high level of the Ti-rich tetragonal phase and reduced influence of the rhombohedral one, leaving sample 0.47 LP/LP somewhere in between.

It is worth mentioning that from the splitting and broadening observed on peak (B) in Figure 4-12, the levels of the tetragonal phase found in the 0.48 LP/LP disk seem higher than those shown by the rhombohedral phase in the 0.46 LP/LP sample, indicating a closer distribution between the phases, comparable to that seen in 0.47 LP/LP. The exact weight % of each phase obtained through cell refinement would be required to confirm this statement.

As the value of x decreases in the samples, referring to the amount of TiO_2 used in the stoichiometric calculations in section 3.1, the percentage of the tetragonal phase would proportionally decrease. Consequently, the doublets associated with this phase would become less pronounced, slowly fusing into a singlet as the composition shifts into a more Zr-rich one, which perfectly explains what the patterns above depict. However, this creates a discrepancy with the assumptions made from the average grain sizes obtained from the SEM scans in section 4.2.1, as these XRD patterns point towards the MPB lying closest to a composition between 0.47 and 0.48, based on the proximity in the registered amounts of the two expected phases, instead of composition 0.46 LP/LP, as previously thought.

Regarding the higher purity sets, Figures 4-13 to 4-15 present the full XRD patterns obtained from the samples with HP/HP compositions. Compared to its LP/LP counterpart, composition 0.46 HP/HP (Figure 4-13) shows a more subtle doublet for peak (110), near 31°, and similar peaks for planes (100) and (200), indicating a higher traces of the tetragonal structure, and a slightly lower level of the rhombohedral phase. Despite being almost imperceivable, these subtle distortions seen in peaks (200) and (210), maintain the presence of the tetragonal phase in the material and suggest its relative proximity to the MPB.
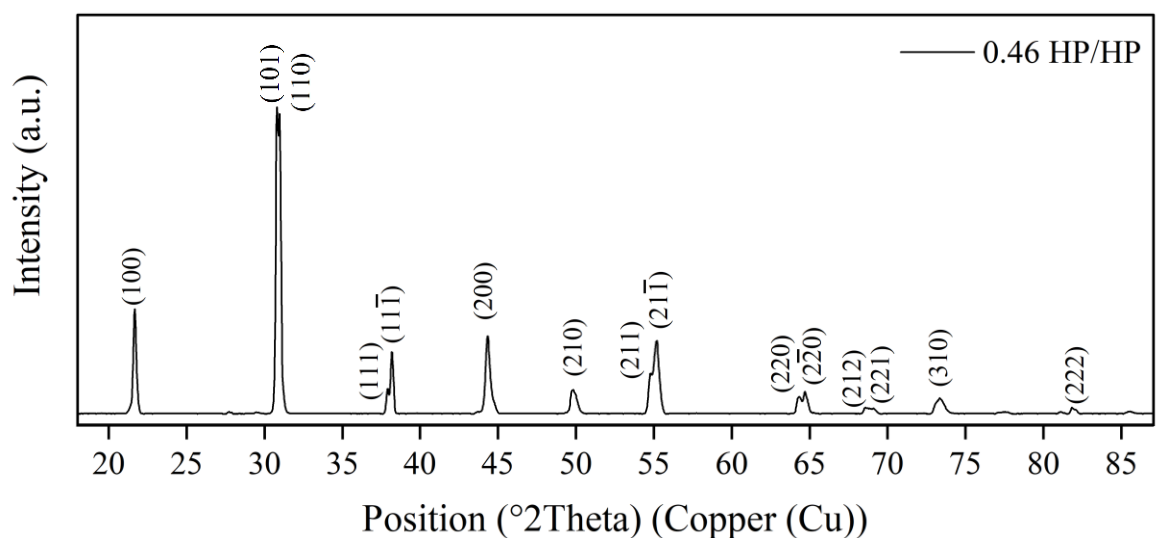
Figure 4-13 Full XRD pattern from composition 0.46 HP/HP PZT (pellet 5-9), after sintering at 1200°C.

Figure 4-14 depicts the diagram of pellet 5-1 with composition 0.47 HP/HP. Even though the pattern shows broadening and splitting in the majority of the registered peaks as the LP/LP equivalent, it exhibits higher intensities for the tetragonal doublets seen overlapping with the rhombohedral singlets in (100) and (200), as well as presenting less widening and distortion in the (110) and (111) diffractions, thus concluding that the predominant phase in this coexistence is the tetragonal structure. As with Figure 4-13, peak (110) shows the splitting occurring on the right side of the peak, although this pattern shows the effect even further, indicating higher amounts of the tetragonal phase.

Consequently, this composition is said to exhibit the expected behaviour of materials near the MPB, with possibly an even closer location to this region than that shown by the 0.47 LP/LP disk. This statement is based on the fact that the relative intensities of the coexisting phases in each transformed peak registered from the sample seem to be closer in magnitude, reflecting a more balanced distribution between them.
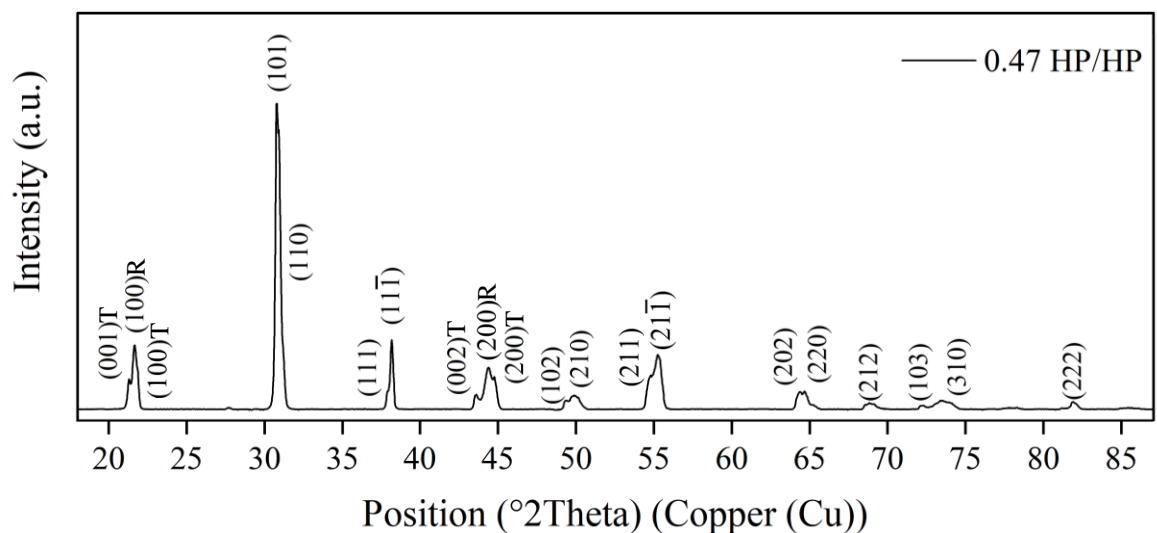
Figure 4-14 Full XRD pattern from composition 0.47 HP/HP PZT (pellet 5-1), after sintering at 1200°C.

The XRD pattern of composition 0.48 HP/HP, obtained from pellet 5-4, can be seen in Figure 4-15. As with the opposite purity sample made with the same percentage of TiO_2, this composition presents the highest levels of tetragonal phase within its purity group, based on the depth of the unfolding of peaks (100) and (200), in addition to the narrowing of peaks (110) and (111). Furthermore, although this composition presents a much higher proportion of the Ti-rich tetragonal phase, coexistence with the rhombohedral structure can still be identified from the subtle distortion of the peak (111), supporting the proper sintering of this sample by proving its permanence near the MPB, just as seen with the previous samples.
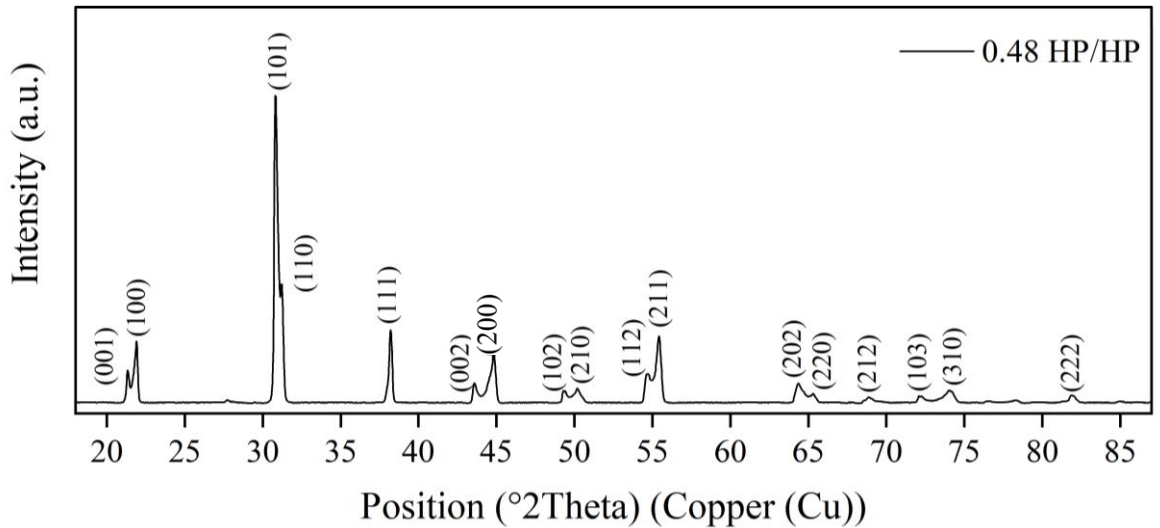
Figure 4-15 Full XRD pattern from composition 0.48 HP/HP PZT (pellet 5-4), after sintering at 1200°C.

Lastly, Figure 4-16 shows the focused comparison of the four main peaks obtained from the HP/HP compositions studied above. The higher level of detail offered by this diagram regarding the distortions, widening and unfolding exhibited by each of these compositions, further confirms the statements made in the previous paragraphs.
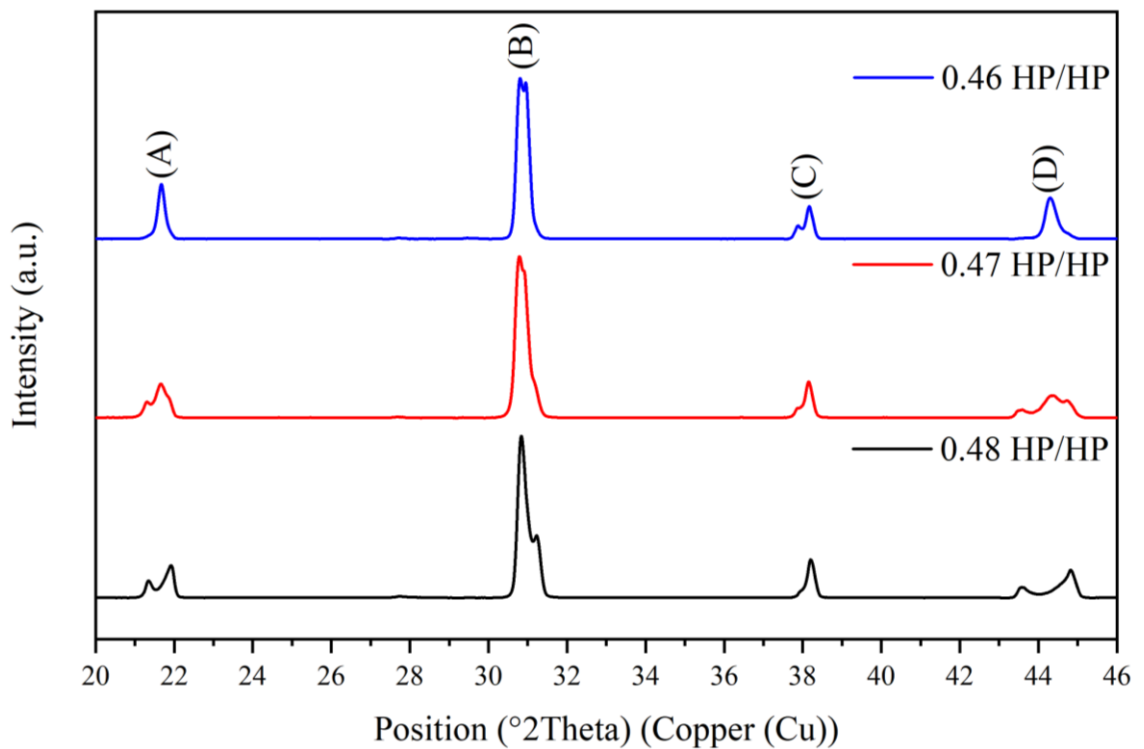
Figure 4-16 Comparison showing XRD peaks (100) (A), (110) (B), (111) (C) and (200) (D) from the PZT compositions 0.46 HP/HP pellet 5-9 (top), 0.47 HP/HP pellet 5-1 (middle) and 0.48 HP/HP pellet 5-4 (bottom), after sintering at 1200°C.

Following a similar analysis as the one done with the lower purity samples, a comparable progression in the encountered phases can be seen in the depicted diffractograms of the three compositions. As anticipated from the previous results, the lowest levels of the tetragonal phase amongst this group can be confirmed to belong to composition 0.46 HP/HP, where the lowest amounts of Ti are found, whilst composition 0.48 LP/LP presents the highest levels of this chemical and lowest traces of Zr.

Compared to Figure 4-12, Figure 4-16 shows a bigger gap in the transition between the two phases encountered in the three compositions. This indicates that the samples made with higher purities for their PZT and PZ components end up being further away from the assumed MPB ($x = 0.47$) as their compositions get further away from this value in either direction, even when the chosen values for x are identical to those of their low purity counterparts. This characteristic agrees with the findings of (Hu, et al., 2019), where the range of coexistence is found to be inversely proportional to the grain size. As discussed in section 4.2.1, Table 4-8 shows that the HP/HP samples presented higher average grain sizes, thus a narrower range of values, where Ti and Zr coexist, would be expected.

Additionally, Figure 4-17 places both purities for each composition in the same graph, displaying the six main patterns together for a clear comparison.
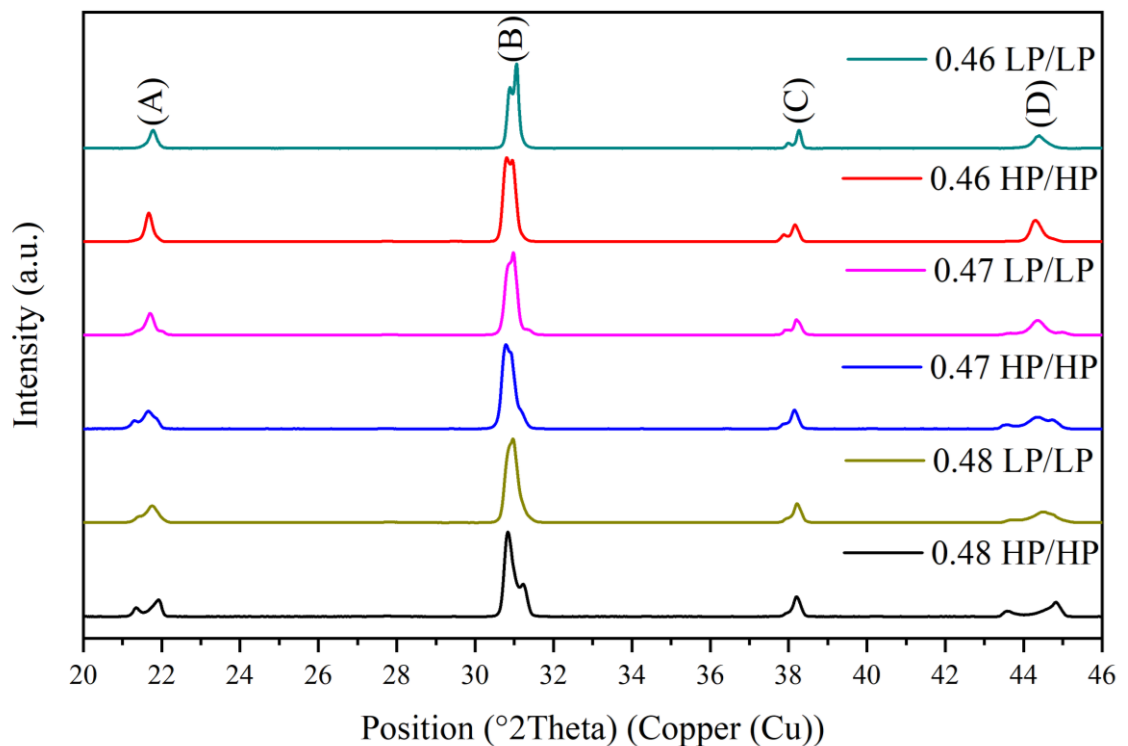
Figure 4-17 Comparison showing XRD peaks (100) (A), (110) (B), (111) (C) and (200) (D) from the six main sets of the PZT samples after sintering at 1200°C.

Out of the six samples, it can be observed that, although varying slightly, the peaks registered present consistent intensities amongst the corresponding planes throughout the patterns, indicating a uniform sintering process. Additionally, from these results it can be observed that the pellet found furthest from the MPB is the one belonging to composition 0.48 HP/HP, as it shows the smallest coexistence of both phases, presenting mainly as a typical tetragonal structure. Contrastingly, the composition exhibiting the highest levels of coexistence seems to be coming from the 0.48 LP/LP sample. The presentation of all the patterns through a vertical stack allows for an evident progression of the phases to be seen through the transformations of the peaks concerning their compositions and purities.

As part of the complete analysis of this material, the zoomed-in XRD patterns obtained from the four alternative compositions made with the opposite grade of purity for their PbO compensation, are presented in Figure 4-18. Although the full patterns registered for these samples are available (Appendix F), only the section on the diffractograms focusing on the four key peaks was chosen to be included in this section, due to its proven sufficiency in exploring the determining features of each composition. The specific pellet ID used from each composition can be found in the caption of Figure 4-18.
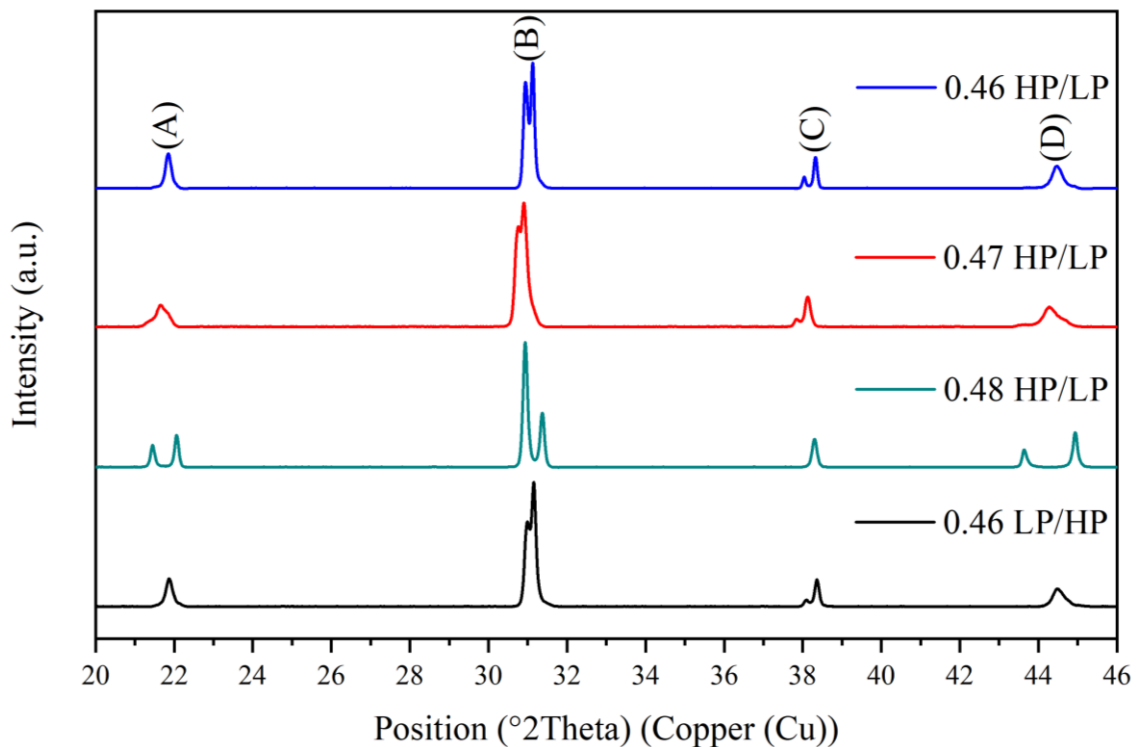
Figure 4-18 Comparison showing XRD peaks (100) (A), (110) (B), (111) (C) and (200) (D) from compositions 0.46 HP/LP PZT (pellet 6-7), 0.47 HP/LP PZT (pellet 4-7), 0.48 HP/LP PZT (pellet 4-5), 0.46 LP/HP PZT (pellet 6-9), after sintering at 1200°C.

Based on the behaviours observed in the peaks presented in Figure 4-18, it can be concluded that both 0.46 mixed purity compositions present a mainly rhombohedral structure, with the HP/LP sample showing a more pronounced splitting of peaks (B) and (C), implying an even higher level of the Zr-rich phase. Furthermore, composition 0.48 HP/LP appears to display the most defined splitting in peaks (A) and (D), as well as the tetragonal form of the unfolding of peak (B), and no identifiable visual traces of rhombohedral features, suggesting its contents are made up of entirely tetragonal structures.

Although phase coexistence can be seen in the pattern obtained from composition 0.47 HP/LP, the overlapping of the tetragonal and rhombohedral structures in peaks (A) and (D) seems to be higher than that registered in the LP/LP and HP/HP samples made with the same initial Ti content. The splitting seen in (B) and (C) suggests the rhombohedral structure is slightly more dominant.

The combined diagrams generated by the samples chosen from each of the ten sintered PZT compositions are provided in Figures 4-19 to 4-21. The focused patterns of the PZT samples made with composition $x = 0.46$ are found in Figure 4-19, the ones belonging to the disks with composition $x = 0.47$ are found in Figure 4-20, and the graphs from the PZT specimens with composition $x = 0.48$ are found in Figure 4-21.
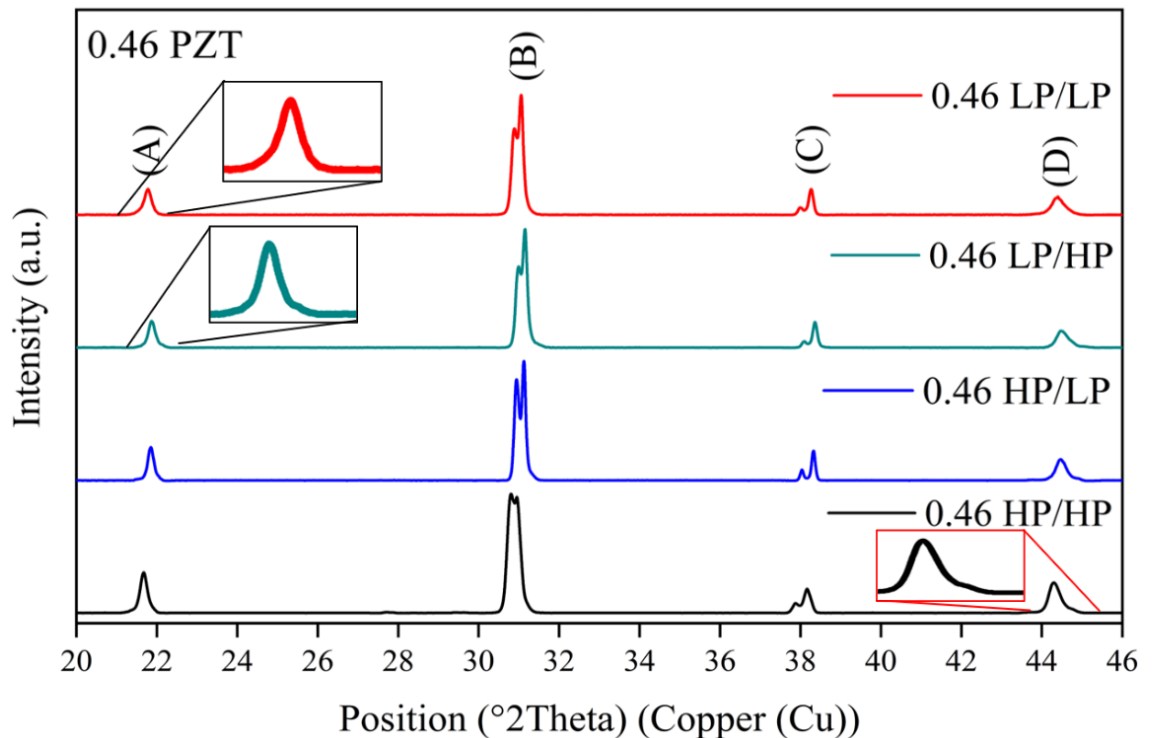
Figure 4-19 XRD patterns showing peaks (100) (A), (110) (B), (111) (C) and (200) (D) from the PZT samples with composition x = 0.46, after sintering at 1200°C.

Picturing all four compositions prior to sintering, from the differences in chemical purity employed, it would be expected that the LP samples exhibit lower levels of Ti, thus explaining why the resulting sintered disks from compositions 0.46 LP/LP and 0.46 LP/HP behave more like a typical rhombohedral than 0.46 HP/HP. Even when the stoichiometric calculations considered the specific purity percentages to obtain the necessary adjusted amounts of each chemical, the PbO compensation provided by the LP PZ could have supplied more Zr when saturating the environment inside the sealed alumina crucibles.

When compared, compositions 0.46 LP/LP and LP/HP present almost identical patterns. The minuscule differences lie in the subtle intensity changes shown between the main peak in (B) and its splitting to the left, as well as the almost imperceivable distortions in (A) for the LP/HP composition, making it ever so slightly more tetragonal. In this case, the LP PZT seems to have a more decisive role in the final phases shown, where changing the purity of the PbO compensation to an HP one, barely changed the phases found.

On the other hand, the HP PZT appears to be more susceptible to the purity of its lead compensation, which would be consistent as a result of the higher losses already seen in the HP PZT samples through their density and SEM analyses in the previous sections of this chapter. Assuming the HP PZT compositions in this group would have experienced the same losses in their PZT disks during sintering, the increased presence of the rhombohedral phases in the HP/LP specimen could be attributed to the Zr provided by the LP PZ atmosphere, as suggested above, showing a stronger bond with any vacancies found, resulting in increased permanence of this component.

Evidently, amongst these four compositions, the 0.46 HP/LP pellet shows the highest degree of rhombohedral structures, making it clear that the purities used during the sintering process have a direct impact on the final composition of the samples. The higher losses in this composition would make it more likely to be affected by the LP PZ atmosphere created, resulting in a more Zr-rich material, surpassing even the LP compositions.

Although sample 0.46 HP/HP could have shown the same volatilisation and susceptibility, the HP PZ used to aid with the losses would have failed to provide the same degree of compensation, thus justifying being able to register the minimal tetragonal traces that can be seen in peak (D) and being the only one from this group displaying the initial stages of the tetragonal form in the unfolding of peak (B).

As the value of *x* increases, the behaviour seen in the previous group slowly starts to shift. Although the 0.47 compositions depicted in Figure 4-20 still show the highest ZrO_2 amounts registered from the HP/LP sample and the highest TiO_2 from the HP/HP pellet, the differences become more subtle, and the compositions appear to share a similar degree of coexistence between the tetragonal and rhombohedral phases. Nevertheless, upon further inspection, the closest proximity to the MPB appears to be associated with a composition located somewhere between samples 0.47 HP/HP and LP/LP.
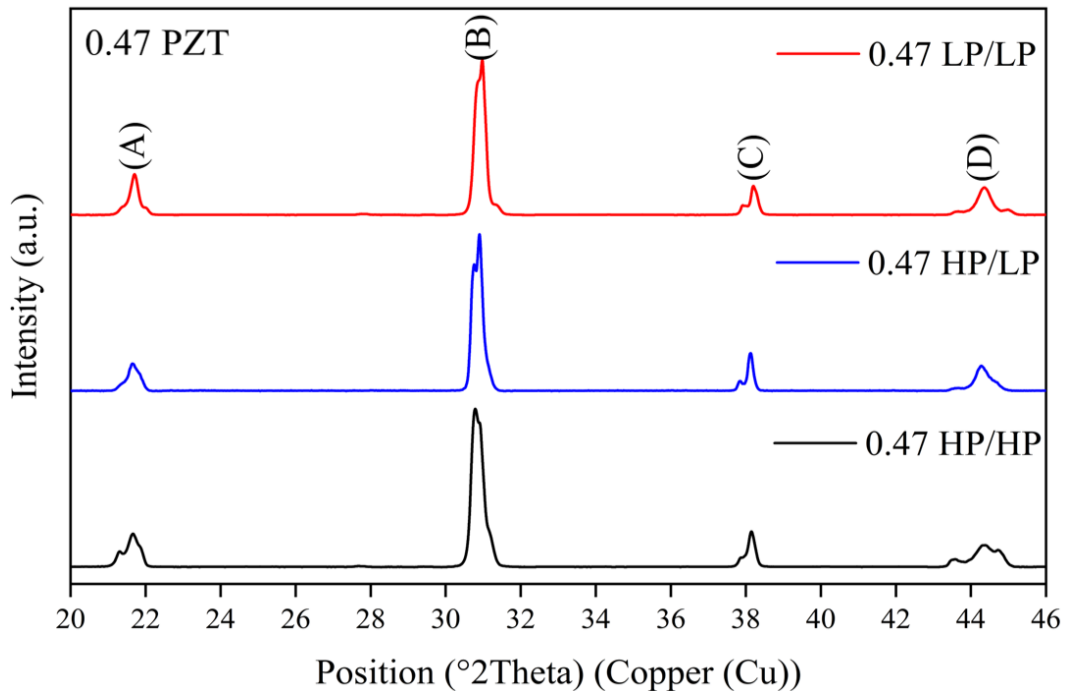
Figure 4-20 XRD patterns showing peaks (100) (A), (110) (B), (111) (C) and (200) (D) from the PZT samples with composition x = 0.47, after sintering at 1200°C.

Finally, as the composition value reaches 0.48, the behaviour from the sample patterns depicted in Figure 4-21 appears to have shifted to the opposite end of the scale. Amongst this group, the highest rhombohedral content is found in the 0.48 LP/LP sample, and the strongest tetragonal influence is seen in the 0.48 HP/LP disk. Despite these observations seeming inconsistent with the ones previously made, they still abide by the same principles.

In this case, the primary exhibited phase is tetragonal and the sample with the highest amounts of this structure is the one belonging to composition 0.48 HP/LP. Analogous to this, amongst the 0.46 and 0.47 compositions, the highest levels of the main phase (rhombohedral) are also found in the HP/LP pellet. This would indicate that the HP/LP arrangement seems to amplify the predominant phase formation found in the material.
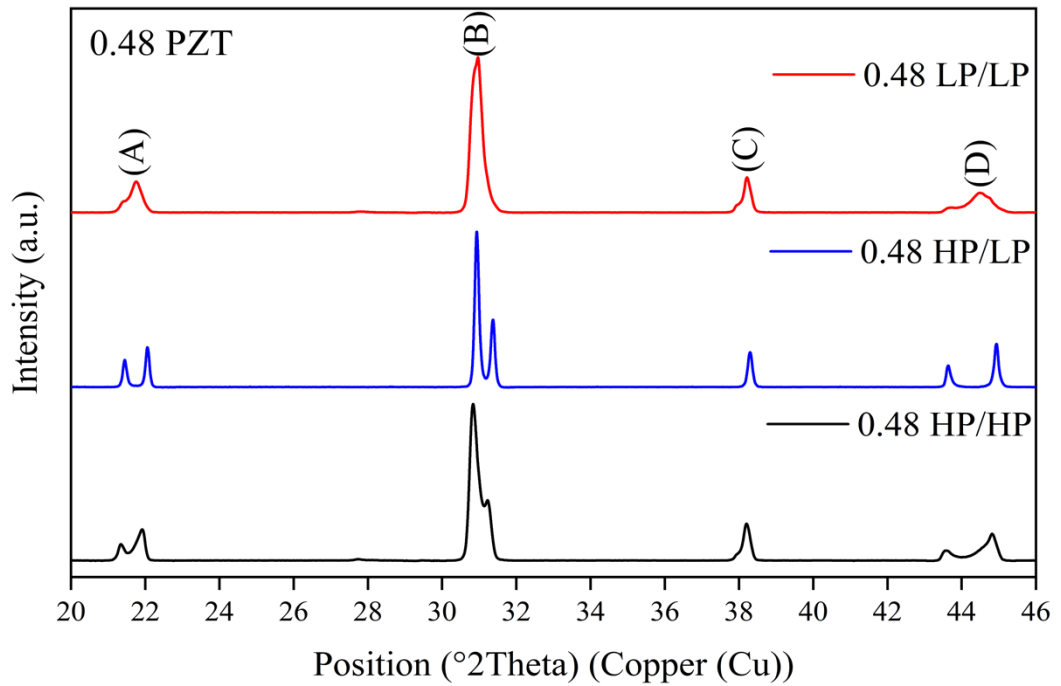
Figure 4-21 XRD patterns showing peaks (100) (A), (110) (B), (111) (C) and (200) (D) from the PZT samples with composition x = 0.48, after sintering at 1200°C.

Regarding the other conjecture made, where the lowest levels of the predominant phase amongst the 0.46 and 0.47 compositions were shown by the HP/HP disks, the diffraction pattern containing the least amount of the predominant structure when the samples are made with even higher percentages of titanium, belongs to the LP/LP sample. This pattern of behaviour would be consistent with the direct relationship between the grade of purities used during sintering and the final phase formation, mentioned before.

HP PZT would inherently contain higher traces of Ti, therefore exhibiting lower levels of rhombohedral structures, which is further exacerbated by the poor performance of their HP PZ atmosphere, inevitably making the HP/HP combination the least rhombohedral of the groups where this phase dominates. Comparably, LP PZT would start with lower levels of TiO_2 compared to the HP counterparts, and when paired with the LP PZ disks, any compensation required would not be able to aid in any addition of Ti, thus making the LP/LP arrangement remain at the bottom of the compositions displaying a more tetragonal structure.

The consistent evidence provided by these results strongly supports the statements made in sections 4.1 and 4.2, where the HP PZT disks were found to suffer higher volatilisation, and the HP atmospheres were found to not compensate the PZT disks as efficiently as their LP counterparts.

To summarise these findings, a composition scale has been created and included in Figure 4-22, where the ten sintered compositions have been placed in relation to the level of displayed amounts of coexistence between the rhombohedral and tetragonal phases in their collected diffractograms. The estimated MPB for pure PZT has been identified and labelled somewhere between LP/LP compositions 0.47 and 0.48, based on their exhibited features.

◆ **Estimated MPB for PbZr$_{1-x}$Ti$_x$O$_3$**
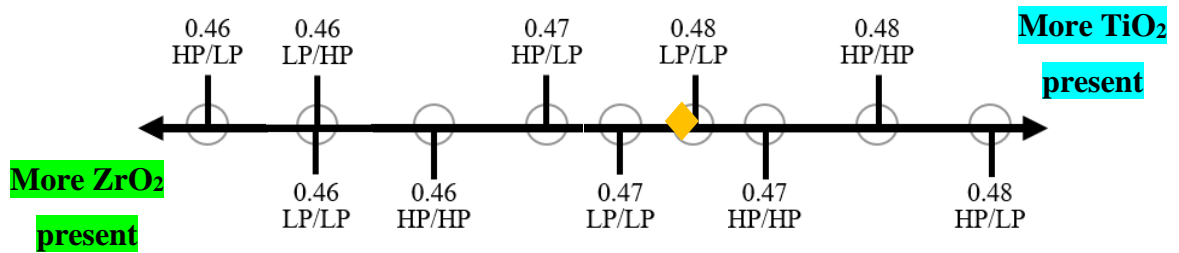
Figure 4-22 Composition scale in relation to the level of coexistence between the rhombohedral and tetragonal phases, showing the estimated MPB for the prepared PZT ceramics.

4.3.1 Pyrochlore

As explained in sections 2.8 and 3.9.1, when PbO evaporation is not properly compensated in lead-based ceramics, like the PZT sets sintered for this research, the internal composition of the piezoelectric material will change due to the lower amounts of lead oxide in the perovskite matrix, allowing a new phase to be formed, known as pyrochlore (Siddiqui, et al., 2020). While perovskites have a lattice with an ABO_3 formula, pyrochlore follows an $A_2B_2O_7$ formula, with two distinct interpenetrating corner-sharing tetrahedra lattices (Garlea & Chakoumakos, 2015).

According to (Kong, et al., 2008), volatilized PbO might remain in the grain boundaries of lead-based ceramic materials during the early stages of any heat treatments applied, such as annealing or sintering. If left to act on the samples without further external compensation for prolonged times, the PbO will commence to escape from the lattice, causing the decomposition of the perovskite into pyrochlore, and limiting the growth of the grains. The presence of this new phase in PZT ceramics intended for energy harvesting will worsen their efficiency due to their poor electrical properties (Kim, et al., 2018).

The presence of this structure in a PZT sample can be identified by a small peak appearing in the XRD patterns before the 30° mark. When this peak is detected, it can be concluded that the sample did not sinter properly, and the material will likely possess diminished piezoelectric and ferroelectric properties.

A clear example of this phase is depicted in Figure 4-23, where the registered XRD peaks from a previously poorly sintered sample made for composition 0.46 LP/LP can be studied. Besides unexpectedly showing splitting associated with the tetragonal phase, this pattern also presents an additional peak around 28°, indicative of the pyrochlore phase.
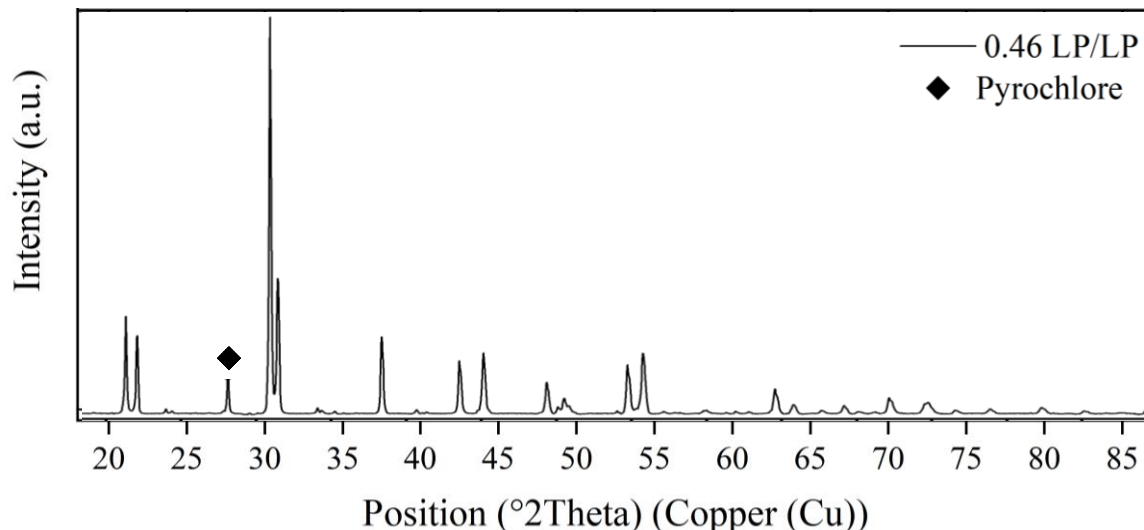
Figure 4-23 Full XRD pattern of sintered PZT sample with composition 0.46 LP/LP exhibiting pyrochlore phase around 28°.

Despite minor levels of pyrochlore shown in some of the diagrams presented throughout this section, the amounts found are considered negligible. The relative intensities of these peaks compared to the rest of the pattern are so small that this phase would not be able to cause any relevant impact on the piezoelectric properties. Therefore, the resulting sintered samples can be deemed as exhibiting the intended pure perovskite structure.

Finally, although seen in varying proportions, the majority of the samples studied exhibited some level of coexistence between the expected phases, indicating some proximity to the MPB, with the exception of composition 0.48 HP/LP. Additionally, almost all the 0.46 PZT disks present virtually unperceivable traces of the tetragonal phase, thus putting their potential piezoelectric performance into question.

The obtained results also provided new information to reassess the statement made at the end of section 4.2.1, where the grain sizes were used to identify the compositions closest to the MPB. From the data obtained from the phase formation analysis, the compositions that are expected to perform the best as energy harvesters are said to be 0.47 HP/HP, 0.47 LP/LP and 0.48 LP/LP, which partially agree with the SEM comments made but would require further analysis to confirm.

4.4 Composition analysis of the PZT ceramic disks

The examination of the chemical composition of nine out of the ten sets of the sintered PZT disks was carried out thanks to the help of Dr Davide Cappelluti. A point analysis of several small areas of the prepared surfaces was completed using the energy dispersive spectrometer (EDS) system (Oxford Instruments Energy 250) attached to the scanning electron microscope (Philips/FEI XL30 ESEM) located in the Joseph Black building at the University of Glasgow, UK.

This study combines some of the processes followed in the SEM and XRD analyses, as it involves bombarding electrons onto the sample through an energy source, where some of the energy is dissipated as an ejected electron from the lower energy levels in the material. To fill this space, a higher electron releases the extra energy, which is then detected and mapped as part of the characteristic pattern of the material. The intensity of the resulting peaks is associated with the concentration of the atom of origin, while the position in the spectrum identifies the element the atom belongs to (Thermo Fisher Scientific Inc., 2023).

This study was done on small pieces that were broken off from one sample of each composition, where more than one was available, which is why composition 0.47 HP/LP was not put through this test, as its destructive nature would have prevented any further characterisation or testing to be carried out on this composition.

The broken pieces were ground to a powder by hand in an agate mortar, placed over a stub, and evenly coated with a fine grain layer of gold (1-20 nanometers) using a Polaron Emitech SC7640 Sputter Coater. Once prepared, the atomic percentages (at%) were calculated for each composition. Since it would be impossible to associate the oxygen with one parent oxide, the measurements obtained were adjusted to ignore this.

The samples were tested on 4 different regions, sampling 2 (~25 x 25μm^2) and 2 points in each region. The results are presented in Table 4-9, Table 4-10 and Table 4-11. The average at% is shown as the result obtained from the values measured from only the areas (At% areas), as well as the areas with the selected points (Total At%). Due to the likely local concentration of one of the elements in the sampling points taken, the Total At% will usually exhibit values outside the average range. This can also be caused by the scattering of electrons created by the powdered samples.

All the presented values are accompanied by their corresponding absolute error, which was calculated using the standard deviation obtained from each group through the statistical analysis tools offered by Microsoft Excel.

Table 4-9 EDS analysis of PZT samples with compositions 0.46 LP/LP (pellet 6-12), 0.47 LP/LP (pellet 4-12), and 0.48 LP/LP (pellet 4-1), after sintering at 1200°C.

	0.46 LP/LP		0.47 LP/LP		0.48 LP/LP	
	At% areas ± Δat%	Total At% ± Δat%	At% areas ± Δat%	Total At% ± Δat%	At% areas ± Δat%	Total At% ± Δat%
Ti	24.39 ± 0.46	23.99 ± 0.35	25.62 ± 0.85	25.61 ± 1.03	26.72 ± 0.74	25.85 ± 0.51
Zr	28.18 ± 0.27	28.41 ± 0.21	27.28 ± 0.54	27.08 ± 0.77	25.96 ± 0.61	26.65 ± 0.45
Pb	47.43 ± 0.45	47.60 ± 0.30	47.10 ± 0.53	47.31 ± 0.72	47.32 ± 0.48	47.50 ± 0.29

Table 4-10 EDS analysis of PZT samples with compositions 0.46 HP/HP (pellet 5-9), 0.47 HP/HP (pellet 5-1), and 0.48 HP/HP (pellet 5-4), after sintering at 1200°C.

	0.46 HP/HP		0.47 HP/HP		0.48 HP/HP	
	At% areas ± Δat%	Total At% ± Δat%	At% areas ± Δat%	Total At% ± Δat%	At% areas ± Δat%	Total At% ± Δat%
Ti	23.98 ± 0.57	25.27 ± 0.98	25.80 ± 0.54	25.67 ± 0.57	26.31 ± 0.59	27.05 ± 0.79
Zr	27.98 ± 0.31	27.52 ± 0.36	27.35 ± 0.61	27.11 ± 0.38	25.76 ± 0.45	25.77 ± 0.69
Pb	48.03 ± 0.58	47.22 ± 0.76	46.85 ± 0.36	47.22 ± 0.41	47.93 ± 0.46	47.17 ± 0.49

Table 4-11 EDS analysis of PZT samples with compositions 0.46 LP/HP (pellet 6-9), 0.46 HP/LP (pellet 6-7), and 0.48 HP/LP (pellet 4-5), after sintering at 1200°C.

	0.46 LP/HP		0.46 HP/LP		0.48 HP/LP	
	At% areas ± Δat%	Total At% ± Δat%	At% areas ± Δat%	Total At% ± Δat%	At% areas ± Δat%	Total At% ± Δat%
Ti	23.66 ± 0.68	23.74 ± 0.62	24.11 ± 0.49	23.94 ± 0.46	26.91 ± 0.58	27.00 ± 0.78
Zr	27.74 ± 0.76	27.69 ± 0.91	27.97 ± 0.32	28.16 ± 0.37	26.57 ± 0.36	26.14 ± 0.45
Pb	48.60 ± 0.70	48.57 ± 0.53	47.93 ± 0.25	47.90 ± 0.21	46.52 ± 0.55	46.86 ± 0.54

Despite the at% being quite consistent throughout the samples, it was found that the highest average content of Ti was measured in the 0.48 HP/LP specimen. In general, the highest values in each composition group agree with the 0.48 disks exhibiting the most titanium. As with the XRD patterns, it would be expected that the concentration of Ti should increase as the value of x increases, therefore the results presented are consistent with this statement.

Contrastingly, when comparing the Zr found in the samples, a pattern can also be observed, as the highest amounts of Zr seem to be associated to the 0.46 compositions in all the groups, reflecting that the samples remained as the most Zr-rich, even after sintering.

Since the full set of compositions is lacking from the samples made with opposite purity PZ, only partial observations can be made regarding the presented data. Amongst the HP/LP disks, the 0.46 disk showed higher levels of Pb and Zr, supporting the phase predominance found in the XRD patterns before.

Sample 0.46 LP/HP, as the rest of the disks with $x = 0.46$, shows that the specimen presents more Zr than Ti, which is also the case of the compositions where $x = 0.47$. The compositions with $x = 0.48$, not only present more Ti than the other two composition groups but also appear to have more Ti than Zr in their own chemical structure, explaining the level of tetragonal phase displayed in their diffractograms.

According to the crystallographic arrangement found in PZT perovskites, each $PbZr_{1-x}Ti_xO_3$ crystal should contain 1 atom of Pb, 3 of oxygen and 1 atom of either Zr or Ti. Therefore, when analysing the adjusted results without the oxygen, a 1:1 ratio would be expected between Pb and Zr + Ti.

Since the projected proportion of Ti and Zr would come from the composition (46:54, 47:53 or 48:52), the final ratio between the elements would be 23:27:50, 23.5:26.5:50 or 24:26:50. Any values moving away from this would indicate higher losses of some of the involved chemicals, resulting in the apparent gain of the others.

Higher losses of Ti and/or Zr would result in higher relative concentrations of Pb, but since the at% measured shows that none of the samples had Pb values higher than the expected 50%, this would suggest that all the sets suffered some level of lead loss, which was greater than any possible compensation provided by their PZ atmospheres and higher than the losses of the remaining two chemicals.

Furthermore, since the starting Zr used in all the samples was higher than the Ti, as $x < 50$, its atomic percentage would end up having a higher relative gain with higher Pb volatilisation. Given that Ti cannot be compensated by the PZ disk placed with the PZT samples during sintering, the increased percentages found must be a consequence of a decrement in the other chemicals, which would be higher than any Ti losses.

To compare their closeness to the original stoichiometry used, Table 4-12 presents the adjusted values between Ti and Zr relative to each other.

Table 4-12 Ti and Zr at% calculated from the EDS analysis of the ten PZT samples.

PZT Composition	at% Ti	at% Zr
0.46 LP/LP	46.39	53.61
0.46 LP/HP	46.04	53.96
0.46 HP/LP	46.27	53.73
0.46 HP/HP	46.11	53.89
0.47 LP/LP	48.38	51.62
0.47 HP/HP	48.55	51.45
0.48 LP/LP	50.70	49.30
0.48 HP/HP	50.52	49.48
0.48 HP/LP	50.29	49.28

Based on the previous assumption made for the samples presenting the highest levels of Ti, Table 4-12 confirms that even when adjusted, the 0.48 compositions contain the most Ti from each group, but challenges disk 0.48 HP/LP being the most Ti-rich amongst the sets.

Nevertheless, due to the random and limited nature of the chosen scanned areas in the EDS analysis, as it is being done on only a small portion of the sample rather than the entire resulting disk, the XRD patterns would have a higher reliability in the conclusions that can be made, particularly when the differences between the percentages measured are so small. To improve this, it would be suggested that for future experiments, an increased number of areas is studied, and an entire pellet is prepared for analysis.

Despite its limitations, the EDS analysis shows that amongst the three composition groups, the 0.46 samples were the ones that remained closer to the starting stoichiometry, which would explain their distance from the MPB and lower levels of phase coexistence in their XRD patterns. Although the ten sintered sets experienced some level of shifting due to the apparent loss of Zr and Pb, as the composition value increases, the shift seems to proportionally increase, leaving the 0.48 samples furthest from their original stoichiometry.

4.5   Chapter 4 Summary

Through the analysis of the physical properties of the sintered samples, the mass and dimensions of each disk were measured after completing the second stage of the ceramic process. The density of the PZT pellets was determined using the measured parameters, and later used to draw correlations to their performance as energy harvesters. Although all the sample dimensions appeared to have reduced after the sintering, the LP/LP samples had the highest densities in general, as well as closer values to the standard found in the literature

($\sim$7.5 g/cm^3). The higher densities that were obtained from these disks would provide a better endurance to the expected impacts associated with power applications.

Additionally, to aid the HP samples it was observed that changing the HP atmosphere to an LP one could potentially increase densification, although this would require further experimentation. It was also observed that there is a direct relationship between the number of samples sintered together in a sealed crucible and showing higher densities, thus encouraging the idea of having more samples placed together through this stage to reduce the loss of material as well as their potential deformation. These arguments further support the statement made regarding an intercalated pellet arrangement for sintering, which begins and ends with a PZ compensation disk to reduce the loss of PbO in the samples located in the middle, granting a more uniform sintering process and therefore higher densities.

A clear visualisation of the microstructure of the resulting disks was obtained using scanning electron microscopy (SEM). The SEM images presented six different areas and magnifications that were collected from each sample's surface, where the typical morphologies could be observed in the scanned crystals, as well as any superficial impurities or defects. Due to restricted access to the equipment, only samples from the six main sets could be scanned before the disks were lapped as described in Chapter 5, which corrupted the observable surfaces, making it impossible to see clear images that could be included as part of this analysis. The average grain size measured for each of the studied compositions showed that amongst the six main sets, the LP/LP samples exhibited smaller grain sizes than the HP/HP disks, with composition 0.46 displaying the smallest grain size of all the specimens.

It was concluded from the scanned SEM images that the HP/HP samples not only had bigger grain sizes and more pores but also exhibited signs of higher levels of PbO losses, which were suspected from the dark spots seen in the scans, further explaining the lower densities obtained from this group. From these observations, it was determined that HP PZT could benefit from having LP PbO compensation to improve their densification whilst also providing an economic advantage.

The expected tetragonal and rhombohedral phases were observed in varying quantities after performing X-ray diffraction (XRD) to obtain the corresponding pattern from each chosen PZT sample. Throughout the collected diffractograms, the peaks associated with planes (100) and (200) in the material, which are identified as two of the four main peaks to

look out for in perovskites, showed that as the amount of TiO₂ increased in the PZT disks, the single sharp peaks that would be typical of a rhombohedral structure would start to broaden until eventually splitting into two or three new peaks with reduced amplitudes.

Multiple overlapping peaks were seen in several of the patterns, usually in the form of a triplet. This indicates a coexistence of several crystal phases in the material, typically caused due to their proximity to the MPB. Despite some of the compositions exhibiting greater coexistences of the two main expected phases (rhombohedral and tetragonal), most of the samples exhibited some degree of both structures in their generated X-ray plots, indicating some proximity to the MPB, with the exception of composition 0.48 HP/LP, which appeared to be entirely tetragonal. It is also worth noting that some of the 0.46 PZT samples had almost no traces of the tetragonal structure and appeared mostly rhombohedral.

The data obtained from this study suggested that the 0.47 HP/HP, 0.47 LP/LP and 0.48 LP/LP compositions were the ones expected to perform the best as energy harvesters, which partially agreed with the SEM observations but needed confirmation from the functional characterisation.

Finally, the energy dispersive analysis (EDS) explored the atomic percentage of each of the chemical elements found in the disks. Amongst the three composition groups, the 0.46 samples were the ones that remained closer to the starting stoichiometry, supporting their estimated location relative to the assumed MPB, and explaining the lower phase coexistence seen in their XRD patterns. Even though the EDS results were quite consistent throughout the samples, the composition analysis showed that the highest levels of Pb in the samples belonged to composition 0.46 LP/HP and the lowest values to composition 0.48 HP/LP.

Although a higher PbO volatilisation had been assumed on the HP samples from the density and SEM results, the EDS showed no particular evidence to support this, aside from the disks with composition 0.47, where the HP/HP pellet displayed lower percentages of Pb on the scanned surfaces. Additionally, due to the apparent loss of Zr and Pb, the distribution between the Zr and Ti found in the samples seems to grow closer as the composition value increases, leaving the 0.48 samples furthest from their original stoichiometry.

Following the physical characterisation presented in this chapter, the functional characterisation was carried out on the best samples from each group after being prepared and processed prior to their coupling. This is described and discussed in Chapter 5.

Chapter 5. FUNCTIONAL CHARACTERISATION OF THE PZT PIEZOELECTRIC CERAMICS

From each of the ten sets, the sample with the least number of imperfections was chosen to conduct the functional characterisation included in the next sections of this chapter, and for the electronic adaptation and performance tests described in Chapter 6, which include coupling the samples as kinetic energy harvesters. This chapter includes the description of the process that was followed to prepare the samples prior to their functional characterisation, which included their polarization response, their main figures of merit (FOM), and their dielectric properties, as well as the correlation of this data with the observations made in the previous chapters, leading to the identification of the optimal fabrication and processing parameters based on the best performing samples from each set.

5.1 Lapping of the sintered piezoelectric ceramic disks

After carrying out the physical characterisation of the sintered pellets, lapping was performed on the samples to get rid of any superficial contaminants and imperfections, whilst also achieving parallel planes between the faces of the disks. In the pursuit of the best possible piezoelectric performance from the ceramics, the new dimensions of each disk were chosen based on the direct effect the reduction of the radius or thickness of the sample has on their power output and density (Pollet, et al., 2019).

Whilst it was observed that a smaller radius leads to a higher power density, it also results in lower power outputs, higher resonant frequencies, more difficulty to achieve control with higher switching losses, and a higher risk of damaging the resonance by the fixture of the piezoelectric material. Alternatively, reducing the thickness based on a fixed radius, would not only provide higher power outputs but also better power densities, thus improving efficiency whilst maintaining the same frequency (Pollet, et al., 2019).

For optimal piezoelectric performance and characterisation, the thickness of each pellet was set to be at least 16 times smaller than its diameter (Alguero, et al., 2004). Therefore, based on the measurements taken in Chapter 4 and included in Appendix B, each sample was initially lapped until reaching a thickness of less than 0.87mm, but this was adjusted if the diameter of the pellet was reduced after all visible significant pores and cracks were removed from the faces and circumference. Figure 5-1 shows the PZT samples before being lapped.
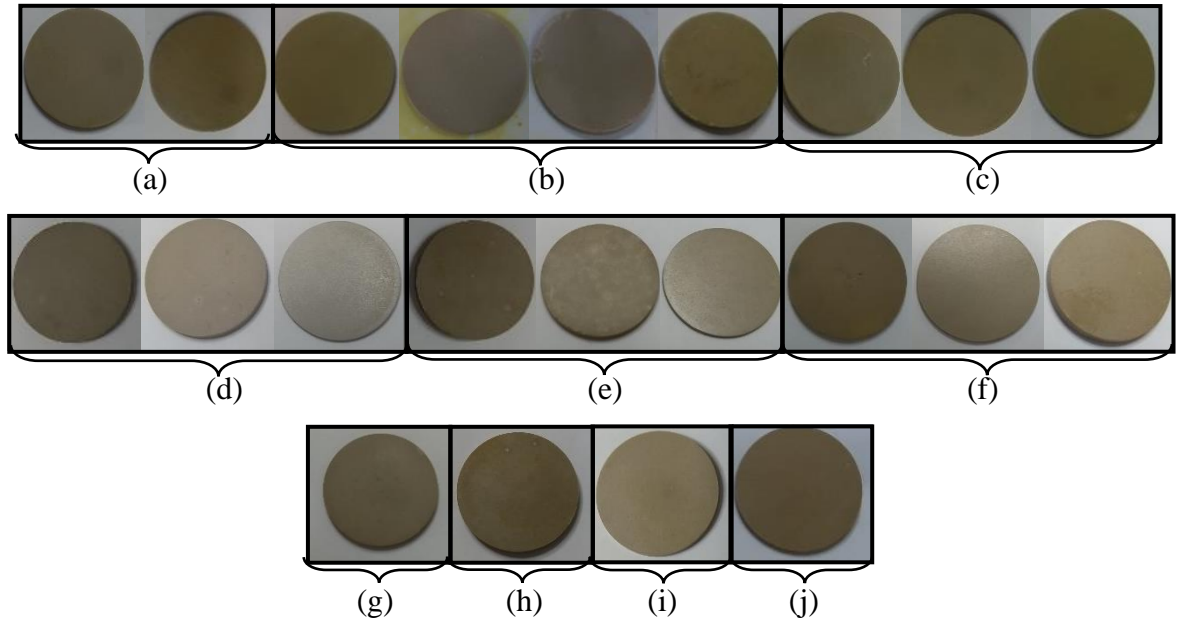
Figure 5-1 PZT sintered samples before being lapped. (a) Pellets 6-4 & 6-12 from 0.46 LP/LP, (b) Pellets 4-8, 4-9, 4-10 & 4-12 from 0.47 LP/LP, (c) Pellets 4-1, 4-3 & 4-4 from 0.48 LP/LP, (d) Pellets 5-7, 5-8 & 6-6 from 0.46 HP/HP, (e) Pellets 5-2, 5-3 & 6-1 from 0.47 HP/HP, (f) Pellets 5-5, 5-6 & 6-3 from 0.48 HP/HP, (g) Pellet 6-8 from 0.46 HP/LP, (h) Pellet 4-7 from 0.47 HP/LP, (i) Pellet 4-6 from 0.48 HP/LP and (j) Pellet 6-10 from 0.46 LP/HP.

A series of different lapping papers (waterproof silicon carbide paper, FEPA, Struers) were used to reduce the thickness and diameter of each sample. Grits 220, 500, and 1000 were employed during the process, where the coarseness of the paper would increase as the grade decreases. The coarser papers were used to take the first layers of the pellet, while the finer grits were used to lap the final millimetres of the surface, leaving a smooth and shiny finish. The lapping was performed using the stainless-steel sample holder shown in Figure 5-2, to guarantee the faces remained parallel through the process and equal pressure was applied to the sample to minimise the risk of breaking.

Figure 5-2 Steel sample holder used for lapping the PZT disks from each composition.

The entire process was carried out in a wet environment by pouring a layer of distilled water on the paper before placing the sample with the holder on top, as depicted in Figure 5-3. This was repeated throughout the process to enable a smooth lapping and prevent harsh movements that could cause the pellet to break. After determining the minimum thickness required based on the diameter of each pellet, the various grits were used accordingly for a few cycles each, frequently measuring the dimensions using the micrometre shown in Figure 5-4, until reaching the desired features.

Figure 5-3 Sample holder on top of wet silicon carbide lapping paper.

Figure 5-4 Micrometre used for measuring thickness during lapping.

The new dimensions and diameter/thickness ratios are included in Table 5-1, along with the difference from the original values. The absolute error for the thickness and diameter is half of the measuring device resolution, while the absolute error for the area was obtained from the rules of error propagation and taken as the average across all the samples.

Table 5-1 Diameter, thickness, ratio, and surface area of the lapped PZT samples with their IDs.

PZT Composition	Pellet ID	Th ± 0.0005 (mm)	Thickness reduction (mm)	d ± 0.005 (mm)	Diameter reduction (mm)	Diameter/ Thickness Ratio	Surface Area (mm²) (± 0.12)
0.46 LP/LP	6-4	0.535	0.59	14.80	2.53	27.66	172.03
0.47 LP/LP	4-8	0.600	1.01	16.70	0.47	27.83	219.04
0.48 LP/LP	4-4	0.506	1.23	13.65	3.55	26.98	146.34
0.46 HP/HP	5-8	0.500	1.33	17.60	0.07	35.20	243.28
0.47 HP/HP	5-3	0.380	1.24	14.95	2.83	39.34	175.54
0.48 HP/HP	5-5	0.515	1.31	17.75	0.03	34.47	247.45
0.46 HP/LP	6-8	0.660	0.47	17.30	0.27	26.21	235.06
0.47 HP/LP	4-7	0.660	1.21	17.40	0.05	26.36	237.79
0.48 HP/LP	4-6	0.780	0.46	13.11	4.58	16.86	135.81
0.46 LP/HP	6-10	0.684	0.48	14.80	2.66	21.64	172.03

To determine the parameters needed for the sample polarization, another pellet from each set, where available, was broken into smaller pieces, usually two or three, reshaped by rounding off the edges and put through a similar lapping process as the main disks, except for not pursuing a circular surface area or such a strict ratio with the thickness.

Figure 5-5 shows the chosen samples for this process. Some can be seen already reshaped (top of (d)), while others show portions of the original pellets ((b), (c), (e) & (f)) or the entire sintered disk ((a), (g), (h) & (i)). Since composition 0.47 HP/LP only had one sample, this was kept whole to be able to carry its functional characterisation and electronic adaption. The parameters used for this composition were extrapolated from the results obtained from the other tested samples. Table 5-2 shows the number of small pieces obtained from each composition and their thickness. The relevant surface areas are included in section 5.3.
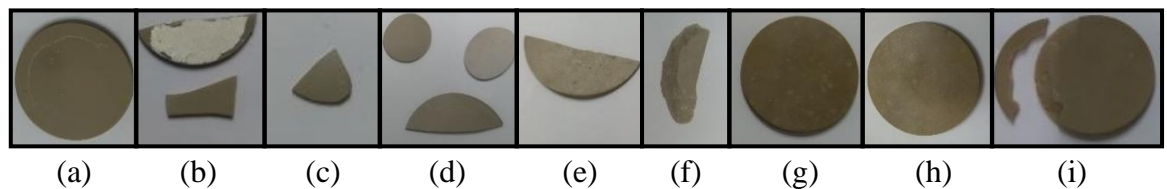
Figure 5-5 PZT samples chosen to create the smaller testing pieces. (a) 0.46 LP/LP (6-11), (b) 0.47 LP/LP (4-11), (c) 0.48 LP/LP (4-2), (d) 0.46 HP/HP (5-9), (e) 0.47 HP/HP (5-1), (f) 0.48 HP/HP (5-4), (g) 0.46 HP/LP (6-7), (h) 0.48 HP/LP (4-5) and (i) 0.46 LP/HP (6-9).

Table 5-2 Thickness of the lapped PZT small sample pieces from each composition.

PZT Composition	Pellet ID	# of Pieces	Thickness (mm) (± 0.0005)
0.46 LP/LP	6-11	3	0.584
0.47 LP/LP	4-11	2	0.818
0.48 LP/LP	4-2	3	0.585
0.46 HP/HP	5-9	2	0.770
0.47 HP/HP	5-1	2	0.592
0.48 HP/HP	5-4	3	0.482
0.46 HP/LP	6-7	2	0.576
0.48 HP/LP	4-5	2	0.532
0.46 LP/HP	6-9	2	0.572

Once lapping was completed for all the samples and corresponding small pieces, they were individually submerged in a Pyrex beaker with ~20mL of pure acetone, and placed in an ultrasonic bath (PACISA Selecta, Ultrasons, Spain) for about 3 min, (Figure 5-6), taking the beaker out and swirling its contents every minute to improve the cleaning process.

Figure 5-6 PZT pellet being cleaned with ethanol inside an ultrasonic bath.

Afterwards, the samples were taken out using forceps and airdried on a lint-free moisture absorbent towel. Throughout the remaining processes described in this chapter, the pellets were only handled using forceps and/or nitrile gloves to prevent any contamination from bare hands. Figure 5-7 and Figure 5-8 show the main disks and small sample pieces, respectively, after being lapped, cleaned, and dried. Their caption indicates the composition and specific pellet that was put through this process.
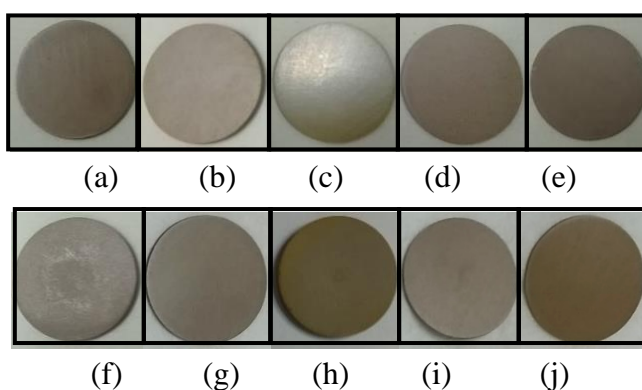
Figure 5-7 Resulting PZT samples after being lapped, cleaned, and dried. (a) 0.46 LP/LP (6-4), (b) 0.47 LP/LP (4-8), (c) 0.48 LP/LP (4-4), (d) 0.46 HP/HP (5-8), (e) 0.47 HP/HP (5-3), (f) 0.48 HP/HP (5-5), (g) 0.46 HP/LP (6-8), (h) 0.47 HP/LP (4-7), (i) 0.48 HP/LP (4-6), and (j) 0.46 LP/HP (6-10).
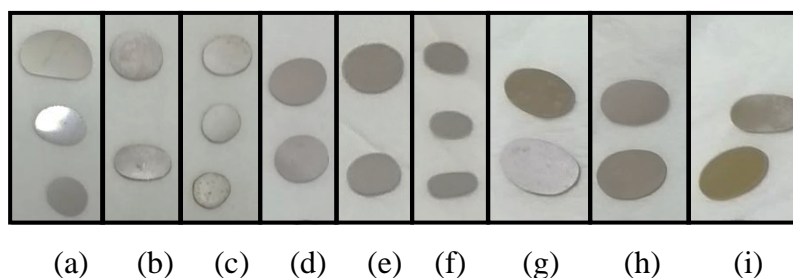
Figure 5-8 Resulting PZT small sample pieces after being lapped, cleaned, and dried. (a) 0.46 LP/LP (6-11), (b) 0.47 LP/LP (4-11), (c) 0.48 LP/LP (4-2), (d) 0.46 HP/HP (5-9), (e) 0.47 HP/HP (5-1), (f) 0.48 HP/HP (5-4), (g) 0.46 HP/LP (6-7), (h) 0.48 HP/LP (4-5) and (i) 0.46 LP/HP (6-9).

5.2 Electrode placement on the lapped PZT piezoelectric ceramics.

After drying, the lapped pellets were coated with a thin smooth layer of silver paint (Low-temperature Du-Pont conductor paste) on one of their faces. No bubbles or irregularities should be left on the surface. Before applying the paste on the remaining face, the first side was dried by placing the samples in an oven at 110°C for 30min with no specific heating or cooling ramp. This was repeated after taking the samples out and coating the other side of the disks in the same way as before. To ensure the coat was thick enough to withstand the necessary lapping to leave a smooth, flat surface where the wires could be soldered, a second layer of the paste was applied to both sides following the previous steps.

Once the silver paint has been applied and dried on both sides of the pellets with the desired thickness, acetone or lapping can be used to remove any paint from the circumference to guarantee there is no connection between the faces of the disks and prevent them from short-circuiting during the coming tests. Acetone can be applied to a cotton bud and slowly rubbed against the circumference while holding and turning the sample diameter-wise between the index finger and thumb. A lapping machine is not recommended for this due to the orientation of the sample, its thickness, and the location of the layers to be removed. Instead, lapping should be done by hand using a medium grit lapping paper by holding and turning the sample as described before until achieving a smooth, clean edge.

For these samples, the 1000 grit waterproof silicon carbide paper was used without any liquid carrier vehicles (dry environment), to carefully remove any silver paste from the edges and circumference of each pellet before being cured at 600°C for 1h inside an Energon S.L. furnace (Spain) with Eurotherm temperature controller 2416, with a heating/cooling ramp of 3°C/min. The samples were placed inside open alumina crucibles, as seen in Figure 5-9, to facilitate their handling.

Figure 5-9 Alumina crucibles holding the silver-coated small PZT sample pieces inside the Energon furnace before the paint is cured at 600°C for 1h.

The faces of the cured coated samples were lapped again in a wet environment, using distilled water over a 2400 grit waterproof silicon carbide paper to remove the oxide that might have appeared on the surfaces after curing the silver paste. Additionally, the dry lapping process with the 1000 paper was repeated to clean the circumference of each pellet. Following this, each sample was submerged inside a glass beaker with ethanol and placed inside an ultrasonic bath for ~5min to remove any silver particles that might have remained embedded in the ceramic after being lapped. As described at the beginning of this section, the samples were removed from the beaker and dried in a lint-free paper towel, handling them solely with forceps from this point forward.

Images in part (a) of Figure 5-10 show the resulting pellets after applying and curing the silver paste on both faces of each of the small sample pieces, displaying the silver paste looking a matte silver colour after being cured at 600°C. Images in part (b) of the same figure present the same samples after being lapped, cleaned in the ultrasonic bath, and air dried, where a smooth shiny silver finish can be seen. Figure 5-11 shows the equivalent results for the main disks chosen from nine of the ten sintered compositions. Although the process was done on sample 0.47 HP/LP, no image was taken of the resulting disk. The disks showing some gaps of silver paste had the electrodes reapplied to guarantee they were fully covered.

| (i)   (ii)   (iii)   (iv)   (v)   (vi) | (i)   (ii)   (iii)   (iv)   (v)   (vi) |
| (a) | (b) |
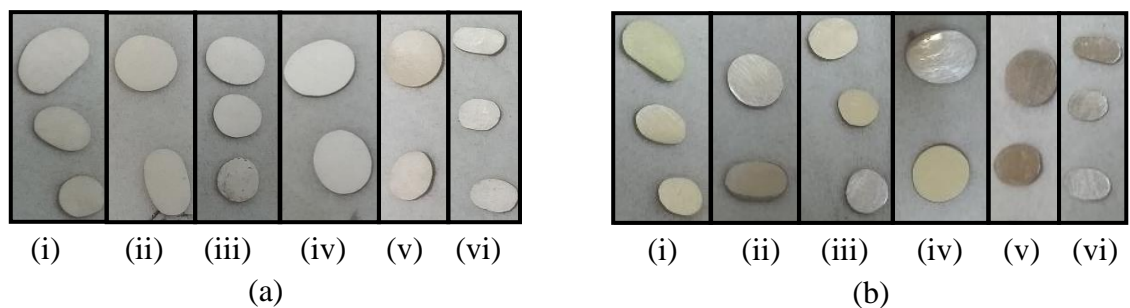
Figure 5-10 Resulting PZT small sample pieces (a) before and (b) after lapping the surface areas. (i) 0.46 LP/LP (6-11), (ii) 0.47 LP/LP (4-11), (iii) 0.48 LP/LP (4-2), (iv) 0.46 HP/HP (5-9), (v) 0.47 HP/HP (5-1), (vi) 0.48 HP/HP (5-4), (vii) 0.46 HP/LP (6-7), (viii) 0.48 HP/LP (4-5) and (ix) 0.46 LP/HP (6-9).

(a)   (b)   (c)   (d)   (e)   (f)   (g)   (h)   (i)
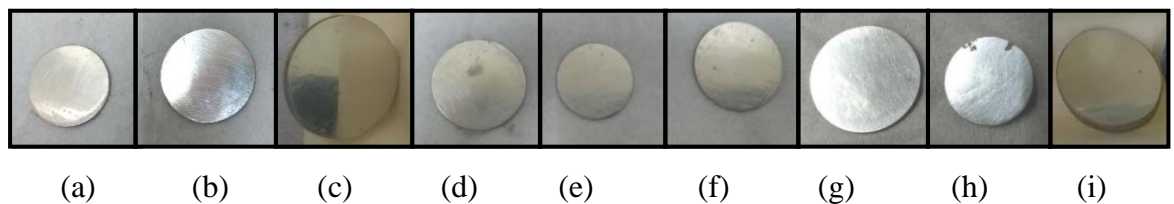
Figure 5-11 Resulting PZT samples after curing the silver paste and being lapped, cleaned, and dried. (a) 0.46 LP/LP (6-4), (b) 0.47 LP/LP (4-8), (c) 0.48 LP/LP (4-4), (d) 0.46 HP/HP (5-8), (e) 0.47 HP/HP (5-3), (f) 0.48 HP/HP (5-5), (g) 0.46 HP/LP (6-8), (h) 0.48 HP/LP (4-6), and (i) 0.46 LP/HP (6-10).

5.3   Hysteresis (P-E) Loops

To determine the best polarization parameters for the chosen samples from each composition, the prepared small silver-coated pieces mentioned in the previous section were placed in a high-voltage setup, detailed below, to study their polarization behaviour with respect to an applied electric field at room temperature, also known as hysteresis or P-E loops. The Material Science Institute in Madrid (CSIC) provided the programs used for the data acquisition and processing involved in this analysis. The hysteresis loops need to be measured before the pellets are polarized in preparation for their functional characterisation and electronic adaptation to observe their true behaviour.

Each pellet was placed on a sample holder before being submerged in a plastic beaker filled about halfway with dielectric fluid (FC40, 3M Fluorinert), as shown in Figure 5-13. To achieve full contact with the disk's surface and the proper conduction of the applied voltage, no air bubbles should be left between the sample and the holding plates. Figure 5-14 depicts the setup that was used for this analysis, where a voltage amplifier (Advanced Energy Trek 10/40A) is connected to a voltage source before being fixed to the submerged sample holder, and a multimeter and picoammeter are used to keep track of the system settings.

Figure 5-12 Front view of the sample holder submerged in dielectric fluid (FC40).

Figure 5-13 Upper view of the sample holder submerged in dielectric fluid (FC40).

Figure 5-14 Hysteresis loop test setup.

The P-E graphs are the result of integrating the current response detected from the material. The picoammeter performs an analysis of the charge and current, deriving the polarization from those. A standard curve will end in two horizontal peaks in the upper right and lower left corners, where the sample starts exhibiting its commutating behaviour. Table 5-3 shows the dimensions of the small sample pieces that were used for the polarization-field (P-E) analysis. The absolute error included for the thickness is half of the instrument precision, while the estimated surface area was roughly calculated from the average width of the small pieces and its error was taken as the mean of the individual errors.

Table 5-3 Thickness and surface area of the chosen lapped PZT small sample pieces.

PZT Composition	Pellet ID	Thickness (mm) (± 0.0005)	Estimated Surface Area (mm^2) (± 0.25)
0.46 LP/LP	6-11	0.584	30.0
0.47 LP/LP	4-11	0.818	41.0
0.48 LP/LP	4-2	0.585	38.2
0.46 HP/HP	5-9	0.770	56.4
0.47 HP/HP	5-1	0.592	31.0
0.48 HP/HP	5-4	0.482	21.0
0.46 HP/LP	6-7	0.576	48.1
0.48 HP/LP	4-5	0.532	37.1
0.46 LP/HP	6-9	0.572	38.5

Starting at 0.5kV/mm, the applied voltage (peak-peak) was increased in steps of 0.5kV with a constant frequency of 0.1Hz. This low frequency allows for a quasistatic measurement of the hysteresis loop, where the dipoles in the material can switch directions. As the frequency increases, the dipoles cannot switch immediately, thus resulting in the coercive field increasing. The remanent polarization remains almost constant at frequencies where a full switch of the entire sample takes place, typically values below the kHz range, but this starts decreasing when surpassing the frequency at which the maximum coercive field is reached, as only a portion of the dipoles will be able to respond to the applied external field (Main, et al., 2015).

For the first measurements (<3kV/mm), the sample was left at each point for about 4min to allow a few cycles to be completed and their initial behaviour evaluated. If there is an offset at the end of the generated curve, where the last point of the cycle does not meet the starting point, this could mean that there is an issue with the instrument or that the sample is conducting or about to break, which is why several cycles are needed to ensure it is safe to proceed.

When doing this, the HP/HP samples (pellets 5-1, 5-4 and 5-9) appeared highly conductive and would commutate too quickly after turning the external electric field to ~1kV/mm. Due to this, the voltage source would be turned off to prevent any potential damage to the specimens. Figure 5-15 shows the resulting hysteresis loops of the HP/HP samples under an applied field of 1kV/mm and 0.1Hz, as well as including the curves from the other compositions under the same parameters for comparison, displaying a clear difference in behaviour between the HP/HP pellets and the rest of the compositions.
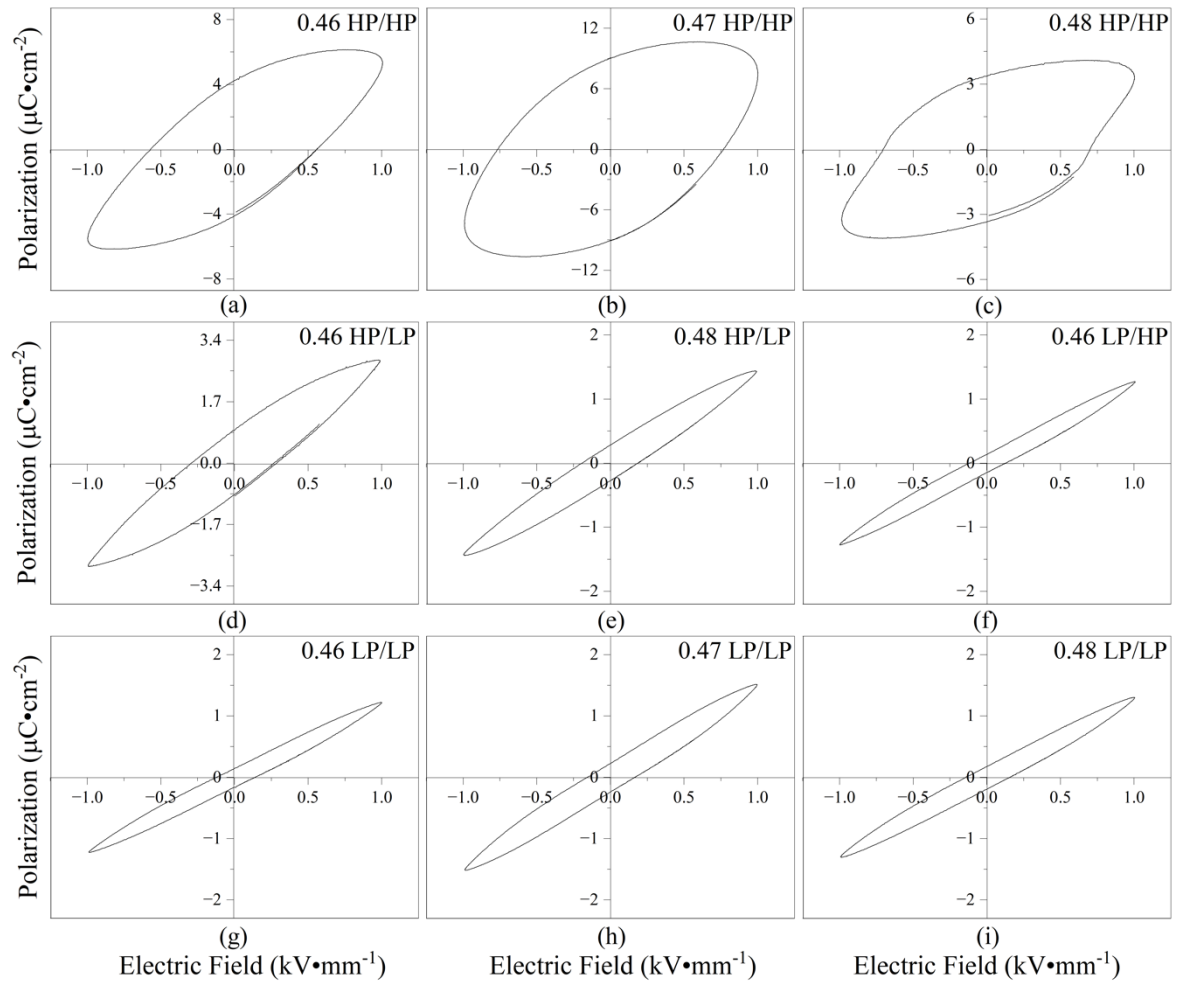
Figure 5-15 Hysteresis loops of the small PZT sample pieces under an applied electric field of 1kV/mm and a frequency of 0.1Hz. (a) 0.46 HP/HP (pellet 5-9), (b) 0.47 HP/HP (pellet 5-1), (c) 0.48 HP/HP (pellet 5-4), (d) 0.46 HP/LP (pellet 6-7), (e) 0.48 HP/LP (pellet 4-5), (f) 0.46 LP/HP (pellet 6-9), (g) 0.46 LP/LP (pellet 6-11), (h) 0.47 LP/LP (pellet 4-11), and (i) 0.48 LP/LP (pellet 4-2).

As indicated before, the HP/HP samples would not be able to withstand higher fields and the loops would become too broad, whilst also displaying a lack of continuity between the start and end points of the curve. Although seen in smaller proportions, the HP/LP specimens also displayed this behaviour. Unlike the HP/HP pellets, the HP/LP compositions were able to withstand ~2kV/mm before becoming too unstable, suggesting that the LP

119

compensation influenced the material's conductivity. Amongst these compositions, pellet 0.47 HP/HP presented the highest commutation and polarization, but all the HP/HP samples showed values at least twice as big as their counterparts in the other purity arrangements.

The LP/LP samples (pellets 4-11, 6-11 and 4-2), as well as the 0.46 LP/HP piece did not show the rapid-changing behaviour of their HP PZT counterparts; instead, they exhibited pronounced pinching near the middle of the loop as the applied voltage increased, resisting commutation. When the domains exhibit a higher resistance to any modification in their direction, the material can be categorised as a hard ceramic. Hard PZT is usually encountered due to oxygen vacancies that get linked to another element, usually the Ti cations present or some of the impurities left from the parent oxides.

Figure 5-16 includes the P-E loops obtained for the LP PZT samples at 3kV/mm and 0.1Hz, showing the double loop formed from the opposition of the material to be polarized. As with the HP PZT, composition 0.47 seems to stand out from its group, this time by exhibiting less pinching and more defined ends in the curve.
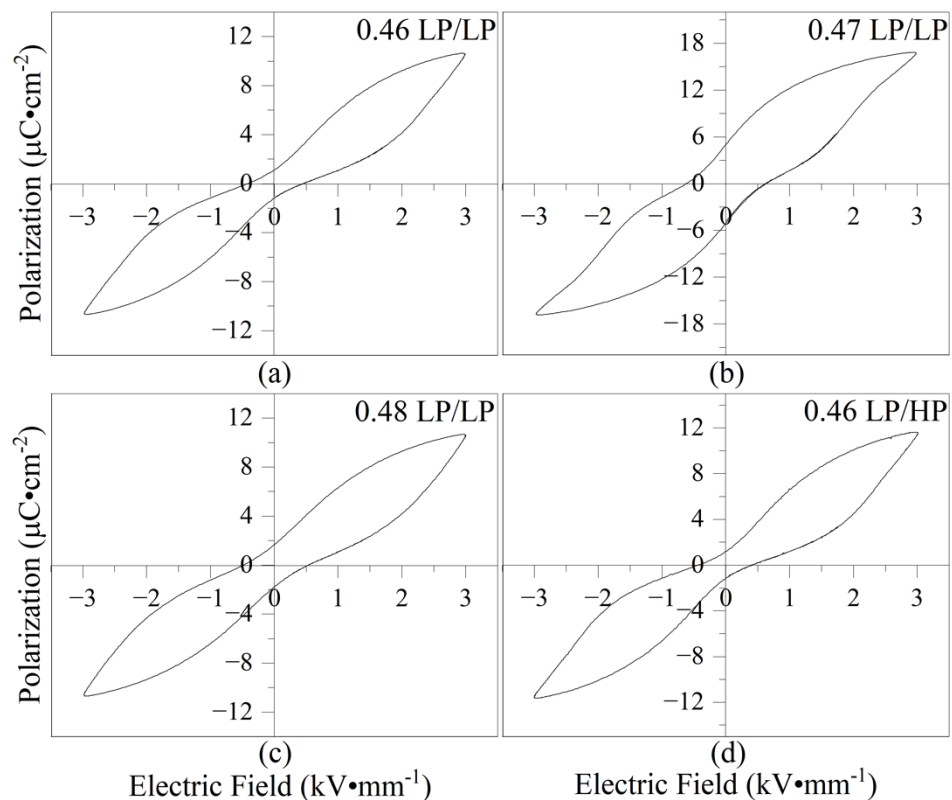
Figure 5-16 Hysteresis loops of the small PZT sample pieces under an applied electric field of 3kV/mm and a frequency of 0.1Hz. (a) 0.46 LP/LP (pellet 6-11), (b) 0.47 LP/LP (pellet 4-11), (c) 0.48 LP/LP (pellet 4-2) and (d) 0.46 LP/HP (pellet 6-9).

If the sample was not conductive, the applied field was increased in steps of 0.5kV until reaching 4kV/mm but changing the exposure time at each point to ~30 minutes after the 3kV/mm mark. This gave the material enough time to react, displaying any changes in the plot. After allowing a few cycles to be completed at 4kV/mm, the pellet was left to be polarized for a further 30min by lowering the frequency to 0.01Hz and maintaining the 4kV/mm throughout the process. When subjected to low frequencies, the current accumulates rapidly in the material, resulting in an easier commutation. Longer exposure times are needed for higher frequencies, as the dipoles resist the change. Since the HP samples became conductive, only the LP pellets were left polarized using these parameters.

To correct the unsuitable behaviours observed on the PZT samples, including both the rapid commutation and pinching, the small pieces were subjected to a heat treatment, known as quenching. This process involves taking the material to a high enough temperature where the domains will relax, usually related to where the original crystallographic phase would occur, after which a rapid cooling is forced on the samples by taking them out of the furnace immediately after completing the treatment and leaving them to cool down on a tabletop until reaching room temperature (Fernández-Posada, et al., 2016).

By cooling the samples rapidly after being exposed to high temperatures, the material does not have time for the dipole moments to organise nor for the domains to form. This allows the domains to appear more naturally, making them easier to change. Nevertheless, the effects of quenching are not permanent, as the dipole moments will continue to adjust with time and begin to align with the domains as previously described. For this study, quenching was performed at 600°C for 1h with a 3°C/min heating ramp, as this is the temperature where the cubic phase occurs, thus guaranteeing that the material would have surpassed its Curie point and lost its original set structure. The quenched PZT samples were cleaned after the process was completed by submerging them in ethanol for a few seconds and drying them on a lint-free paper absorbent towel, similar to the process done after lapping but without requiring the ultrasonic bath.

After quenching, the hysteresis analysis was conducted again on the same small sample pieces as before to evaluate if the treatment had been successful and the behaviour of the PZT specimens had changed. From the measurements, it was noticed that the LP PZT samples no longer exhibited the double loop or pinching that was seen previously, and a more natural commutation was displayed by the compositions in these sets, including both the LP/LP and LP/HP pellets.

Additionally, after being quenched, all the HP specimens stopped being highly conductive and were put through the same fields as the LP samples, reaching the maximum set voltage of 4kV/mm at 0.1Hz. Figure 5-17 shows the P-E loops obtained at 0.1Hz from the PZT compositions after being quenched, with an applied voltage of 3kV/mm for the LP pellets, and 1kV/mm for the HP ones. These parameters were chosen for the presented figure to allow for an equivalent comparison to the ones presented in Figures 5-15 and 5-16.
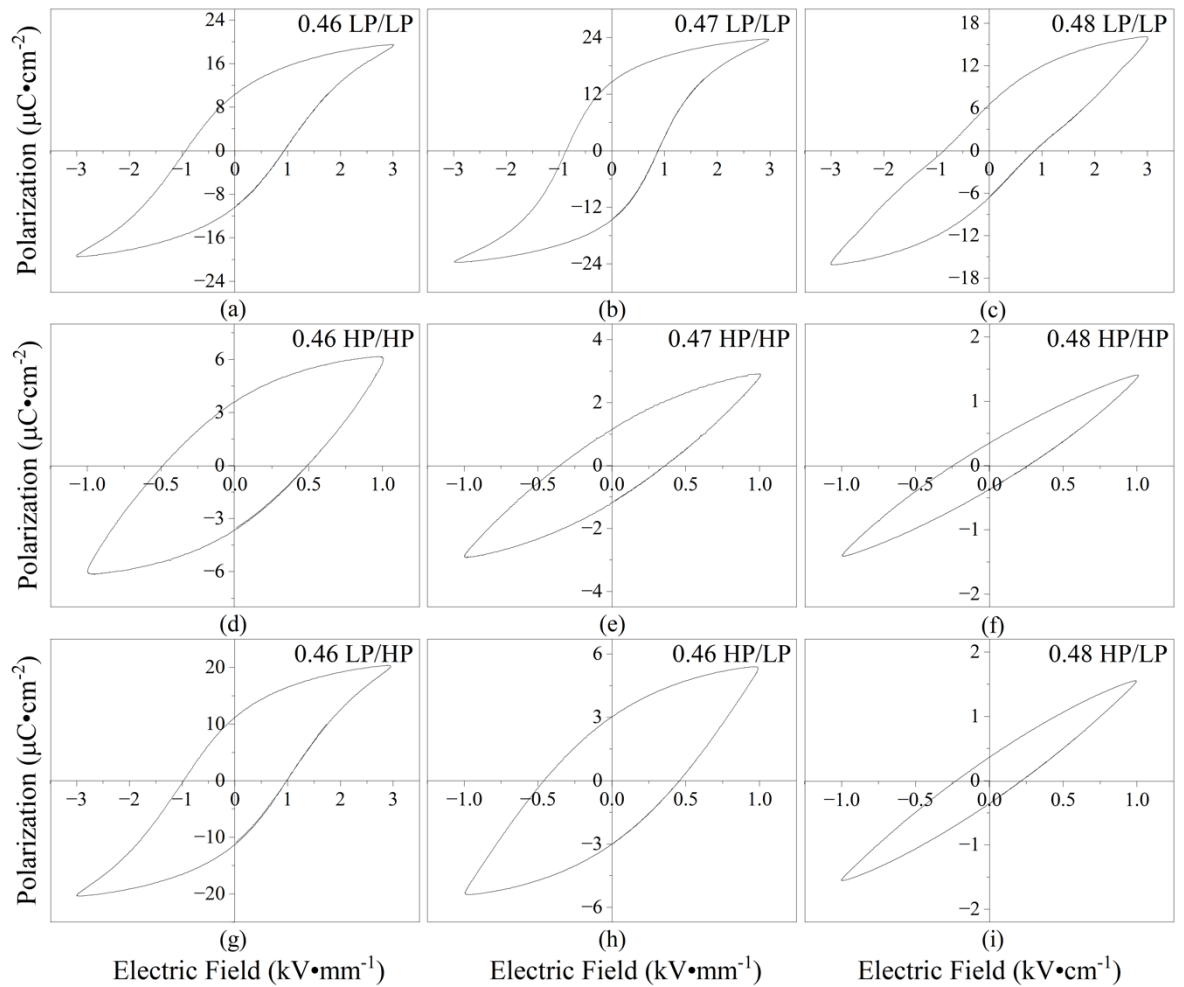
Figure 5-17 Hysteresis loops of the small PZT sample pieces after being quenched under an applied electric field of 1kV/mm (HP PZT) and 3kV/mm (LP PZT), with a frequency of 0.1Hz. (a) 0.46 LP/LP (pellet 6-11), (b) 0.47 LP/LP (pellet 4-11), (c) 0.48 LP/LP (pellet 4-2), (d) 0.46 HP/HP (pellet 5-9), (e) 0.47 HP/HP (pellet 5-1), (f) 0.48 HP/HP (pellet 5-4), (g) 0.46 LP/HP (pellet 6-9), (h) 0.46 HP/LP (pellet 6-7), and (i) 0.48 HP/LP (pellet 4-5).

Compared to their curves prior to quenching, the LP plots now exhibit the expected commutation, although slight pinching is still seen in (c). The same response was obtained from another piece of this composition, thus indicating a link to the material and not the test. Although the HP curves do not show the same level of definition, their behaviour is consistent with the first signs of commutation, with steady loops over multiple cycles.

Since the heat treatment was successful for both PZT purities, correcting the original behaviours observed for the two groups, all the studied sample pieces were left polarized at 4kV/mm with 0.01Hz, following the steps detailed for the LP/LP samples prior to quenching. The final P-E loops obtained under these parameters are included in Figure 5-18, where the LP/LP samples are shown at the top of the figure in plots (a), (b) and (c), the HP/HP presented in images (d), (e) and (f), and the combined purity PZT/PZ pellets shown in (g), (h) and (i). The vertical scale was chosen individually for each plot to maximize the shape of the displayed curve, keeping the horizontal axis identical for all the samples.

To keep track of any specific characteristics or possible correlations with the analyses discussed in the previous sections and chapters, the corresponding IDs of the samples that were used throughout this study are included in the captions of the figures presented.
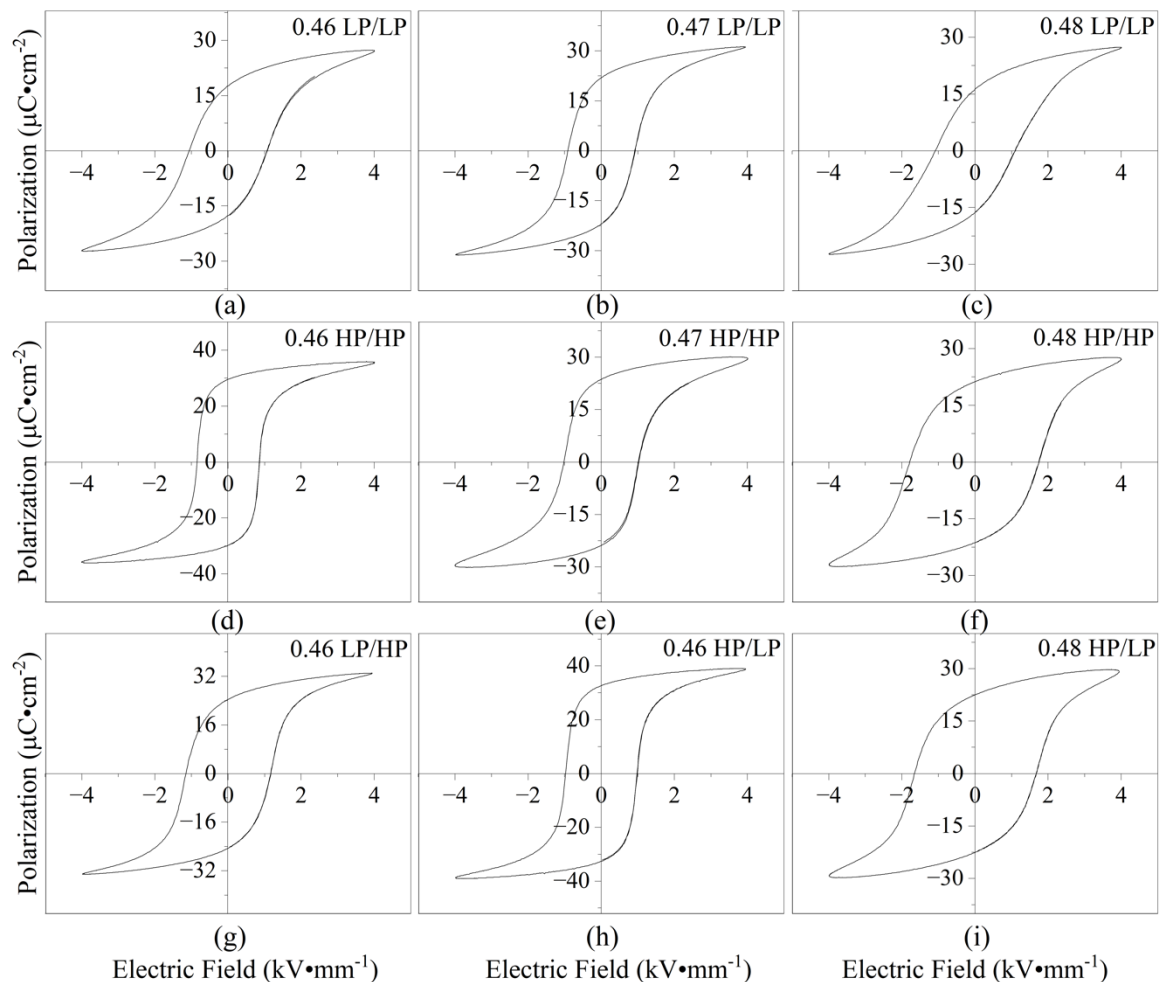
Figure 5-18 Hysteresis loops of the PZT sample pieces after quenching and under an applied electric field of 4kV/mm, with a frequency of 0.01Hz. (a) 0.46 LP/LP (pellet 6-11), (b) 0.47 LP/LP (pellet 4-11), (c) 0.48 LP/LP (pellet 4-2), (d) 0.46 HP/HP (pellet 5-9), (e) 0.47 HP/HP (pellet 5-1), (f) 0.48 HP/HP (pellet 5-4), (g) 0.46 LP/HP (pellet 6-9), (h) 0.46 HP/LP (pellet 6-7), and (i) 0.48 HP/LP (pellet 4-5).

The ferroelectric nature of the ceramics can be seen from the fully developed saturated loops achieved and presented in Figure 5-18, where the relationship between the polarization and applied electric field is reflected in the shifting demonstrated by each studied composition. The polarization-field loops that were obtained from this analysis can be used to identify several important characteristics, including their nature (hard or soft ceramics), composition, and dominant phases, as well as indicating the relative magnitude of some of the associated figures of merit, which are further discussed in section 5.5.

According to (Haertling, 1999), a characteristic that can be determined from the generated loops is the material's electrical resistivity, where higher values are associated with sharper loop tips. Although most of the plots presented in Figure 5-18 display sharp ends, compositions 0.47 LP/LP (b) and 0.46 LP/HP (g) appear to be the sharpest, suggesting the highest resistance is found in these specimens. A more detailed analysis of this is included in section 6.1, as part of the impedance tests conducted on the samples.

Furthermore, the shape of the loop can help determine the degree of homogeneity in the composition and level of uniformity of the grain sizes, where the best values would be assumed for the diagrams depicting a more squared shape (Haertling, 1999). In this case, the plots that seem to show this feature the most are (d) and (h) in Figure 5-18, corresponding to pellets 5-9 and 6-7, with compositions 0.46 HP/HP and 0.46 HP/LP. Comparing these assumptions to the results obtained in the previous chapter, it can be observed that composition 0.46 HP/HP does show the smallest percentage error from the average grain size calculated amongst the HP/HP samples, and composition 0.46 HP/LP has the smallest absolute error associated to the atomic percentages found from the EDS study.

In their research, (Qian, et al., 2013) state that low values of coercive fields, E_c, and a high remanent polarization, P_r, will result in narrower or thinner curves, which is consistent with the patterns shown by these two 0.46 HP PZT compositions. Contrastingly, the plots with the least sharpness were obtained from the two 0.48 HP PZT samples in (f) and (i), which also exhibit the highest values of the coercive field, E_c, resulting in broader curves.

Regarding the phase formation, low remanent polarization and high coercive fields tend to be attributed to a more tetragonal structure (Qian, et al., 2013), which agrees with the XRD patterns displaying the highest levels of tetragonality in the HP disks with a composition of 0.48. On the other hand, the largest P_r with a small value of E_c, seems to belong to the 0.46 HP/LP pellet, which supports the statements made in section 4.3.

An additional relationship can be established between the curve shape and the proximity of the spontaneous polarization (P_s) and the remanent polarization (P_r). Once the internal domains are no longer experiencing any reorientation, a linear behaviour will be seen between P and E. Since P_s can be identified as the value where the extrapolated linear response intercepts the vertical axis, and P_r is the value of the polarization when E = 0, a smaller difference between these values would not only indicate fewer domains need reorienting but would also result in smaller slopes at the top and bottom of the loop.

Although some observations can be made from the presented diagrams in the previous figure, the resolution and similarity in the results make it difficult to fully assess the individual characteristics displayed by each studied sample piece. Therefore, the specific values for the remanent polarization (P_r) as well as the positive and negative coercive fields (E_c+ and E_c-) have been measured and are presented in Table 5-4. This table also includes ΔE_c, which was calculated as the absolute value of the difference between E_c+ and E_c-. The measured values of P_r, E_c+ and E_c- at each test point chosen between 0.5 and 4 kV/mm for all the sample pieces are included in Appendix G.

Table 5-4 Remanent polarization, P_r, and positive and negative coercive fields, E_c+ and E_c-, of the small PZT sample pieces after reaching saturation and poling the sample by applying 4kV/mm at 0.01 Hz, after being quenched at 600°C.

PZT Composition	Pellet ID	P_r ($\mu C/cm^2$)	E_c+ (kV/mm)	E_c- (kV/mm)	ΔE_c (kV/mm)
0.46 LP/LP	6-11	17.60	1.09	-1.09	0.000
0.47 LP/LP	4-11	22.01	0.95	-0.86	0.089
0.48 LP/LP	4-2	16.35	1.08	-1.03	0.051
0.46 HP/HP	5-9	29.66	0.88	-0.84	0.032
0.47 HP/HP	5-1	23.77	0.98	-0.95	0.025
0.48 HP/HP	5-4	21.25	1.92	-1.93	0.012
0.46 HP/LP	6-7	32.59	0.99	-0.99	0.008
0.48 HP/LP	4-5	22.58	1.70	-1.69	0.018
0.46 LP/HP	6-9	24.48	1.23	-1.21	0.026

Amongst their findings, Haertling indicated that a higher remanent polarization appeared to be linked to higher polarizability, strain, and electromechanical coupling (Haertling, 1999). Since the HP PZT samples exhibited larger coercive fields than the ones shown by their LP counterparts, this would suggest a better performance and associated piezoelectric properties would be expected from the higher-purity ceramics. Nevertheless, amongst the LP/LP samples, composition 0.47 has the highest P_r, while in the HP/HP and HP/LP groups, the pieces with a concentration of 0.46 show the highest value.

Finally, the symmetry of the hysteresis loops has also been found to be associated with the homogeneity and number of defects present in the studied materials, where a higher symmetry in the resulting curve would be indicative of fewer defects and a more consistent composition throughout the ceramic. Therefore, based on the data presented for ΔE_c in Table 5-4, the sample with fewer defects appears to be the one with a composition of 0.46 LP/LP, followed by 0.46 HP/LP. Despite this initial assumption, when comparing the rest of the values presented in Appendix G, sample 0.46 HP/LP consistently shows a higher symmetry between the positive and negative coercive fields measured, which would agree with the results obtained from the EDS and the shape of the loop.

A higher discrepancy in the measured values would be expected from the LP PZT as the parent oxides used with this grade of purity already start with a higher percentage of impurities or contaminants. Although the LP PZT sample pieces appear to show the biggest difference between the measured coercive fields, the highest percentage error comes from sample 0.47 LP/LP with a 10% uncertainty, which is consistent with exhibiting the highest percentage error amongst the average grain sizes calculated for the LP/LP specimens and presenting the largest absolute error in the composition analysis. Despite this, when studying the response of pellet 0.47 LP/LP in the other voltage test points, an average percentage error of 4% is found, which shows a primarily symmetrical behaviour in its polarization curve and thus, a good sintering of the composition with a relatively sparse number of defects.

Nevertheless, this observation would be seemingly contrasting, as the measured P_r appears to indicate that the best piezoelectric response would come from sample 0.47 LP/LP, even if it has the highest number of defects or variation in its homogeneity. When analysing the HP/HP group, a similar behaviour is observed, where pellet 0.46 HP/HP not only has the highest P_r but also the biggest ΔE_c. A higher number of defects would cause an increase in the electrical conductivity of the samples and consequently, higher dielectric losses, presumably resulting in lower efficiencies and piezoelectric coefficients when coupled as energy harvesters.

After reaching saturation after being exposed to 4kV/mm at 0.01Hz for approximately 30min, the voltage source would be disconnected from the sample holder when the voltage was close to zero in the observed P-E loops, allowing the small sample specimens to be safely taken out before measuring their piezoelectric charge coefficient d_{33} using a Berlincourt meter at 100Hz (Channel Products, Inc., USA, Figure 5-19).

The frequency for these measurements was chosen based on the equipment resolution (20 - 320Hz) and considering that the material response is kept almost constant at low frequencies. Moreover, 100Hz tends to be a standard when measuring d_{33}, staying far away from the resonance peak of the sample (Stewart, et al., 2001). The d_{33} was taken before quenching when this was made available by the sample's behaviour. The comparison of the measured d_{33} before and after quenching is presented in Table 5-5.

Figure 5-19 Berlincourt meter used to measure the piezoelectric charge coefficient (d_{33}) at 100Hz.

Table 5-5 Piezoelectric charge constant d_{33}, of the small PZT sample pieces after being poled through their hysteresis analysis at 4kV/mm and 0.01Hz for 30min before and after being quenched.

PZT Composition	Pellet ID	d_{33} before quenching (pC/N) (± 0.5)	d_{33} after quenching (pC/N) (± 0.5)
0.46 LP/LP	6-11	55	110
0.47 LP/LP	4-11	120	146
0.48 LP/LP	4-2	75	118
0.46 HP/HP	5-9	NA	206
0.47 HP/HP	5-1	NA	200
0.48 HP/HP	5-4	NA	180
0.46 HP/LP	6-7	NA	220
0.48 HP/LP	4-5	NA	175
0.46 LP/HP	6-9	152	147

When focusing on the obtained measurements after quenching, the HP PZT samples in Table 5-5 show the highest values of d_{33} amongst the studied groups, even when using LP PZ as PbO compensation. From the LP/LP specimens, composition 0.47 shows the best result before and after quenching, which agrees with this sample having the largest P_r in the group. The same is also true for compositions 0.46 HP/HP and 0.46 HP/LP after quenching, where the largest P_r matches with the sample presenting the highest d_{33}. This stems from the observation that the highest remanent polarization is exhibited when nearest to the material's MPB, where the best piezoelectric properties are expected, as the increase in the polarization efficiency facilitates the rearrangement of domains (Kim & Lee, 2021).

The d_{33} values for the HP/LP samples before being quenched were not included as these also showed a behaviour similar to that of the HP/HP disks and were stopped before reaching 2kV/mm. Nevertheless, a clear increment can be seen amongst most pellets after being quenched, except for the 0.46 LP/HP sample, which was left polarized at 6kV/mm before being quenched instead of 4kV/mm, after exhibiting a similar hard PZT behaviour as the LP/LP samples, thus a higher d_{33} would be consistent with the higher applied field.

5.4   Poling of the resulting piezoelectric ceramic disks

As previously mentioned, the values obtained from the hysteresis loops were used to set the polarization parameters required to enable the piezoelectric properties of the studied specimens. For the small sample pieces, this process was performed in the opposite direction to the one done during the P-E analysis to reverse the commutation in the sample and ease the shift of the domains in the material. Poling was done along the thickness axis.

Prior to their poling, the ten main PZT disks were put through a similar heat treatment as the small pieces, but this was done with a heating ramp of 2°C/min and left at 600°C for two hours, before cooling them down to room temperature with a ramp of 1°C/min. This process, known as annealing, frees any tensions and relaxes the domains in the material by eliminating any stress that might have been induced by the lapping process. The experiment setup and components involved in the poling can be seen in Figure 5-20.

| (a) | (b) |
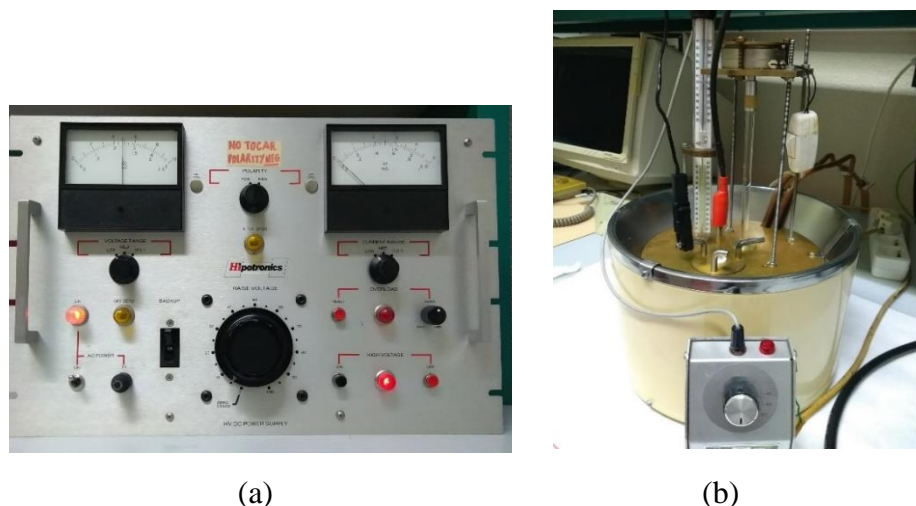
Figure 5-20 Experiment setup for poling the PZT samples, showing (a) the DC power supply, (b) the sample holder filled with silicon oil with the motorised mixer and heating system on top,

The chosen electric field was applied to the pellet by connecting the DC power supply in Figure 5-20 (a) to the sample holder shown in Figure 5-20 (b), whilst the specimen

was submerged in silicon oil to isolate the current. Once submerged, the sample holder is connected, the desired temperature is selected, and a motor is used to mix the oil to guarantee a homogeneous temperature is reached inside the container.

Similar to the hysteresis loop analysis, an initial test is performed at a low voltage (1kV/mm) to see if the sample is short-circuited or conductive, which would cause the current gauge to oscillate and the voltage to remain unchanged even when turning the dial.

If the sample is not conductive after the initial test, the voltage source is turned off and the oil heater is turned on, to increase the temperature to the desired value. Once reached, the voltage source is turned back on and the chosen field is applied to the sample for ~15min, after which the heater is turned off.

Whilst still applying the same field, the cooling process is sped up by turning on a cold water system that uses a motor to extract water from a separate container placed under the table and circulates it through a hose that runs through the main container, as depicted in Figure 5-21. When reaching <40°C, the field is removed, the cooling and mixing are stopped, the cables are disconnected, and the sample is removed.

Figure 5-21 Cooling mechanism employed during the poling of the PZT samples.

Before leaving the small samples polarized at 4kV/mm, the process was completed at 2 and 3kV/mm, reversing the sample's direction every time. Although higher temperatures help reduce the required field exposure, a higher value would take longer to be reached, thus a suitable value must be chosen, whilst also remaining under the Curie point of the material.

In this case, the tests were completed using a temperature of ~130°C, which halved the polarization time without going near the estimated *Tc* value (~400°C), obtained from Figure 2-5 presented in section 2.5.1 as part of the literature review chapter.

To verify the efficiency of the poling at the various test points chosen, the piezoelectric charge constant d_{33} was measured for the available small sample pieces using a Berlincourt meter at 100Hz, as done previously after reaching saturation during the hysteresis loop analysis. Unfortunately, due to time constraints, this was only performed on the LP/LP and HP/HP PZT pieces. The measured d_{33} values are presented in Table 5-6.

Table 5-6 d_{33} of the LP/LP and HP/HP PZT pieces, poled with 2, 3 and 4 kV/mm at 130°C for 15min.

PZT Composition	Pellet ID	d_{33} at 2kV/mm (pC/N) (± 0.5)	d_{33} at 3kV/mm (pC/N) (± 0.5)	d_{33} at 4kV/mm (pC/N) (± 0.5)
0.46 LP/LP	6-11	185	192	200
0.47 LP/LP	4-11	191	220	220
0.48 LP/LP	4-2	201	287	290
0.46 HP/HP	5-9	285	293	305
0.47 HP/HP	5-1	300	350	370
0.48 HP/HP	5-4	252	300	317

Compared to Table 5-5, although a direct relationship can be established between the applied field and the piezoelectric charge constant, composition 0.48 LP/LP now presents the highest d_{33} in the low purity group, while composition 0.47 takes the lead amongst the HP/HP group. Nonetheless, Table 5-6 still supports that the higher purity PZT samples exhibit better values than the LP specimens. Furthermore, these results indicate that these two compositions might be the closest to the MPB amongst their respective groups, which would be consistent with the assumptions made after the XRD analysis in section 4.3.

Before polarizing the big PZT disks, it was noticed that when the cooling mechanism was on, the voltage would appear to drop and the current would increase, suggesting that the sample was becoming conductive whilst the field was still being applied. Although there was no clear explanation for this, it was observed that the system would normalize once the cooling motor was turned off, and that the effect was not seen at lower temperatures, thus a value of ~100°C was set for the poling of the main pellets.

The d_{33} coefficients measured after 15min under applied fields of 4 and 5kV/mm are presented in Table 5-7. The higher field was chosen to present an additional set of values to compare to the 4kV/mm results.

Table 5-7 d_{33} of the big PZT disks poled with 4kV/mm and 5kV/mm at ~100°C for 15min.

PZT Composition	Pellet ID	d_{33} at 4kV/mm (pC/N) (± 0.5)	d_{33} at 5kV/mm (pC/N) (± 0.5)
0.46 LP/LP	6-4	215	220
0.47 LP/LP	4-8	226	235
0.48 LP/LP	4-4	275	294
0.46 HP/HP	5-8	305	335
0.47 HP/HP	5-3	370	375
0.48 HP/HP	5-5	295	312
0.46 HP/LP	6-8	265	280
0.47 HP/LP	4-7	320	335
0.48 HP/LP	4-6	286	318
0.46 LP/HP	6-10	205	218

As seen with the small sample pieces, the behaviour of the big PZT disks is consistent with that shown through the hysteresis analysis, where the HP PZT presents the highest piezoelectric charge coefficients, and a proportional relationship is observed between the applied field and the measured d_{33}. Amongst these samples, when polarized at 4kV/mm, compositions 0.48 LP/LP and 0.47 HP/HP still surpassed the other compositions in their arrangement groups by more than 20%, which is similar to the values found in Table 5-6.

It was also observed that although the d_{33} values showed a slight increase when measured at 5kV/mm, the difference remained within a range of 5 to 32pC/N. The potential benefits of registering slightly higher piezoelectric coefficients would need to be compared against the costs and risks involved in applying higher electric fields to evaluate its suitability for the intended purposes as energy harvesters. Additionally, the measured values seem to be quite close to those seen in the small sample pieces, indicating a good level of homogeneity and consistency throughout the final samples that were obtained from each set, where more than one disk was sintered.

Furthermore, amongst the samples with the opposite PZ compensation, composition 0.47 showed the largest piezoelectric charge constant in the HP/LP group, whilst the 0.46 LP/HP specimen displayed the lowest d_{33} from the ten studied sets, closely followed by sample 0.46 LP/LP. When analysing these results, no immediate pattern could be identified as each arrangement group seems to follow different tendencies. For example, the LP/LP group appears to show a direct relationship between the amount of Ti and the measured d_{33}, while the HP/HP group shows an increment in d_{33} from the 0.46 Ti concentration to the 0.47 one but then decreases when reaching the 0.48 value.

A comparison between the results presented in this dissertation and those found in the literature is carried out and presented in the following sections of this chapter.

This could potentially indicate that for the LP/LP group, the MPB is found somewhere after composition 0.48, whilst the HP PZT arrangements suggest it would be located close to the 0.47 Ti concentrations. This would be consistent with the findings obtained from the XRD and SEM analysis, considering that the grain sizes calculated for the sample with composition 0.46 LP/LP cannot be directly compared with the other two LP/LP compositions due to the variations in their sintering, which is further discussed in Chapter 7.

5.5   Figures of merit associated with the sintered PZT samples

Through the help of the research staff in the Material Science Institute in Madrid (CSIC), particularly Dr Miguel Alguero, the real and imaginary components of the main figures of merit of the PZT samples were determined through an iterative method proposed by (Alemany, et al., 1994). Thes tests were carried out on the poled PZT disks and employed complex impedance spectrometry techniques coupled with data acquisition equipment.

The piezoelectric characterisation of the samples was carried out in radial mode after achieving resonance by applying a sinusoidal electric stimulation with 1V RMS through a HE-4192A impedance analyser, which was controlled by an interface board (GPIB-PCIIA, National Instruments). The data acquisition equipment can be seen in Figure 5-22.

Figure 5-22 Data acquisition system used to calculate the figures of merit of the poled PZT disks.

Figure 5-23 depicts the characteristics and dimensional arrangement used when testing a sample in the shape of a circular disk, under radial excitation mode. The figure shows labels x_1, x_2 and x_3 as the directions of the axes used, the voltage source being applied to the sample along its thickness, and polarization P parallel to the x_3 axis.
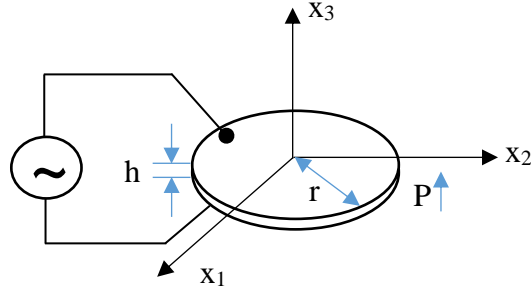
Figure 5-23 Radial resonance mode of a circular disk excited along its thickness (ANSI/IEEE, 1987).

Using a 20-point-minimum frequency range, the fundamental resonance and antiresonance frequencies of each sample, f_r, and f_a, as well as the first overtone (f_{s1}), were calculated. The resonance and antiresonance frequencies correspond to where the maximum resistance and conductance were observed. and vary depending on the dimensions of the sample (Lee, et al., 2012). Through these sweeps, the absolute electrical admittance $|Y|$ and its phase angle were also measured and stored to generate the associated electrical parameters like conductance G, susceptance B, resistance R and reactance X.

In radial excitation mode, the electrical admittance of a ceramic disk polarized along its thickness is given by equation (5-1), combininng the dielectric, piezoelectric and elastic contributions of the system (Alguero, et al., 2004). The real components include the frequency f, the thickness h, the radius r, and the density ρ, while the permittivity under constant stress parallel to poling ε^T_{33}, Poisson's planar ratio σ^p, the elastic stiffness c^p_{11}, the piezoelectric charge constant d_{31}, and Onoe's function $\mathfrak{I}_1$, are considered complex.

$$Y = G + \mathrm{i}B = i\left(\frac{2\pi^2 f r^2}{h}\right)\left(\varepsilon^T_{33} + 2d^2_{31}\left(\frac{c^p_{11}}{\frac{1}{2-\mathfrak{I}_1[z]} - \frac{1}{1+\sigma^p}}\right)\right) \tag{5-1}$$

Poisson's planar ratio, the elastic stiffness and Onoe's function were derived from Equations (5-2), (5-3) and (5-4), respectively, before being used in Equation (5-1).

$$\sigma^p = -\left(\frac{s^E_{12}}{s^E_{11}}\right) \tag{5-2}$$

$$c^p_{11} = \frac{s^E_{11}}{(s^E_{11})^2 - (s^E_{12})^2} \tag{5-3}$$

$$\mathfrak{I}_1(z) = \frac{zJ_0(z)}{J_1(z)} \tag{5-4}$$

133

Where s^E_{11} and s^E_{12} are the elastic compliances for strain applied perpendicular (x_1) to the poling and stress applied in direction 1 or 2 (x_1 or x_2), under a constant electric field, and J_i is the Bessel function of the first kind and i-th order of the argument $z = 2\pi fr(\rho/c^p_{11})^{1/2}$.

The complex piezoelectric coefficients d_{31}, ε^T_{33}, σ^p and c^p_{11}, are determined by solving the set of nonlinear equations that result when the electrical admittance values are measured at four different frequencies, chosen near the fundamental resonance, through an iterative method that includes the associated losses of the calculated constants (Alemany, et al., 1995). Two of these frequencies are set as the values obtained for the resonance and antiresonance frequencies, while the other two additional frequencies, f_1 and f_2, are determined from the experimental values of the maximum and minimum susceptance B near the resonance frequency, as shown in Equation (5-5) (Alemany, et al., 1994).

$$f_{1,2} = f_r \pm \Delta f_r \tag{5-5}$$

Table 5-8 shows the four frequencies, f_r, f_a, f_1 and f_2, used to calculate the main figures of merit and other related piezoelectric coefficients, along with the first overtone (f_{s1}) obtained from the admittance data gathered from each of the ten PZT compositions. The resonance frequency is of particular interest since it is where the optimal vibration occurs in the ceramic, leading to the best energy conversion efficiency. The uncertainties of the parameters in this section were taken as half of the instrument's resolution when collected directly and as the result of the rules of propagation when derived from other values.

Table 5-8 The four main experimental frequencies calculated for the poled PZT pellets.

PZT Composition	Pellet ID	$f_r \pm 0.05$ (kHz)	$f_a \pm 0.05$ (kHz)	$f_1 \pm 0.005$ (kHz)	$f_2 \pm 0.005$ (kHz)	$f_{s1} \pm 0.05$ (kHz)
0.46 LP/LP	6-4	158.5	178.2	128.73	227.85	415.7
0.47 LP/LP	4-8	137.9	157.1	111.13	203.25	363.0
0.48 LP/LP	4-4	160.1	185.1	127.87	243.48	419.4
0.46 HP/HP	5-8	121.9	135.5	99.75	171.25	319.0
0.47 HP/HP	5-3	139.9	155.5	114.49	196.52	366.3
0.48 HP/HP	5-5	120.4	129.1	101.44	156.59	313.0
0.46 LP/HP	6-10	154.3	174.6	124.85	224.48	406.9
0.46 HP/LP	6-8	123.6	138.7	100.49	177.10	324.5
0.47 HP/LP	4-7	121.4	141.0	96.71	186.37	318.3
0.48 HP/LP	4-6	161.9	178.1	133.36	223.17	418.0

A specific range can be established when comparing the resonance frequencies measured from all the samples (120 and 162kHz). Although some patterns can be seen amongst the compositions, it would not be possible to draw any relationships directly from these values as they are linked to the dimensions of each sample, and these vary slightly from composition to composition as detailed in Table 5-1.

Since the pellets were under radial excitation, the resonance frequencies were found to be linked to the diameter of the disks through an inverse relationship. Disk 5-5, from composition 0.48 HP/HP, presents the largest diameter (17.75mm) and lowest f_r (120.4kHz), while disk 4-6, from composition 0.48 HP/LP, has the smallest diameter (13.11mm) and highest value for its resonance frequency (161.9kHz). This behaviour is seen in the ten samples but is particularly followed within each group based on their PZT/PZ purity. Table 5-9 includes the diameters and resonance frequencies found for each of the processed PZT disks, presenting them next to each other for further discussion and analysis.

Table 5-9 Diameter and resonance frequency of the poled PZT samples.

PZT Composition	Pellet ID	Diameter (mm)	Resonance frequency f_r (kHz)
0.46 LP/LP	6-4	14.80	158.5
0.47 LP/LP	4-8	16.70	137.9
0.48 LP/LP	4-4	13.65	160.1
0.46 HP/HP	5-8	17.60	121.9
0.47 HP/HP	5-3	14.95	139.9
0.48 HP/HP	5-5	17.75	120.4
0.46 HP/LP	6-8	17.30	123.6
0.47 HP/LP	4-7	17.40	121.4
0.48 HP/LP	4-6	13.11	161.9
0.46 LP/HP	6-10	14.80	154.3

From Table 5-9, it can be seen that for disks with similar diameters, like compositions 0.46 LP/LP and LP/HP, the resonance frequency seems to decrease when the arrangement includes the opposite purity oxides for the PbO compensation. This could suggest that either the opposite purity arrangement is responsible for the variation or perhaps it is related to the HP oxides included in the sample's sintering. Comparing the other two arrangements for concentration 0.46, the disk with the opposite purity (HP/LP) presents a higher frequency with a slightly smaller diameter than that of 0.46 HP/HP, which appears to be in line with the previous statement, thus not providing further evidence to support either theory.

When comparing the values of the 0.47 LP/LP and HP/HP disks, a decrement of 1.75mm seems to be related to an increment of only 2kHz, which seems to be disproportionate when observing the resulting frequencies of other samples with similar diameters, like 0.46 LP/LP and LP/HP. In those cases, a difference of 1.9mm caused an increment of ~18.5 ± 2.1kHz, thus suggesting that the HP PZT samples appear to consistently have lower resonant frequencies. Theoretically, this could represent an advantage over the LP PZT as it would be easier to achieve resonance, although the difference between the measured values is not big enough to provide a significant advantage.

From the iterative method described at the beginning of this section, a main and a derived characterisation were obtained for each PZT sample tested. Table 5-10 presents the values obtained from the main characterisation that are not discussed individually as one of the five figures of merit associated with piezoelectric materials. This includes Poisson's planar ratio (σ^p), the elastic stiffness ($c^p_{11})^E$ and elastic compliances, s^E_{11} and s^E_{12}, under a constant electric field, and the permittivity under constant stress in direction x_3 (ε^T_{33}).

Table 5-10 Main piezoelectric characterisation of the poled PZT samples.

PZT Composition	Pellet ID	σ^p ± 0.005	$(c^p_{11})^E$ ± 0.005 (GN/m^2)	s^E_{11} ± 0.005 ($\times10^{-12}$m^2/N)	s^E_{12} ± 0.005 ($\times10^{-12}$m^2/N)	ε^T_{33} ± 0.05 ($\times$8.85 pF/m)
0.46 LP/LP	6-4	0.31	94.95	11.66	-3.63	466.4 – i5.1
0.47 LP/LP	4-8	0.30	90.28	12.14	-3.59	462.4 – i4.0
0.48 LP/LP	4-4	0.32	80.25	13.84	-4.36	817.3 – i4.5
0.46 HP/HP	5-8	0.32	67.32	16.54	-5.28	478.0 – i4.9
0.47 HP/HP	5-3	0.32	68.65	16.18	-5.11	665.6 – i6.3
0.48 HP/HP	5-5	0.35	65.14	17.43	-6.02	936.1 – i6.8
0.46 LP/HP	6-10	0.29	86.19	12.67	-3.68	494.9 – i6.5
0.46 HP/LP	6-8	0.31	73.29	15.06	-4.62	496.3 – i6.1
0.47 HP/LP	4-7	0.31	62.94	17.60	-5.49	803.9 – i3.7
0.48 HP/LP	4-6	0.37	62.90	18.43	-6.83	1045.0 – i5.8

Except for ε^T_{33}, the rest of the parameters are presented solely as the real part of the measured value, since although the imaginary part was also obtained through the proposed method, its contribution is too small to have any significant impact. The complete set of complex values that were obtained from this analysis has been included in Appendix H as a set of screen captures taken from the results shown by the processing software after performing the radial resonance analysis on the ten PZT disks.

Although not the main focus of this work, Poisson's planar ratio (σ^p) appears consistent throughout the samples, displaying a similar proportion between the lateral contraction strain and the longitudinal extension strain experienced by the disk under a strain applied perpendicular to the direction used during poling (direction x_1). On the other hand, the highest elastic stiffness at constant electric field ((c^p_{11})^E) was measured from the LP PZT samples, including the 0.46 disk with opposite purity, whilst the lowest resistance to deformation seems to be mainly generated by the HP/LP samples, with the exception of concentration 0.46, which surpasses the results of the HP/HP pellets. This characteristic further supports the idea that the LP PZT disks behave like a hard ceramic.

Additionally, the elastic compliance values, s^E_{11} and s^E_{12}, used to calculate these two characteristics through Equations 5-2 and 5-3, are also included in Table 5-10. These values were measured under a constant electric field, meaning that the electrodes on the sample were shorted together, with the first subscript indicating the direction of the strain and the second the direction of the stress. The compliance with stress in direction 1 shows a certain proportional relationship with the TiO_2 concentration, as the values of s^E_{11} increase as the concentration increases in each arrangement group, except for the HP/HP samples, where composition 0.47 has a slightly lower value than composition 0.46.

Opposite to the elastic stiffness, the compositions with the highest strain produced by the PZT per unit stress are the HP PZT, with a similar behaviour as before, where the HP/LP specimens have the highest s^E_{11}, with the exception of composition 0.46, which lies below the HP/HP values. Furthermore, this behaviour is consistent with the s^E_{12} measurements but lacks the proportional relationship between the TiO_2 concentration and the compliance in the LP/LP group.

Finally, the permittivity obtained under constant stress, where the PZT disk is mechanically unconstrained and with both the displacement and electric field in the same direction the ceramic was poled in, showed an interesting pattern amongst the samples with the same concentration, where the LP/LP group showed the lowest values, followed by the HP/HP group and finally, by the HP/LP sets with the highest measurements. The HP/LP and LP/HP samples with a concentration of 0.46 displayed very proximal values. Moreover, concerning the samples' titanate percentage within each group, except for the LP/LP disks, the ε^T_{33} shows a direct relationship with the TiO_2 concentration.

Additionally, composition 0.46 displayed higher values when using opposite purity PZ compared to the disks made with the same purity for the PZT and PZ disks. Particularly, sample 0.46 LP/LP had the lowest of the four specimens, whilst composition LP/HP had the highest at this concentration. This is also seen in the other two higher concentrations, with even bigger differences between the calculated values, giving composition 0.48 HP/LP the largest permittivity. Nevertheless, since these groups do not have any disks with the LP/HP arrangement, it is impossible to determine if this behaviour would have been repeated.

Similar to Table 5-10, Table 5-11 presents the real values of the parameters obtained through the derived characterisation of the studied PZT disks. These parameters include the shear compliance at a constant electric field in the same direction as poling (s^E_{66}), and the elastic stiffness ((c^p_{11})^D) and compliances (s^D_{11} and s^D_{12}) in the same directions as before but under constant displacement. Where $s^E_{66} = 2(s^E_{11} - s^E_{12})$.

Table 5-11 Derived piezoelectric characterisation of the poled PZT samples.

PZT Composition	Pellet ID	$s^E_{66} \pm 0.005$ ($\times10^{-12}$m^2/N)	(c^p_{11})$^D \pm 0.005$ (GN/m^2)	$s^D_{11} \pm 0.005$ ($\times10^{-12}$m^2/N)	$s^D_{12} \pm 0.005$ ($\times10^{-12}$m^2/N)
0.46 LP/LP	6-4	30.57	117.55	10.59	-4.70
0.47 LP/LP	4-8	31.47	114.36	10.89	-4.84
0.48 LP/LP	4-4	36.40	105.34	12.31	-5.89
0.46 HP/HP	5-8	43.64	81.60	15.17	-6.65
0.47 HP/HP	5-3	42.58	83.16	14.83	-6.46
0.48 HP/HP	5-5	46.91	73.93	16.48	-6.97
0.46 LP/HP	6-10	32.70	100.77	11.42	-4.93
0.46 HP/LP	6-8	39.38	90.39	13.69	-6.00
0.47 HP/LP	4-7	46.19	83.41	15.59	-7.50
0.48 HP/LP	4-6	50.53	75.37	17.13	-8.14

As before, the compliances s_{ij} show the same behaviour amongst the arrangement groups, with the highest values belonging to the 0.47 and 0.48 HP/LP sets, followed by the HP/HP disks and the 0.46 HP/LP sample. The three compliances included exhibit the same tendencies, with the highest values belonging to the same concentration within each group, as well as showing a direct relationship with the TiO_2 concentration, with the exception of the HP/HP group, where the 0.47 disk has slightly lower values than composition 0.46. The opposite is seen for (c^p_{11})^D, where the highest values are shown by the LP PZT sets, and the parameters have an inverse relationship with the amount of TiO_2. As before, sample 0.47 HP/HP surpasses the value obtained for the 0.46 HP/HP disk.

The five main FOM associated with the PZT samples obtained through the main and derived characterisations carried out through the iterative method proposed by (Alemany, et al., 1994), are detailed in the following subsections. These include the piezoelectric charge constants d_{33} and d_{31}, the electromechanical coupling factors k_p and k_{31}, the piezoelectric charge constant g_{33}, the mechanical quality factor Q_m, and the acoustic impedance Z_c.

.

5.5.1 Piezoelectric strain/charge constant d_{ij}

Two piezoelectric charge coefficients were found for the chosen PZT samples, these include the longitudinal piezoelectric coefficient, also known as d_{33}, and the transverse piezoelectric constant, d_{31}, which was calculated through the main characterisation done after achieving radial resonance in the PZT disks poled along their thickness. Although the values for d_{33} have already been briefly discussed during the poling analysis (Table 5-7), Table 5-12 presents both coefficients for their comparison and further discussion. The two charge constants measure the polarization response from the PZT samples along their thickness (x_3) per unit stress applied in the same direction for d_{33}, and radially towards the centre of the sample for d_{31}, thus explaining the negative sign in the transverse coefficients.

Table 5-12 Piezoelectric charge constants d_{33} and d_{31} measured from the poled PZT disks.

PZT Composition	Pellet ID	$d_{33} \pm 0.5$ (pC/N)	$d_{31} \pm 0.005$ (pC/N)
0.46 LP/LP	6-4	215	-66.46
0.47 LP/LP	4-8	226	-71.44
0.48 LP/LP	4-4	275	-105.08
0.46 HP/HP	5-8	305	-76.14
0.47 HP/HP	5-3	370	-89.06
0.48 HP/HP	5-5	295	-88.89
0.46 LP/HP	6-10	205	-74.10
0.46 HP/LP	6-8	265	-77.68
0.47 HP/LP	4-7	320	-119.5
0.48 HP/LP	4-6	286	-109.72

Unlike the longitudinal values, where the highest d_{33} was measured from the HP PZT samples, the highest d_{31} was obtained from the 0.47 and 0.48 HP/LP disks, followed by the 0.48 LP/LP sample. Contrastingly, the lowest value corresponds to one of the lowest values for the d_{33} presented in Table 5-7, belonging to the 0.46 LP/LP sample. This would indicate that that particular composition appears to perform poorly when excited, whether it is along their thickness or radius, and would not represent any direct link with the longitudinal result.

Similar to the observations made from Table 5-7, Table 5-12 shows no initial distinctive pattern throughout the sets but certain tendencies can be identified when looking at the individual arrangement groups or when focusing on the amount of TiO_2 used. The highest d_{31} in each group corresponds to the sample also showing the highest d_{33} within that specific arrangement, where the HP/HP and HP/LP have composition 0.47 taking the lead. On the other hand, samples in the LP/LP group show a link with the amount of titanate, presenting sample 0.48 as the one with the highest piezoelectric charge coefficients. This would further support the estimations made in the previous sections about the possible location of the MPB within each arrangement group based on their composition.

Compared to the reference values included in Table 2-4, it can be seen that the best-performing samples (0.47 HP/HP and 0.47 HP/LP) display values nearing those registered from materials like PZT-4 and PZT-5A, which are both widely used in sensing and actuating applications. In general, the pellets appear to show results closer to PZT-4, even when comparing the density ρ and elastic compliance s^E_{11} included in Table 2-4 to the values previously included in Table 4-6 and Table 5-10, respectively. PZT-4 is considered one of the most common "hard" piezoelectric ceramics employed in ultrasonic transducer applications (DeAngelis & Schulze, 2016), thus the proximity of these results to the commercial standards would confirm the quality and effectiveness of the preparation and processing techniques used with the various compositions of undoped PZT chosen for this study.

5.5.2 Piezoelectric voltage constant g_{ij}

The piezoelectric voltage constant g_{31} was measured as part of the derived piezoelectric characterisation. Similar to the piezoelectric charge constant d_{31}, the g_{31} coefficient refers to the response of the material to a strain or stress in direction 1, perpendicular to poling, but now related to the electric field or displacement in direction 3.

Although not measured directly, the voltage coefficient parallel to the poling direction, g_{33}, was found using the relationship included in equation (2-3), where $g_{33} = d_{33}/\varepsilon^T_{33}$. It should be noted that the permittivities included in Table 5-10 are not only expressed as complex numbers but also as a function of the permittivity of free space or vacuum, ε_0. Therefore, to calculate g_{33}, the values included for the permittivity of the material at constant stress were multiplied by ε_0 (8.854 pF/m), after calculating the modulus of the complex number.

The data acquired for both piezoelectric voltage coefficients is presented in Table 5-13, akin to the results included in Table 5-12. As previously mentioned, the negative sign seen in the g_{31} values indicates the direction of the stress or strain pointing towards the centre of each disk as part of the radial resonance that was sought during the iterative method used.

Table 5-13 Piezoelectric voltage constants g_{33} and g_{31} measured from the poled PZT disks.

PZT Composition	Pellet ID	g_{33} ($\times 10^{-3}$ Vm/N)	$g_{31} \pm 0.005$ ($\times 10^{-3}$ Vm/N)
0.46 LP/LP	6-4	52.09 ± 0.12	-16.09
0.47 LP/LP	4-8	55.22 ± 0.12	-17.44
0.48 LP/LP	4-4	38.02 ± 0.07	-14.52
0.46 HP/HP	5-8	72.10 ± 0.12	-17.99
0.47 HP/HP	5-3	62.81 ± 0.09	-15.11
0.48 HP/HP	5-5	35.61 ± 0.06	-10.72
0.46 LP/HP	6-10	46.80 ± 0.11	-16.91
0.46 HP/LP	6-8	60.33 ± 0.11	-17.67
0.47 HP/LP	4-7	44.98 ± 0.07	-16.79
0.48 HP/LP	4-6	30.91 ± 0.05	-11.85

Just like with the piezoelectric charge coefficients, Table 5-13 shows that the highest voltage coefficient belongs to the same pellet within each arrangement group, but these differ from the compositions that had shown the best values of d_{33} and d_{31}. In this case, the 0.46 compositions seem to exhibit the highest coefficients from the HP PZT groups, while composition 0.47 has the highest values amongst the LP/LP samples. Additionally, the HP PZT samples show an inverse relationship between the amount of TiO_2 and the voltage coefficients. From the ten sets, compositions 0.48 appear to have the lowest values of both constants, with the HP samples showing even lower values than the LP disk of the same composition. The overall highest value was obtained from the 0.46 HP/HP disk, thus exhibiting the largest gap between the results of each arrangement group (~36.5×10^{-3} Vm/N), which was 24% higher than the gap in the HP/LP group and more than twice the difference in the LP/LP one.

Unlike the d_{33}, the g_{33} values surpass those presented in Table 2-4, where PZT-4 registered a maximum of 26.1×10^{-3} Vm/N amongst the PZT-based compositions included in the table. The voltage coefficients measured for the PZT samples in this project showed values between 1.2 and 2.8 times higher than those of the PZT-4 composition reported by (Haertling, 1999), and compares closer to other lead-based piezoelectric ceramics like PMN-PT, at 30.6×10^{-3} Vm/N, or $PbNb_2O_6$, at 43.1×10^{-3} Vm/N. Other research, (Harikrishnan, et

al., 2018), shows values for PZT up to 44×10^{-3} Vm/N and for PLZT at 63×10^{-3} Vm/N, but both presenting lower values for d_{33} (181 and 14.9pC/N, respectively).

Since the piezoelectric voltage and charge constants are related to each other, a high voltage coefficient for a given charge coefficient would only be possible if the permittivities of the material were kept low. As mentioned in section 2.14.2, having large g_{ij} in a ceramic usually indicates that a material will present some difficulty or opposition to being polarized, which is a behaviour associated with hard ceramics. This would provide a contrasting argument to the observations made from some of the previous sections, as the highest values seem to be displayed by the HP samples, which had been identified as exhibiting behaviours closer to those associated with soft piezoceramics rather than hard PZT. Nevertheless, these results would support the response seen in the hysteresis curves included in Figure 5-18, where the samples with the highest g_{ij} had the squarest and narrowest loops.

5.5.3 Electromechanical coupling factor k_{ij}

As part of the main figures of merit associated with piezoelectric ceramics, the electromechanical coupling factor k_{ij} was obtained. This value indicates the conversion efficiency from mechanical to electrical energy or vice versa, thus being closely linked to the expected performance of the pellets when coupled as energy harvesters. Although the k_{ij} can refer to the direct or converse piezoelectric effect, for this study, the values are taken as the efficiency that would be expected when converting kinetic energy into electrical. As part of the analysis carried out, the values of k_p and k_{31} were measured to quantify the efficiency of the material in various directions of excitation and can be found in Table 5-14 below.

Table 5-14 Electromechanical coupling factors k_p and k_{31} measured from the poled PZT disks.

PZT Composition	Pellet ID	$k_p \pm 0.005$ (%)	$k_{31} \pm 0.005$ (%)
0.46 LP/LP	6-4	51.61	30.29
0.47 LP/LP	4-8	54.01	32.04
0.48 LP/LP	4-4	56.76	33.21
0.46 HP/HP	5-8	49.33	28.78
0.47 HP/HP	5-3	49.32	28.85
0.48 HP/HP	5-5	40.88	23.39
0.46 LP/HP	6-10	52.80	31.45
0.46 HP/LP	6-8	51.29	30.19
0.47 HP/LP	4-7	57.57	33.77
0.48 HP/LP	4-6	47.37	26.57

Table 5-14 shows that the obtained planar efficiencies k_p for the prepared PZT compositions agree with the expected high electromechanical coupling that has been observed in piezoelectric ceramics, like PZT, by exhibiting values >40%, indicating an efficient conversion of energy. Despite the values of k_{31} being lower than those of k_p, the highest percentages from each arrangement group seem to come from the same sample, with the exception of the HP/HP group, where disks 0.46 and 0.47 have almost identical values. A similar observation can be made when focusing on the amount of titanium in the samples, as specimens 0.46 LP/LP and 0.46 HP/LP registered nearly the same efficiencies.

Even though k_{31} was obtained from the iterative process, it is usually of interest only when analysing the longitudinal vibrations in a material, typically in specimens that are shaped as rods, thus the main focus in this section is the planar coupling factor k_p, which refers to the energy conversion efficiency in a thin disk with radial resonance.

When observing the results presented in Table 5-14, although the best performance appears to be from the 0.47 HP/LP disk, the LP/LP samples exhibited consistently high values on both measured coupling factors, whilst also showing a direct relationship with the percentage of TiO_2 in the sample, which was not seen amongst the other arrangement groups. Additionally, the worst energy conversion was obtained from the 0.48 HP/HP disk, displaying values of ~17.7% below the best value, and ~8.5% below the other two compositions within the same arrangement group. The lower performance of this sample would be consistent with this particular disk showing to lowest density ($6.25 g/cm^3$), amongst the tested samples, as well as the least square loop in the P-E curves shown in Figure 5-18.

As previously suggested, these results indicate that the best compositions for energy harvesting seem to be the LP samples, further supporting the potential that had been identified from the higher densities that were obtained from these specimens, and that would provide better resistance to the expected impact associated to probable power applications. In general, the highest efficiencies amongst these samples are comparable to the values shown in Table 2-4 for commercially available PZT-4 (58%), which would align with the observations made from the d_{33} results being closest to this typical ferroelectric ceramic.

Finally, sample 0.47 HP/LP provided an interesting behaviour, where the combination of an HP PZT with an LP PZ atmosphere not only resulted in one of the highest values of d_{33} but also showed the best efficiency of all the prepared samples, whilst

additionally involving an economical advantage over the HP/HP disks due to the lower costs of the LP parent oxides, which is further discussed in Chapter 6.

5.5.4 Mechanical quality factor Q_m

The mechanical quality factor Q_m, is an important parameter used to investigate the performance of piezoelectric materials. This FOM mainly reflects the energy consumption required to overcome the internal mechanical frictions that occur when reaching resonance in the material. In practical applications, accurately characterising the mechanical quality factor in piezoelectrics is critical when selecting the right materials for high-power ultrasonic devices, as a higher Q_m would anticipate a better performance (Chen, et al., 2023). In general, the quality factor represents the absolute value of the ratio between the real and the imaginary parts of any measured parameter.

For this study, although it is possible to obtain the quality factor for the other characteristics, only the mechanical quality factor Q_m is of interest, as this value represents the quality of the mechanical parameters measured from each sample. The complete set of quality factors obtained through the iterative method performed on the samples can also be found in the data presented in Appendix H. Table 5-15 presents the Q_m ($\pm$ 0.005) calculated from the elastic parameters found from the functional characterisation of the PZT disks. The quality factors included show the corresponding parameters they were calculated from in brackets in the top row of the table.

Table 5-15 Mechanical quality factors obtained from the mechanical parameters measured from the poled PZT disks, along with a colour coding based on their magnitude (Red=Lowest, Green=Highest).

PZT Composition	Pellet ID	Q_m $((c^p_{11})^E)$	Q_m (s^E_{11})	Q_m (s^E_{12})	Q_m (s^E_{66})	Q_m $((c^p_{11})^D)$	Q_m (s^D_{11})	Q_m (s^D_{12})
0.46 LP/LP	6-4	275.65	274.39	268.67	273.01	371.28	304.04	221.94
0.47 LP/LP	4-8	317.42	335.28	474.13	359.31	495.84	401.89	290.11
0.48 LP/LP	4-4	348.72	335.64	286.90	322.50	535.53	375.15	249.36
0.46 HP/HP	5-8	201.75	203.15	209.56	204.66	334.62	241.24	152.07
0.47 HP/HP	5-3	181.26	163.50	113.36	147.81	210.73	167.49	116.39
0.48 HP/HP	5-5	196.39	187.61	161.04	179.98	348.48	223.84	123.03
0.46 LP/HP	6-10	237.46	235.60	225.95	233.36	337.94	266.01	181.73
0.46 HP/LP	6-8	210.72	212.22	219.75	213.95	282.88	236.46	175.75
0.47 HP/LP	4-7	174.48	174.03	171.93	173.52	505.38	225.42	117.34
0.48 HP/LP	4-6	185.77	155.72	103.29	136.92	350.84	174.89	93.96

MIN ◄───────► MAX

The collected data shows that the mechanical quality factors oscillated between 94 and 536, with a mean value of 246 and a standard deviation of ~97. The highest Q_m was calculated from the LP/LP samples, followed by the 0.46 LP/HP disk. In particular, composition 0.47 LP/LP showed the best mechanical quality coefficients, although the 0.46 and 0.48 specimens in that group showed a better consistency throughout the studied parameters. On the other hand, the HP PZT appeared to exhibit the lowest quality factors, where composition 0.47 HP/HP and 0.48 HP/LP displayed the worst results from all the sets.

After performing a colour coding on the data based on the magnitude of the quality factors, it was observed that the majority of the samples had similar values throughout the three mechanical parameters measured during their main characterisation, as well as when compared to the Q_m found for the s^E_{66}. This was primarily identified in the samples with a composition of 0.46 from the four available arrangement groups.

Through this analysis, it was also identified that the highest Q_m was found from the elastic stiffness $(c^p_{11})^D$, while the lowest values appeared to be from the elastic compliance s^D_{12}, both under constant displacement. Since Q is found through the ratio of the real and imaginary parts of each parameter, it would be expected that the highest values would be found from the complex measurements that are practically real numbers, since the imaginary part is significantly smaller than the real part of the value. In addition to the Q_m included in Table 5-15, the quality factors of the piezoelectric coefficients, d_{31} and g_{31}, as well as the dielectric permittivity under constant stress, ε^T_{33}, were calculated as part of the iterative process and are listed in Table 5-16.

Table 5-16 Quality factors associated with the piezoelectric coefficients d_{31}, g_{31}, and dielectric permittivity ε^T_{33} measured from the poled PZT disks.

PZT Composition	Pellet ID	Q ± 0.005 (d_{31})	Q ± 0.005 (g_{31})	Q ± 0.005 (ε^T_{33})
0.46 LP/LP	6-4	110.36	526.41	91.23
0.47 LP/LP	4-8	124.87	1418.19	114.76
0.48 LP/LP	4-4	181.95	675.03	182.45
0.46 HP/HP	5-8	83.81	625.52	96.78
0.47 HP/HP	5-3	116.09	1119.32	105.18
0.48 HP/HP	5-5	72.78	153.74	138.23
0.46 LP/HP	6-10	92.04	454.84	76.55
0.46 HP/LP	6-8	92.01	745.44	81.90
0.47 HP/LP	4-7	97.51	176.30	218.20
0.48 HP/LP	4-6	94.35	196.45	181.53

As before, the quality of these characteristics appears to be highest in the LP/LP samples, particularly in composition 0.47, although a few anomalies can be seen throughout the data, mainly when comparing the values obtained for the piezoelectric voltage coefficient g_{31}. Since a decrement in Q is expected when the porosity of the material is higher, as this is related to the domain shifts experienced during polarization (Li, 2022), high-quality factors would be associated with materials that resist any reorientation of the internal domains, such as the LP samples studied in this work. Typically, high Q values lead to lower d_{33} and k_p, which supports the previous findings.

From this analysis, yet another characteristic seems to support the LP samples being the best candidates for their coupling as energy harvesters or as components in electrical systems for power applications. Furthermore, similar to the observations made from the previous FOM, it appears that composition 0.47 HP/LP exhibits better values than those shown by its HP/HP counterpart, meaning that the use of the LP PZ might be associated with the enhancement of some of the piezoelectric properties whilst reducing the fabrication costs. A similar behaviour can be seen in sample 0.46 HP/LP, although this is less prominent.

5.5.5 Acoustic Impedance Z_c

The final FOM that was calculated for the PZT compositions was the acoustic impedance Z_c. Knowing the material's acoustic properties would allow the best coupling to be achieved, particularly with low-impedance mechanical energy sources. As stated in section 2.14.5, Z_c can be obtained by multiplying the material's density ρ and the transverse sound speed c_1, where $c_1 = 2d*f_a$. The calculated values are included in Table 5-18, along with ρ (g/cm^3), the estimated c_1 (m/s), and their corresponding absolute errors.

Table 5-17 Acoustic impedance Z_c calculated for the poled PZT disks.

PZT Composition	Pellet ID	$\rho \pm 0.03$ (g/cm^3)	$c_1 \pm 0.001$ (m/s)	$Z_c \pm 0.19$ (MRayls)
0.46 LP/LP	6-4	7.39	5274.72	38.98
0.47 LP/LP	4-8	7.22	5247.14	37.88
0.48 LP/LP	4-4	7.23	5053.23	36.53
0.46 HP/HP	5-8	6.30	4769.60	30.05
0.47 HP/HP	5-3	6.74	4649.45	31.34
0.48 HP/HP	5-5	6.25	4583.05	28.64
0.46 LP/HP	6-10	6.99	5168.16	36.13
0.46 HP/LP	6-8	6.85	4799.02	32.87
0.47 HP/LP	4-7	6.04	4906.80	29.64
0.48 HP/LP	4-6	6.19	4669.78	28.91

The sound speed values calculated for the prepared PZT samples in this work were found to be close to those presented in the literature for similar materials (~4800 m/s), indicating good reliability from the calculations (Bui, et al., 1988).

The resulting impedances appear to be quite large (>28 MRayls), as well as being relatively similar amongst the samples in each arrangement group, whilst all remaining quite proximal to the standard of ~30MRayls found in the literature (Wang, et al., 2018). As with other FOM, the LP PZT samples displayed the highest values of the analysed specimens, while the lowest was obtained from the HP sets, particularly from the 0.48 compositions. Contrastingly, composition 0.46 resulted in the largest impedances in the LP/LP and HP/LP groups, which would be consistent with the densities displayed by the samples, as a more compact composition would signify a higher resistance to any type of conduction through the material. Additionally, since the sound of speed in the material is related to the diameter of the sample, smaller diameters with similar antiresonance frequencies would result in slower speeds and subsequently reduce the acoustic impedance associated with the PZT disk.

Although these magnitudes of Z_c have been found to provide the best sensitivity should the studied specimens be used as piezoelectric transducers coupled with imaging electronics; unfortunately, when considering applications involving the human body, the acoustic impedance found from PZT would cause high ultrasound energy losses at the interface and consequently poor sensitivity due to the value significantly surpassing the acoustic impedance of the human body (~1.5 MRayls (Chan & Perlas, 2011)). Therefore, in this case, having the highest values would not necessarily be a positive characteristic, and the right applications would be required to make the most of the material.

5.6   Relative permittivity ε_r and dielectric loss factor $tan\ \delta$

Due to limited time and access to the necessary equipment, only the small sample pieces of the six main compositions, where the same degree of purity was used for the PZT and PZ compensation disks, were left in the Material Science Institute of Madrid (CSIC) after being poled at 4kV/mm. The tests to measure their relative dielectric permittivities (ε_r) and related losses (tan δ) were carried out thanks to the help of Dr Harvey Amorin, who provided the acquired data for their subsequent processing and analysis. The dielectric properties were measured as a function of the temperature using an HP4284A precision LCR Meter (Agilent, Palo Alto, CA) and a range of frequencies between 100Hz and 1MHz. The resulting graphs were obtained after measuring the heating and cooling behaviour exhibited

by the samples when taken from room temperature (~22°C) up to ~550°C and cooled back down using ramps of 2°C/min.

Although the ε_r was measured through the heating and cooling of the samples, Figure 5-24 shows only the data obtained through the cooling stage, as this is where the pellets display a behaviour closer to that of an unpolarized material, allowing for a more accurate comparison. The plots included in this figure also show the estimated Curie point T_C, which is discussed in greater detail in the subsequent analysis of the results.
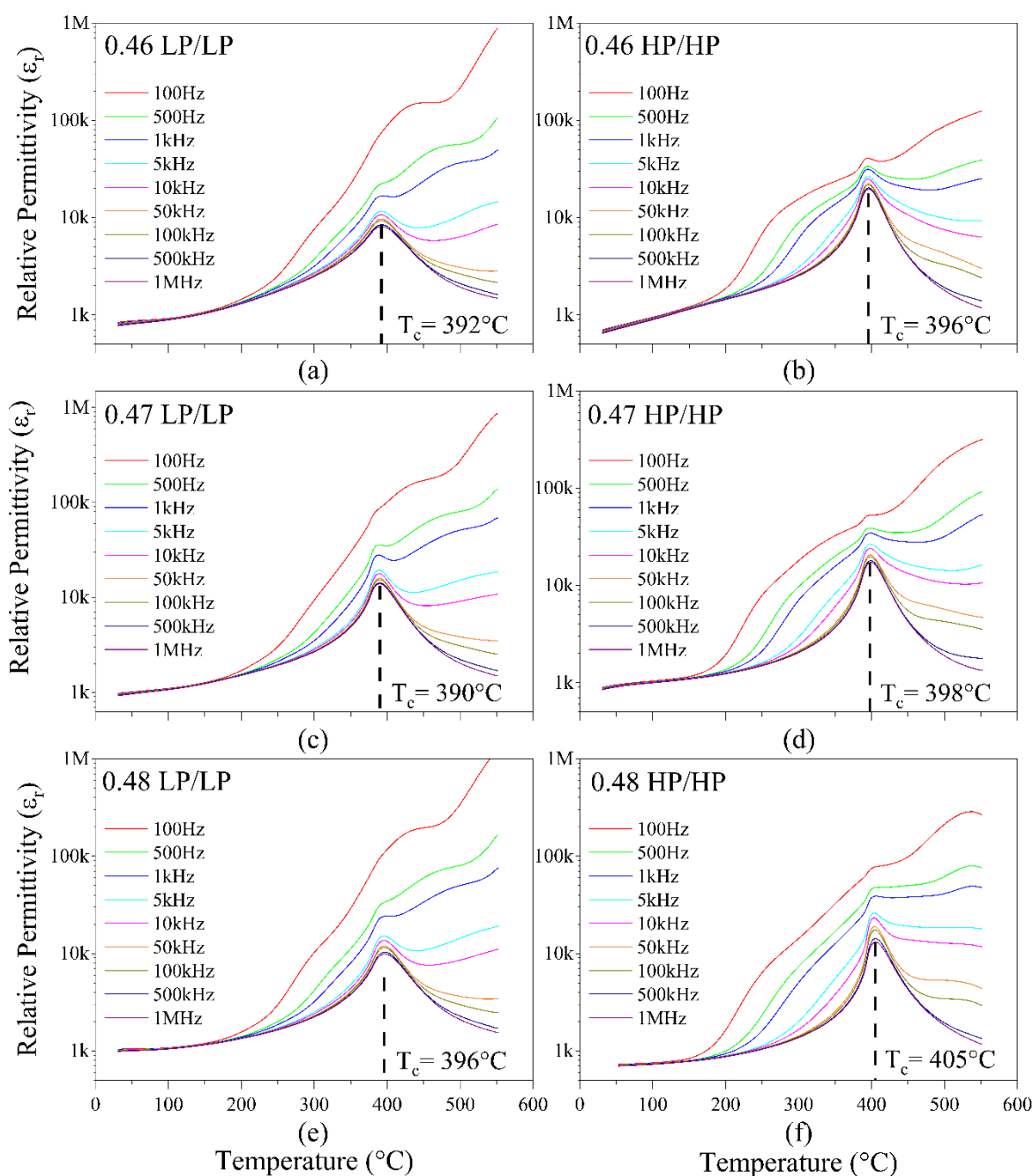
Figure 5-24 Relative permittivity of the PZT samples with respect to temperature using a range of frequencies between 100Hz and 1MHz during cooling. (a) 0.46 LP/LP, (b) 0.46 HP/HP, (c) 0.47 LP/LP, (d) 0.47 HP/HP, (e) 0.48 LP/LP and (f) 0.48 HP/HP.

The plots seen in Figure 5-24 show that the HP/HP PZT pellets had the highest ε_r throughout the majority of the frequencies tested for this analysis when comparing the values at T_C, with the exception of the data collected at 100Hz, where the LP/LP disks registered the largest relative permittivities and widest peak dispersion from the specimens.

Additionally, when focusing on the values at T_R, it can be seen that each of the LP/LP compositions surpassed the values registered by their HP/HP counterparts. This would mean that the LP/LP samples would outperform the HP/HP disks at the lower temperatures that would be usually expected from the implementation of these devices as energy harvesters, as well as showing higher relative permittivities at the lowest tested frequency, which is much closer to the anticipated frequencies associated to daily human activities and any kinetic energy that could be harvested from the environment.

Higher dielectric constants are usually indicative of better grain distribution, with finer grains and higher consistency throughout their sizes, which has been consequently associated with denser materials and low porosity. This supports the results and observations made in Chapter 4 as part of the density and microstructure analysis, where the HP/HP PZT samples exhibited lower densities, bigger grains, and higher porosity than the LP/LP pellets.

Nevertheless, the width of the ε_r peaks has been reported to be linked to the number of defects and chemical homogeneity in a material (Coondoo, et al., 2015). In this case, thinner peaks would be associated with samples with fewer impurities, making HP parent oxides favour higher relative permittivities at T_C. This can be seen in Figure 5-24, as the HP/HP samples exhibited higher dielectric constants at the phase transition point in the graphs.

In addition to this, (Qian, et al., 2013) reported that piezoelectric ceramics with a higher rhombohedral structure generate broader peaks where the T_C appears to change as a function of the frequency, while a more tetragonally-rich material would exhibit narrower and sharper peaks, with the Curie point remaining constant regardless of the frequency.

As with some of the previous characteristics, the materials closer to the MPB would present a combination of both behaviours in their dielectric response, as well as the enhanced properties that have previously been mentioned as being associated with the MPB proximity.

Amongst the LP/LP plots, composition 0.47 displayed the sharpest dielectric response from the group, as well as the highest ε_r at T_C, indicating that this composition would be the most proximal to the MPB.

Composition 0.46 appears to be the most dispersed from this group, which would be consistent with the previous findings that identify this composition as being mostly rhombohedral. Although not as dispersed, composition 0.48 shows lower values of ε_r than the 0.47 sample at T_C but the highest when measured at T_R, also suggesting proximity to the MPB.

From the HP/HP plots, the dielectric response at T_C appears to decrease as the concentration of Ti increases and the frequencies surpass the resonance values found in section 5.5, while the opposite occurs at the lower frequencies, with ε_r increasing proportionally to the sample's Ti concentration.

At T_R, the dielectric permittivity of the HP/HP samples seems to increase from composition 0.46 to 0.47 and decrease to its lowest in composition 0.48. This can be attributed to the densification of the sample and estimated grain size, as a larger grain/particle size would be associated to a higher number of defects or gaps, negatively impacting the ability to displace the electric charge across the sample.

Furthermore, from the HP/HP dielectric curves, it appears that a higher presence of the tetragonal structure might be related to an increment in the estimated Curie Point of the studied samples. This would be consistent with the information in the phase diagram included in Figure 2-5, where the transition from the ferroelectric tetragonal/rhombohedral phases to the paraelectric cubic phase for PZT occurs at higher temperatures when the concentration of TiO_2 increases, indicating that T_C is proportional to the Ti% in the sample.

Figure 5-25 shows the particular case where the permittivity was measured throughout the heating and cooling of the PZT pellets with a set frequency of 1MHz, to provide a clearer comparison of the measurements obtained from the six main compositions.

The observations made from Figure 5-24, can be confirmed through the plots included in Figure 5-25, as the dielectric behaviour of the samples at 1MHz has been isolated, allowing for a clearer appreciation of the generated peaks and their character, as well as exemplifying the response seen during the heating stages of the dielectric tests.
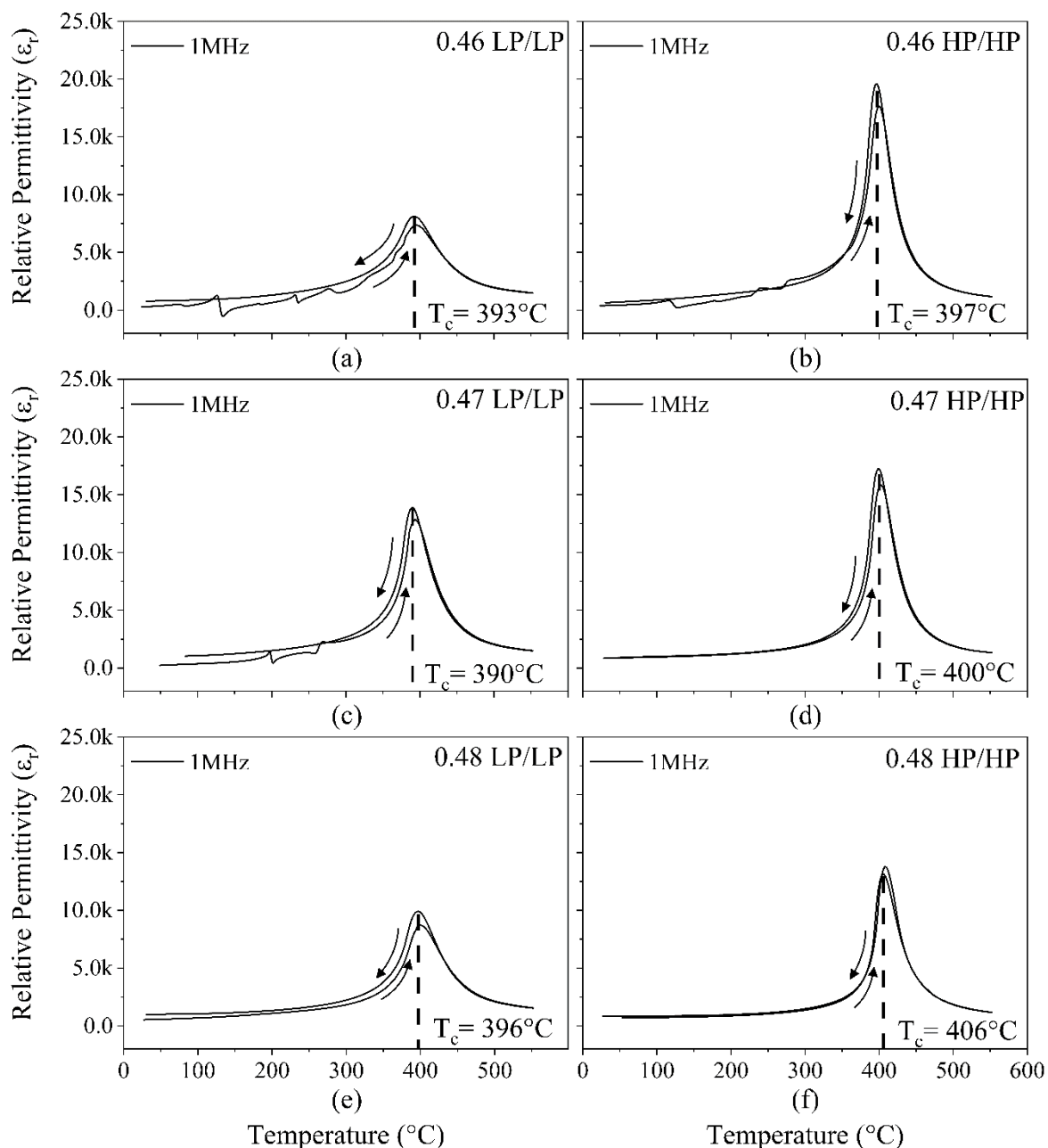
Figure 5-25 Relative permittivity of the six main PZT samples with respect to temperature at 1MHz through heating and cooling. (a) 0.46 LP/LP, (b) 0.46 HP/HP, (c) 0.47 LP/LP, (d) 0.47 HP/HP, (e) 0.48 LP/LP and (f) 0.48 HP/HP.

Figure 5-25 supports the inverse relationship established between the relative permittivity and the Ti concentration in the HP/HP samples, as well as identifying composition 0.47 as being the best-performing pellet from the LP/LP group. Additionally, the graphs show that the largest ε_r at T_C belongs to the 0.46 HP/HP disk, while the smallest value seems to be displayed by its LP/LP counterpart. Figure 5-24 and 5-25 show the T_C of each composition, which was identified by locating the temperature where the maximum ε_r occurs in the cooling segments of the dielectric response obtained at 1MHz.

This ferroelectric to paraelectric transition appears as a single anomaly around 400°C when f >50kHz for the LP/LP samples, and above the 500kHz for the HP/HP disks. Although a difference of 1 or 2°C was found amongst the T_C presented in both figures, they consistently show that the HP/HP specimens displayed the highest T_C, with the LP/LP disks showing values less than 10°C below their HP equivalents.

When focusing on the composition of the samples, disk 0.48 of both arrangement groups shows the highest T_C, whilst composition 0.46 had the lowest transition temperature in the HP/HP group and 0.47 in the LP/LP one. This would suggest that the HP samples have a direct relationship between the amount of titanium and the Curie temperature, while the LP PZT present a less proportional behaviour. Compared to the values included for PZT-4 and PZT-5A in Table 2-4, a difference of 40 to 70°C is seen with respect to the studied PZT samples.

Although a higher Curie point would mean that the material is capable of retaining its piezoelectric properties for a wider range of temperatures, it would also mean that the required temperature to reach the maximum permittivity on the material is further away from naturally occurring values, i.e. room temperature or the operational temperature. Therefore, similar to the acoustic impedance, this characteristic could be considered an advantage or disadvantage depending on the application it is intended to be coupled with.

Since the T_C is closely related to the grain size and distribution, as well as the density, porosity, and impurities in a material (Kong, et al., 2008), it would be expected that a link can be made between these values and the previously studied characteristics. In this case, the higher Curie points exhibited by the HP/HP samples could have a direct relationship with the increased grain size and porosity displayed by the compositions in this group, while an inverse relationship could be established with the density.

Before the ferroelectric-paraelectric transition, the LP/LP PZT disks show a small anomaly in Figure 5-24 when tested at 100Hz before reaching 300°, which has been reported as the point where the rhombohedral-tetragonal transition occurs in the material (Coondoo, et al., 2015). This behaviour can also be seen in the HP/HP plots of the same figure but occurring at a lower temperature (~250°C) and appearing on the measurements obtained at frequencies below or equal to 1kHz.

Additional ferroelectric to ferroelectric transitions can be seen on the ε_r that was measured during the heating stage of some of the studied PZT samples. These anomalies appear below the T_C and are more noticeable during this stage as the disks were tested after already being polarized. Nevertheless, these are not of particular interest to this work and thus are not analysed further.

Dielectric loss in general arises from conductivity and relaxation related to the polarization of the material as heat is produced during the interaction of the electric field with the dielectric polarization (University of Cambridge, 2023). In ferroelectric ceramics, this parameter is also related to domain wall movement or reorientation, where larger grain sizes have been known to be linked to a higher freedom regarding the adjustment of their domain walls (Coondoo, et al., 2015). As mentioned during the polarization of the samples, elevated temperatures can also increase domain wall movement and make their reorientation easier at lower electric fields, although this results in higher dielectric losses.

As part of the dielectric analysis, the dielectric losses were calculated as the ratio between the imaginary and the real parts of the relative permittivity ε_r. Although the losses were calculated for all the permittivities obtained from the previous test and can also be plotted as a function of the temperature throughout the same range of frequencies, it was decided that the most effective processing and presentation of the acquired data would be to include the variations in the dielectric dissipation factor, $tan\ \delta$, with respect to the frequency at three different temperatures, T_R, T_c and T_{max}, as included in Figure 5-26.

The individual values of the chosen temperatures can be seen in the legend of each plot along with the PZT composition it belongs to. While the Curie point changes according to the previously presented values, the room temperature T_R was consistently found at 31°C, while the maximum temperature T_{max} was set at 552°C. It is worth noting that the values presented in Figure 5-26 were selected from the permittivities measured during the cooling stage of the tests, as these are the ones closer to the behaviour from unpolarized specimens.

The plots in Figure 5-26 show that the $tan\ \delta$ varies its behaviour depending on the temperature at which it is measured. For example, the values included at T_{max} and T_C show that the dielectric losses decrease as the frequency increases, resulting in curves close to those seen in exponential decay, particularly when observing the dielectric losses at T_C.

Contrastingly, the values at T_R appear to behave in the opposite manner, where the losses very slowly increase as a function of the frequency but appear almost constant after an initial drop occurring near the lowest measured frequencies (<10kHz).
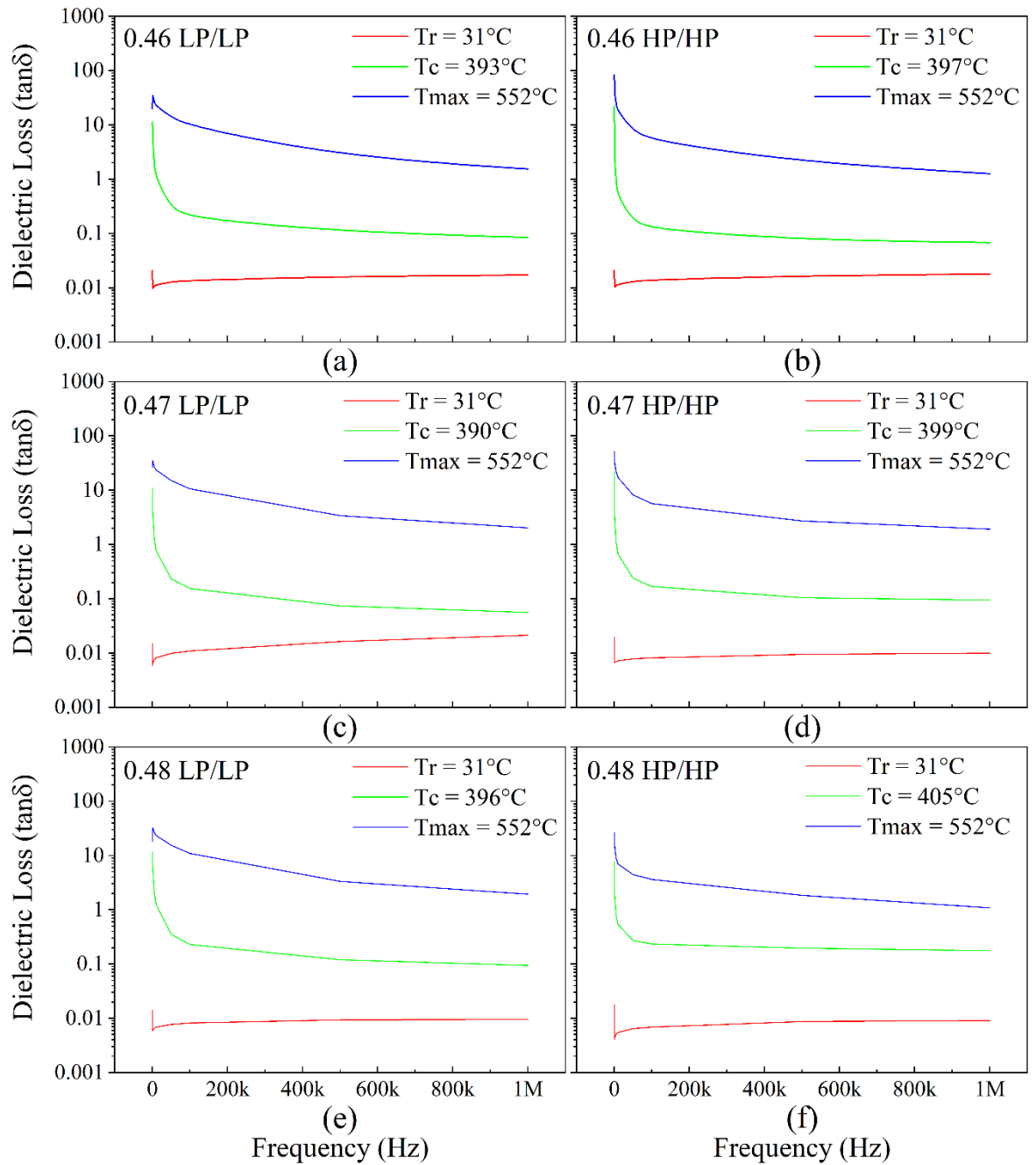
Figure 5-26 Dielectric loss of the six main PZT samples with respect to frequency at T_R, T_C and T_{max}. (a) 0.46 LP/LP, (b) 0.46 HP/HP, (c) 0.47 LP/LP, (d) 0.47 HP/HP, (e) 0.48 LP/LP and (f) 0.48 HP/HP.

Despite the dielectric losses appearing to be directly proportional to the temperature, the maximum value of *tan δ* at the three chosen temperatures was achieved near the lowest frequencies, although the magnitude of these is kept quite close throughout the studied range when working near room temperature.

Furthermore, it can be seen that the LP/LP PZT ceramics exhibited slightly lower dielectric losses than the HP/HP PZT samples when measured at T_{max} and the lowest frequencies (<10kHz), which is consistent with the larger relative dielectric permittivities displayed by the LP compositions at those temperatures and low frequencies. Nevertheless, after this initial behaviour the losses from the LP samples seem to surpass does calculated from the HP/HP disks at higher frequencies.

At T_R, the values of $tan\ \delta$ seem to be remarkably similar between the two PZT purity groups, although the LP/LP samples display slightly higher results as the frequencies increase. Regarding the data obtained at T_C, despite the HP/HP samples exhibiting higher relative permittivities at this point, the 0.47 and 0.48 LP/LP disks registered lower losses than their HP counterparts, even at the highest measured frequencies, with composition 0.46 LP/LP being the only one to display higher values of $tan\ \delta$ than the 0.46 HP/HP sample.

In order to compare the acquired dielectric values more clearly, Table 5-18 presents the estimated Curie Points, relative permittivities, and dielectric losses obtained from the six main PZT disks that were studied during this section, as well as the calculated capacitance C, which was obtained through equation 2-6. The values of the ε_r and $tan\ \delta$ included in this table were selected as the ones measured at 1kHz and T_R (31°C), as this is usually the standard found for similar piezoelectric materials characterised in the literature.

Table 5-18 Curie point, relative permittivity, and dielectric loss at 1kHz and T_R, and capacitance of the six main PZT compositions.

PZT Composition	Pellet ID	$T_C \pm 1$ (°C)	$\varepsilon_r \pm 0.05$ (At 1kHz and T_R)	$tan\ \delta \pm 0.00005$ (At 1kHz and T_R)	C (pF)
0.46 LP/LP	6-4	393	816.5	0.0096	2324.6 ± 3.9
0.47 LP/LP	4-8	390	960.6	0.0064	3104.9 ± 4.5
0.48 LP/LP	4-4	396	1021.4	0.0059	2615.5 ± 4.9
0.46 HP/HP	5-8	397	684.8	0.0102	2950.1 ± 4.6
0.47 HP/HP	5-3	399	874.0	0.0067	3574.7 ± 7.4
0.48 HP/HP	5-5	405	717.5	0.0043	3052.4 ± 4.7

It is immediately observed that under the fixed frequency and temperature (1kHz and 31°C), the LP/LP disks exhibited higher relative permittivities than their HP/HP equivalents. The inverse proportion between the ε_r and $tan\ \delta$ can be seen throughout the majority of the PZT compositions, except for the 0.48 HP/HP sample, where the smallest dielectric loss does not correspond to the highest relative permittivity.

Although some relationships were made between the dielectric permittivities and the TiO$_2$ concentration of the samples from the HP/HP group based on their grain size, back in the discussion included for the graphs shown in Figure 5-24, the particular response seen in sample 0.48 HP/HP would require further analysis to determine the particular causes of the lowest losses not belonging to the highest permittivity in this group.

Amongst the LP/LP samples, as the value of x increases, the relative permittivity increases, whilst the dielectric losses decrease. This behaviour is seen in the first two compositions of the HP/HP group, and throughout all three values of $tan\ \delta$. It seems that the only value that falls outside this pattern is the ε_r from the disk with composition 0.48 HP/HP, which is smaller than the dielectric constant found for the other two compositions made originally with less TiO$_2$. The associated dielectric losses from the HP/HP disks can be linked to the higher porosity found in the PZT samples (Siddiqui, et al., 2020). This is a result not only of the larger pore size identified in this arrangement group through the SEM analysis performed in section 4.3 but also influenced by the distribution or frequency of these pores in the material. From these values, the best dielectric properties appear to come from the compositions with the highest relative permittivities and lowest losses, which correspond to the 0.47 and 0.48 LP/LP disks, followed by the 0.47 HP/HP specimen.

Additionally, the capacitance found from the samples at the set ε_r showed that the LP/LP disks have lower values than their HP/HP counterparts, with both groups having composition 0.47 displaying the highest C, and composition 0.46 showing the lowest. As actuators, a higher capacitance would create a slower system and require more current to operate. In their research, (Alemany, et al., 1995) measured a capacitance of 4808pF at 1kHz for a sample of PZT (PZ27 Ferroperm with h = 1.0 mm, d = 20.0 mm) whilst another source, (Mide Technology, 2024), registered 4000pF for a PZT-5A disk (T216-A4NO-05 with h = 0.41 mm, d = 12.7 mm), which although higher than the values presented in Table 5-18, confirms that the results are in the right order of magnitude for similar morphologies and materials.

The difference in the capacitance measured can be explained by the difference in the sample dimensions, as both the thickness and radius of the studied samples differ from those shown by the samples taken from the literature, as well as the specific composition of the samples.

Unfortunately, due to the data from the HP/LP and LP/HP samples not being collected because of the limited time and access to the equipment, it is not possible to draw further comparisons about the arrangements and their dielectric properties. Therefore, no observations can be made about any possible benefits or advantages associated with the arrangements made with opposite purity for the PbO compensation as it was done with some of the previous parameters in this chapter.

5.7   Chapter 5 Summary

Following the physical characterisation of the PZT samples, the best pellets from each set were chosen and lapped until reaching a thickness at least 16 times smaller than the sample's diameter, leaving smooth, parallel surfaces where the silver paste was applied and cured as electrodes. The diameter of the pellets was lapped if needed, to remove any evident defects on the surface, including superficial cracks and irregularities.

The polarization loops were measured for the available compositions by preparing small pieces from each PZT arrangement after breaking one disk from each set into multiple parts when more than one was available, and following a similar process as previously described, lapping the samples and applying silver electrodes to both faces of the pieces. Once prepared, one small piece from each composition was placed in the P-E setup under a frequency of 0.1Hz and their behaviour was studied by increasing the applied field from 0 to 4kV/mm, using 0.5kV/mm increments.

This analysis showed that the HP PZT samples were highly conductive and commutated quickly once the applied electric field surpassed ~1kV/mm, while the LP disks showed behaviours similar to those seen in hard PZT ceramics, resisting polarization and resulting in pinching in the middle of the generated polarization curves.

To correct these behaviours, the samples were quenched at 600°C for 1h and cooled down rapidly to prevent the dipole moments from aligning, after which the analysis was repeated, and their piezoelectric constants (d_{33}) measured to compare the change in properties before and after the quenching was done. It was observed that the samples presenting the largest polarization were also the ones that showed the best piezoelectric properties in their respective groups when tested before and after quenching.

When looking at the individual arrangement groups, the P-E loops showed that composition 0.47 had the highest remanent polarization amongst the LP/LP samples, while the HP/HP and HP/LP groups had the highest values coming from the pieces with concentration 0.46.

Using the data from the P-E loops generated by the small sample pieces, the big PZT disks were poled at 4kV/mm and 100°C for 15min until reaching saturation. This was completed after putting the samples through a similar heat treatment at 600°C for 2h, to remove any tensions in the material that could have been left by the lapping. Following this, the piezoelectric charge constant, d_{33}, was measured using a Berlincourt meter at 100Hz. This study showed that the HP samples had the highest d_{33}, even when using LP PZ as PbO compensation, which was also seen throughout the values measured from the small PZT sample pieces. Amongst the samples with the opposite PZ compensation, composition 0.47 showed the largest piezoelectric charge constant in the HP/LP group, whilst the 0.46 LP/HP specimen displayed the lowest d_{33} from all ten studied sets, closely followed by sample 0.46 LP/LP.

When analysing the results obtained for these coefficients, no immediate pattern could be identified. On one hand, the LP/LP group showed a direct relationship between the amount of titanium and the d_{33}, with composition 0.46 generating the lowest value, while on the other, the HP/HP sets exhibited an increment in d_{33} from the 0.46 PZT disk to the sample with composition 0.47 but then decreased when reaching the 0.48 specimen.

These results pointed to composition 0.48 being the most proximal to the MPB amongst the LP/LP group, whilst the HP/HP arrangement had the 0.47 specimen closer to this ideal location. This would be consistent with the findings obtained from the XRD graphs, as well as the statements made from the SEM analysis, if considering that the grain sizes listed for composition 0.46 LP/LP cannot be directly compared with the other two LP/LP compositions due to slight variations that were already mentioned, regarding some of the steps followed through the conventional ceramic method used in this work.

The figures of merit associated with piezoelectric ceramics were obtained through an iterative process, where the admittance of the materials was measured after achieving radial resonance in the polarized samples and used to determine the resonance and antiresonance frequencies of each PZT disk, followed by the main and derived characterisation of each individual pellet.

This characterisation included parameters like Poisson's planar ratio, the elastic stiffness and compliance coefficients, and the relative dielectric constant. In particular, the five main figures of merit (FOM) that were of significant interest for this study included the piezoelectric charge and voltage coefficients, d_{31} and g_{31}, the electromechanical coupling factors, k_p and k_{31}, the mechanical quality factor, Q_m, and the acoustic impedance Z_c.

Unlike the longitudinal values, where the highest d_{33} was measured from the HP/HP and HP/LP samples, the highest d_{31} was obtained from the 0.47 and 0.48 HP/LP disks, followed by the 0.48 LP/LP sample, while the lowest value was found in the 0.46 LP/LP pellet, suggesting that particular composition performs poorly when excited radially or longitudinally, as both the d_{31} and d_{33} were the lowest in this composition.

The obtained k_p (>40%) anticipated a good energy conversion potential from the samples, which resembled the high electromechanical coupling that has been observed in piezoelectric ceramics like PZT (Haertling, 1999). Although the highest k_p was from the 0.47 HP/LP disk, the LP samples exhibited consistently high values on both measured coupling factors and were up to 10% better than the HP counterparts. The LP/LP group also showed a direct relationship with the percentage of TiO_2 in the sample, which was not seen amongst the other groups.

Composition 0.47 LP/LP showed the highest mechanical quality coefficients, although the 0.46 and 0.48 specimens in that group showed a better consistency throughout the entire set of the elastic parameters that were studied. The HP PZT samples appeared to exhibit the lowest quality factors, where composition 0.47 HP/HP and 0.48 HP/LP displayed the worst results from all the disks. In addition to this, the dielectric properties appeared to vary with the amount of TiO_2 in the sample, with the highest losses and lowest relative permittivities seen from the 0.46 compositions in each group.

From the obtained functional characterisation, although the HP PZT samples displayed higher piezoelectric coefficients and polarizability, the LP PZT compositions consistently exhibited higher planar electromechanical coupling factors and quality coefficients along with higher dielectric constants and lower losses. This could be taken as a more influencing characteristic when evaluating their potential for the conversion of mechanical energy to electrical. Therefore, it is anticipated that the LP disks will be the best materials for the intended energy harvesting, which is presented and explored in Chapter 6.

Chapter 6. ELECTRONIC ADAPTATION AND TESTING OF THE PZT CERAMIC DISKS

Following the functional characterisation completed on the ten PZT pellets that were processed and poled as presented and discussed in Chapter 5, the electrical impedance of each sample was measured before proceeding to the impact tests intended to evaluate their performance as kinetic energy harvesters.

The assessment of the impedance involved the measurement of its magnitude, as well as the associated electrical resistance of the specimens. Additional parameters, related to those discussed in the latter sections of the previous chapter, were also calculated and included properties such as the resonance and antiresonance frequencies, and the mechanical quality factor Q_m.

After this, each chosen disk from the ten available PZT compositions was electrically coupled as an energy harvester by using controlled impact tests at two different frequencies, where the output alternating current, and voltage were collected. Subsequently, the output power (μW) and energy (μJ) were calculated along with the densities of these values per unit area (μW/cm^2) and per unit volume (μW/cm^3), with both the average and maximum values presented for these parameters.

Finally, this chapter includes a cost analysis of the different arrangements that were chosen and prepared for this dissertation. This analysis presents the specifications of the various chemical powders required for the preparation of the PZT disks and compares the cost in pounds sterling per gram of material obtained from 2020 and 2023, as well as the ratios between the cost per disk found between the HP and LP specimens.

6.1 Electrical Impedance *Z* and Resistance *R*

Although the acoustic impedance Z_c is considered one of the main FOM associated with piezoelectric ceramics, for this study, the electrical impedance Z was considered a more representative parameter due to its closer relationship with the intended electrical coupling of the PZT samples as energy harvesters, which is the primary focus of this chapter. Although the impedance phase and associated reactance were also measured as part of this analysis, only the magnitude of Z and the corresponding resistance R of the PZT samples were included in this section based on their relevance to this work. These parameters were obtained using a 4395A Impedance Analyser (Agilent, USA), which is shown in Figure 6-1.
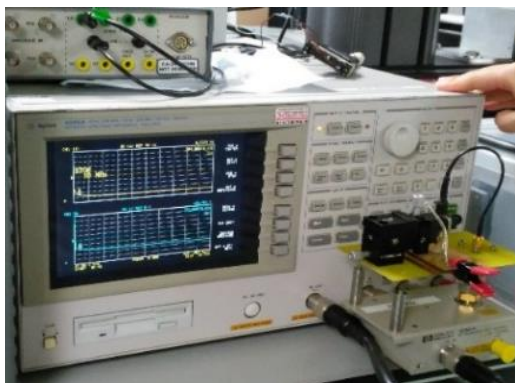
Figure 6-1 Impedance analyser (4395A) setup used to obtain the impedance of the PZT samples.

For each sample, 801 test points were taken through a frequency sweep that took 3.148s, using a linear frequency and employing a power source of 15 dBm (~32 mW). The measurements were obtained both in the thickness and radial resonance modes for a thin disk poled along its thickness, where the thickness mode used frequencies ranging from 1 kHz to 10 MHz, while the radial mode was swept from 1 kHz to 1 MHz.

Figures 6-2 to 6-5 present the impedance and resistance of the ten PZT samples in the two previously mentioned resonance modes. The two first figures present the impedance plots and the last two the resistance ones, starting with the graphs obtained from achieving radial resonance, followed by the thickness resonance measurements.

When analysing the resulting plots, it can be seen that the larger peaks displayed in the graphs of each PZT disk correspond to the main nodes, while the smaller peaks are harmonics. In addition to the information provided in section 5.5, where the resonance and antiresonance frequencies were defined as the points where the maximum values are registered for the resistance and conductance, it has also been established that the frequency where the minimum impedance Z is measured corresponds to the resonance frequency f_r, while the maximum Z is found at the antiresonance frequency f_a (Kong, et al., 2008).

The piezoelectric effect is a convenient way to observe the interaction of the mechanical resonance in the samples with their electric response by producing the elastic waves seen in the figures below through excitation. Furthermore, it was mentioned during the FOM analysis that the geometry of the pellets is linked to the resonance frequencies in the material, hence why these values vary when the disk's thickness and/or diameter are changed, depending on the type of mode being evaluated.

Below, Figure 6-2 presents the impedance measured after reaching radial resonance in the PZT disks. The scale of the vertical axis of the plots was kept constant throughout the

ten samples in Figures 6-2, 6-3 and 6-5 to allow for a direct visual comparison of their amplitudes and corresponding frequencies, while the vertical scale in Figure 6-4 was set individually for each plot to maximise the shape of the displayed curve. The horizontal axis was kept the same for all the samples in each of the four figures.
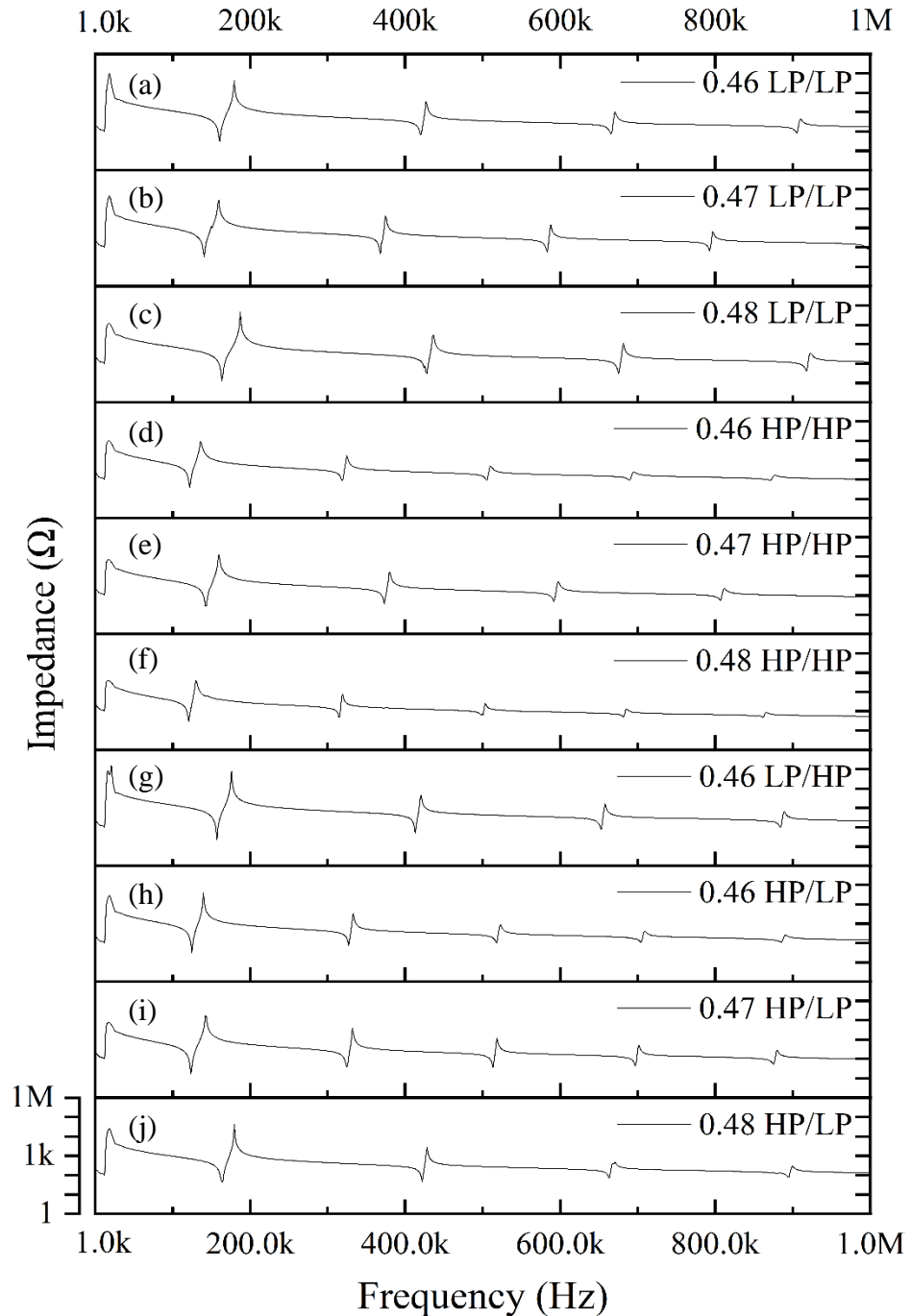
Figure 6-2 Impedance of the 10 PZT disks in radial mode (1kHz – 1MHz). (a) 0.46 LP/LP (6-4), (b) 0.47 LP/LP (4-8), (c) 0.48 LP/LP (4-4), (d) 0.46 HP/HP (5-8), (e) 0.47 HP/HP (5-3), (f) 0.48 HP/HP (5-5), (g) 0.46 HP/LP (6-8), (h) 0.47 HP/LP (4-7), (i) 0.48 HP/LP (4-6), and (j) 0.46 LP/HP (6-10).

Figure 6-2 shows that the minimum and maximum impedance, *Z*, is achieved by the samples when the applied vibration frequency is between 100 and 200kHz, which would be consistent with the values measured in section 5.5 and presented in Table 5-8. The precise

resonance frequencies of each of the 10 PZT compositions were found from the collected data and are included in Table 6-1, along with the corresponding resonance impedances Z_r.

Table 6-1 Resonance frequency f_r, antiresonance frequency f_a and resonance impedance Z_r of the ten processed PZT disks.

PZT Composition	Pellet ID	$f_r \pm 0.62$ (kHz)	$f_a \pm 0.62$ (kHz)	$Z_r \pm 0.005$ (Ω)
0.46 LP/LP	6-4	160.84	179.57	30.67
0.47 LP/LP	4-8	140.86	159.59	32.90
0.48 LP/LP	4-4	163.34	187.06	12.96
0.46 HP/HP	5-8	122.13	135.87	40.11
0.47 HP/HP	5-3	143.36	159.59	27.23
0.48 HP/HP	5-5	120.88	129.62	30.86
0.46 LP/HP	6-10	157.09	175.83	23.10
0.46 HP/LP	6-8	124.63	139.61	32.56
0.47 HP/LP	4-7	123.38	142.11	17.42
0.48 HP/LP	4-6	164.59	179.57	47.39

The slight discrepancies between these values and the ones presented in the previous chapter are due to the differences in the experimental setup and equipment, particularly based on the specific instrument resolution and sweeping step used. These results confirm the prior observations made throughout the FOM analysis but provide the additional parameter of the minimum impedance exhibited by the samples at f_r. The Z_r measured showed no distinctive pattern when comparing all 10 disks, as each arrangement group appeared to have a different composition displaying the highest resonance impedance.

Amongst the LP/LP disks, composition 0.47 had the highest Z_r followed closely by the 0.46 disk, with sample 0.48 showing a value less than half the magnitude of the other two compositions. Regarding the HP/HP samples, composition 0.46 displayed a resonance impedance of ~23% above the 0.48 disk and ~32% above the 0.47 specimen. Additionally, composition 0.48 had the highest values of the HP/LP samples, surpassing composition 0.46 by ~31% and composition 0.47 by ~63%. Finally, the 0.46 LP/HP pellet registered the lowest value of the four samples with a composition of 0.46. Nevertheless, it should be noted that just as with the resonance frequencies, the resulting impedances cannot be directly compared as these are not constant parameters but a function of the sample's geometry.

Akin to the previous figure, Figure 6-3 presents the impedance measured with respect to the frequency from the ten PZT samples but this time when excited along their thickness.
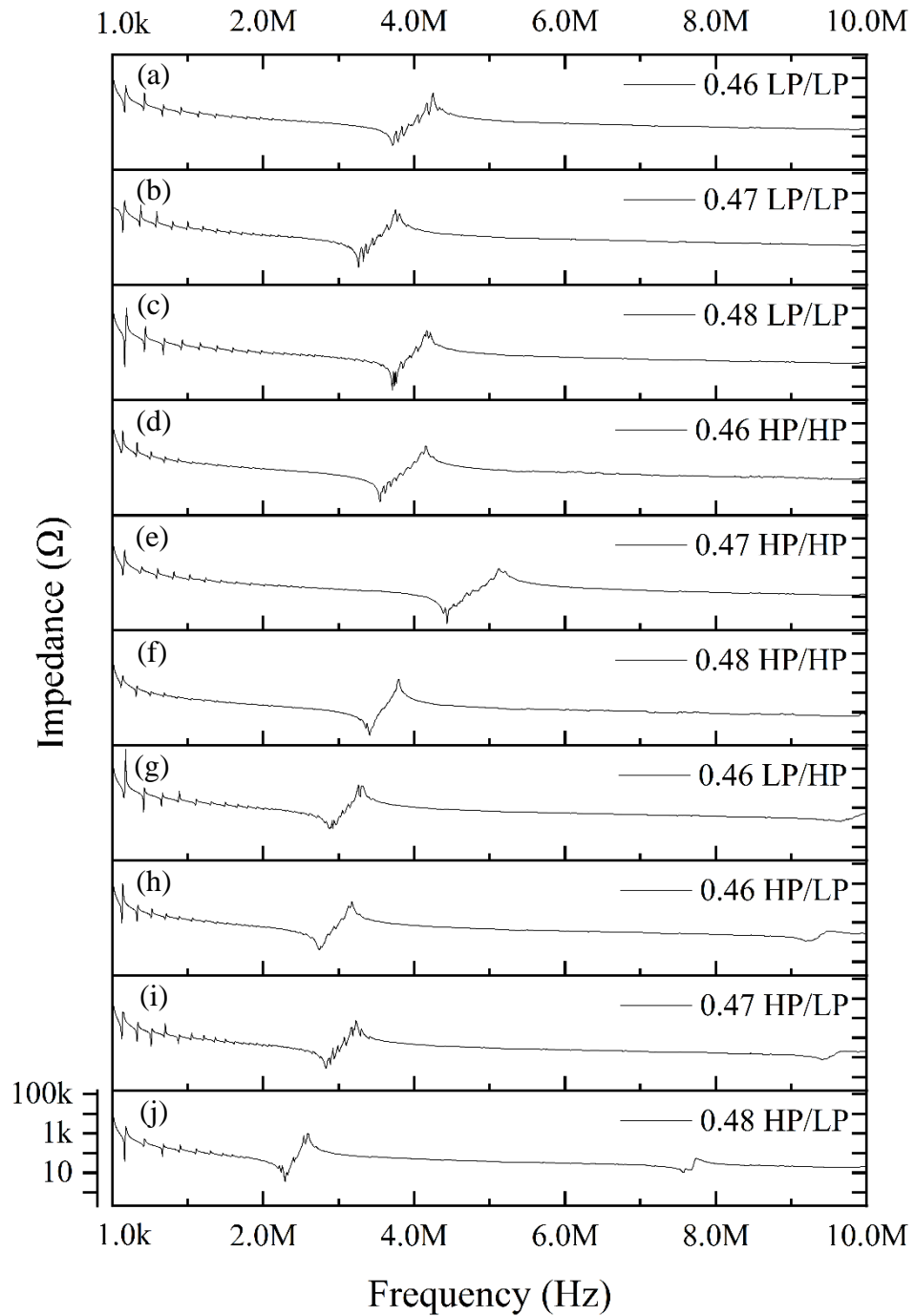
Figure 6-3 Impedance of the 10 PZT disks in thickness mode (1kHz – 10MHz). (a) 0.46 LP/LP (6-4), (b) 0.47 LP/LP (4-8), (c) 0.48 LP/LP (4-4), (d) 0.46 HP/HP (5-8), (e) 0.47 HP/HP (5-3), (f) 0.48 HP/HP (5-5), (g) 0.46 HP/LP (6-8), (h) 0.47 HP/LP (4-7), (i) 0.48 HP/LP (4-6), and (j) 0.46 LP/HP (6-10).

Unlike the f_r and f_a values obtained through the radial resonance tests, found between 100 and 200 kHz, the resonance frequencies from the PZT samples after achieving resonance along their thickness were identified somewhere between 2 and 6MHz, with sample 0.47 HP/HP reaching the maximum and minimum impedance at the highest frequencies and disk 0.48 HP/LP at the lowest frequencies from the all the studied specimens. As these values are not employed for any further analysis or calculations and are simply included to show the

variation of the data when the samples are tested with respect to their thickness instead of their radius, the precise values for the f_r and f_a are not included or discussed further.

Despite this, it can be seen that the samples with combined arrangement purities registered the lowest frequencies from the entire group, which was not the case for the radial resonance measurements. They also appear to display the narrowest peaks, indicating closer proximity between the resonance and antiresonance frequencies. Furthermore, the 0.46 LP/HP disk seems to display the largest resonance impedance, followed closely by the HP/LP and LP/LP disks of the same composition and by the 0.48 HP/LP pellet.

As highlighted before, the geometry dependency of these parameters explains why the samples with the highest values in radial mode do not correspond to the ones from the thickness resonance, as well as assigning completely different frequencies where resonance is reached in each pellet. These observations are further discussed in the following sections after completing the electrical coupling and performance tests of the chosen PZT disks.

Using the values of Z_r, f_a and f_r obtained from Table 6-1, the mechanical quality factor Q_m was calculated using equation (2-4) from the literature review (Chapter 2). The values obtained are included in Table 6-2.

Table 6-2 Mechanical quality factor Q_m of the ten processed PZT disks.

PZT Composition	Pellet ID	Q_m
0.46 LP/LP	6-4	141.75
0.47 LP/LP	4-8	121.87
0.48 LP/LP	4-4	180.55
0.46 HP/HP	5-8	93.57
0.47 HP/HP	5-3	88.35
0.48 HP/HP	5-5	89.75
0.46 LP/HP	6-10	229.21
0.46 HP/LP	6-8	142.16
0.47 HP/LP	4-7	140.51
0.48 HP/LP	4-6	89.75

Although not identical, the Q_m calculated for the PZT disks resembles those obtained for the piezoelectric coefficient d_{31} (Table 5-16), showing the highest quality factors coming from the LP PZT samples and the lowest from the HP/HP disks. Interestingly, the combined PZT specimens exhibited higher values than the pure HP samples, suggesting that the presence of the LP parent oxides can improve the mechanical quality of the compositions.

The resistance of the samples in both resonance modes, corresponding to the real part of the measured *Z,* is presented in Figures 6-4 and 6-5. The values of interest for *R* are the ones displayed at the same resonance frequencies found in the two previous figures. Figure 6-4 shows the resistance from the 10 PZT disks obtained in radial resonance mode.
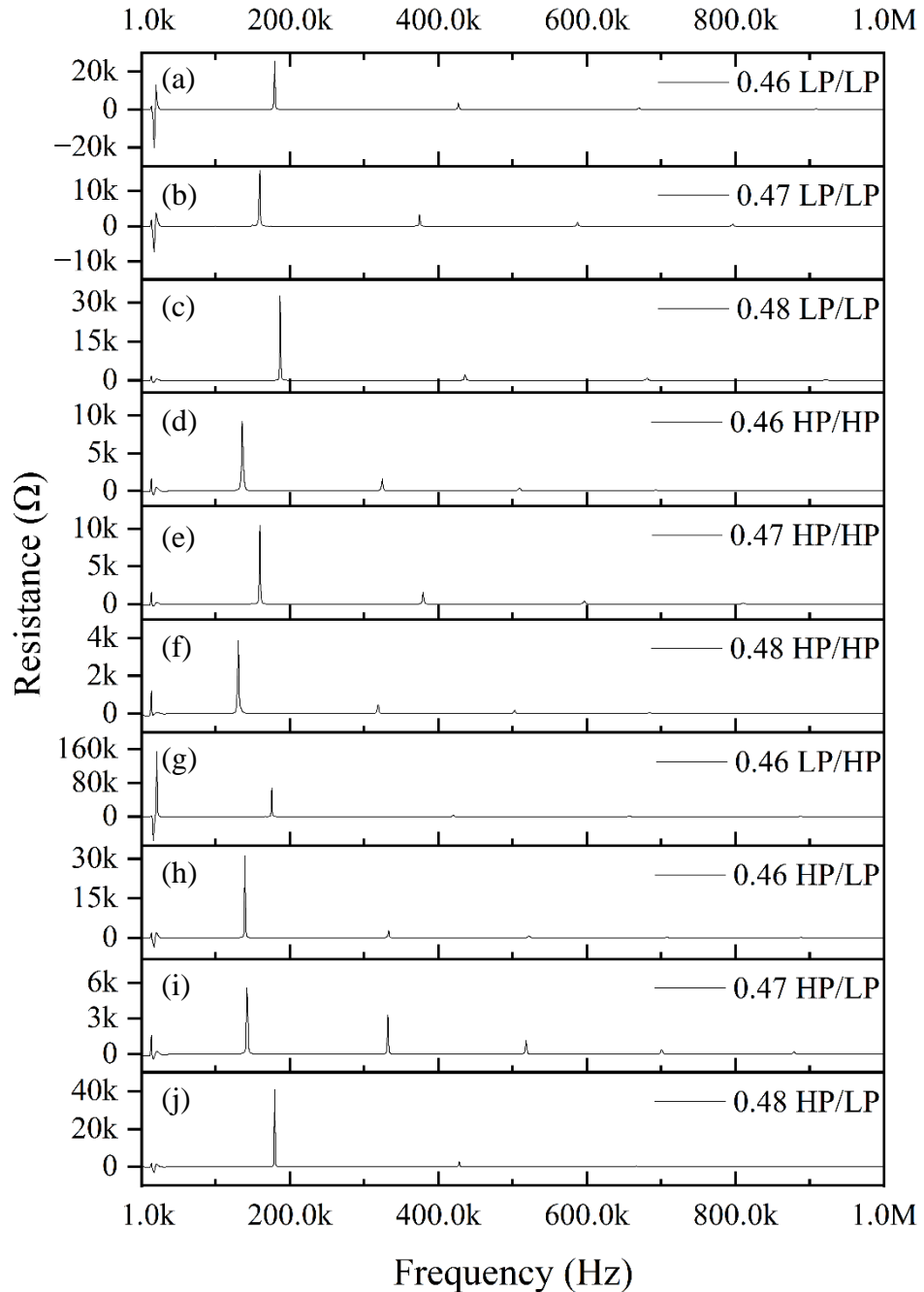
Figure 6-4 Resistance of the 10 PZT disks in radial mode (1kHz – 1MHz). (a) 0.46 LP/LP (6-4), (b) 0.47 LP/LP (4-8), (c) 0.48 LP/LP (4-4), (d) 0.46 HP/HP (5-8), (e) 0.47 HP/HP (5-3), (f) 0.48 HP/HP (5-5), (g) 0.46 HP/LP (6-8), (h) 0.47 HP/LP (4-7), (i) 0.48 HP/LP (4-6), and (j) 0.46 LP/HP (6-10).

As with the radial resonance impedances, the radial resonance resistances for the PZT samples are found between 100 and 200kHz. The individual values for this parameter

can be found in Table 6-3, corresponding to the maximum resistance measured from each arrangement group and located at the antiresonance frequencies found for Z.

Table 6-3 Resistance R of the ten processed PZT disks.

PZT Composition	Pellet ID	R ± 0.005 (kΩ)
0.46 LP/LP	6-4	25.67
0.47 LP/LP	4-8	15.69
0.48 LP/LP	4-4	32.55
0.46 HP/HP	5-8	9.21
0.47 HP/HP	5-3	10.46
0.48 HP/HP	5-5	3.86
0.46 LP/HP	6-10	67.94
0.46 HP/LP	6-8	31.10
0.47 HP/LP	4-7	5.57
0.48 HP/LP	4-6	40.92

From Table 6-3, it can be seen that the maximum resistances registered by the PZT samples vary between 3.86kΩ (composition 0.48 HP/HP) and 67.94kΩ (composition 0.46 LP/HP). As expected from the observations made regarding Z, the highest resistances are seen amongst the LP PZT disks, whilst the lowest is displayed by the HP/HP group. Unlike this arrangement, where the highest values are measured from composition 0.47, the LP/LP and HP/LP sets have composition 0.47 displaying the lowest R from their groups and the 0.48 specimens with the highest values.

Furthermore, Figure 6-4 shows that when tested outside of the resonance frequencies, the resistance plot obtained from each PZT disk becomes almost a constant line with a significantly smaller magnitude relative to the other values measured at the resonance peaks. Although explained in greater detail in section 6.5, when considering that the parameters associated with their coupling as energy harvester involve a range of frequencies that are much lower than the estimated resonance values, the expected resistance exhibited by the material would become negligible, especially when compared to the load resistance of 1MΩ used in the required coupling system.

Finally, Figure 6-5 shows the resistance that was obtained from the PZT disks excited along their thickness as a function of frequency.
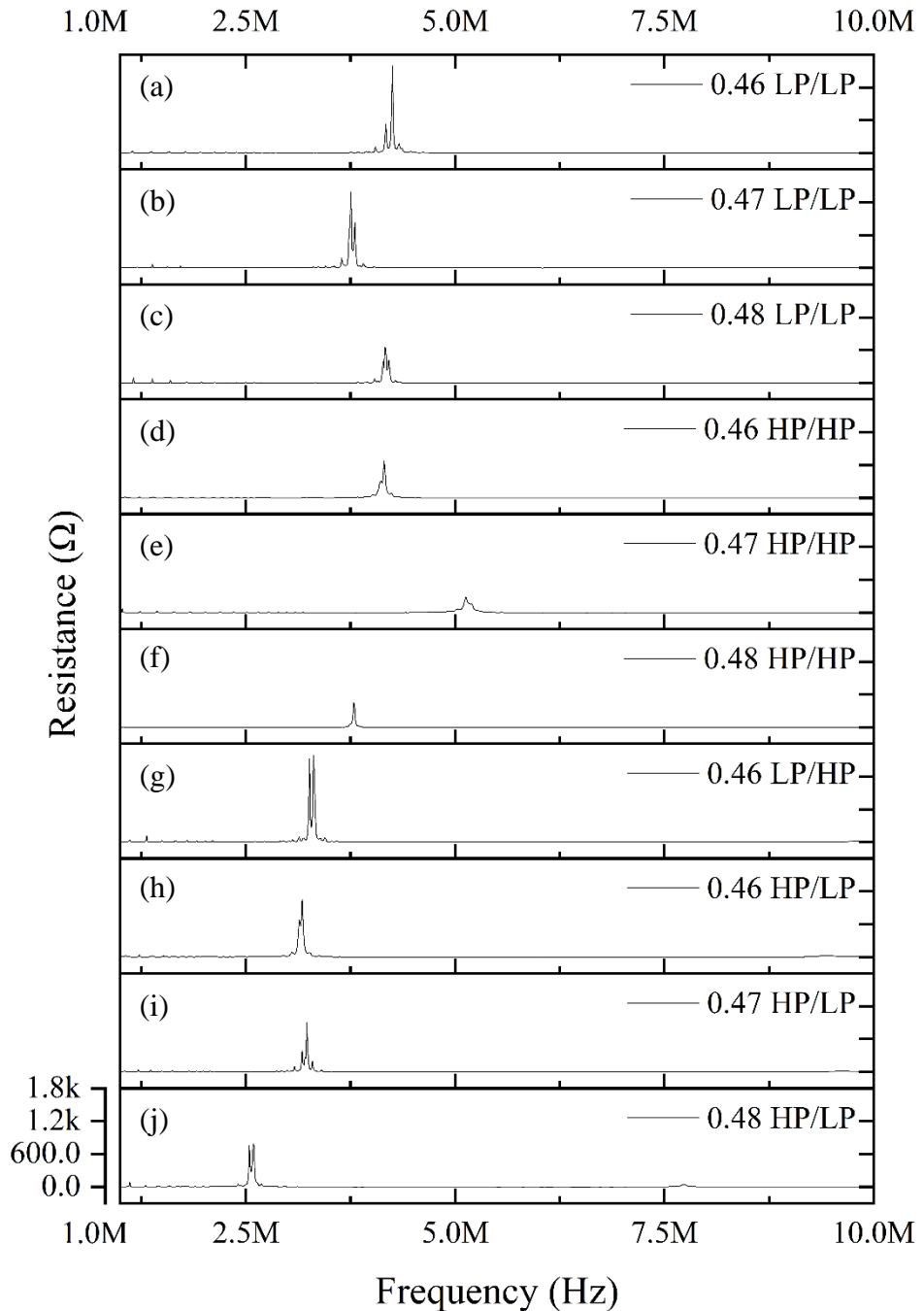
Figure 6-5 Resistance of the 10 PZT disks in thickness mode (1 kHz – 10 MHz). (a) 0.46 LP/LP (6-4), (b) 0.47 LP/LP (4-8), (c) 0.48 LP/LP (4-4), (d) 0.46 HP/HP (5-8), (e) 0.47 HP/HP (5-3), (f) 0.48 HP/HP (5-5), (g) 0.46 HP/LP (6-8), (h) 0.47 HP/LP (4-7), (i) 0.48 HP/LP (4-6), and (j) 0.46 LP/HP (6-10).

Although not used for any further calculations, the resistance plots seen in Figure 6-5 display a similar behaviour as the one shown in Figure 6-4, following the pellet pattern identified and discussed for their corresponding impedances, with the highest values measured at the same antiresonance frequencies but with the particular difference of showing peaks with a lot more splitting or dispersion compared to the ones seen from the radial resonance measurements. The highest values of R appear to come from the LP/HP and LP/LP samples with composition 0.46, followed by composition 0.47 from the LP/LP group.

Unlike the impedance plots, where the harmonics can be seen throughout the majority of the frequency range, the resistance values seem to appear mainly in the first half of the range, with only some of the samples showing relatively small harmonics after the resonance values. This is more noticeable in thickness mode, although the corresponding harmonics of the impedance in this mode are also smaller and less frequent than the ones registered when achieving radial resonance in the samples.

Proportionally, the two parameters analysed in this section are of significantly smaller magnitudes when the samples are excited along their thickness than their radius (approximately 10 times smaller for the impedance and between 2.2 and 22 times smaller for the resistance). Contrastingly, the transversal resonance frequencies are at least 15 times greater than the radial values. This indicates that it would be easier to generate the frequencies required to achieve resonance from typical vibration sources in our surroundings when exciting the pellets radially than trying to do so transversally, but with the specimens exhibiting larger impedances, and consequently higher resistances, although it has already been pointed out that the expected values would be insignificant if the operating frequencies are far from the resonant frequencies of the material. Specific technological applications based on the capabilities of the samples under each type of vibration would require further tests and analysis, which are not covered under the scope of this work.

6.2   Soft and hard ceramics

After completing the characterisation of the PZT samples, it is possible to use all the parameters from the prepared compositions to determine if the chosen piezoelectric ceramics are categorised as "soft" or "hard" materials. Soft ceramics are typically created when metal (cation) vacancies are created in the crystal structure of the ceramic by adding small amounts of a donor dopant, resulting in the enhancement of the piezoelectric properties in the material. Alternatively, when oxygen (anion) vacancies are created by an acceptor dopant, a hard ceramic is formed.

In order to evaluate the category in which the prepared PZT samples fall, Table 6-4 shows the typical properties that would be compared when assessing the type of ceramic as well as the type of value that would be displayed by these parameters when belonging to the "soft" or "hard" ceramic group. Next to the columns displaying the soft and hard ceramic expected response to each property, the specific grade of PZT purity (HP or LP) that met this behaviour is included.

Table 6-4 Characteristics of soft and hard ceramics with the best suited PZT chemical purity.

Characteristics	Soft Ceramics	PZT Purity	Hard Ceramics	PZT Purity
Piezoelectric Constants	larger	HP	smaller	LP
Dielectric Properties	larger	HP	smaller	LP
Electromechanical Coupling	large	HP	larger	LP
Mechanical Quality Factors	low	HP	high	LP
Coercive Field	low	HP	higher	LP
Polarization / Depolarization	easier	HP	harder	LP
Hysteresis	greater	HP	lower	LP
Mechanical load R	lower	HP	high	LP

When selecting the chemical purity that best suited the characteristics of each group, it is seen that the HP PZT exhibited the main characteristics that are associated with soft ceramics while the LP disks behaved as a hard PZT. Amongst the two, soft ceramics are characterised by having larger piezoelectric and dielectric properties, electromechanical coupling factors and electrical resistance, as well as being easier to polarize or depolarize.

Although able to produce larger displacements and wider signal bandwidths, soft ceramics are mainly used in sensors rather than power applications due to their difficulty dealing with high-frequency inputs (>10MHz) because of their large permittivities and dielectric losses (APC International, Ltd, 2016). On the other hand, hard ceramics have higher mechanical quality factors and coercive fields, as well as better linearity, making them better candidates for these applications. Despite this, it is important to acknowledge that either of these ceramics can be prepared to exhibit some characteristics that would approach those of the other. Thus, when choosing a material for a particular application, it is necessary to carefully compare the specific characteristics of the ceramic, rather than just basing the decision purely on the general categorization (APC International, Ltd, 2016).

6.3   PZT sample preparation prior to their electronic coupling

In order to test the processed PZT samples as piezoelectric energy harvesters, copper tape was applied to both faces of the disks by cutting the tape to the required shape and leaving a short rectangular extension coming out of the electrode to provide a space where the copper wires could be soldered without creating a stress point on the surface. The conducting tape was placed with the wires facing opposite directions, as seen in Figure 6-6, to avoid any accidental contact, which would cause incorrect readings. The sides of the tape where the wires were not soldered, were covered with a piece of PET that was cut to size.

Figure 6-6 Conductive copper tape placed on both faces of a PZT disk with copper wires soldered in opposite directions.

Additionally, commercially available double-sided tape with a thickness of 3mm was placed on top of the copper electrodes after cutting it to the same shape as the surface areas of the PZT samples. This was done to protect the material from the impact force applied whilst being evaluated for its electric response, allowing this force to be distributed equally throughout the contact surface and preventing the sample from shattering. The protective film that comes with the double-sided tape was left on the side that was not in direct contact with the copper tape as this provided a smooth surface to place the pellet on the testing plate without adhering it to the surface or the impacting weight. The top and side views of this arrangement are depicted in Figure 6-7.
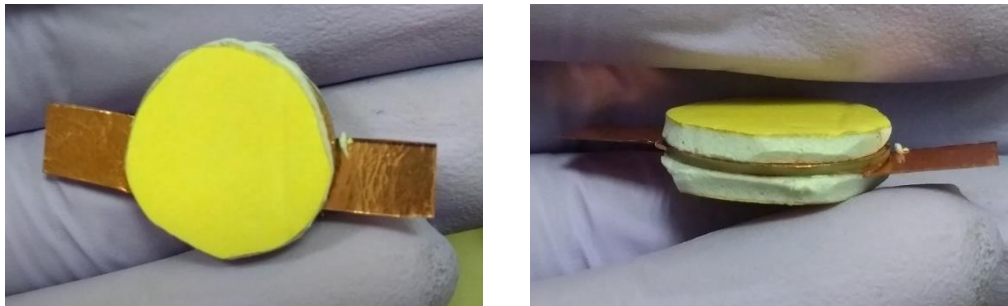
Figure 6-7 Top and side view of a PZT disk covered with copper tape and placed between two pieces of double-sided tape cut to shape.

6.4 Current and voltage curves of the PZT samples

With the help of Dr Sachin Kumar Singh, controlled impact tests were completed in the Indian Institute of Science Education and Research (IISER) to measure the performance of the samples as energy harvesters. The machine used for the electrical characterisation was a modified version of a sewing machine where the front cover and needle holder were removed and replaced with a weight holder, as seen in Figure 6-8. The motor and pedal were also replaced with a potentiometer to regulate the impact frequency.

Figure 6-8 Impact test setup made up of a modified sewing machine connected to a potentiometer.

The weight used measured 2.5cm in diameter and 1.1cm in height, travelling a total distance of 3.1cm from the highest to the lowest point of the movement, with an impact force of ~40N. This element can be seen in Figure 6-9, attached to the front of the modified sewing machine and located directly above an adjustable testing plate.

Figure 6-9 Weight of 40N used during the controlled impact tests for the PZT samples.

The sample was fixed to the adjustable plate, as shown in the images included in Figure 6-10, by securing it with multiple pieces of invisible matt tape, thus minimising any shifting that might occur from the starting position during the impact tests.
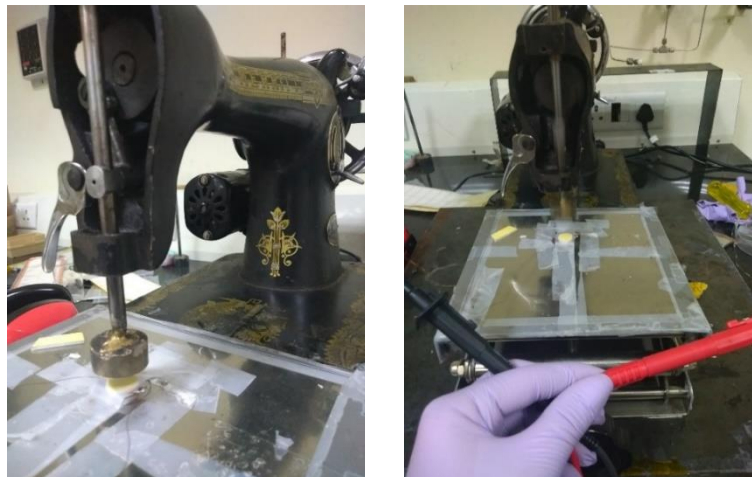
Figure 6-10 Placement configuration of the PZT samples for the electrical performance tests.

As mentioned in the previous section, as part of the electrical coupling and to obtain the I-V curves of the prepared PZT disks, each sample was connected in series to a 10MΩ resistor before being connected to a multimeter (DMM7510 Keithley, USA - Figure 6-11) and after being secured to the testing plate, employing the Kickstart software to collect the output data using the "digitize voltage" function of the program.

Figure 6-11 DMM7510 Keithley multimeter used to collect the I-V data from the coupled PZT samples.

For these tests, two different values were chosen for the potentiometer, 110 and 140 on the adjustable scale, which roughly equated to 6 and 14 hits per second, respectively. An average of 4 iterations were taken for each PZT composition, each lasting ~10 to 12s, taking the best one from each batch for its subsequent analysis and comparison. The variation in the testing interval is a result of having to ignore some of the starting or ending values measured by the multimeter in some of the PZT samples due to significant discrepancies with the rest of the plot. Figure 6-12 depicts the internal behaviour of the electrical charges in the poled ceramics before and after an external stress is applied to the device.
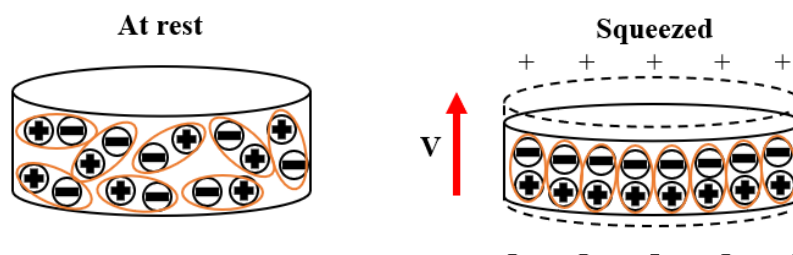
Figure 6-12 Internal behaviour of the electrical charges in the material when it is at rest (left) and after being deformed by external stress (right).

When the samples are at rest, the internal charges are balanced, hence the electric dipole moments cancel each other out and the net charge of the material equals zero. When an external force is applied to the sample's faces, the mechanical displacement caused by compression of the disk, forces the electric charges out of balance, resulting in a net dipole moment different than zero and generating a voltage difference across the material. This illustrates the basic working principle of the piezoelectric effect which is sought to be used in this research for its potential use as kinetic energy harvesters.

The following figures (6-13 to 6-16), show the current plots as a function of time, obtained from each of the ten coupled PZT disks at the two chosen impact frequencies. As done with the previous plots in this work, all the graphs included in this section were created using the OriginPro Software, which was also employed for data analysis, including statistical calculations to obtain the mean, max and standard deviation (σ) from the measured parameters. The first two figures show the data collected at 6 hits/s, starting with the 6 main PZT disks (Figure 6-13) and followed by the four combined purity disks (Figure 6-14).
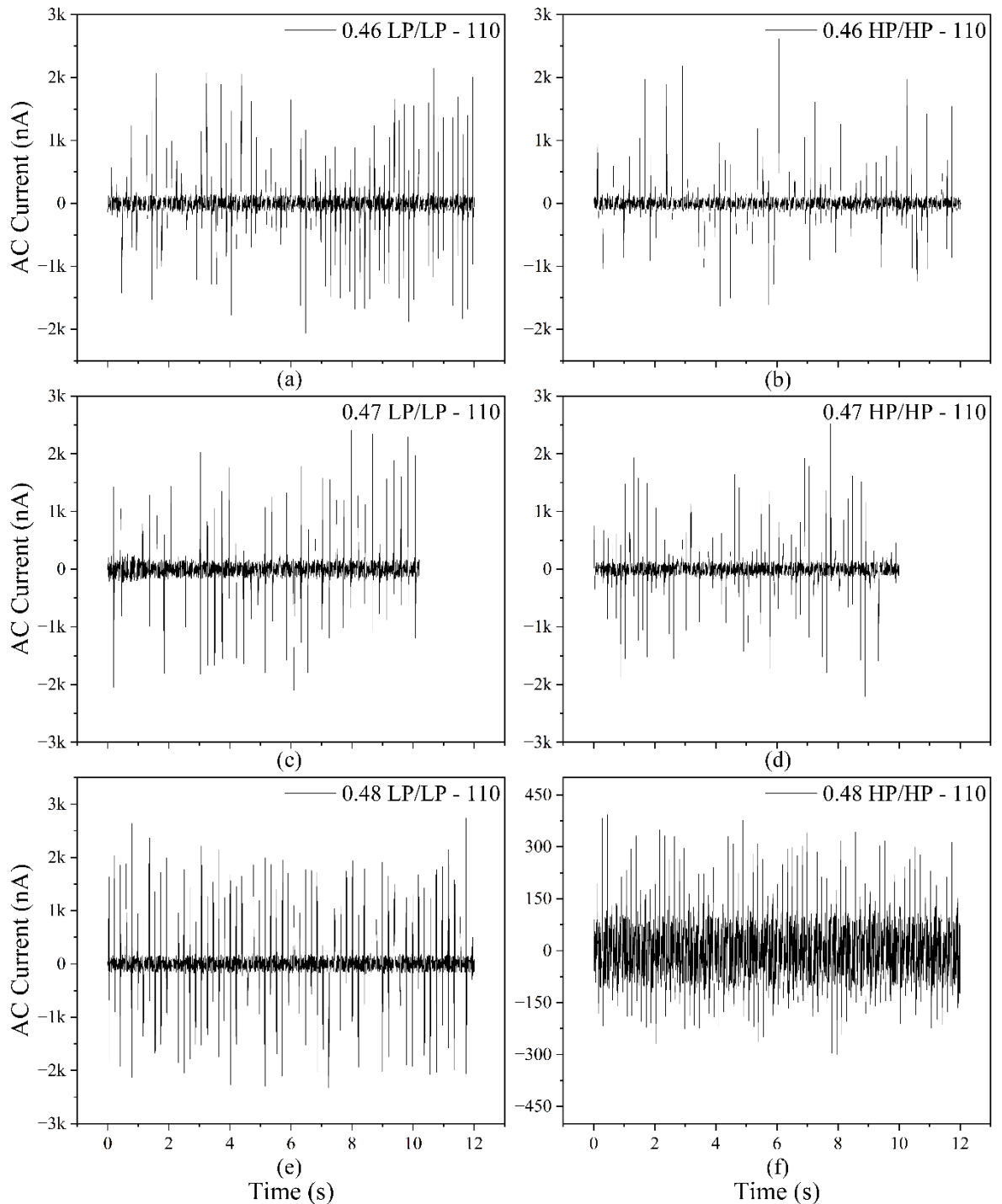
Figure 6-13 AC curves obtained from the LP/LP and HP/HP PZT samples at ~6Hits/s. (a) 0.46 LP/LP, (b) 0.46 HP/HP, (c) 0.47 LP/LP, (d) 0.47 HP/HP, (e) 0.48 LP/LP, and (f) 0.48 HP/HP.
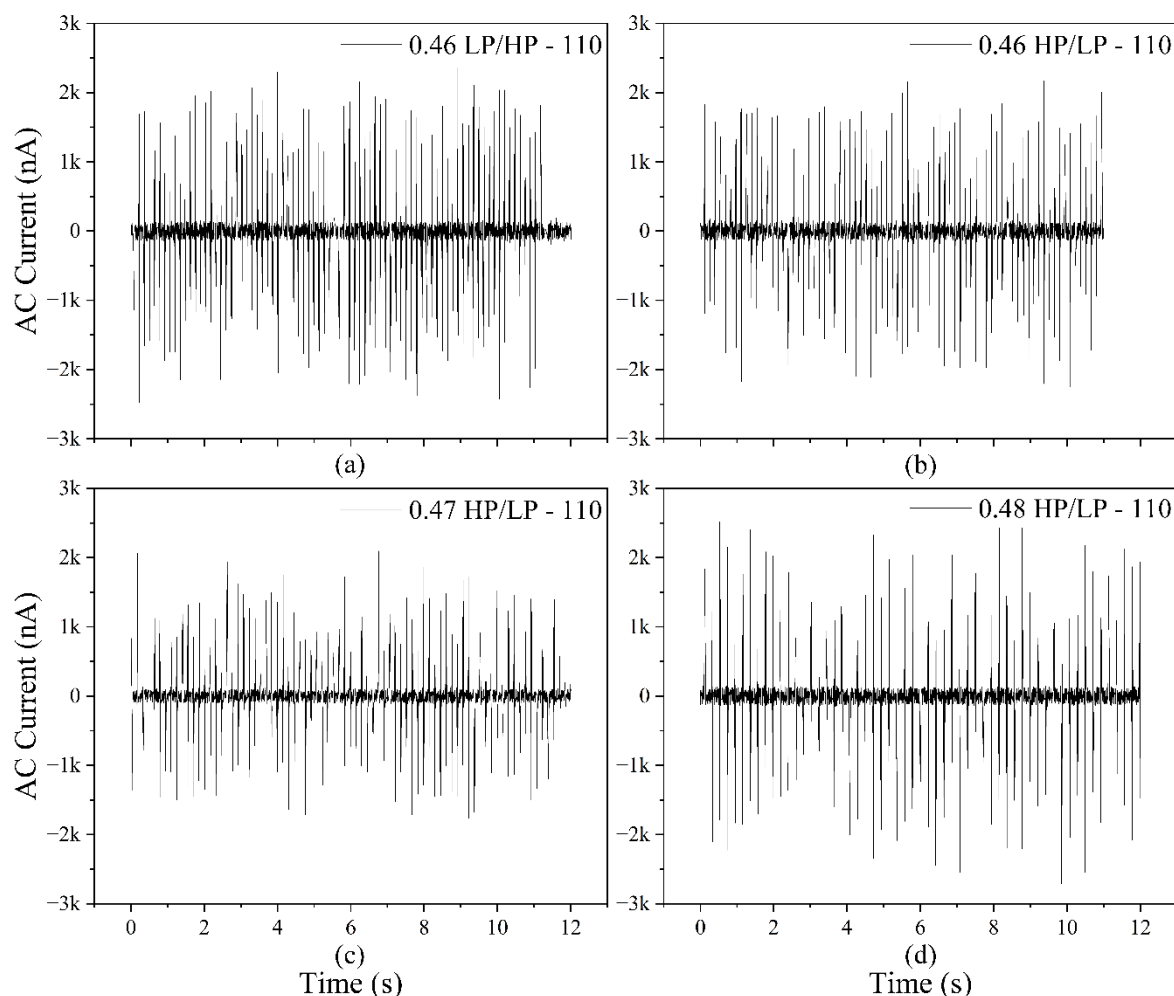
Figure 6-14 AC curves obtained from the LP/HP and HP/LP PZT samples at ~6Hits/s. (a) 0.46 LP/HP, (b) 0.46 HP/LP, (c) 0.47 HP/LP, and (d) 0.48 HP/LP.

It can be immediately seen in the last two figures that all the samples have been plotted using the same horizontal axis scale, with the vertical axis scale set between -3000nA and 3000nA, with the exception of sample with composition 0.48 HP/HP, which was set at a much smaller scale (-500 to 500nA) due to the measurements being significantly smaller than the rest of the samples and would have not been clear enough to compare if fixed at the larger scale. This indicates that from the entire analysed set, this sample registered the lowest currents, even when tested multiple times as previously described.

Additionally, it appears that the samples with an opposite purity arrangement displayed a higher consistency throughout the currents obtained during the tests. This can be confirmed through the mean value calculated for the specimens, which is presented in Table 6-5 included after Figure 6-16. Although some estimations can be made from the visual comparison of the current magnitudes presented in the figures above, Figure 6-17 provides an accurate and direct contrast of the average current (I_{ave}) and max current (I_{max}) of each disk.

175

Similar to the previous figures, Figure 6-15 and Figure 6-16 present the measured AC currents from the coupled PZT samples throughout the impact tests carried out for ~12s, with an identical horizontal scale for all the compositions. Unlike the last figures, the impact frequency used for these iterations was increased to ~14 hits/s, using a vertical scale between -2k and 2.5k for the six main PZT sets and between -2.5k and 3k for the combined samples.
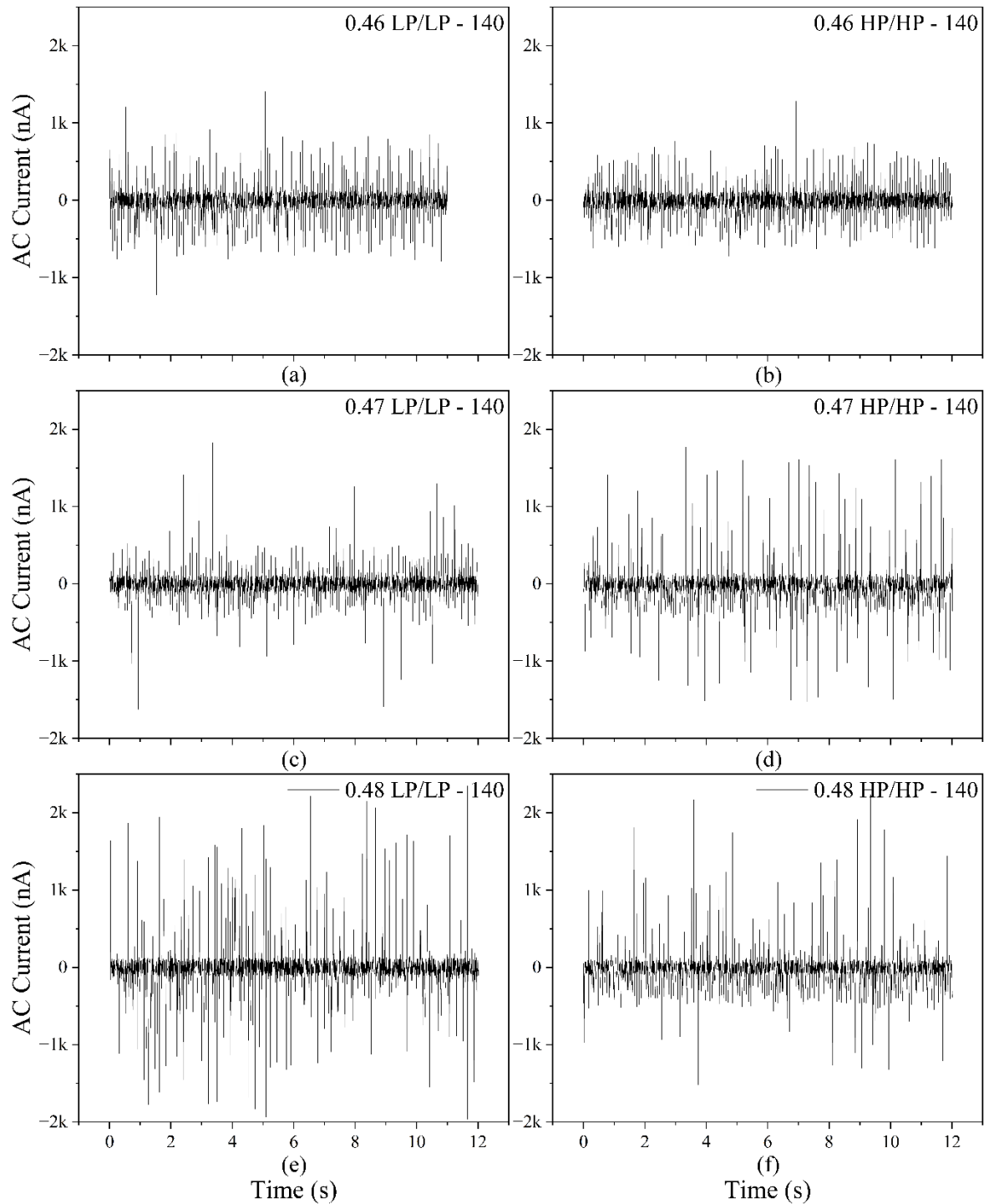
Figure 6-15 AC curves obtained from the LP/LP and HP/HP PZT samples at ~14Hits/s. (a) 0.46 LP/LP, (b) 0.46 HP/HP, (c) 0.47 LP/LP, (d) 0.47 HP/HP, (e) 0.48 LP/LP, and (f) 0.48 HP/HP.

Prior to comparing the data presented in Table 6-5, Figure 6-15 shows that the disks with composition 0.46 HP/HP and LP/LP registered the lowest currents from all the sets at the higher impact frequency of 14 hits/s, followed by sample 0.47 LP/LP and 0.48 HP/HP. From this figure, it seems that sample 0.48 LP/LP showed the highest magnitude and consistency throughout the current measurements, which appears to also be the case when tested at 6 hits/s. This would be consistent with the results obtained for this composition regarding their piezoelectric charge coefficient, electromechanical coupling factor and mechanical quality factor, which were the highest from their arrangement group and amongst the highest of all the studied samples.
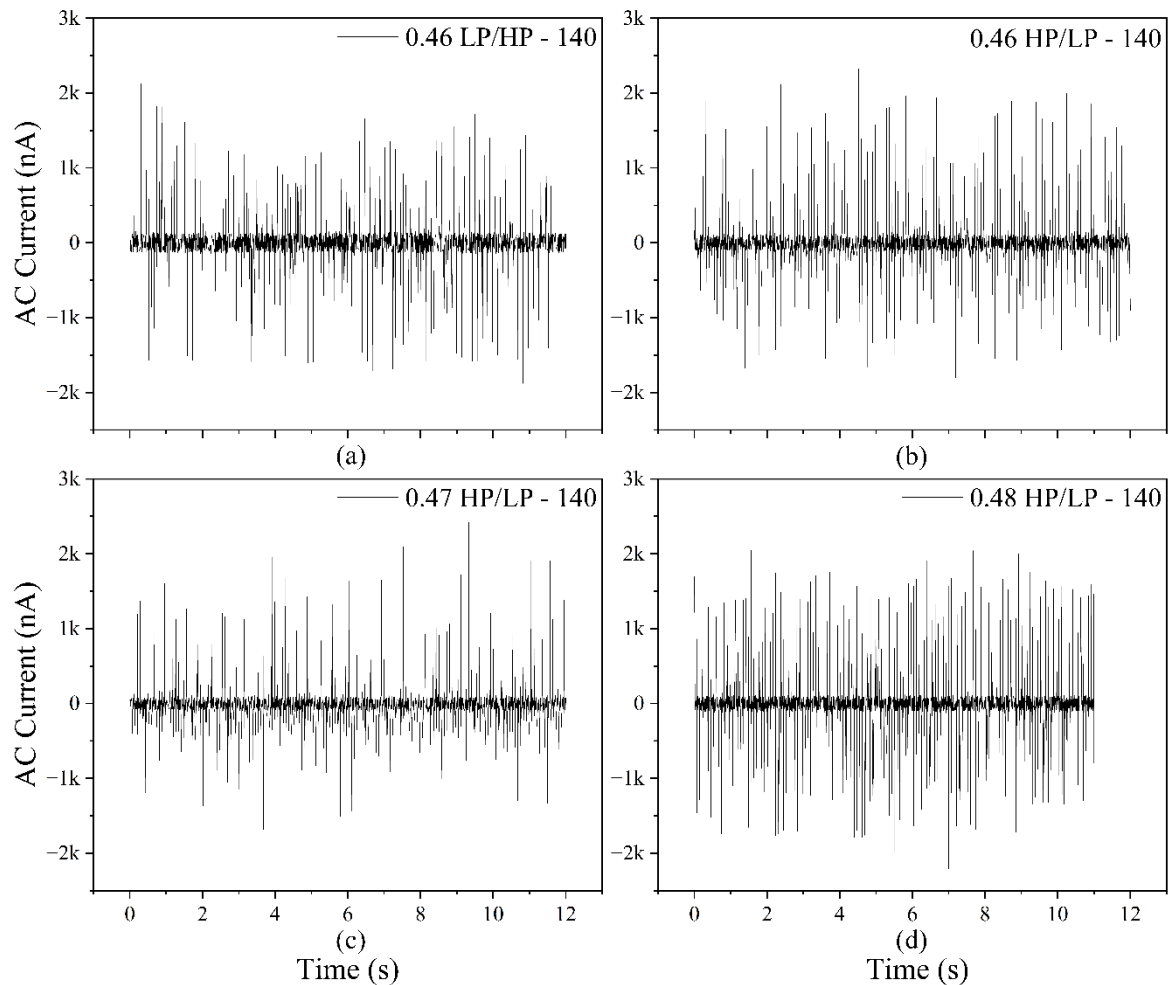
Figure 6-16 AC curves obtained from the LP/HP and HP/LP PZT samples at ~14Hits/s. (a) 0.46 LP/HP, (b) 0.46 HP/LP, (c) 0.47 HP/LP, and (d) 0.48 HP/LP.

Amongst the combined arrangement samples, Figure 6-16 shows that the highest currents were obtained from the 0.48 HP/LP disk, which also displayed the most consistent peaks throughout the plot. Nevertheless, this behaviour is not seen in the lower frequency plots and does not appear to be consistent with the physical characterisation registered from this composition.

As indicated previously, to allow for a clear comparison amongst the measured currents, the mean and maximum values were calculated after obtaining the absolute of the collected data. The associated standard deviation is also included along with the statistical calculations obtained for each PZT composition at the two chosen frequencies. These characteristics are presented in Table 6-5 and plotted in Figure 6-17, below.

Table 6-5 Average, standard deviation and maximum registered currents from the PZT devices tested at 6 hits/s and 14 hits/s.

Frequency		6 hits/s			14 hits/s		
PZT Composition	Pellet ID	I_{ave} (nA)	σ	$I_{max} \pm 0.005$ (nA)	I_{ave} (nA)	σ	$I_{max} \pm 0.005$ (nA)
0.46 LP/LP	6-4	185.30	343.23	2561.49	147.65	179.35	1410.19
0.47 LP/LP	4-8	191.60	346.73	2413.77	130.81	174.42	1820.80
0.48 LP/LP	4-4	276.05	489.92	2746.07	194.92	347.78	2343.40
0.46 HP/HP	5-8	122.10	238.53	2616.70	136.52	156.05	1280.53
0.47 HP/HP	5-3	158.16	299.84	2520.19	180.79	281.70	1772.84
0.48 HP/HP	5-5	84.07	61.08	392.99	159.87	252.17	2237.13
0.46 LP/HP	6-10	300.15	525.48	2625.91	197.31	341.64	2121.09
0.46 HP/LP	6-8	244.79	459.29	2492.24	210.12	374.80	2839.55
0.47 HP/LP	4-7	195.22	360.64	2123.32	168.70	282.89	2422.67
0.48 HP/LP	4-6	236.87	468.37	3134.50	261.51	462.46	2210.18

Table 6-5 shows that the maximum currents that were displayed by the PZT disks reached values of up to ~3.14μA at 6 hits/s and ~2.84μA at 14 hits/s, corresponding to disk 0.48 HP/LP and 0.46 HP/LP, respectively. Throughout the arrangement groups that have more than one PZT composition, it can be seen that composition 0.48 displayed the highest currents at both impact frequencies, with the exception of the HP/HP group at 6 hits/s and the HP/LP at 14 hits/s. Sample 0.48 HP/HP exhibited the lowest values as anticipated from the plots included in Figure 6-16 but contrastingly had the highest value from its group when tested at a higher frequency.

Additionally, the LP PZT groups (LP/LP and LP/HP) exhibited smaller I_{ave} and I_{max} when increasing the number of impacts per second, while the HP/HP only showed this behaviour through the maximum values of the 0.46 and 0.47disks, with the mean currents measured at 6 hits/s being less than those measured at 14hits/s. Finally, the HP/LP group showed the opposite pattern in its majority, with compositions 0.46 and 0.47 having larger mean values at the lower frequency but with smaller peak currents and disk 0.48 behaving like the first two HP/HP specimens.

Figure 6-17 shows a comparative graph of the data included in Table 6-5, which uses the standard deviation as the error bars of the mean values.
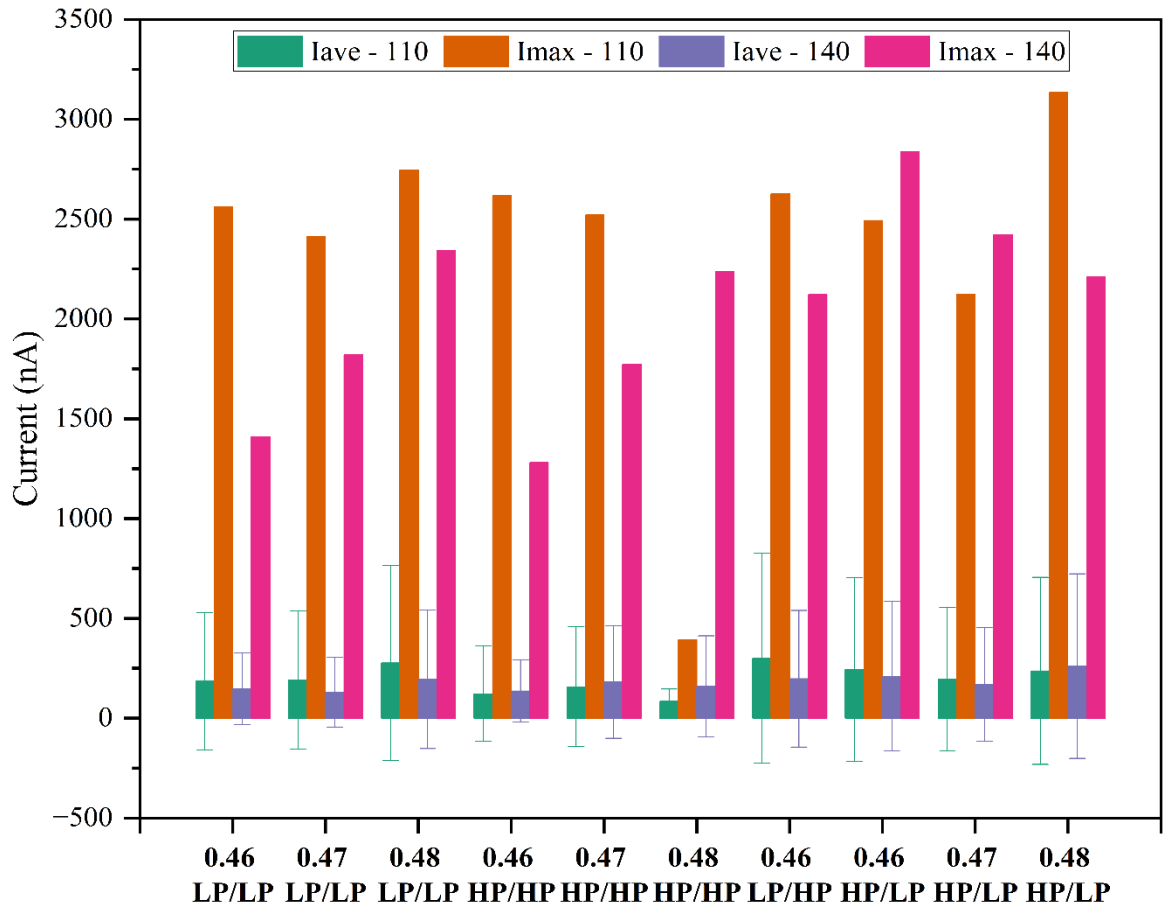
Figure 6-17 Mean (with standard deviation error bars) and maximum AC from the PZT samples tested at ~6 and 14Hits/s.

Although the mean values appear quite consistent throughout all ten disks, Figure 6-17 shows that the largest errors were calculated from composition 0.48 LP/LP and the majority of the combined PZT disks, with the exception of sample 0.47 HP/LP. Nevertheless, it can also be observed from the presented figure and table that these specimens are the ones registering the highest average values during both impact tests, whilst also having some of the highest maximum currents from all the studied samples.

A similar data processing was done with the voltages measured from the ten PZT samples that were prepared for their coupling as kinetic energy harvesters and tested under the two previously mentioned frequencies and applied impact force. The following figures present the collected data from the best iteration obtained from each sample at the two test frequencies, starting with the lower frequency (6 hits/s) plots in Figure 6-18 and Figure 6-19, and followed by the results obtained at ~14 hits/s in Figures 6-20 and 6-21.

Like with the current curves, the horizontal axis was identical for all the samples at both testing frequencies when measuring the generated voltage. Additionally, the time interval used for these tests was also ~12s, with only a couple of samples ending with a reduced interval after filtering some of the unsuitable data at the plot extremes, likely caused by faulty readings from the system. Nevertheless, for this parameter, the vertical axis scale was kept constant throughout the presented plots, with a range between -50 to 50V.
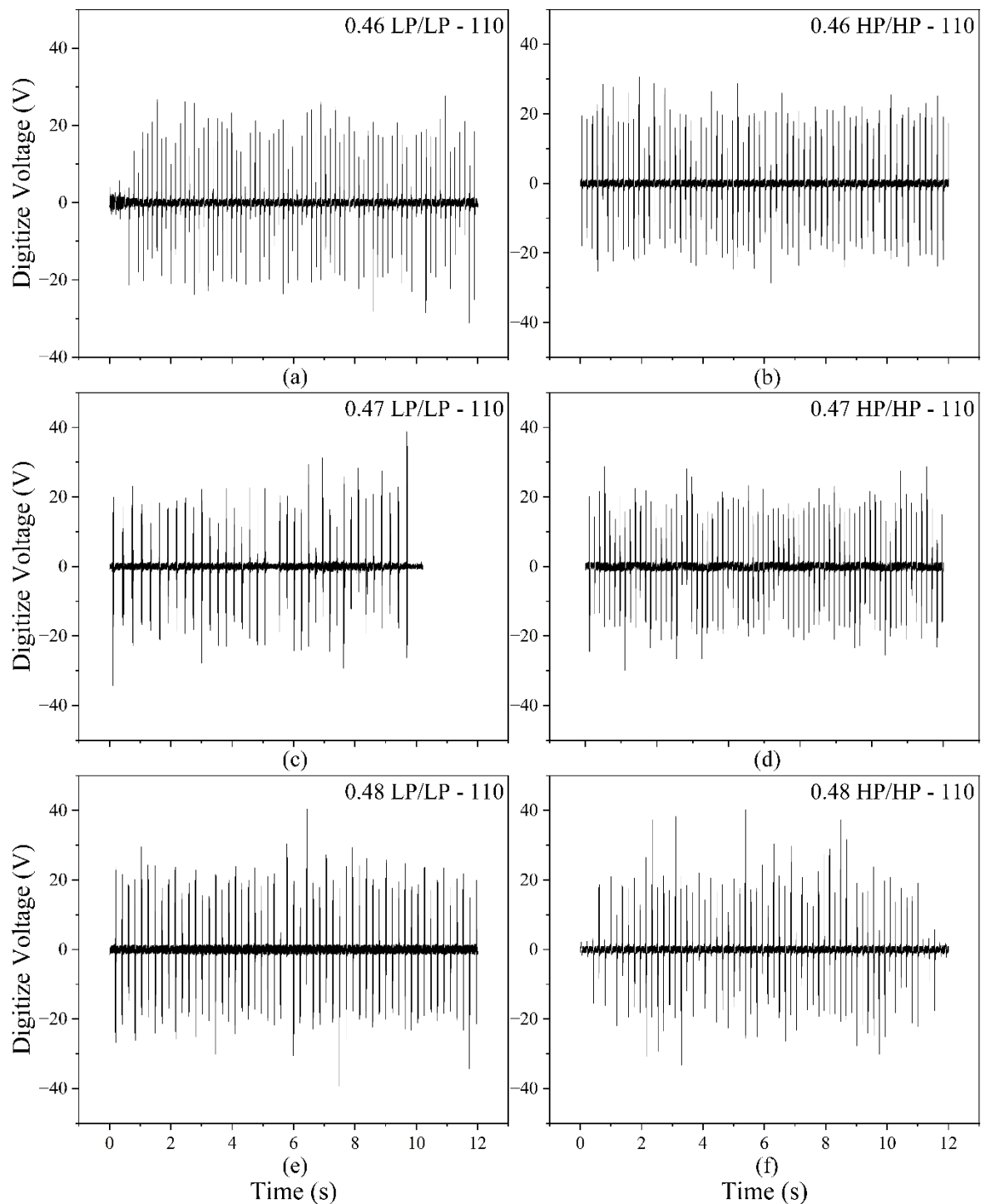
Figure 6-18 Digitize voltage curves obtained from the LP/LP and HP/HP PZT samples at ~6Hits/s. (a) 0.46 LP/LP, (b) 0.46 HP/HP, (c) 0.47 LP/LP, (d) 0.47 HP/HP, (e) 0.48 LP/LP, and (f) 0.48 HP/HP.

Whilst Figure 6-18 displayed the *V* plots for the six PZT compositions made with the same purity for the PZT and PZ disks during sintering, Figure 6-19 shows the graphs created for the PZT compositions prepared with the opposite purity for the PbO compensation.
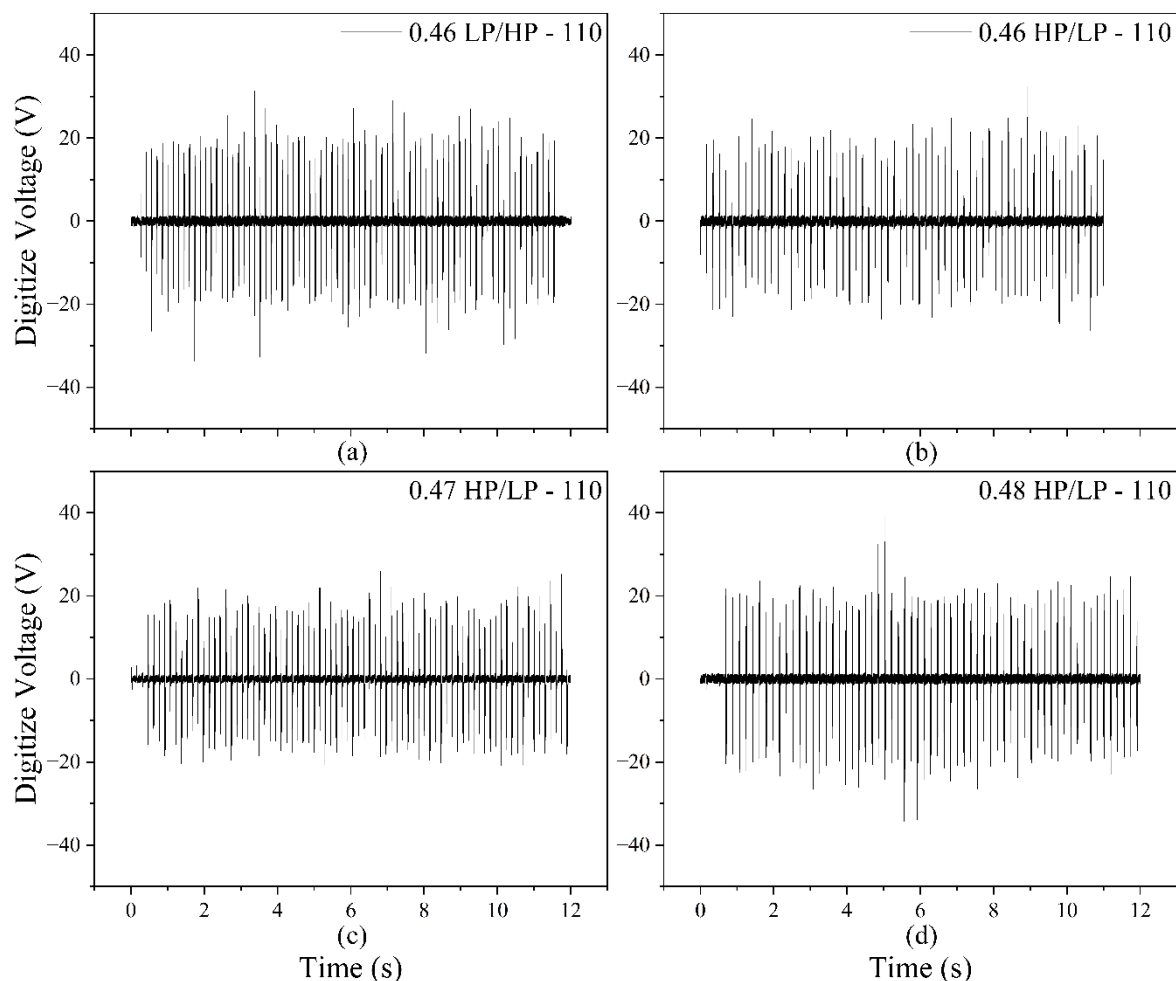
Figure 6-19 Digitize voltage curves obtained from the LP/HP and HP/LP PZT samples at ~6Hits/s. (a) 0.46 LP/HP, (b) 0.46 HP/LP, (c) 0.47 HP/LP, and (d) 0.48 HP/LP.

These two figures show high consistency throughout the magnitude of the registered peaks in each graph, mainly throughout the mixed purity PZT samples in Figure 6-19, and much less on samples 0.47 LP/LP and 0.48 HP/HP (Figure 6-18). Furthermore, the plotted curves show similar values for the generated voltages amongst all the tested PZT specimens, making it difficult to distinguish which compositions had the best and worst performances. Therefore, to aid with the analysis of the collected data, Table 6-6 and Figure 6-22 are included after the next two figures to show the average and maximum voltages, along with the associated standard deviation, of the results obtained at the two tested frequencies.

Analogous to the previous plots at 6 hits/s, Figure 6-20 and Figure 6-21 present the corresponding voltages measured from the PZT pellets at ~14 hits/s.
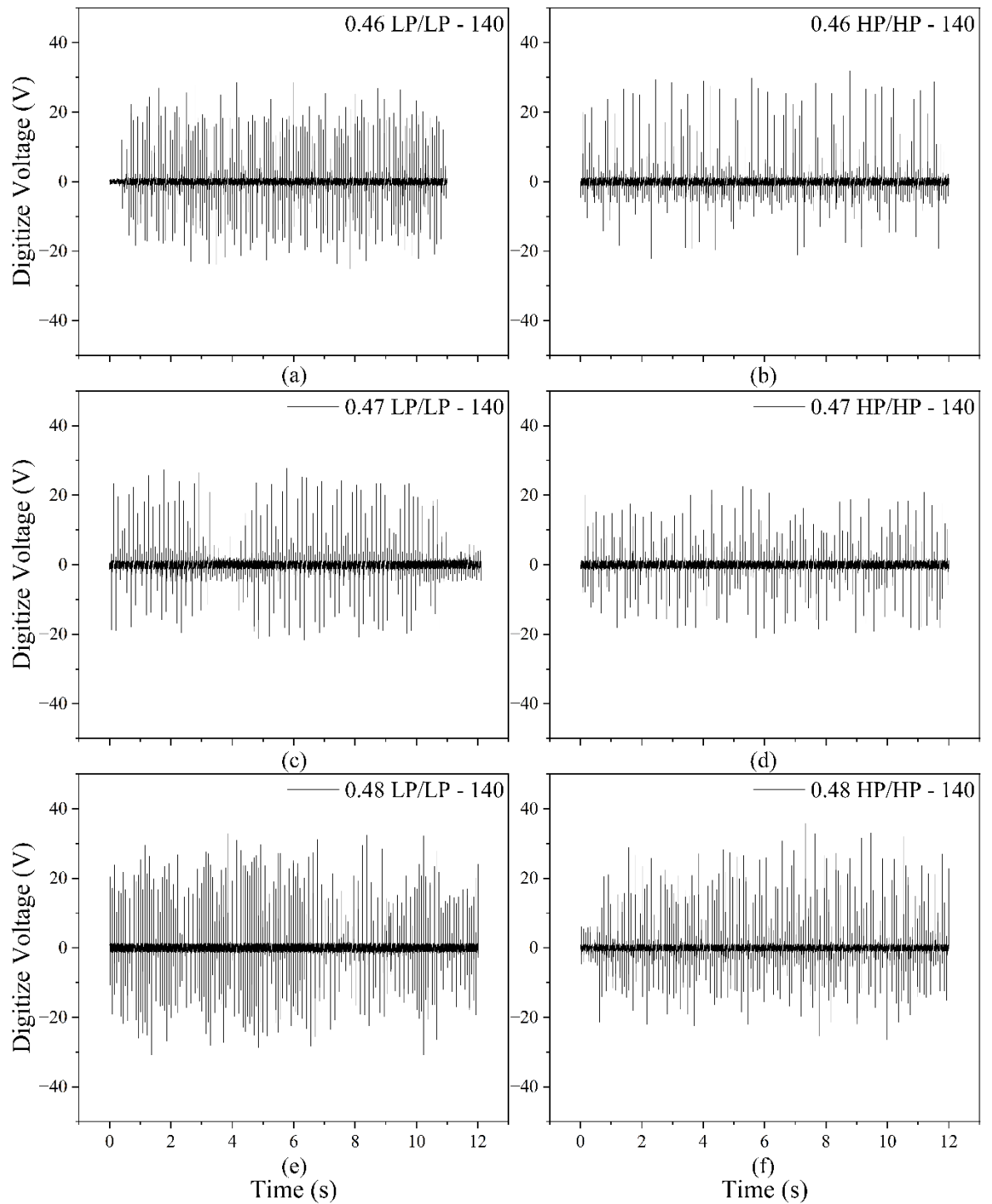
Figure 6-20 Digitize voltage curves obtained from the LP/LP and HP/HP PZT samples at ~14Hits/s. (a) 0.46 LP/LP, (b) 0.46 HP/HP, (c) 0.47 LP/LP, (d) 0.47 HP/HP, (e) 0.48 LP/LP, and (f) 0.48 HP/HP.

Although the overall voltage magnitudes registered from the disks are still within a similar range as the previous values, the consistency of the voltage peaks plotted for each PZT composition seems to have decreased, with greater variations amongst the measurements. Nevertheless, a slightly higher homogeneity is seen in the opposite purity PZT samples, which was also observed in the figures pertaining to the lower frequency. This could indicate a higher stability and repeatability from the combined PZT disks.
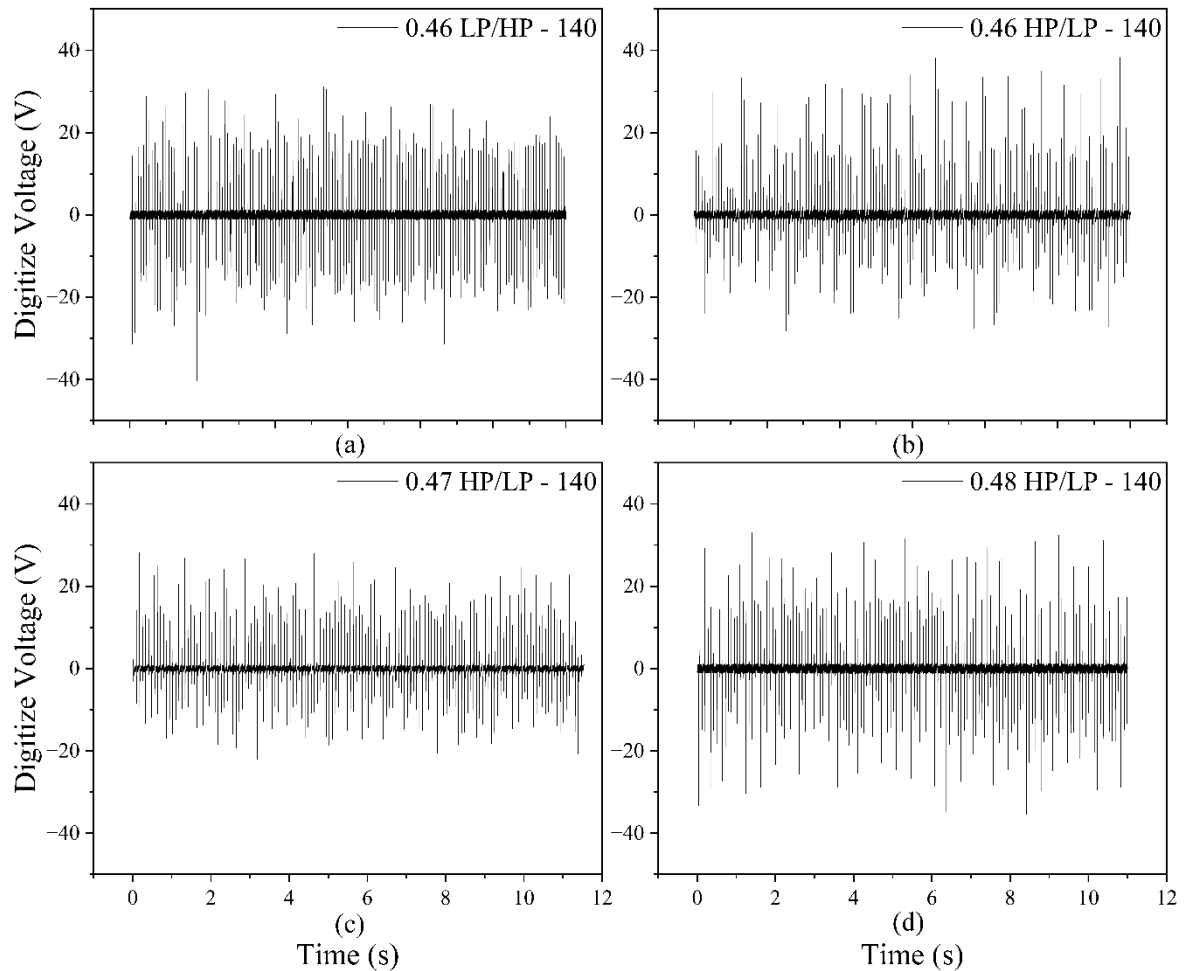
Figure 6-21 Digitize voltage curves obtained from the LP/HP and HP/LP PZT samples at ~14Hits/s. (a) 0.46 LP/HP,) 0.46 HP/LP, (c) 0.47 HP/LP, and (d) 0.48 HP/LP.

Table 6-6 shows V_{ave}, σ, and V_{max} from the absolute values of V at both frequencies.

Table 6-6 Average, standard deviation and maximum registered voltages from the PZT devices tested at 6 hits/s and 14 hits/s.

Frequency		6 hits/s			14 hits/s		
PZT Composition	Pellet ID	V_{ave} (V)	σ	$V_{max} \pm 0.005$ (V)	V_{ave} (V)	σ	$V_{max} \pm 0.005$ (V)
0.46 LP/LP	6-4	1.79	3.67	37.20	2.26	4.12	32.04
0.47 LP/LP	4-8	1.94	4.22	38.85	1.59	2.62	27.77
0.48 LP/LP	4-4	2.64	5.04	40.50	2.11	4.08	32.91
0.46 HP/HP	5-8	2.35	4.64	35.29	1.52	2.64	36.31
0.47 HP/HP	5-3	2.55	4.61	29.89	1.47	2.47	22.57
0.48 HP/HP	5-5	1.85	4.03	40.21	2.17	3.95	35.79
0.46 LP/HP	6-10	2.47	4.77	37.98	2.52	4.71	40.29
0.46 HP/LP	6-8	2.09	4.07	33.27	2.20	4.06	38.24
0.47 HP/LP	4-7	2.21	4.10	25.97	1.95	3.65	28.29
0.48 HP/LP	4-6	2.38	4.76	44.83	2.17	4.36	35.51

As expected from the observations made from the previous figures, Table 6-6 confirms a relatively small variation amongst the peak voltages at both frequencies, maintaining the measurements between ~23 and 45V, and between ~1.5 and 2.6V for the calculated mean values.

The absolute maximum voltages at 6 hits/s appear to correspond to samples with composition 0.48 (>40V), whilst at 14 hits/s, the 0.46 disks displayed the highest voltages from the majority of the groups, closely followed by composition 0.48. This is confirmed by the plots included in Figure 6-22 below.
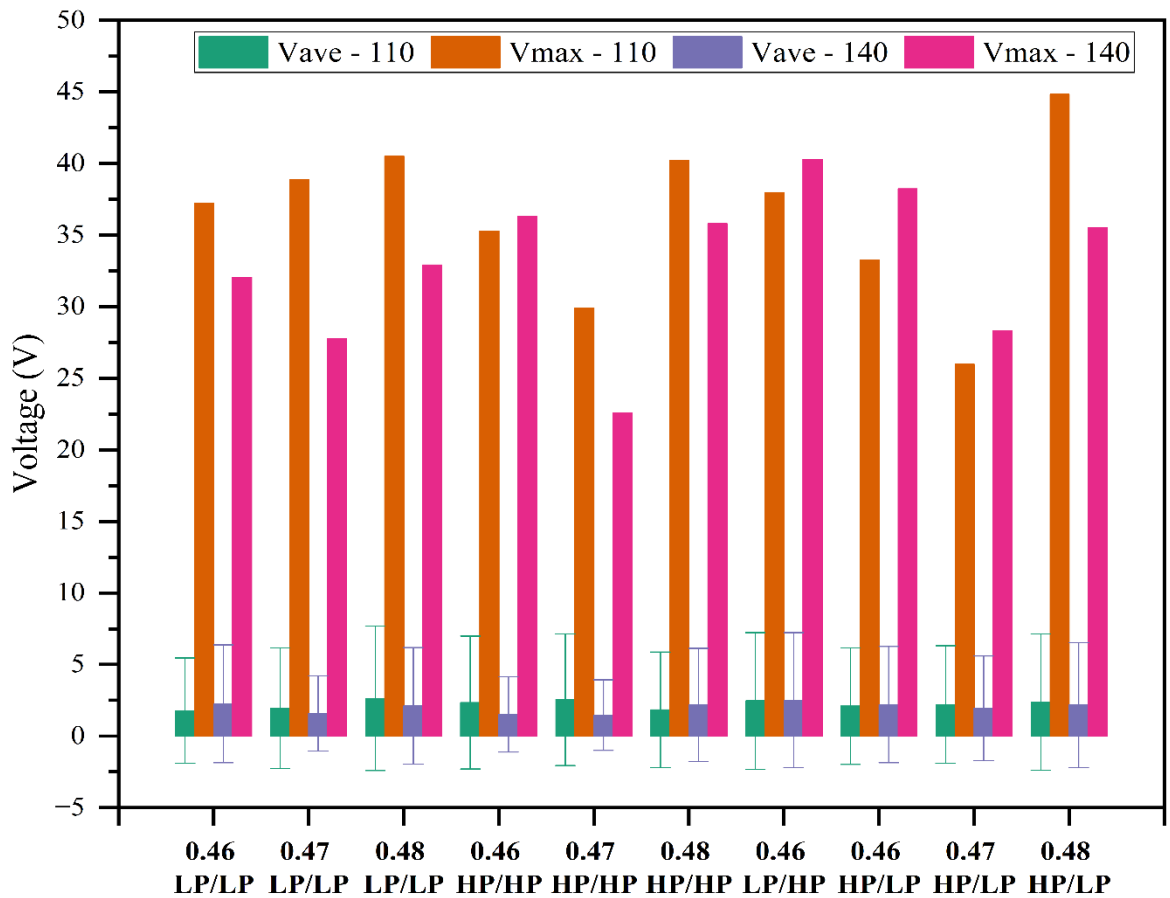
Figure 6-22 Mean (with standard deviation error bars) and maximum digitize voltage from the PZT samples tested at ~6 and 14Hits/s.

From the table and figure presented, it can be seen that the average values exhibited a more unpredictable behaviour, making a pattern harder to identify. At the lower frequency tests, the 0.46 and 0.47 LP/LP pellets seem to register the lowest voltages, along with the 0.48 HP/HP disk. On the contrary, the highest values were seen from the combined PZT samples, which was also consistent with the majority of the results obtained at the higher frequency, with the exception of the 0.47 HP/LP disk.

At 14 hits/s the HP/HP samples appear to have inverted the behaviour seen when testing the coupled pellets at 6 hits/s, with compositions 0.46 and 0.47 registering the lowest average voltages of the group, and the 0.48 HP/HP disk being amongst the top five mean voltages measured.

Moreover, sample 0.46 LP/HP consistently showed high values for both electrical parameters presented in this section of the thesis, at the two chosen impact frequencies, which was unexpected, as this composition had not displayed any particularly exceptional values throughout the functional characterisation discussed in Chapter 5, although its measured coupling factor k_p was amongst the top half of the group. Since this sample belongs to one of the sets made with combined purity, several of the tests included in this work were not performed on this composition due to time constraints and equipment availability. Therefore, to provide an accurate discussion of the contributing factors for the behaviour of this composition, the full set of tests would have to be completed on all the mixed purity arrangements, including the two compositions that were not prepared for this project.

Despite the current and voltage being the parameters measured from the samples during their performance testing as kinetic energy harvesters, these values are not predominantly significant on their own and are mainly intended to provide valuable information when used to calculate the corresponding output power and energy from each of the available PZT compositions, which is presented in the next section of this chapter.

6.5   Power and energy outputs and densities

From the measured I-V curves, the output voltages were taken to calculate the average and maximum power and energy outputs. This parameter was chosen as it showed a higher consistency throughout the measurements and similar values amongst the pellets. It is worth noting that since the voltages and currents were not measured simultaneously, the standard formula to calculate power (P = VI) could not be used; instead, the instantaneous output power was obtained by dividing the square of the measured voltages by the set load resistance that was connected in series with the device (P = V^2/R, where R = 10 MΩ). Additionally, since the formula already squares the voltages, it was not necessary to use the transformed values that were obtained from finding the absolute of each measurement. Either option would have rendered the same results. The OriginPro Software was employed to find the maximum values from the calculated output power, whilst the average power required a bit more processing.

It would be expected that P_{max} would show similar tendencies as the ones seen with the measured voltages, as this parameter would be directly proportional to the square of the measured V since the load resistance is kept constant throughout the tests. Nevertheless, since the average voltages were calculated using the full set of collected values, the resulting mean voltage from each PZT composition was a lot smaller than expected. This was due to the programme also taking the measurements between impacts into account for the statistical analysis. Although has little impact when analysing the individual parameters presented in the previous section, as these are not used directly to evaluate the performance of the samples, and the maximum values provide a good enough picture of the electrical responses from the studied specimens, this would be misleading if used for the derived electrical characterisation, involving the output powers and energies generated by the PZT samples.

To correct this, the instantaneous output power was plotted for each sample as a function of time and then integrated to find the total output energy generated during the testing intervals. The total output energy was then divided by the total interval time to find the average output power from each PZT disk. Finally, the values of the average and maximum output power, as well as the total energy, were divided by the sample's volume to provide a more accurate comparison of these parameters based on the individual dimensions.

The derived outputs and their densities (per unit volume) for the two chosen impact frequencies, ~6 and 14 hits/s, can be seen in Table 6-7 and Table 6-8, respectively.

Table 6-7 Maximum and average output power and power densities (per unit volume), as well as the output energy and energy density (per unit volume) calculated for the PZT samples at 6 hits/s.

PZT Composition	Pellet ID	P_{max} (μW)	P_{ave} (μW)	P_{max} Density (μW/cm^3)	P_{ave} Density (μW/cm^3)	Energy (μJ)	Energy Density (μJ/cm^3)
0.46 LP/LP	6-4	138.37	1.66	1503.44	18.09	19.99	217.22
0.47 LP/LP	4-8	150.93	2.16	1148.40	13.97	22.04	167.72
0.48 LP/LP	4-4	164.03	3.24	2215.17	43.71	38.87	525.00
0.46 HP/HP	5-8	124.53	2.70	1023.73	22.21	32.45	266.80
0.47 HP/HP	5-3	89.34	2.78	1339.33	41.61	27.78	416.44
0.48 HP/HP	5-5	161.67	1.97	1268.67	15.42	23.60	185.18
0.46 LP/HP	6-10	144.24	3.15	1225.75	26.79	34.70	294.86
0.46 HP/LP	6-8	110.68	1.92	713.43	12.38	23.05	148.54
0.47 HP/LP	4-7	67.46	2.17	429.86	13.82	26.04	165.93
0.48 HP/LP	4-6	201.01	2.83	1897.47	26.70	33.98	320.80

Table 6-8 Maximum and average output power and power densities (per unit volume), as well as the output energy and energy density (per unit volume) calculated for the PZT samples at 14 hits/s.

Composition	Pellet ID	P_{max} (μW)	P_{ave} (μW)	P_{max} Density (μW/cm^3)	P_{ave} Density (μW/cm^3)	Energy (μJ)	Energy Density (μJ/cm^3)
0.46 LP/LP	6-4	102.67	2.21	1115.54	23.99	24.31	264.08
0.47 LP/LP	4-8	77.12	0.95	586.78	7.20	11.37	86.48
0.48 LP/LP	4-4	108.28	2.11	1462.38	28.43	25.28	341.47
0.46 HP/HP	5-8	131.88	0.93	1084.14	7.63	11.15	91.65
0.47 HP/HP	5-3	50.96	0.83	764.00	12.43	9.96	149.31
0.48 HP/HP	5-5	128.10	2.03	1005.18	15.95	24.42	191.60
0.46 LP/HP	6-10	162.32	2.85	1379.47	24.24	34.23	290.90
0.46 HP/LP	6-8	146.21	2.13	942.44	13.73	25.59	164.95
0.47 HP/LP	4-7	80.06	1.71	510.11	11.45	19.76	125.93
0.48 HP/LP	4-6	126.11	2.37	1190.45	20.53	26.12	246.58

As anticipated from the measured voltages, the peak output power was found to be the highest amongst the disks with composition 0.48 at ~6 hits/s and amongst the disks with composition 0.46 at ~14 hits/s but closely followed by the 0.48 samples. This behaviour is consistent with composition 0.48 displaying some of the largest charge constants, d_{33} and d_{31}, and the lowest voltage constants, g_{33} and g_{31}. Moreover, the total generated energy appears to remain within 20 to 40μJ for all the PZT samples when tested at the lower impact frequency but decreases for the majority of the samples to between 10 to 34μJ when increasing the number of impacts per second, maintaining the same applied force on both tests.

However, when analysing the calculated values per unit volume (P_{max}/cm^3, P_{ave}/cm^3 and E/cm^3), it can be seen that the order of the pellets shift, and the highest values for the HP/HP are now spotted from the disk with composition 0.47 at 6 hits/s, while at the higher frequency, these parameters show that composition 0.48 registered the highest results from their arrangement groups.

With the exception of composition 0.47 LP/LP, the LP PZT samples consistently showed higher output powers and energies per unit volume than the HP PZT arrangement groups at both set frequencies, which would be consistent with the electromechanical coupling factors showing higher conversion efficiencies for the compositions that were made with this type of purity. This pattern can be visually confirmed from the density plots created for P_{ave}, P_{max} and E, which are included in Figure 6-23.
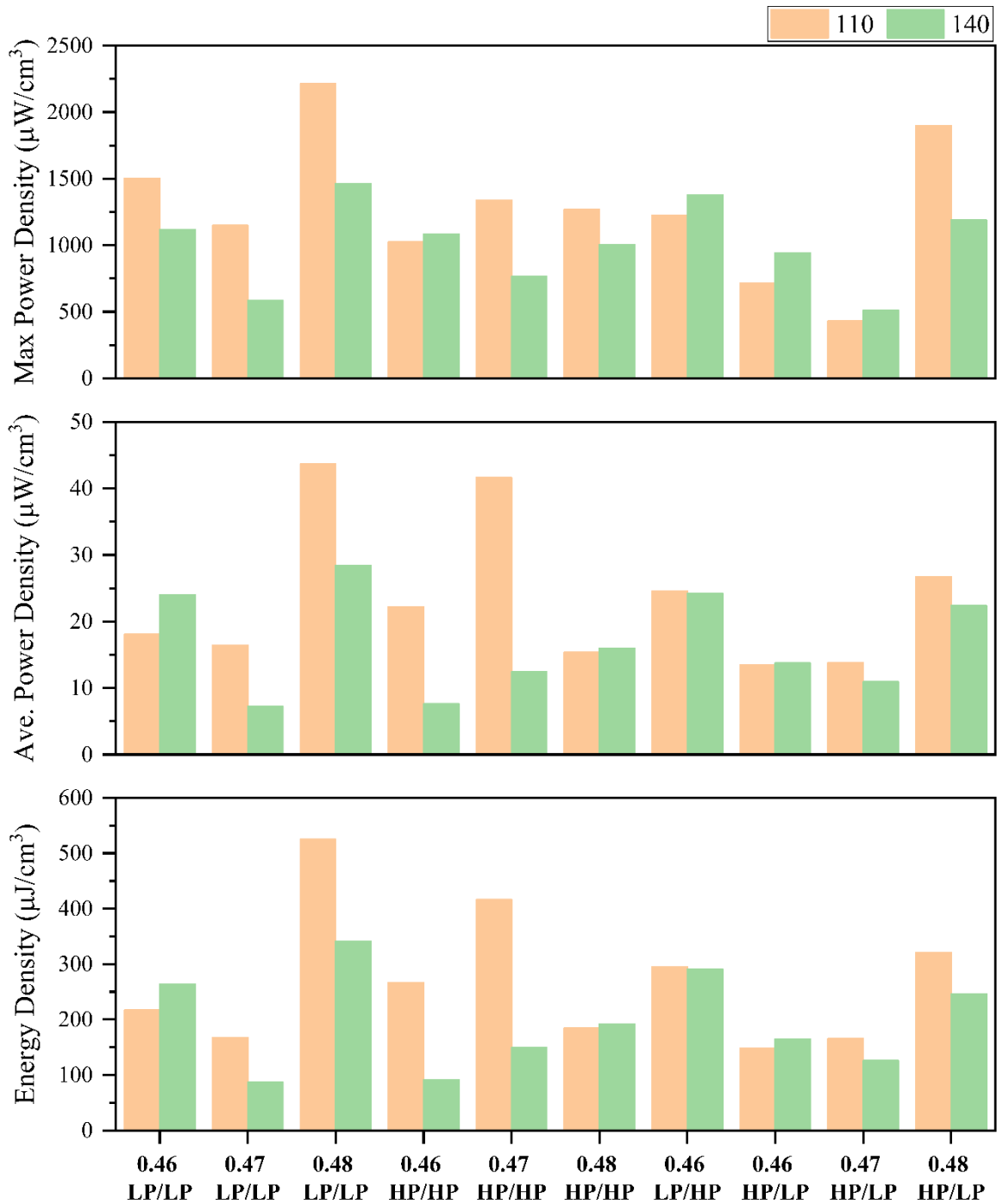
Figure 6-23 Max power density (top), average power density (middle) and energy density (bottom) calculated per unit volume of the PZT samples at ~6hits/s (110) and ~14hits/s (140).

Specifically, the tables and figure show that sample 0.48 LP/LP displayed the largest electrical output densities of the 10 analysed PZT samples, which provides a key piece of evidence that supports the observations made during the past two chapters. This disk was the specimen that showed the second largest k_p and k_{31} in section 5.5.3, with the highest piezoelectric charge coefficients from its group. Additionally, this sample had the lowest electrical impedance at resonance (Z_r), the largest permittivity (ε_r at 1kHz and T_R), the second lowest dielectric losses and the second highest mechanical quality factor (Q_m).

Moreover, the 0.48 LP/LP disk was shown to be in closest proximity to the estimated MPB presented in Figure 4-22 and to be one of the compositions showing an almost even split between the Ti and Zr measured in the samples through EDS. Finally, this composition showed the second most dense pellets when comparing the average values calculated for all the disks that were sintered for each arrangement group.

Surprisingly, the sample that had shown the highest k_p, which was the 0.47 HP/LP disk, had the lowest peak power density, and some of the lowest average power and energy densities of the entire group of pellets at both tested frequencies. Furthermore, the 0.47 LP/LP disk, which had displayed similar values on some of the parameters that were highlighted for the 0.48 LP/LP pellet in the previous paragraph, performed a lot more poorly than expected when compared to the other compositions in the same group.

In order to be able to compare against the reference values included in Table 2-2 presented as part of the literature review in Chapter 2, the maximum and average output power densities were calculated with respect to the surface area (mm^2). These values are presented in Table 6-9.

Table 6-9 Maximum and average output power densities (per unit area) calculated for the PZT samples at 6 and 14 hits/s.

Frequency		6 hits/s	14 hits/s	6 hits/s	14 hits/s
PZT Composition	Pellet ID	Max Power Density ($\mu W/cm^2$)		Average Power Density ($\mu W/cm^2$)	
0.46 LP/LP	6-4	80.43	59.68	0.97	1.28
0.47 LP/LP	4-8	68.90	35.21	0.98	0.43
0.48 LP/LP	4-4	112.09	74.00	2.21	1.44
0.46 HP/HP	5-8	51.19	54.21	1.11	0.38
0.47 HP/HP	5-3	50.89	29.03	1.58	0.47
0.48 HP/HP	5-5	65.34	51.77	0.79	0.82
0.46 LP/HP	6-10	83.84	94.36	1.83	1.66
0.46 HP/LP	6-8	47.09	62.20	0.82	0.91
0.47 HP/LP	4-7	28.37	33.67	0.91	0.72
0.48 HP/LP	4-6	148.00	92.86	2.08	1.75

From Table 2-2, it was indicated that the estimated harvested power from human and industrial vibration sources was around $4\mu W/cm^2$ and $100\mu W/cm^2$, respectively. Therefore, from the results seen in Table 6-9, it can be observed that the peak power densities from the 0.48 LP/LP and HP/LP disks at 6 hits/s surpass the values from industrial vibration.

On the other hand, the remaining pellets at 6 hits/s show values between 28% and 84% of the max reference harvested power. The largest values from each arrangement group are still coming from the samples with a composition of 0.48, followed by the specimens made originally with 46% TiO_2. This pattern is also seen at the higher impact frequency but with sample 0.46 LP/HP displaying the highest peak power per unit area, closely followed by the 0.48 HP/LP disk. In general, the values that were found for this parameter at 14 hits/s were lower than the ones seen at 6 hits/s, with three measurements located below $36\mu W/cm^2$ in comparison to the single value found at the lower frequency. Additionally, the slower impacts resulted in four devices generating output power densities over $80\mu W/cm^2$, whilst the faster compressions only had 2 samples registering values above this.

Regarding the average output powers, it can be observed that the calculated values are significantly smaller than the peak densities, oscillating between 0.8 and 2.2 $\mu W/cm^2$ for the 6 hits/s tests, and 0.4 to 1.8 $\mu W/cm^2$ at 14 hits/s. Despite this, the same compositions showed the highest values for the average densities, highlighting the potential benefits and overall improved performances from the disks that contain some of the LP chemicals.

As mentioned in section 5.1, some of the properties of a harvesting device will be affected by the dimensions of the piezoelectric element (Pollet, et al., 2019), which was noticed with the measured resonance frequencies, permittivities and acoustic impedances. In order to establish correlations between the performance and morphology, Table 6-10 lists the electrical parameters next to the samples' dimensions.

Table 6-10 Thickness, diameter, d/h ratio, surface area, and peak output power and energy at 6 and 14 hits/s, obtained from the ten PZT samples with a colour analysis (Red=Lowest, Green=Highest).

Frequency						6 hits/s	14 hits/s	6 hits/s	14 hits/s
PZT Composition	Pellet ID	h (mm)	d (mm)	d/h	A (mm²)	P_{max} (µW)	P_{max} (µW)	E (µJ)	E (µJ)
0.46 LP/LP	6-4	0.54	14.8	27.7	172.0	138.37	102.67	19.99	24.31
0.47 LP/LP	4-8	0.60	16.7	27.8	219.0	150.93	77.12	22.04	11.37
0.48 LP/LP	4-4	0.51	13.7	27.0	146.3	164.03	108.28	38.87	25.28
0.46 HP/HP	5-8	0.50	17.6	35.2	243.3	124.53	131.88	32.45	11.15
0.47 HP/HP	5-3	0.38	15.0	39.3	175.5	89.34	50.96	27.78	9.96
0.48 HP/HP	5-5	0.52	17.8	34.5	247.5	161.67	128.10	23.60	24.42
0.46 LP/HP	6-10	0.68	14.8	21.6	172.0	144.24	162.32	34.70	34.23
0.46 HP/LP	6-8	0.66	17.3	26.2	235.1	110.68	146.21	23.05	25.59
0.47 HP/LP	4-7	0.66	17.4	26.4	237.8	67.46	80.06	26.04	19.76
0.48 HP/LP	4-6	0.78	13.1	16.9	135.8	201.01	126.11	33.98	26.12

MIN ◄———► MAX

It can be seen from the colour analysis done on the data presented in Table 6-10 that the maximum output power and energy show an inverse proportion with the diameter and a direct relationship with the thickness of the disks in the majority of the PZT compositions. Since the densities of these parameters are calculated concerning the volume or surface area of the samples, it would also be expected that the power and energy densities would increase with the decrement of either or both dimensions. Additionally, when comparing samples with similar surface areas, the measured values seem to be larger for thicker pellets, suggesting that the conversion efficiencies become worse when the ratio between the diameter and the thickness is increased.

Although the colour analysis is done throughout the ten prepared PZT samples, it is important to compare the same compositions throughout the available arrangement groups. For example, composition 0.46 LP/HP and HP/LP have a similar thickness, but the diameter of the LP/HP sample is ~2.5mm smaller than the HP/LP disk, resulting in larger values for the peak power and energy measured at both impact frequencies. This is supported further by samples 0.48 LP/LP and HP/HP, which also presented a similar thickness but slightly different radius, where the smaller radius seen in the LP/LP disk appears to be linked to better electrical performance, except for the peak power at 14 hits/s.

The opposite is proven when comparing samples 0.46 LP/LP and 0.46 LP/HP, where the diameter is kept constant, but the mixed PZT disk was 0.14mm thicker than the LP/LP disk. In this case, the thicker specimen had a higher response as a piezoelectric energy harvester. This could be interpreted as the thickness being the most important parameter to try to maximize in order to improve the conversion efficiency seen in the samples.

These results provide an interesting perspective regarding the ideal proportion sought from the PZT disks, as it can be seen that the highest ratio between the dimensions corresponds to one of the samples with the lowest registered electrical responses, whilst some of the highest values were obtained from the sample with the lowest measured ratio.

It is worth noting that the electromechanical coupling factors found in Chapter 5 correspond to the material's response under resonance frequencies, therefore a much lower energy conversion would be expected when using frequencies that are significantly below the required values, which is what occurred in this instance and can be seen reflected in the low outputs registered by the PZT disks.

Nevertheless, the reason behind choosing such low frequencies for these experiments is that these were set to resemble some of the typical values seen in daily human movements, such as walking or running. The maximum frequency related to human movement is approximately 10Hz, with the average human gait oscillating between 4 and 6Hz (Khusainov, et al., 2013).

Generating power from daily human movement was one of the main applications that were thought for this research. Roadways, walkways, public transport, stairways, and private homes are some of the ideal places where piezoelectric devices could be implemented to harvest vibrations and generate electricity. The energy harvested from these sources could contribute to fulfilling some of the global energy demand, thus lowering the need for fossil fuels and consequently, the associated negative effects (APC International, Ltd, 2016).

According to BMC Public Health, based on data obtained from 2005, researchers found that the average body mass across the entire world population was ~62kg, although this number varies depending on the region and fails to differentiate between age and gender. In particular, the average human weight has been determined to be between 72.7 and 87kg for adult males, and between 62.5 and 74.4 for adult females (Walpole, et al., 2012). Therefore, the expected average forces that could be applied on the piezoelectric devices from human adults in these applications would be around 783.3N and 671.5N, respectively for men and women, typically bearing half of these values on each foot when standing.

However, when thinking about the potential of the studied PZT samples as kinetic energy harvesters, the force must be taken as the amount that would be exerted on the feet whilst moving, either walking or running, as the materials need to be compressed and decompressed in order to generate the potential difference across the disk. It has been found that during the heel rise stage of walking, the forces that go through the foot can be up to 3 times the person's weight, with running experiencing forces around 4 or 5 times the standing values, and up to 7 times this quantity, if sprinting (Greisberg, 2019).

Despite the number of steps recommended to be taken daily as part of a healthy lifestyle being ~10,000, the average adult in the USA has been found to walk only around 5,900 steps every day, with other countries experiencing more or less this amount depending on the area and culture (Tudor-Locke, et al., 2011). Although children are estimated to take between 12,000 and 16,000 daily steps, their lower average weight would result in a much smaller force applied on the harvesters when walking, thus resulting in much lower outputs.

Therefore, for this application, the ideal use would be amongst male and female adults, preferably with a moderate to high active lifestyle, which could potentially result in total applied forces between ~10.1MN, for an average woman walking around 5,900 steps every day, up to 23.5MN, for an average man taking 10,000 daily steps. These values would be significantly bigger when considering people who typically surpass the recommended values, and even more so if using high-performance runners or sprinters.

Even though these examples might seem like a great source of vibration, as the estimated forces significantly surpass the 40N used during the impact tests presented and discussed in this Chapter, as previously highlighted, it is important to consider the associated resonance frequencies for each device when thinking about potential applications, as these determine where the best efficiency could be achieved by the PZT harvesters and would reduce the losses experienced by the piezoelectric devices.

6.6   Cost analysis of the PZT samples

As part of the intended outcomes of this work, a comparison between the costs involved in the preparation of the various compositions of bulk undoped PZT is necessary to fully evaluate the benefits or advantages associated with the individual studied specimens, beyond their performance as energy harvesters.

Although it is expected that the use of lower purity chemicals involves some level of monetary savings since the parent oxides tend to be less expensive than the higher purity powders that are typically chosen for the fabrication of these samples, to fully appreciate the overall cost implications and variations amongst the ten chosen PZT compositions, the individual costs of the three required parent oxides, from year 2020 and 2023, have been included in Tables 6-11 and 6-12, below.

Specifically, the following two tables (Tables 6-11 and 6-12) display the cost of each chemical at three different grades of purity, which were labelled as "Max" for the highest purity found in the market, "HP" for the high purity powders that were used in this work, and "LP" for the lower purities that best matched the chemical grades that were employed for the preparation of the studied PZT samples. Beyond the prices for each parent oxide and the specific purity percentage, these two tables include the corresponding quantities for the listed prices, as well as the proportion of the costs per gram of each chemical, followed by the last row containing the associated brand or supplier.

Table 6-11 Cost in pound sterling (£) and physical specifications of the three parent oxides required to prepare PZT ceramics in 2020, at maximum, high and lower chemical purities.

Parent Oxide	PbO			TiO$_2$			ZrO$_2$		
Purity	Max	HP	LP	Max	HP	LP	Max	HP	LP
Purity (%)	99.999	99.9	99	99.995	99.98	97	99.99	99.8	99
Quantity (g)	50	100	2500	25	25	2000	10	100	500
Price (£)	222	53.2	54.6	280.8	109.3	6.4	105.5	96.4	102.9
Price/gram (£/g)	4.440	0.532	0.022	11.230	4.370	0.003	10.550	0.960	0.206
Brand	Sigma-Aldrich	Jalmek		Sigma-Aldrich	DuPont		Sigma-Aldrich	New Met	Sigma-Aldrich

Table 6-12 Cost in pound sterling (£) and physical specifications of the three parent oxides required to prepare PZT ceramics in 2023, at maximum, high and lower chemical purities.

Parent Oxide	PbO			TiO$_2$			ZrO$_2$		
Purity	Max	HP	LP	Max	HP	LP	Max	HP	LP
Purity (%)	99.999	99.9	99	99.995	99.98	99	99.99	99.6	99
Quantity (g)	50	100	2500	25	25	1000	10	500	500
Price (£)	243	24.4	71.3	308	120	4.55	116	226	112
Price/gram (£/g)	4.860	0.244	0.029	12.320	4.800	0.005	11.600	0.452	0.674
Brand	Sigma-Aldrich	Jalmek		Sigma-Aldrich	DuPont		Sigma-Aldrich		

It is observed that in the two chosen years, the quantities in which the chemicals can be bought increase as the purity decreases, making it even cheaper to buy bulk quantities of these powders, which does not seem to be an option when looking at the higher purity components.

Additionally, for the chemicals that were found from the same supplier and in the same presentation, the expected price increase can be seen between the values found in 2023 and 2020. Even though the cost per gram variations can also be observed throughout the data presented in these tables, Table 6-13 was created to facilitate a more direct comparison between the ratios found amongst the cost/g of the Max, HP, and LP chemicals.

Table 6-13 Price per gram ratios of the three parent oxides required to prepare PZT ceramics calculated from the data collected in 2020 and 2023.

	2020			2023		
	Ratio (Max/HP)	Ratio (HP/LP)	Ratio (Max/LP)	Ratio (Max/HP)	Ratio (HP/LP)	Ratio (Max/LP)
PbO	8.34	24.36	203.19	19.92	8.56	170.41
TiO$_2$	2.57	1360.72	3495.15	2.57	1054.95	2707.69
ZrO$_2$	10.94	4.69	51.28	25.66	2.02	51.79

Table 6-13 shows that for all the required powders in both years, decreasing the purity percentage by <3%, can reduce the prices per gram of the chemical by at least 38%. It is important to notice that these values are considering the worst-case scenario, taking the largest purity difference and the smallest ratio found between the £/g calculated for each type of chemical purity. The savings seem to increase significantly between the HP and LP TiO_2, which would be consistent with this chemical being the one that has the largest purity difference.

For a deeper understanding of how these variations would affect the total fabrication costs for mass-produced PZT disks, the data collected from 2020 was used to find the values for the total costs involved in the preparation of 1 single disk from each of the chosen compositions, which included the total costs per disk of PZT plus the costs derived from the corresponding PZ compensation pellet. The values from 2020 were chosen as these were the ones closer to the starting data and that most accurately reflected the specifications of the chemicals used in this work.

Using the quantities provided in section 3.1 and Table 6-11, the total costs were calculated for the 15g of PZT that were planned for each arrangement group by multiplying the necessary amount of each chemical by its cost/gram and adding them to the total found for 7.5g of the corresponding PZ. These values were then transformed to find the total cost per gram of PZT, already considering the necessary PZ. Following this, the average densities presented in Table 4-6 were employed to find the total mass that would result from preparing PZT disks with a 20mm diameter and 1mm thickness, which would abide by the ideal ratio mentioned in the lapping discussion presented in section 5.1 of Chapter 5 (h < d/16). Finally, these values were multiplied by the cost per gram mentioned in the previous paragraph to find the cost per PZT disk of each composition that was studied in this work.

The results showed that, on average, one disk of LP/LP PZT would cost ~£0.24 ± 0.003 for any of the three compositions, ~£2.93 ± 0.007 for any of the HP/HP, ~£2.26 ± 0.13 for any of the HP/LP, and ~£0.88 for the 0.46 LP/HP. Therefore, this clearly shows that the samples made with an LP/LP arrangement would be the most inexpensive, followed by the LP/HP sample. Whilst both arrangements containing HP PZT would be the most expensive, presenting similar costs, the HP/LP appears to be ~67 pence cheaper per disk than the HP/HP PZT. The ratios of these values are presented in Table 6-14, where the data was calculated as the price per disk of the arrangement at the top of each column divided by the arrangement on the far left of each row.

Table 6-14 Price per disk ratios between the four sintering arrangements that were used for the preparation of the PZT samples in this work.

	HP/HP	HP/LP	LP/HP
LP/LP	12.45	9.59	3.72
LP/HP	3.35	2.58	1.00
HP/LP	1.30	1.00	0.39

As anticipated, the largest financial savings are seen when comparing the HP/HP and LP/LP samples, but it is worth noting that even when simply changing the purity of the chemicals in the PZ atmosphere disk for the HP PZT, the cost per sample would decrease by approximately 23%. Additionally, if looking to take advantage of some of the piezoelectric properties displayed by the HP chemicals but with the benefits seen from the LP powders, it was found that the LP/HP would be 3.35 times cheaper than the HP/HP and 2.58 times cheaper than the HP/LP composition. Finally, the LP/LP mixes appear to be 73% less costly than the LP/HP, 90% less than the HP/LP, and over 91% less than the HP/HP.

6.7 Chapter 6 Summary

The efficiency and performance of the ten PZT disks were tested by using a modified sewing machine to perform controlled impact tests, where the pellets were hit by a constant weight of 40N at two different speeds (~6 and 14 hits/s). The output voltage and current were measured and used to calculate the corresponding average and peak values for the output power and energy, as well as the respective densities of these parameters in relation to the surface area and volume corresponding to each PZT sample. From the measured values, the peak output power was found to be the highest amongst the disks with composition 0.48 at 6 hits/s and composition 0.46 at ~14 hits/s but closely followed by the 0.48 samples. This would be consistent with composition 0.48 displaying some of the largest piezoelectric charge constants, d_{33} and d_{31}, and the lowest voltage constants, g_{33} and g_{31}.

Although it might have been thought that the HP chemicals would result in higher quality PZT ceramics and therefore, better harvesting devices, properties like the lower relative dielectric permittivities and densities, have been linked to lead vacancies created by the previously discussed PbO volatilisation that can occur during sintering if left untreated. This would indicate that the HP PZT disks might have experienced slightly higher PbO losses, which was suggested through the microstructure analysis carried out in section 4.2, with some of the negative effects seen in the lower performances registered through the impact tests done after the devices were coupled for energy harvesting.

When analysing the calculated values per unit volume (P_{max}/cm^3, P_{ave}/cm^3 and E/cm^3), the LP PZT samples, with the exception of composition 0.47 LP/LP, consistently showed higher values than their HP counterparts at both impact frequencies, which would be expected from the higher conversion efficiencies that were seen from these arrangement groups during their FOM analysis. Nonetheless, the majority of the samples registered values for the measured characteristics that stayed within the same order of magnitude.

In particular, sample 0.48 LP/LP displayed the largest electrical output densities of the 10 analysed PZT disks, with 1462.4μW/cm^3 for peak power per unit volume, 28.4μW/cm^3 for average power per unit volume, and 341.5μJ/cm^3 for energy per unit volume, consolidating the observations made in the two previous chapters. Additionally, this specimen showed the second largest efficiencies, the highest piezoelectric charge coefficients from its group, the lowest resonance impedance, and the second highest mechanical quality factor, it also appeared as one of the compositions nearest to the MPB from its XRD pattern and showed an almost even Ti/Zr split through the EDS measurements.

Although this composition did not show the smallest grain size, it would be necessary to do another attempt at the analysis in the future, following the identical preparation conditions as the ones followed by the 0.46 LP/LP and HP PZT pellets, as this seems to have been the determining factor to achieve smaller grain sizes and therefore, a higher number of crystals per area of the ceramic.

Furthermore, the maximum output power and energy measured from the PZT samples showed an inverse proportion with the diameter and a direct relationship with the thickness of the disks in the majority of the PZT compositions, suggesting that the conversion efficiencies become worse when the ratio between the diameter and the thickness is increased, thus indicating that particular attention has to be given when choosing the ideal proportion sought between the dimensions of the PZT disks.

It is worth noting that the significantly smaller measured outputs do not reflect the electromechanical coupling factors that were found for each composition. This is because the measured coupling factors represent the efficiencies at resonance, and these were not achieved during the impact tests as these were meant to resemble values closer to those found in daily human movement (~4 to 6Hz) since this is one of the potential intended applications that were thought for the prepared PZT disks when coupled as piezoelectric energy harvesters.

Since the measured resonance frequencies for the PZT pellets range in the hundreds of kHz, they would be significantly higher than the maximum frequency related to human movement (~10Hz), and in particular, than the 4 to 6Hz estimated from the average human gait. Although these high frequencies would most likely be found only in industrial settings, generated by machines, they could be achieved by using cantilever-type systems, where the lower frequencies from human movement could be amplified until reaching the required values. Nevertheless, this process would inevitably compromise the size and simplicity of the original design described for piezoelectric harvesters.

After observing the electric performance of the ten PZT samples when coupled as energy harvesters, a cost analysis was completed by comparing the cost, in pounds sterling, per gram of each parent oxide involved in the preparation of the bulk PZT, at three different grades of purity and from two separate years, 2020 and 2023. This was done so the variations in prices could be easily appreciated when the chemical purities change by even relatively small percentages, as well as illustrating how the costs have changed throughout the last few years. In addition to this, the cost per disk of each type of PZT composition was included, using the values obtained from 2020 and considering the costs of the associated PZ atmosphere disk. Using these results, the ratios between the chosen PZT arrangements were calculated to estimate the potential economic advantages involved.

Although it was expected that the largest financial savings would be seen between the HP/HP and LP/LP samples, a 23% decrement was calculated when replacing the HP PZ pellet for an LP disk during the second stage of the ceramic process. Additionally, it was found that the LP/HP composition would be 3.35 times cheaper than the HP/HP and 2.58 times cheaper than the HP/LP composition, thus offering greater reductions in the preparation costs, whilst offering some of the advantages seen from the LP specimens combined with a few of the benefits displayed by the HP chemicals.

Finally, the most significant comparison is seen when noticing that the LP/LP mixes appeared to be 73% cheaper than the LP/HP compositions and around 90% less expensive than the samples containing HP PZT. These values would represent prominent economic advantages when considering the possibility of producing these devices in bulk for commercial purposes and when looking the create the most affordable product for the market.

For example, considering that the average contact area of an adult foot is ~81.8cm^2 (Birtane & Tuna, 2004), creating a network of multiple disks to cover that surface would require about 26 samples (with a 20mm diameter), or 52 for a pair of shoes for one person. This would mean that on materials alone, fabricating 52 HP/HP disks would cost ~£152.58, whilst the LP/LP samples would only be ~£11.98, making a significant impact on the affordability of this material and therefore, its viability as a commercial product when considering possible uses as personal kinetic energy harvesters.

Chapter 7.   CONCLUSIONS AND FUTURE WORK

In summary, ten different sets of piezoelectric ceramic disks were successfully sintered using three different chemical compositions of pure (undoped) $PbZr_{1-x}Ti_xO_3$, commonly known as PZT, with x fixed as 0.46, 0.47 and 0.48, and prepared near the estimated morphotropic phase boundary (MPB), where the best piezoelectric properties are said to be exhibited by the materials. Additionally, two different grades of purity were used for the parent oxides required to prepare the bulk piezoelectric samples, as well as the non-stoichiometric lead zirconate (PZ) disks that were used to aid in the compensation of the PbO losses typically experienced by these materials at the high temperatures (>888°C) used during the second stage of the conventional ceramic process that was followed in this work.

Six of the sets belong to the pellets made with the same grade of purity for the parent oxides and the PZ compensation, one for each of the three chosen chemical compositions and the two grades of purity available, whilst the other four sets correspond to the samples made with the opposite grade of purity for the PZ disk, with three sets belonging to each of the HP PZT compositions with LP PZ compensation, and the last set coming from composition 0.46 LP PZT made with HP PZ, due to time constraints.

The following sections include the final conclusions from the work presented in this thesis, followed by the recommendations and future areas of study for this project, and final thoughts.

7.1   Conclusions

The overall work in this thesis focused on the preparation, processing, and characterisation of the ten different PZT compositions that were chosen based on their purity and chemical composition. The intended outcome was not only to identify and understand the differences encountered in their physical and functional properties when modifying the purity of the involved starting powder oxides and the TiO_2 content of the sample, but also to highlight and discuss potential areas of improvement during the preparation of these materials, like the sample arrangement and the morphology of the PZ compensation used during the sintering stage of the process followed in this thesis.

Furthermore, it was observed that although correlations could be established between the studied characteristics and the individual compositions and starting oxide purities, the

differences in the parameters employed during the ball milling processes performed as part of the two-stage ceramic method should also be considered as an alternative influencing factor, as the adjustments could be responsible for some of the results obtained from the physical and functional characterisation of the materials.

The focus of the work also extended to include an analysis of the effects in the fabrication costs and the monetary implications derived from the specific parameters followed during the sample preparation. Despite not being explored further in this work, this would be of particular interest when looking at mass production of these specimens for commercial use and their potential affordability amongst the general public.

Contrastingly, as mentioned in the summary of Chapter 3, the mixed purity arrangements showed some interesting results. In this case, sample 0.47 HP/LP showed that the combination of an HP PZT with an LP PZ atmosphere not only resulted in one of the highest values of d_{33} but also showed the best efficiency of all the prepared samples. This temporarily indicated some promising behaviour from this composition, which although would provide an economical advantage over the HP/HP disk, displayed some of the lowest performances when coupled as an energy harvester.

Finally, it was concluded that although the LP PZT compositions exhibited an overall advantage over the HP disks, not only through their physical and functional characteristics but also with the associated major reductions in related costs, the observed values of the electromechanical coupling factors amongst all the ten PZT specimens coupled with the relatively low mechanical quality factors, high relative dielectric permittivities, and low dielectric losses, suggest that if needed, any of the prepared PZT compositions would be suitable for applications as ultrasonic transducers or any other system where high sensitivity is important.

7.2 Recommendations and areas of future study

Although this research attempted to provide alternative and innovative ways to reduce the production costs of bulk PZT ceramics intended for kinetic energy harvesting purposes, such as the combination of chemical purities and an intercalated arrangement between the PZT samples and the PZ compensation atmosphere disks, some limitations were encountered due to time constraints and equipment availability.

These limitations, which should be investigated as part of future work, include the lack of any samples from compositions 0.47 and 0.48 from the LP/HP group, as well as the preparation of more samples from the HP/LP sets to match the number of disks obtained from the other arrangements. Maintaining a consistent number of samples would not only provide more opportunities to complete diverse analyses of the compositions but would also provide a more accurate range to compare their characteristics, behaviours and performances.

Since some of the best parameters were measured from the 0.48 LP/LP disk, suggesting this composition was located closer to the estimated MPB for this purity arrangement, it would also be recommended to explore the response that could be obtained from a 0.49 LP/LP sample, as this could exhibit even better results or confirm that the optimal composition might be located around the 0.48 concentration when using LP chemicals as the starting powders.

Regarding the conventional sintering process that was followed in this work, it was concluded that for future experiments, the smaller agate balls would be the best option to achieve a smaller particle size in the mix and thus, a higher crystal density in the microstructure of the ceramics, potentially enhancing their piezoelectric properties and overall performance.

It was also concluded that if using the intercalated arrangement during the second stage of the conventional ceramic process, instead of making the same number of disks out of the PZ powders, an additional pellet should be made to place at the top of the arrangement so the PbO is also contained as best as possible on this surface, thus preventing any physical deformation from the PZT disk located at the top.

Additionally, further experimentation would be required to test how well changing the composition and purity of the PZ compensation disk could improve the density and performance of the PZT samples, including the possibility of using a non-stoichiometric PZT or PT disk as PbO compensation.

Furthermore, for future experiments it would be recommended to prepare the ceramic disks using the alternative method where a single cylinder is pressed for both stages of the ceramic process, thus only requiring superficial lapping to remove the outer layers of the ceramic before cutting it into the required number of thin disks that fulfils the ideal

proportion between their dimensions. This would reduce the total amount of time required to process and prepare the samples before coupling them as energy harvesters, as well as maintaining the samples' dimensions a lot more consistent throughout the sintered sets.

Although it was considered and briefly described in section 2.94.1, the Archimedes method should be employed in future iterations to calculate the density of the samples in addition to the theoretical value calculated from the dimensions and weight of each disk. The comparison of these two parameters would relevant insights regarding the porosity of the ceramics.

Regarding the composition analysis conducted on the PZT disks, due to EDS analysis being confined to only a small portion of the sample's surface rather than the entire resulting disk, the XRD patterns were found to be more reliable when analysing the collected data and deriving any corresponding conclusions from it. To improve this, it would be suggested that for future iterations of this work, an increased number of areas is studied, and an entire pellet is left unprocessed for the EDS analysis.

Considering the recommendations made concerning the number of samples per composition and the variety of arrangements to be tested, it is advised that the analyses that were not able to be conducted for all the involved PZT disks in this work, such as the SEM and dielectric analyses, be repeated in order to obtain the full spectrum of the data.

Moreover, when tested near the estimated human walking frequencies (~6 Hz), the studied PZT disks were found to generate micro amounts of energy and power (µJ and µW). Hence, if looking to use the PZT disks as generators to power small electronic devices (<50W), such as mobile phones, tablets, or cameras, without using frequency amplifiers, it would be necessary to combine the outputs from multiple disks, as suggested at the end of the cost analysis, when calculating the total costs involved in covering a pair of shoe insoles.

Finally, as seen in section 6.4, the instantaneous electrical response from the chosen PZT materials, generates alternating voltages and currents, thus requiring a rectifying component to transform the AC measurements into DC values, which would then need to be regulated through DC/DC conversion for the specific intended use. The circuit for this can be rather simple, requiring only a rectifier, a capacitor, and an LED to discharge the circuit, which conforms with the elements of a piezoelectric energy harvesting system.

Although this system was created and tested for several commercially available piezoelectric devices prior to this work, it was not implemented to rectify the outputs of prepared PZT in this research, and therefore, would be left to be completed in future studies.

Based on some of the limitations that have been typically found to be associated with piezoelectric ceramics, further tests are recommended to explore new paths involving the creation of hybrid nanogenerators, such as PVDF-PZT systems or composites that can combine the piezoelectric contributions along with potential triboelectric generation from porous polymers or doped materials. Despite PVDF being considered as a material that has low and thermally unstable piezoelectric properties, its low mechanical impedance, flexibility, and toughness, make it a suitable candidate to combine with PZT to overcome each other's shortcomings.

Although some of these ideas have been briefly researched through subsequent collaborations with fellow researchers, their results go beyond the scope of this thesis and would require a dedicated set of tests and analyses to fully explore their potential and capabilities. Nevertheless, even when not discussed further or included in this work, these experiments exemplify some of the promising paths where this research could be taken and provide the foundation for future work that would enable the continuous exploration of the potential of these materials as sustainable energy harvesters.

7.3   Final thoughts

In general, kinetic energy harvesting using piezoelectric materials has been the focus of many researchers and industries alike due to the relative simplicity of implementing these systems, as well as of the elements involved, especially as these combine the energy conversion, storage and load-bearing components in a single device. These materials are becoming more and more innovative each day, and so are their potential applications. Amongst these, piezoelectric materials have been used in car and bike tires to harvest power that could be used to run onboard devices or to recharge electric vehicles (Anil & Sreekanth, 2014). To improve this type of application, the researchers at Siemens Corporate Technology in Munich are using fluid-structure interaction simulation to ensure the cost-effective optimization of a cantilever in a MEMS generator designed to power a tire pressure monitoring system driven by motion (Hand, 2012).

New methods are being developed to improve piezoelectric characteristics and their range of applications, such as integrating highly efficient energy conversion materials onto stretchable, biocompatible rubbers that could yield breakthroughs in implantable or wearable energy harvesting systems (Qi, et al., 2010); or creating a variety of novel hybrid energy harvesters that integrate piezoelectric and electromagnetic energy harvesting mechanisms, containing a piezoelectric cantilever of multilayer PZT transducer ceramics, permanent magnets, and coils (Yang, et al., 2010; Yu, et al., 2014).

An additional alternative worth pursuing in future iterations of this work would be to investigate the effects of doping piezoelectric materials to improve their physical and chemical properties, as shown in the work presented by (Benam, 2013). Although this area of research has been identified and exploited by several authors and industries throughout the years, with proven advantages over the undoped bulk PZT ceramics, these have not been explored in this dissertation.

Realistically, due to their small outputs, a large-scale application would be challenging, not only because the final dimensions of the system would most likely become impractical but also because the associated costs would proportionally amplify when scaling up the technology to meet the required values. Consequently, the most feasible applications for solid-state multilayer piezoelectric harvesters would be as wireless sensors, controls, or lights, leaving powering any high-consumption electronics still far in the future (APC International, Ltd, 2016).

Nevertheless, the contribution of piezoelectric harvesters should not be dismissed, as although their performance as generators might not be nearly enough to become an entirely new source on their own, they should be taken as one of many potential systems providing small incremental energy savings. Every application that can be powered by a PZT harvester, equates to one less system drawing power from the main source, leading to a reduction in the consumption of fossil fuels when attempting to tackle the current global energy crisis and its inevitable repercussions to the environment and thus, humanity.

APPENDICES

Appendix A.   Sections 1, 2 & 8.2 of Lead (II) Oxide Safety Data Sheet

SAFETY DATA SHEET

Version 6.3
Revision Date 01/10/2020
Print Date 01/27/2020

SECTION 1: Identification of the substance/mixture and of the company/undertaking

1.1   Product identifiers

Product name   : Lead(II) oxide

Product Number   : 203610
Brand   : Aldrich
Index-No.   : 082-001-00-6
CAS-No.   : 1317-36-8

1.2   Relevant identified uses of the substance or mixture and uses advised against

Identified uses   : Laboratory chemicals, Synthesis of substances

1.3   Details of the supplier of the safety data sheet

Company   : Sigma-Aldrich Inc.
                          3050 Spruce Street
                          ST. LOUIS MO 63103
                          UNITED STATES

Telephone   : +1 314 771-5765
Fax   : +1 800 325-5052

1.4   Emergency telephone number

Emergency Phone #   : +1-703-527-3887

SECTION 2: Hazards identification

2.1   Classification of the substance or mixture

GHS Classification in accordance with 29 CFR 1910 (OSHA HCS)

Acute toxicity, Oral (Category 4), H302
Acute toxicity, Inhalation (Category 4), H332
Carcinogenicity, Oral (Category 2), H351
Reproductive toxicity (Category 1A), H360
Effects on or via lactation, H362
Specific target organ toxicity - repeated exposure, Oral (Category 1), Central nervous system, Kidney, Blood, H372
Specific target organ toxicity - repeated exposure, Inhalation (Category 1), Kidney, Central nervous system, Blood, H372
Short-term (acute) aquatic hazard (Category 1), H400
Long-term (chronic) aquatic hazard (Category 1), H410

For the full text of the H-Statements mentioned in this Section, see Section 16.

2.2   GHS Label elements, including precautionary statements

Pictogram

Signal word   Danger

Hazard statement(s)

H302 + H332	Harmful if swallowed or if inhaled.
H351	Suspected of causing cancer if swallowed.
H360	May damage fertility or the unborn child.
H362	May cause harm to breast-fed children.
H372	Causes damage to organs (Central nervous system, Kidney, Blood) through prolonged or repeated exposure if swallowed.
H372	Causes damage to organs (Kidney, Central nervous system, Blood) through prolonged or repeated exposure if inhaled.
H410	Very toxic to aquatic life with long lasting effects.

Precautionary statement(s)

P201	Obtain special instructions before use.
P202	Do not handle until all safety precautions have been read and understood.
P260	Do not breathe dust/ fume/ gas/ mist/ vapours/ spray.
P263	Avoid contact during pregnancy/ while nursing.
P264	Wash skin thoroughly after handling.
P270	Do not eat, drink or smoke when using this product.
P271	Use only outdoors or in a well-ventilated area.
P273	Avoid release to the environment.
P280	Wear protective gloves/ protective clothing/ eye protection/ face protection.
P301 + P312 + P330	IF SWALLOWED: Call a POISON CENTER/doctor if you feel unwell. Rinse mouth.
P304 + P340 + P312	IF INHALED: Remove person to fresh air and keep comfortable for breathing. Call a POISON CENTER/doctor if you feel unwell.
P308 + P313	IF exposed or concerned: Get medical advice/ attention.
P391	Collect spillage.
P405	Store locked up.
P501	Dispose of contents/ container to an approved waste disposal plant.

2.3 Hazards not otherwise classified (HNOC) or not covered by GHS - none

---

SECTION 8: Exposure controls/personal protection

8.2 Exposure controls

Appropriate engineering controls
Handle in accordance with good industrial hygiene and safety practice. Wash hands before breaks and at the end of workday.

Personal protective equipment

Eye/face protection
Face shield and safety glasses Use equipment for eye protection tested and approved under appropriate government standards such as NIOSH (US) or EN 166(EU).

Skin protection
Handle with gloves. Gloves must be inspected prior to use. Use proper glove removal technique (without touching glove's outer surface) to avoid skin contact with this product. Dispose of contaminated gloves after use in accordance with applicable laws and good laboratory practices. Wash and dry hands.

Full contact
Material: Nitrile rubber
Minimum layer thickness: 0.11 mm
Break through time: 480 min
Material tested:Dermatril® (KCL 740 / Aldrich Z677272, Size M)

Appendix B. Mass, diameter, thickness, and volume of each sintered PZT samples, along with their absolute errors.

x	PZT Purity	PZ Purity	Pellet Identifier	Mass (g) (± 0.00005)	Diameter (mm) (± 0.005)	Thickness (mm) (± 0.005)	Volume (mm³) (± 1.61)
0.46	LP	LP	6-11	1.9685	17.43	1.27	303.03
			6-12	1.9542	17.36	1.15	272.20
			6-4	1.9512	17.33	1.12	264.18
0.47			4-8	2.6927	17.17	1.61	372.78
			4-9	2.8916	17.21	1.86	432.68
			4-10	2.7319	17.14	1.63	376.10
			4-11	2.6606	17.26	1.57	368.04
			4-12	2.7487	16.99	1.66	376.34
0.48			4-1	2.7968	17.10	1.72	395.01
			4-2	2.4189	17.48	1.43	343.17
			4-3	2.8384	17.23	1.65	384.72
			4-4	2.9230	17.20	1.74	404.29
0.46	HP	HP	5-7	2.8278	17.57	1.78	431.57
			5-8	2.8265	17.67	1.83	448.76
			5-9	2.8068	17.61	1.80	438.41
			6-6	1.8894	17.50	1.14	274.20
0.47			5-1	2.7109	17.78	1.60	397.26
			5-2	2.7430	17.65	1.66	406.15
			5-3	2.7126	17.78	1.62	402.22
			6-1	2.7103	17.58	1.73	419.93
0.48			5-4	2.8152	17.77	1.72	426.57
			5-5	2.8248	17.78	1.82	451.88
			5-6	2.8355	17.71	1.71	421.23
			6-3	1.8998	17.40	1.22	290.10
0.46	HP	LP	6-7	1.8779	17.50	1.10	264.58
			6-8	1.8772	17.57	1.13	273.98
0.47			4-7	2.6996	17.45	1.87	447.22
0.48			4-5	1.8748	17.64	1.14	278.61
			4-6	1.8879	17.69	1.24	304.77
0.46	LP	HP	6-9	1.9176	17.46	1.22	292.10
			6-10	1.9415	17.46	1.16	277.74

Appendix C.   Absolute and relative errors associated to the volume and density of each sintered PZT disk.

x	PZT Purity	PZ Purity	Pellet identifier	ΔV (mm³)	Relative Error $\Delta V/V$	$\Delta \rho$ (g/cm³)	Relative Error $\Delta \rho/\rho$
0.46	LP	LP	6-11	1.54	0.005	0.03	0.005
			6-12	1.50	0.005	0.04	0.006
			6-4	1.48	0.006	0.04	0.006
0.47			4-8	1.59	0.004	0.03	0.004
			4-9	1.67	0.004	0.03	0.004
			4-10	1.59	0.004	0.03	0.004
			4-11	1.60	0.004	0.03	0.004
			4-12	1.58	0.004	0.03	0.004
0.48			4-1	1.61	0.004	0.03	0.004
			4-2	1.59	0.005	0.03	0.005
			4-3	1.61	0.004	0.03	0.004
			4-4	1.63	0.004	0.03	0.004
0.46	HP	HP	5-7	1.70	0.004	0.03	0.004
			5-8	1.73	0.004	0.02	0.004
			5-9	1.72	0.004	0.03	0.004
			6-6	1.52	0.006	0.04	0.006
0.47			5-1	1.69	0.004	0.03	0.004
			5-2	1.68	0.004	0.03	0.004
			5-3	1.69	0.004	0.03	0.004
			6-1	1.69	0.004	0.03	0.004
0.48			5-4	1.72	0.004	0.03	0.004
			5-5	1.75	0.004	0.02	0.004
			5-6	1.71	0.004	0.03	0.004
			6-3	1.52	0.005	0.03	0.005
0.46	HP	LP	6-7	1.51	0.006	0.04	0.006
			6-8	1.52	0.006	0.04	0.006
0.47			4-7	1.71	0.004	0.02	0.004
0.48			4-5	1.54	0.006	0.04	0.006
			4-6	1.57	0.005	0.03	0.005
0.46	LP	HP	6-9	1.53	0.005	0.03	0.005
			6-10	1.52	0.005	0.04	0.005

Appendix D. Specifications used for the XRD analysis performed on the sintered PZT pellets 0.46HP, 0.47 HP, 0.48HP, 0.47LP and 0.48LP.

Configuration:	R&T Spinner
Goniometer:	PW3050/60 (Theta/Theta)
Minimum step size 2Theta:	0.001
Minimum step size Omega:	0.001
Sample stage:	Reflection-Transmission Spinner PW3064/60
Minimum step size Phi:	0.1
Diffractometer system:	XPERT-3
Raw Data Origin:	XRD measurement (*. XRDML)
Scan Axis:	Gonio
Start Position [°2θ]:	10.0231
End Position [°2θ]:	89.9731
Step Size [°2θ]:	0.0260
Scan Step Time [s]:	296.5650
Scan Type:	Continuous
PSD Mode:	Scanning
PSD Length [°2θ]:	3.35
Offset [°2θ]:	0.0000
Divergence Slit Type:	Fixed
Divergence Slit Size [°]:	0.4354
Specimen Length [mm]:	10.00
Measurement Temperature [°C]:	25.00
Anode Material:	Cu
K-Alpha1 [Å]:	1.54060
K-Alpha2 [Å]:	1.54443
K-Beta [Å]:	1.39225
K-A2 / K-A1 Ratio:	0.50000
Generator Settings:	40 mA, 45 kV
Diffractometer Type:	0000000011165102
Diffractometer Number:	0
Goniometer Radius [mm]:	240.00
Dist. Focus-Diverg. Slit [mm]:	100.00
Incident Beam Monochromator:	No
Spinning:	No

Appendix E. Specifications used for the XRD analysis performed on the sintered PZT pellets 0.46LP, 0.46HP/LP, 0.47HP/LP, 0.48HP/LP and 0.46LP/HP.

Configuration:	R&T Spinner
Goniometer:	PW3050/60 (Theta/Theta)
Minimum step size 2Theta:	0.001
Minimum step size Omega:	0.001
Sample stage:	Reflection-Transmission Spinner PW3064/60
Minimum step size Phi:	0.1
Diffractometer system:	XPERT-PRO
Raw Data Origin:	XRD measurement (*. XRDML)
Scan Axis:	Gonio
Start Position [°2θ]:	18.0104
End Position [°2θ]:	91.9774
Step Size [°2θ]:	0.0170
Scan Step Time [s]:	99.6950
Scan Type:	Continuous
PSD Mode:	Scanning
PSD Length [°2θ]:	2.12
Offset [°2θ]:	0.0000
Divergence Slit Type:	Fixed
Divergence Slit Size [°]:	0.5000
Specimen Length [mm]:	10.00
Measurement Temperature [°C]:	25.00
Anode Material:	Cu
K-Alpha1 [Å]:	1.54060
K-Alpha2 [Å]:	1.54443
K-A2 / K-A1 Ratio:	0.50000
Generator Settings:	40 mA, 40 kV
Diffractometer Type:	0000000011062266
Diffractometer Number:	0
Goniometer Radius [mm]:	240.00
Dist. Focus-Diverg. Slit [mm]:	100.00
Incident Beam Monochromator:	Yes
Spinning:	No

Appendix F.   Full XRD patterns for all PZT samples made with opposite purity PZ, after sintering at 1200°C.
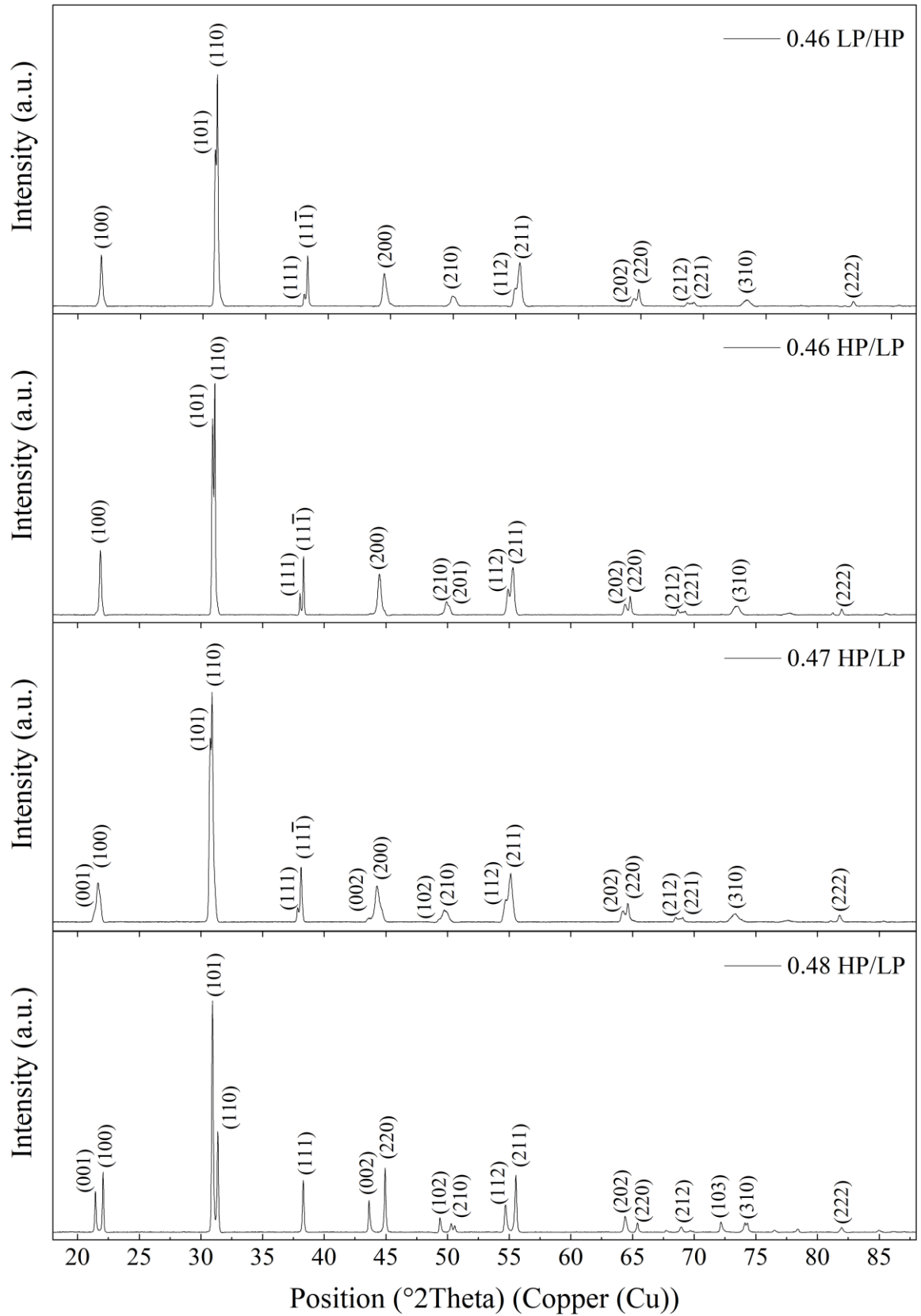
Appendix G. Remanent polarization and coercive fields of the PZT sample pieces at voltages ranging from 0.5 to 4kV/mm and 0.1 Hz, after quenching at 600°C.

PZT/PZ	0.46 LP/LP			0.47 LP/LP			0.48 LP/LP		
Pellet ID	6-11			4-11			4-2		
Applied Voltage	P_r ($\mu C/cm^2$)	E_c+ (kV/mm)	E_c-	P_r ($\mu C/cm^2$)	E_c+ (kV/mm)	E_c-	P_r ($\mu C/cm^2$)	E_c+ (kV/mm)	E_c-
0.5 kV/mm	0.23	4.87	-4.59	0.18	4.85	-4.73	0.10	1.25	-4.82
1 kV/mm	1.13	9.81	-9.56	1.65	9.69	-9.09	0.47	9.80	-9.27
1.5 kV/mm	2.87	14.46	-14.54	5.58	13.76	-14.29	1.16	14.33	-14.48
2 kV/mm	5.77	18.94	-19.03	10.01	19.17	-19.35	2.76	18.86	-19.45
2.5 kV/mm	8.71	24.33	-22.06	11.99	8.58	-9.71	4.72	24.25	-24.33
3 kV/mm	11.36	29.21	-26.60	16.26	8.87	-9.23	7.25	28.96	-25.00
3.5 kV/mm	14.16	12.38	-9.09	18.63	9.35	-9.53	12.39	7.66	-10.94
4 kV/mm	16.97	12.71	-13.05	21.31	10.72	-10.42	16.27	13.55	-10.52

PZT/PZ	0.46 HP/HP			0.47 HP/HP			0.48 HP/HP		
Pellet ID	5-9			5-1			5-4		
Applied Voltage	P_r ($\mu C/cm^2$)	E_c+ (kV/mm)	E_c-	P_r ($\mu C/cm^2$)	E_c+ (kV/mm)	E_c-	P_r ($\mu C/cm^2$)	E_c+ (kV/mm)	E_c-
0.5 kV/mm	0.39	4.99	-4.82	0.18	4.68	-1.06	0.07	4.75	-4.90
1 kV/mm	4.41	8.20	-9.58	1.16	9.71	-9.77	0.36	9.61	-7.45
1.5 kV/mm	14.94	7.23	7.67	4.66	14.71	-13.37	1.00	14.55	-14.50
2 kV/mm	17.72	7.86	-7.74	8.84	9.85	-12.00	2.96	18.18	-19.45
2.5 kV/mm	21.73	8.31	-8.18	12.32	9.60	-9.68	5.74	22.58	-20.87
3 kV/mm	25.22	8.81	-8.88	16.45	10.01	-10.26	10.66	15.99	-15.75
3.5 kV/mm	26.63	9.13	-9.01	19.29	10.35	-10.01	13.96	32.84	-33.69
4 kV/mm	28.44	9.39	-9.13	21.62	10.84	-10.68	19.17	18.80	-19.41

PZT/PZ	0.46 HP/LP			0.48 HP/LP			0.46 LP/HP		
Pellet ID	6-7			4-5			6-9		
Applied Voltage	P_r ($\mu C/cm^2$)	E_c+ (kV/mm)	E_c-	P_r ($\mu C/cm^2$)	E_c+ (kV/mm)	E_c-	P_r ($\mu C/cm^2$)	E_c+ (kV/mm)	E_c-
0.5 kV/mm	0.43	4.85	-4.84	0.11	4.01	-4.56	0.22	4.83	-4.53
1 kV/mm	3.10	8.91	-8.87	0.36	9.63	-9.09	1.12	9.70	-9.47
1.5 kV/mm	7.88	14.40	-14.38	0.81	14.58	-12.71	3.01	14.55	-14.55
2 kV/mm	12.93	8.92	-6.98	1.53	18.61	-14.10	6.15	18.85	-19.10
2.5 kV/mm	20.87	9.35	-8.92	2.86	22.94	-24.14	8.62	24.41	-20.47
3 kV/mm	25.04	9.85	-9.85	5.99	28.01	-28.74	12.50	13.11	-9.25
3.5 kV/mm	26.85	10.19	-10.27	8.09	18.98	-33.17	14.71	12.85	-12.42
4 kV/mm	31.15	10.61	-10.61	20.74	19.07	-18.15	23.90	13.54	-13.28

Appendix H. Screen captures of the results obtained from the radial resonance performed on the resulting PZT sintered disks.

- Composition 0.46 LP/LP

- Composition 0.47 LP/LP

- Composition 0.48 LP/LP

```
RESONANCIA RADIAL: - Modo fundamental -
PZT44                                                              24
Densidad= 7.23 gr/cm3
Espesor= 0.51 mm                          Superficie= 146 mm²

DATOS EXPERIMENTALES
 Resonancia:          Fs= 160.1 kHz                  Qs(exp)= 385.26
                      Y = .1909691 + 3.437814E-03 i S
 Antirresonancia:  Fp= 185.1 kHz                     Qp(exp)= 635.91
                      Y = 1.349998E-05 - 2.024999E-08 i S
 Frecuencias auxiliares:  F1= 127.87 kHz  y  F2= 243.48 kHz
 Frecuencia del primer sobretono 419.4 kHz

CARACTERIZACION PRINCIPAL
 Np= 2182.84 (kHz.mm)                            n= 7 iteraciones.
 Kp= 0.56763 - 0.00078 i                         |Kp|  = 56.76 %
 K31= 0.33211 - 0.00042 i                        |K31| = 33.21 %
 Coeficiente de Poisson σ= 0.31535 - 0.00016 i   Qs(calc)= 366
 c11p^E= 8.0252 + 0.0230 i (x10^10 N·m⁻²)        Qm(c11pE)=  348.72
 s11^E= 13.8366 - 0.0412 i (x10-12 m²·N-1)       Qm(s11E)=  335.64
 s12^E= -4.3633 + 0.0152 i (x10-12 m²·N-1)       Qm(s12E)=  286.90
 d31  = -105.0871 + 0.5775 i (x10-12 C·N-1)      Qp(d31)=  181.95
 €33^T= 817.26 - 4.48 i                          Qe(€33T)=  182.45
 CARACTERIZACION DERIVADA                        Qp(calc)= 592.4
 s66^E= 36.3999 - 0.1129 i (x10-12 m²·N-1)       Qm(s66E)=  322.50
 c11p^D= 10.5342 + 0.0197 i (x10^10 N·m⁻²)       Qm(c11pD)=  535.53
 s11^D= 12.3105 - 0.0328 i (x10-12 m²·N-1)       Qm(s11D)=  375.15
 s12^D= -5.8895 + 0.0236 i (x10-12 m²·N-1)       Qm(s12D)=  249.36
 g31  = -14.5225 + 0.0002 i (x10-3 m·V·N-1)      Qp(g31)= %67502.51
.... Pulsa una tecla para continuar ....
```

- Composition 0.46 HP/HP

```
RESONANCIA RADIAL: - Modo fundamental -
PZT58                                                            22.8
Densidad= 6.3 gr/cm3
Espesor= 0.5 mm                           Superficie= 243 mm²

DATOS EXPERIMENTALES
 Resonancia:          Fs= 121.9 kHz                  Qs(exp)= 206.94
                      Y = 6.059848E-02 + 1.18182E-03 i S
 Antirresonancia:  Fp= 135.5 kHz                     Qp(exp)= 359.65
                      Y = 2.238428E-05 + 5.059709E-07 i S
 Frecuencias auxiliares:  F1= 99.75 kHz  y  F2= 171.25 kHz
 Frecuencia del primer sobretono 319 kHz

CARACTERIZACION PRINCIPAL
 Np= 2144.18 (kHz.mm)                            n= 9 iteraciones.
 Kp= 0.49330 - 0.00211 i                         |Kp|  = 49.33 %
 K31= 0.28780 - 0.00124 i                        |K31| = 28.78 %
 Coeficiente de Poisson σ= 0.31927 + 0.00005 i   Qs(calc)= 216.67
 c11p^E= 6.7317 + 0.0334 i (x10^10 N·m⁻²)        Qm(c11pE)=  201.75
 s11^E= 16.5408 - 0.0814 i (x10-12 m²·N-1)       Qm(s11E)=  203.15
 s12^E= -5.2810 + 0.0252 i (x10-12 m²·N-1)       Qm(s12E)=  209.56
 d31  = -76.1430 + 0.9085 i (x10-12 C·N-1)       Qp(d31)=  83.81
 €33^T= 477.98 - 4.94 i                          Qe(€33T)=  96.78
 CARACTERIZACION DERIVADA                        Qp(calc)= 361.33
 s66^E= 43.6436 - 0.2132 i (x10-12 m²·N-1)       Qm(s66E)=  204.66
 c11p^D= 8.1599 + 0.0244 i (x10^10 N·m⁻²)        Qm(c11pD)=  334.62
 s11^D= 15.1708 - 0.0629 i (x10-12 m²·N-1)       Qm(s11D)=  241.24
 s12^D= -6.6510 + 0.0437 i (x10-12 m²·N-1)       Qm(s12D)=  152.07
 g31  = -17.9921 + 0.0288 i (x10-3 m·V·N-1)      Qp(g31)=  625.52
.... Pulsa una tecla para continuar ....
```

- Composition 0.47 HP/HP


```
RESONANCIA RADIAL: - Modo fundamental -
PZT53
Densidad= 6.74 gr/cm3                                              22.0
Espesor= 0.38 mm                        Superficie= 175.5 mm²

DATOS EXPERIMENTALES
 Resonancia:          Fs= 139.9 kHz                  Qs(exp)= 219.41
                      Y = 9.170661E-02 + 7.886963E-04 i S
 Antirresonancia:     Fp= 155.5 kHz                  Qp(exp)= 230.35
                      Y = 4.981935E-05 - 2.540809E-07 i S
 Frecuencias auxiliares:  F1= 114.49 kHz  y  F2= 196.52 kHz
 Frecuencia del primer sobretono 366.3 kHz

CARACTERIZACION PRINCIPAL                         n= 9 iteraciones.
 Np= 2091.28 (kHz.mm)                             |Kp|  = 49.32 %
 Kp= 0.49323 - 0.00070 i                          |K31| = 28.85 %
 K31= 0.28849 - 0.00023 i                         Qs(calc)= 203.45
 Coeficiente de Poisson σ= 0.31579 - 0.00085 i    Qm(c11pE)= 181.26
 c11p^E= 6.8645 + 0.0379 i (x10^10 N·m-²)         Qm(s11E)=  163.50
 s11^E= 16.1809 - 0.0990 i (x10-12 m²·N-1)        Qm(s12E)=  113.36
 s12^E= -5.1097 + 0.0451 i (x10-12 m²·N-1)        Qp(d31)=   116.09
 d31  = -89.0879 + 0.7674 i (x10-12 C·N-1)        Qe(ε33T)=  105.18
 ε33^T= 665.64 - 6.33 i                           Qp(calc)= 226.18
CARACTERIZACION DERIVADA                          Qm(s66E)=  147.81
 s66^E= 42.5812 - 0.2881 i (x10-12 m²·N-1)        Qm(c11pD)= 210.73
 c11p^D= 8.3164 + 0.0395 i (x10^10 N·m-²)         Qm(s11D)=  167.49
 s11^D= 14.8342 - 0.0886 i (x10-12 m²·N-1)        Qm(s12D)=  116.39
 s12^D= -6.4563 + 0.0555 i (x10-12 m²·N-1)        Qp(g31)= 1119.32
 g31  = -15.1156 - 0.0135 i (x10-3 m·V·N-1)
.... Pulsa una tecla para continuar ....
```

- Composition 0.48 HP/HP


```
RESONANCIA RADIAL: - Modo fundamental -
PZT55
Densidad= 6.25 gr/cm3                                              22.0
Espesor= 0.52 mm                        Superficie= 247 mm²

DATOS EXPERIMENTALES
 Resonancia:          Fs= 120.4 kHz                  Qs(exp)= 137.29
                      Y = 7.571461E-02 - 1.481283E-02 i S
 Antirresonancia:     Fp= 129.1 kHz                  Qp(exp)= 392.17
                      Y = 5.534993E-05 + 1.723096E-05 i S
 Frecuencias auxiliares:  F1= 101.44 kHz  y  F2= 156.59 kHz
 Frecuencia del primer sobretono 313 kHz

CARACTERIZACION PRINCIPAL                         n= 10 iteraciones.
 Np= 2135.16 (kHz.mm)                             |Kp|  = 40.88 %
 Kp= 0.40679 - 0.00314 i                          |K31| = 23.39 %
 K31= 0.23386 - 0.00174 i                         Qs(calc)= 213.89
 Coeficiente de Poisson σ= 0.34543 - 0.00030 i    Qm(c11pE)= 196.39
 c11p^E= 6.5136 + 0.0332 i (x10^10 N·m-²)         Qm(s11E)=  187.61
 s11^E= 17.4320 - 0.0929 i (x10-12 m²·N-1)        Qm(s12E)=  161.04
 s12^E= -6.0215 + 0.0374 i (x10-12 m²·N-1)        Qp(d31)=   72.78
 d31  = -88.8890 + 1.2213 i (x10-12 C·N-1)        Qe(ε33T)=  138.23
 ε33^T= 936.07 - 6.77 i                           Qp(calc)= 344.17
CARACTERIZACION DERIVADA                          Qm(s66E)=  179.98
 s66^E= 46.9070 - 0.2606 i (x10-12 m²·N-1)        Qm(c11pD)= 348.48
 c11p^D= 7.3928 + 0.0212 i (x10^10 N·m-²)         Qm(s11D)=  223.84
 s11^D= 16.4788 - 0.0736 i (x10-12 m²·N-1)        Qm(s12D)=  123.03
 s12^D= -6.9747 + 0.0567 i (x10-12 m²·N-1)        Qp(g31)=  153.74
 g31  = -10.7253 + 0.0698 i (x10-3 m·V·N-1)
.... Pulsa una tecla para continuar ....
```

- Composition 0.46 LP/HP

- Composition 0.46 HP/LP

- Composition 0.47 HP/LP


```
RESONANCIA RADIAL: - Modo fundamental -
PZT47                                                          25.0
Densidad= 6.04 gr/cm3
Espesor= 0.66 mm                        Superficie= 238 mm²

DATOS EXPERIMENTALES
 Resonancia:          Fs= 121.4 kHz                Qs(exp)= 149.68
                      Y = 8.911656E-02 - 5.05833E-03 i S
 Antirresonancia:  Fp= 141 kHz                     Qp(exp)= 541.16
                      Y = 1.447179E-05 - 1.406722E-06 i S
 Frecuencias auxiliares:  F1= 95.71 kHz  y  F2= 186.37 kHz
 Frecuencia del primer sobretono 318.3 kHz

CARACTERIZACION PRINCIPAL
 Np= 2113.31 (kHz.mm)                           n= 8 iteraciones.
 Kp= 0.57569 - 0.00294 i                        |Kp| = 57.57 %
 K31= 0.33765 - 0.00172 i                       |K31| = 33.77 %
 Coeficiente de Poisson σ= 0.31202 - 0.00002 i  Qs(calc)= 161.83
 c11p^E= 6.2940 + 0.0361 i (x10^10 N·m⁻²)        Qm(c11pE)= 174.48
 s11^E= 17.6013 - 0.1011 i (x10-12 m²·N-1)       Qm(s11E)=  174.03
 s12^E= -5.4919 + 0.0319 i (x10-12 m²·N-1)       Qm(s12E)=  171.93
 d31  = -119.5056 + 1.2256 i (x10-12 C·N-1)      Qp(d31)=   97.51
 ε33^T= 803.86 - 3.68 i                          Qe(ε33T)=  218.20
CARACTERIZACION DERIVADA                         Qp(calc)=  451.2
 s66^E= 46.1863 - 0.2662 i (x10-12 m²·N-1)       Qm(s66E)=  173.52
 c11p^D= 8.3408 + 0.0165 i (x10^10 N·m⁻²)        Qm(c11pD)= 505.38
 s11^D= 15.5948 - 0.0692 i (x10-12 m²·N-1)       Qm(s11D)=  225.42
 s12^D= -7.4984 + 0.0639 i (x10-12 m²·N-1)       Qm(s12D)=  117.34
 g31  = -16.7907 + 0.0952 i (x10-3 m·V·N-1)      Qp(g31)=   176.30
          Pulsa una tecla para continuar ....
```

- Composition 0.48 HP/LP


```
RESONANCIA RADIAL: - Modo fundamental -
PZT46                                                          24.
Densidad= 6.19 gr/cm3
Espesor= 0.78 mm                        Superficie= 135 mm²

DATOS EXPERIMENTALES
 Resonancia:          Fs= 161.9 kHz                Qs(exp)= 276.22
                      Y = 6.074696E-02 + 6.074899E-04 i S
 Antirresonancia:  Fp= 178.1 kHz                   Qp(exp)= 447.35
                      Y = 2.072931E-05 - 3.990957E-06 i S
 Frecuencias auxiliares:  F1= 133.36 kHz  y  F2= 223.17 kHz
 Frecuencia del primer sobretono 418 kHz

CARACTERIZACION PRINCIPAL
 Np= 2122.60 (kHz.mm)                           n= 8 iteraciones.
 Kp= 0.47370 - 0.00265 i                        |Kp| = 47.37 %
 K31= 0.26571 - 0.00123 i                       |K31| = 26.57 %
 Coeficiente de Poisson σ= 0.37076 - 0.00121 i  Qs(calc)= 215.83
 c11p^E= 6.2896 + 0.0339 i (x10^10 N·m⁻²)        Qm(c11pE)= 185.77
 s11^E= 18.4325 - 0.1184 i (x10-12 m²·N-1)       Qm(s11E)=  155.72
 s12^E= -6.8339 + 0.0662 i (x10-12 m²·N-1)       Qm(s12E)=  103.29
 d31  = -109.7261 + 1.1630 i (x10-12 C·N-1)      Qp(d31)=   94.35
 ε33^T= 1044.99 - 5.76 i                         Qe(ε33T)=  181.53
CARACTERIZACION DERIVADA                         Qp(calc)=  407.14
 s66^E= 50.5327 - 0.3691 i (x10-12 m²·N-1)       Qm(s66E)=  136.92
 c11p^D= 7.5368 + 0.0215 i (x10^10 N·m⁻²)        Qm(c11pD)= 350.84
 s11^D= 17.1312 - 0.0980 i (x10-12 m²·N-1)       Qm(s11D)=  174.89
 s12^D= -8.1351 + 0.0866 i (x10-12 m²·N-1)       Qm(s12D)=   93.96
 g31  = -11.8594 + 0.0604 i (x10-3 m·V·N-1)      Qp(g31)=   196.45
          Pulsa una tecla para continuar ....
```

RELATED WORK

The research work presented in this thesis has contributed to the creation of the following oral and poster presentations.

Oral Presentations

Garcia-Caballero, V. *Light up your moves!* Explorathon 16, 30 September 2016, Rosshall Academy, UK

Garcia-Caballero, V. *Piezoelectricity.* PhD Information Day, 11 January 2017, University of Glasgow, UK

Garcia-Caballero, V. *Light up your moves!* Explorathon 17, 29 September 2017, St Thomas Aquinas Secondary, UK

Garcia-Caballero, V. *Power up your moves with the Piezoelectric groove.* Science Slam VI, 05 July 2018, University of Glasgow, UK

Garcia-Caballero, V. *Efficiency and properties comparison between PZT pellets sintered with three different compositions near the MPB and two different grades of purity of the parent oxides.* XVI Symposium of Mexican Students and Studies in the UK, 11-13 July 2018, University of Southampton, UK

Garcia-Caballero, V. *Comparison between different compositions and purities of PZT pellets sintered through a two-stage ceramic method.* Indian Institute of Science Education and Research, 01 September 2018, Pune, India

Garcia-Caballero, V. *Development of PDMS/PZT composite films using multiwall CNTs as an additive for flexible nanogenerators.* XVII Symposium of Mexican Studies and Students in the UK, 26-28 June 2019, University of Cambridge, UK

Garcia-Caballero, V. *Efficiency and characterisation comparison between PZT piezoelectric ceramics sintered through the conventional ceramic method for energy harvesting purposes.* University of Glasgow, 11 February 2020, Glasgow, UK

Poster Presentations

Garcia-Caballero, V., Watson, I. A. & Cossar, C. *Efficiency Analysis of Different Energy Harvesters*. XIII Symposium of Mexican Students and Studies in the UK, 23-25 July 2015, University College London, UK

Garcia-Caballero, V., Watson, I. A. & Cossar, C. *Sintering of PT and PZT pellets using the conventional ceramic method.* All-Energy Conference 2016, 4-5 May 2016, SECC Glasgow, UK

Garcia-Caballero, V., Watson, I. A. & Cossar, C. *Sintering of piezoelectric materials through the conventional ceramic method.* XIV Symposium of Mexican Students and Studies in the UK, 16-18 June 2016, University of Edinburgh, UK

Garcia-Caballero, V., Watson, I. A. & Cossar, C. *Sintering of PZT Pellets through the conventional ceramic method for energy harvesting.* XV Symposium of Mexican Students and Studies in the UK, 12-14 July 2017, Durham University, UK

Garcia-Caballero, V., Watson, I. A. & Cossar, C. *Sintering of Piezoelectric PZT Pellets through a Two-Stage Conventional Ceramic Method for Kinetic Energy Harvesting*. XVI Symposium of Mexican Students and Studies in the UK, 10-12 July 2018, University of Southampton, UK

Garcia-Caballero, V., Watson, I. A. & Cossar, C. *Efficiency comparison between flexible hybrid PDMS triboelectric and PVDF piezoelectric films used as nanogenerators*. XVII Symposium of Mexican Students and Studies in the UK, 26-28 June 2019, University of Cambridge, UK

REFERENCES

Adu-Manu, K. et al., 2018. Energy-harvesting wireless sensor networks (EH-WSNs): A review. *ACM Transactions on Sensor Networks,* 14(2), p. 10.

Aguilar, G. V., 2018. Introductory Chapter: A Brief Semblance of the Sol-Gel Method in Research. In: G. V. Aguilar, ed. *Sol-Gel Method - Design and Synthesis of New Materials with Interesting Physical, Chemical and Biological Properties.* Mexico: IntechOpen.

Alemany, C. et al., 1995. Automatic determination of complex constants of piezoelectric lossy materials in the radial mode. *Journal of Physics D: Applied Physics,* Volume 28, pp. 945-956.

Alemany, C. et al., 1994. Automatic iterative evaluation of complex material constants inI piezoelectric ceramics. *Journal of Physics D Applied Physics ,* 27(1), pp. 148-155.

Alguero, M., Alemany, C. & Pardo, L., 2004. Method for Obtaining the Full Set of Linear Electric, Mechanical, and Electromechanical Coefficients and All Related Losses of a Piezoelectric Ceramic. *Journal of the American Ceramic Society,* 87(2), pp. 209 - 215.

Anil, K. & Sreekanth, N., 2014. Piezoelectric power generation in tires. *International Journal of Electrical, Electronics and Computer Systems (IJEECS),* pp. 11-16.

ANSI/IEEE, 1987. *IEEE Standard on Piezoelectricity (176-1987),* New York: American National Standards Institute/Institute of Electrical and Electronics Engineers.

APC International Ltd, 2016. *Piezoelectric Constants.* [Online]
Available at: https://www.americanpiezo.com/knowledge-center/piezo-theory/piezoelectric-constants.html [Accessed 17 January 2020].

APC International, Ltd., 2015. *Ceramic Manufacturing Series – Pressing PZT Powders.* [Online]
Available at: https://www.americanpiezo.com/blog/ceramic-manufacturing-series-pressing-pzt-powders/ [Accessed 17 January 2020].

APC International, Ltd, 2016. *After Manufacturing 1: Connecting to PZT Components.* [Online]
Available at: https://www.americanpiezo.com/blog/after-manufacturing-1-connecting-to-pzt-components/ [Accessed 18 January 2020].

APC International, Ltd, 2016. *SOFT VS. HARD CERAMICS.* [Online] Available at:
https://www.americanpiezo.com/piezo-theory/ceramics.html [Accessed 16 January 2020].

Bai, D. Y. et al., 2018. Water Energy Harvesting and Self-Powered Visible Light Communication Based on Triboelectric Nanogenerator. *Energy Technology,* 6(10), pp. 1859-2081.

Basheer, U. M., 2014. *What is the difference between sintering and calcination?*. [Online]
Available at: https://www.researchgate.net/post/What_is_the_difference_between_sintering_and_calcination [Accessed 17 January 2020].

Basset, P. et al., 2014. Electrostatic vibration energy harvester with combined effect of electrical nonlinearities and mechanical impact. *IOP Publishing: Journal of Micromechanics and Microengineering,* pp. 1-14.

Batra, A. K. & Aggarwal, M. D., 2013. Chapter 7: Pyroelectric Energy Harvesting. In: *Pyroelectric Materials: Infrared Detectors, Particle Accelerators, and Energy Harvesters.* Washington: SPIE Press.

Bayne, S. & Thompson, J., n.d. *CERAMICS: Properties 1 (Physical, Chemical, Mechanical).* [Online]
Available at: http://www-personal.umich.edu/~sbayne/dental-materials/022-Ceramics-Prop1/022-Handouts/22-Ceram-Prop1-Notes-CL.pdf
[Accessed 24 January 2020].

Benam, M. R., 2013. Investigation the dielectrical and electromechanical properties of PZT thin films. *International Journal of Engineering Research and Applications,* pp. 680-682.

Berdy, D., Valentino, D. & Peroulis, D., 2015. Kinetic energy harvesting from human walking and running using a magnetic levitation energy harvester. *El Sevier: Sensors and Actuators A,* pp. 262-271.

Birtane, M. & Tuna, H., 2004. The evaluation of plantar pressure distribution in obese and non-obese adults. *Clinical Biomechanics,* Volume 19, pp. 1055-1059.

Bokhimi, X., 2016. *Could anyone explain generally why XRD peak splitting is occurred?.* [Online]
Available at: https://www.researchgate.net/post/Could-anyone-explain-generally-why-XRD-peak-splitting-is-occurred/579212aaed99e1ad5f5de2e4/citation/download.
[Accessed 20 February 2024].

Britannica, T. Editors of Encyclopaedia, 2019. *Encyclopedia Brittanica.* [Online]
Available at: https://www.britannica.com/science/massicot

Bui, T., Chan, H. & Unsworth, J., 1988. Specific acoustic impedances of piezoelectric ceramic and polymer composites used in medical applications. *Journal of Aoustical Society of America,* 83(6), pp. 2416-2421.

BYJU, 2020. *Density of Unit Cell - Primitive unit cell.* [Online]
Available at: https://byjus.com/chemistry/density-of-unit-cell/ [Accessed 17 January 2020].

Cacopardo, L., 2018. *Piezoelectric Materials.* [Online] Available at: https://www.centropiaggio. unipi.it/sites/default/files/course/material/l5._piezoelettrici.pdf [Accessed 17 January 2020].

Catacuzzeno, L. et al., 2019. Energy harvesting from a bio cell. *Elsevier,* Volume 56, pp. 823-827.

Center for Sustainable Systems, 2022. *Photovoltaic Energy Factsheet,* s.l.: University of Michigan.

Chang, C. et al., 2010. Direct-Write Piezoelectric Polymeric Nanogenerator with High Energy Conversion Efficiency. *NanoLetters,* pp. 726-731.

Chan, V. & Perlas, A., 2011. Basics of Ultrasound Imaging. In: *Atlas of Ultrasound-Guided Procedures in Interventional Pain Management.* Toronto: Springer Science+Business Media, LLC, pp. 13-19.

Chaudhari, V. A. & Bichile, G. K., 2013. Synthesis, Structural, and Electrical Properties of Pure PbTiO3 Ferroelectric Ceramics. *Hindawi Publishing Corporation: Smart Materials Research,* pp. 1-9.

Chen, Z., Song, L. & Cao, W., 2023. Characterization of high-power mechanical quality factor of piezoelectric ceramic discs under self-heating condition. *Journal of Materials Research and Technology,* Volume 23, pp. 5040-5049.

CM Furnaces Inc., 2015. *Annealing, Sintering and Calcining Processes.* [Online] Available at: https://cmfurnaces.com/annealing-sintering-and-calcining-processes/ [Accessed 17 January 2020].

Conserve Energy Future, 2017. *Causes and Solutions to the Global Energy Crisis.* [Online] Available at: http://www.conserve-energy-future.com/causes-and-solutions-to-the-global-energy-crisis.php [Accessed May 2017].

Coondoo, I. et al., 2015. Enhanced Piezoelectric Properties of Praseodymium-Modified Lead-Free (Ba0.85Ca0.15)(Ti0.90Zr0.10)O3. *Ceramics. J. Am. Ceram. Soc.,* Volume 98, pp. 3127-3135.

Curie, J. & Curie, P., 1880. Development by pressure of polar electricity in hemihedral crystals with inclined faces. *Bull. Soc. Min. France 3,* p. 90.

De Pasquale, G., Soma, A. & Fraccarollo, F., 2011. Piezoelectric energy harvesting for autonomous sensors network on safety-improved railway vehicles. *Proc. IMechE Vol. 226 Part C: J. Mechanical Engineering Science,* pp. 1107-1117.

DeAngelis, D. A. & Schulze, G. W., 2016. Performance of PZT8 Versus PZT4 Piezoceramic Materials in Ultrasonic Transducers. *Physics Procedia,* Volume 87, pp. 85-92.

Dingle, A., 2021. *Explainer: What is an electrode?,* Washington, D.C.: Society for Science and the Public.

Encyclopaedia Britannica, 2022. *Curie Point.* [Online] Available at:
http://www.britannica.com/science/Curie-point [Accessed 20 August 2022].

Enescu, D., 2019. Thermoelectric Energy Harvesting: Basic Principles and Applications. In: D. Enescu, ed. *Green Energy Advances.* Targoviste: IntechOpen.

Esterly, D. M., 2002. Manufacturing of Poly(vinylidene fluoride) and Evaluation of its Mechanical Properties, Virginia: Virginia Polytechnic Institute and State University.

Falin, J., 2013. *Texas Instruments.* [Online] Available at: https://training.ti.com/introduction-energy-harvesting-technology?keyMatch=ENERGY%20HARVESTING%20ESTIMATES&tisearch=Search-EN-everything [Accessed 15 January 2020].

Fernández-Posada, C. et al., 2016. A novel perovskite oxide chemically designed to show multiferroic phase boundary with room-temperature magnetoelectricity.. *Nature Communications,* Volume 7, p. 12772.

Flynn, A. M. & Sanders, S. R., 2002. Fundamental limits on energy transfer and circuit considerations for piezoelectric transformers. *IEEE Transactions on Power Electronics,* pp. 8-14.

Fritsch GmbH, 1987. Operating Instructions: Laboratory Planetary Mill "pulverisette 5", Idar Oberstein: FRITSCH.

Fu, H., Chen, G. & Bai, N., 2018. Electrode Coverage Optimization for Piezoelectric Energy Harvesting from Tip Excitation. *Sensors,* 18(804), pp. 1-14.

Gamba, Z., 2009. *Introduccion a la Fisica del Estado Solido.* Buenos Aires: Universidad Nacional de General San Martin .

Garlea, V. O. & Chakoumakos, B. C., 2015. Chapter 4 - Magnetic Structures. In: D. L. P. Felix Fernandez-Alonso, ed. *Experimental Methods in the Physical Sciences.* s.l.:Academic Press, pp. Pages 203-290.

Greisberg, J., 2019. *Biomechanics of Walking,* California: FootEducation LLC.

Haertling, G. H., 1999. Ferroelectric Ceramics: History and Technology. *Journal of the American Ceramic Society,* 82(4), pp. 797-818.

Hand, J., 2012. Modeling optimizes a piezoelectric energy harvester used in car tires. *COMSOL Multiphysics: Special Advertising Section,* pp. 12-15.

Harikrishnan, K. et al., 2018. PZT/PLZT - elastomer composites with improved piezoelectric voltage coefficient. *International Conference on Advances in Metallurgy, Materials and Manufacturing,* Volume 314, p. 012007.

Hausler, E. & Stein, E., 1984. Implantable physiological power supply with PVDF film. *Ferroelectronics 60,* p. 277–82.

Haynes, W., 2015. Lead(II) Oxide. In: W. Haynes, ed. *CRC Handbook of Chemistry and Physics.* 95th ed. Boca Raton: CRC Press LLC, pp. 4-70.

Hong, L. S. & Wei, C. C., 2000. Effect of oxygen pressure upon composition variation during chemical vapor deposition growth of lead titanate films from tetraethyl lead and titanium tetraisopropoxide. *Materials Letters, vol. 46, no. 2-3,* p. 149–153.

Hu, C.-C.et al., 2019. Phase field simulation of grain size effects on the phase coexistence and magnetostrictive behavior near the ferromagnetic morphotropic phase boundary. *Applied Physics Letter,* 115(16), p. 162402.

IDTechEx, 2015. *Energy Harvesting Intelligence Services.* [Online]
Available at: http://www.idtechex.com/research/topics/energy-harvesting.asp

IEA, 2022. *World Energy Outlook,* Paris: s.n.

IOP Institute of Physics., 2012. *Energy harvesting.* [Online]
Available at: http://www.iop.org/resources/energy/

IOP Institute of Physics, 2012. *State of the art.* [Online]
Available at: http://www.iop.org/resources/energy/stateofart/page_50301.html

IOP Institute of Physics, 2012. *Types of energy harvesting materials.* [Online]
Available at: http://www.iop.org/resources/energy/materials/page_50300.html

IUPAC Commission on Isotopic Abundances and Atomic Weights., 2021. *ATOMIC WEIGHTS OF THE ELEMENTS 2021.* [Online] Available at: https://iupac.qmul.ac.uk/AtWt/

Jin, L., Li, F., Zhang & Shujun, 2014. Decoding the Fingerprint of Ferroelectric Loops: Comprehension of theMaterial Properties and Structures. *Journal of the American Ceramic Society,* 97(1), pp. 1-27.

Jona, F. & Shirane, G., 1962. *Ferroelectric Crystals.* New York, NY, USA: MacMillan.

Jung, H.-J., Lee, S.-W. & Jang, D.-D., 2009. Feasibility Study on a New Energy Harvesting Electromagnetic Device Using Aerodynamic Instability. *IEEE TRANSACTIONS ON MAGNETICS, VOL. 45, NO. 10,* pp. 4376-4379.

Kermet International Ltd, 2019. *What is Lapping?.* [Online]
Available at: https://www.kemet.co.uk/products/flatlapping/flat-lapping-questions
[Accessed 17 January 2020].

Khusainov, R., Azzi, D., Achumba, I. & Bersch, S., 2013. Real-time human ambulation, activity, and physiological monitoring: taxonomy of issues, techniques, applications, challenges and limitations. *Sensors (Basel),* 13(10), pp. 12852-902.

Kim, J. et al., 2018. Enhanced Ferroelectric and Piezoelectric Properties of (1-x)PMN-xPT Ceramics Based on a Partial Oxalate Process. *Materials (Basel),* Volume 11, p. 2247.

Kim, S. & Lee, H., 2021. Piezoelectric Ceramics with High d33 Constants and Their Application to Film Speakers. *Materials (Basel).,* 14(19), p. 5795.

Kiziroglou, M. & Yeatman, E., 2012. 17 Materials and techniques for energy harvesting. In: S. J. S. P. P. E. John A. Kilner, ed. *Functional Materials for Sustainable Energy Applications.* London: Elsevier, pp. 541-572.

Kolm, H. H. & Kolm, E. A., 1984. *Piezoelectric Acousto-Electric Generator.* United States of America, Patent No. 4,467,236.

Kong, L., Zhang, T., Ma, J. & Boey, F., 2008. Progress in synthesis of ferroelectric ceramic materials via high-energy mechanochemical technique. *Progress in Materials Science,* 53(2), pp. 207-322.

Laboratory Testing Inc., 2020. *SCANNING ELECTRON MICROSCOPY.* [Online]
Available at: https://www.labtesting.com/services/materials-testing/metallurgical-testing/sem-analysis/ [Accessed 31 January 2020].

Landaua, L., Khiezere, I. & Lifshitz, M., 1967. CHAPTER VI - THE THEORY OF SYMMETRY. In: *General Physics.* Oxford: Pergamon Press Ltd., pp. 115-143.

Lapmaster Wolters, 1998. *What is Lapping?.* Mt Prospect, IL: s.n.

Le, C. P. & Halvorsen, E., 2012. MEMS electrostatic energy harvesters with end-stop effects. *IOP publishing: Journal of Micromechanics and Microengineering,* pp. 1-12.

Lee, H. J. et al., 2012. Thickness Dependent Properties of Relaxor-PbTiO3 Ferroelectrics for Ultrasonic Transducers. *Adv Funct Mater,* 23(20), pp. 3154-3162.

Leinonen, M., Palosaari, J., Juuti, J. & Jantunen, H., 2014. Combined electrical and electromechanical simulations of a piezoelectric cymbal harvester for energy harvesting from walking. *Journal of Intelligent Material Systems and Structures,* pp. 391-400.

Lerch, R., 1990. Simulation of Piezoelectric Devices by Two- and Three-Dimensional Finite Elements. *IEEE Transactions on Ultrasonics, Ferroelectrics, and Frequency Control, Vol. 37,* pp. 233-246.

Li, J., 2022. Microstructure and Piezoelectric Properties of Lead Zirconate Titanate Nanocomposites Reinforced with In-Situ Formed ZrO2 Nanoparticles. *Materials,* Volume 15, p. 1389.

Liu, C., 2007. Recent developments in polymer MEMS. *Advanced Materials ,* 19(22), pp. 83-90.

Liu, Y. et al., 2013. Enhanced piezoelectric performance of composite sol-gel thick films evaluated using piezoresponse force microscopy. *Journal of Applied Physics,* 113(18), p. 187205.

Liu, Y. & Wang, Q., 2023. *Piezoelectric polymers.* New York: Encyclopedia of Polymer Science and Technology.

Machado, S. P., Febbo, M. & Osinaga, S. M., 2023. Double Impact-Based Piezoelectric Energy Harvester for Low-Frequency Operation. *IEEE Sensors Journal,* 23(2), pp. 1081-1090.

Main, M., Leschhorn, A. & Kliem, H., 2015. The field and temperature dependence of hysteresis loops in P(VDF–TrFE)copolymer films.. *Physica B,* pp. 306-311.

Martínez Ripoll, M., 2002. The Symmetry of crystals: Representation of Bravais Lattices, Spain: CSIC.

Measurement Specialties, Inc., 1999. *Piezo Film Sensors Technical Manual.* Pennsylvania: 1-86.

Mends, F., 2019. *What Are Piezoelectric Materials?.* [Online] Available at: https://sciencing.com/piezoelectric-materials-8251088.html [Accessed 16 January 2020].

Merck Life Science UK Limited, 2019. *Safety Data Sheet: Titanium(IV) oxide, rutile.* [Online] Available at: https://www.sigmaaldrich.com/MSDS/MSDS/DisplayMSDSPage.do?country=GB&language=en&productNumber=204757&brand=ALDRICH&PageToGoToURL=https%3A%2F%2Fwww.sigmaaldrich.com%2Fcatalog%2Fproduct%2Faldrich%2F204757%3Flang%3Den [Accessed 16 April 2021].

Merck Life Science UK Limited, 2019. *Safety Data Sheet: Zirconium(IV) oxide.* [Online] Available at: https://www.sigmaaldrich.com/MSDS/MSDS/DisplayMSDSPage.do?country=GB&language=en&productNumber=230693&brand=ALDRICH&PageToGoToURL=https%3A%2F%2Fwww.sigmaaldrich.com%2Fcatalog%2Fproduct%2Faldrich%2F230693%3Flang%3Den [Accessed 13 April 2021].

Merriam-Webster, 2017. *Figure of Merit.* [Online] Available at: https://www.merriam-webster.com/dictionary/figure%20of%20merit [Accessed April 2017].

Miclea, C., 2012. Preparation of Piezoelectric Nanoparticles. In: G. Ciofani & A. Menciassi, eds. *Piezoelectric Nanomaterials for Biomedical Applications.* Springer, Berlin, Heidelberg, pp. 29-61.

Mide Technology, 2024. *T216-A4NO-05: Piezoelectric Bending Disc.* [Online]
Available at: https://piezo.com/collections/piezoelectric-actuators-motors/products/piezoelectric-bending-disc-t216-a4no-05

Migoni, R., Bilz, H. & Bauerle, D., 1976. Origin of raman scattering and ferroelectricity in oxidic perovskites. *Physical Review Letters, vol. 37, no. 17,* pp. 1155-1158.

Mitcheson, P. D. et al., 2008. Energy Harvesting From Human and Machine Motion for Wireless Electronic Devices. *Proceedings of the IEEE,* pp. 1457-1486.

Mitcheson, P. & Yeatman, E. M., 2008. *Energy harvesting for pervasive computing.* [Online]
Available at: http://www.perada-magazine.eu/view.php?article=1306-2008-09-22

Molland, A. F. ed., 2008. Chapter 3 - Flotation and stability. In: *The Maritime Engineering Reference Book.* s.l.:Butterworth-Heinemann, pp. 75-115.

Muscat, A., Bhattacharya, S. & Zhu, Y., 2022. Electromagnetic Vibrational Energy Harvesters: A Review. *Sensors (Basel),* 22(15).

Nan, Z., Yokota, H., Glazer, A. & Thomas, P., 2011. *01-080-7943.* s.l.:Acta Crystallogr., Sec. B: Struct. Sci..

Neacşu, I. A., Nicoară, A. I., Vasile, O. R. & Vasile, B. Ş., 2016. Chapter 9 - Inorganic micro- and nanostructured implants for tissue engineering. In: A. M. Grumezescu, ed. *Nanobiomaterials in Hard Tissue Engineering.* Bucharest: Elsevier, pp. 271-295.

Noheda, B., 2002. Structure and high-piezoelectricity in lead oxide solid solutions. *Current Opinion in Solid State and Materials Science,* 6(1), pp. 27-34.

Orfei, F., 2019. Disadvantages and Advantages of Energy Harvesting. *All About Circuits*, 19 August.

Paradiso, J. A. & Starner, T., 2005. Energy Scavenging for Mobile and Wireless Electronics. *IEEE CS and IEEE ComSoc,* pp. 18-27.

Parfit, M., 2020. *Future Power: Where Will the World Get its Next Energy Fix?.* [Online]
Available at: https://www.nationalgeographic.com/environment/global-warming/powering-the-future/ [Accessed 14 01 2020].

Pavlov, D., 2011. Leady Oxide. In: *Lead-Acid Batteries: Science and Technology.* Amsterdam: Elsevier, pp. 223-250.

Penn University - Department of Physics & Astronomy, 2020. *Managing Errors and Uncertainty.* Pennsylvania: University of Pennsylvania.

Pollet, B., Touhami, M., Despesse, G. & Costa, F., 2019. Effects of disc-shaped piezoelectric size reduction on resonant inductorless DC-DC converter. June, pp. 1423-1426.

Pollock, T., 2014. *Design, Modelling, Fabrication & Testing of a Miniature Piezoelectric-based EMF Energy Harvester.* [Online] Available at: https://prezi.com/ssuija42yfiz/design-modelling-fabrication-testing-of-a-miniature-piezoelectric-based-emf-energy-harvester/

Pollock, T., 2014. *MEMS Piezoelectric Cantilever Beam for Energy Harvesting Applications.* [Online] Available at: https://prezi.com/z3hdqy7eokdu/mems-piezoelectric-cantilever-beam-for-energy-harvesting-applications/

Priya, S., 2007. Advances in energy harvesting using low profile piezoelectric transducers. *J Electroceram,* pp. 165-182.

Priya, S. et al., 2017. A Review on Piezoelectric Energy Harvesting: Materials, Methods, and Circuits. *Energy Harvesting and Systems ,* Volume 4, pp. 1-37.

Qian, K. et al., 2013. Phase development and electrical properties of Pb(Mg1/3Nb2/3)O3-PbTiO3 ceramics prepared by partial oxalate route. *Physica Status Solidi (A) Applications and Materials,* 210(6), pp. 1149-1156.

Qi, Y. et al., 2010. Piezoelectric Ribbons Printed onto Rubber for Flexible Energy Conversion. *NanoLetters,* pp. 524-528.

Ramadan, K. S., Sameoto, D. & Evoy, S., 2014. A review of piezoelectric polymers as functional materials for electromechanical transducers. *IOP Publishing: Smart Materials and Structures,* pp. 1-26.

Rastegar, J., Haarhoff, D., Pereira, C. & Nguyen, H.-L., 2006. Piezoelectric-Based Energy Harvesting Power Sources for Gun-Fired Munitions. *Proc. of SPIE Vol. 6174,* pp. 1-6.

RF Wireless World, 2012. *Advantages and Disadvantages of Energy Harvesting Techniques.* [Online] Available at: https://www.rfwireless-world.com/Terminology/Advantages-and-Disadvantages-of-Energy-Harvesting-Techniques.html [Accessed 15 January 2020].

Richards, C. D., Anderson, M. J., Bahr, D. F. & Richards, R. F., 2004. Efficiency of energy conversion for devices containing a piezoelectric component. *IOP Publishing: Journal of Micromechanics and Microengineering,* pp. 717-721.

Sager, F. E. & Matice, C. J., 1998. *PIEZOELECTRIC PUMPS.* Unites States of America, Patent No. 5,798,600.

Sakakibara, T. et al., 1994. *Development of High-Voltage Photovoltaic Micro-Devices for ran Energy Supply to Micromachines.* Osaka, Japan, IEEE 5th International Symposium on Micro Machine and Human Science proceedings.

Sangawar, S. R., Agarwal, J. P. & Sarwade, D. B., 2001. A comprehensive study on some binders for piezo-electric ceramics. *Indian Journal of Engineering & Material Sciences,* Volume 8, pp. 26-35.

Sazonov, E., 2004. *Energy harvesting as enabling factor for bridge monitoring.* [Online] Available at: http://www.intelligent-systems.info/bridge.htm

Schmidt, V. H., 1992. Piezoelectric energy conversion in windmills. *Proc. IEEE Ultrasonics Symposium,* p. 897–904.

Sensor Technology Ltd, 2019. *PIEZOELECTRIC FUNDAMENTALS.* [Online] Available at: https://sensortechcanada.com/2021/07/03/12248/ [Accessed 17 January 2020].

Setter, N. et al., 2006. Ferroelectric thin films: review of materials, properties, and applications. *Journal of Applied Physics 100,* p. 051606.

Sezer, N. & Koç, M., 2021. A comprehensive review on the state-of-the-art of piezoelectric energy harvesting. *Nano Energy,* Volume 80, pp. 2211-2855.

Shuvo, M., Titirsha, T., Amin, N. & Islam, S., 2022. Energy Harvesting in Implantable and Wearable Medical Devices for Enduring Precision Healthcare. *Energies,* 15(20), p. 7495.

Siddiqui, M., Mohamed, J. J. & Ahmad, Z. A., 2020. Structural, piezoelectric, and dielectric properties of PZT-based ceramics without excess lead oxide. *Journal of the Australian Ceramic Society,* Volume 56, pp. 371-377.

Smoker, J., Nouh, M., Aldraihem, O. & Baz, A., 2012. Energy harvesting from a standing wave thermoacoustic-piezoelectric resonator. *JOURNAL OF APPLIED PHYSICS 111,* pp. 1-11.

Solar Impulse Foundation, 2020. *Solutions to the Energy Crisis: How to Achieve Sustainable Energy.* [Online] Available at: https://solarimpulse.com/energy-crisis-solutions [Accessed 14 01 2020].

Speakman, S., 2014. *Basics of X-Ray Powder Diffraction,* Massachusetts: MIT Materials Research Science and Engineering Center.

Stewart, M., Battrick, W. & Cain, M., 2001. Measuring Piezoelectric d33 coefficients using the Direct Method. In: *Measurement Good Practice Guide No. 44.* Middlesex, UK: National Physical Laboratory, pp. 1-10.

Sundar, U., Banerjee, S. & Cook-Chennault, K., 2018. Piezoelectric and Dielectric Properties of PZT-Epoxy Composite Thick Films. *Academic Journal of Polymer Science,* 1(5), pp. 95-109.

Tadigadapa, S. & Materi, K., 2009. Piezoelectric MEMS sensors: state-of-the-art and perspectives. *Meas. Sci. Technology 20,* p. 092001.

Taylor, G. W. et al., 2001. The Energy Harvesting Eel: A Small Subsurface Ocean/River Power Generator. *IEEE JOURNAL OF OCEANIC ENGINEERING, VOL. 26, NO. 4,* pp. 539-547.

The Great Soviet Encyclopedia, 2010. *Hysteresis (electric).* 3rd ed. s.l.:The Gale Group, Inc.

Thermo Fisher Scientific Inc., 2023. *Energy Dispersive Spectroscopy.* [Online]
Available at: https://www.thermofisher.com/uk/en/home/materials-science/eds-technology.html?
cid=cmp-05675-y6b2&utm_source=google-ads&utm_medium=cpc&utm_campaign=ms _xmarket
_gl_eds_search_googleadwords_2022_05&utm_term=%7Bkeyword%7D&gad=1&gclid=CjwKC
Ajwv8qkBhAnEiwAkY-ah [Accessed 21 June 2023].

Tong, W., 2010. Wind Power Generation and Wind Turbine Design. s.l.:Wit Press.

Tudor-Locke, C. et al., 2011. How many steps/day are enough? For adults. *Int J Behav Nutr Phys Act,* Volume 8, p. 79.

Tuna, G. & Güngör, V. Ç., 2015. 2 - Energy harvesting and battery technologies for powering wireless sensor networks. In: R. B. a. S. Kolavennu, ed. *Industrial Wireless Sensor Networks: Monitoring, Control and Automation.* Turkey: Woodhead Publishing, pp. 25-38.

Uchino, K., 2000. *Ferroelectric Devices.* New York: Marcel Dekker, Inc..

Uchino, K., 2003. *Introduction to Piezoelectric Actuators and Transducers,* Pennsylvania: International Center for Actuators and Transducers, Penn State University.

Ueberschlag, P., 2001. PVDF piezoelectric polymer. *Sensor Review Vol. 21 No. 2,* pp. 118-125.

University of Cambridge, 2023. *Loss in dielectrics.* [Online] Available at: ttps://www.doitpoms.ac.uk/tlplib/dielectrics/loss.php#:~:text=Dielectric%20loss%20is%20especial ly%20high,polarisation%20that%20results%20in%20heating.[Accessed July 2023].

Vinogradov, A. M., Schmidt, V. H., Tuthill, G. F. & Bohannan, G. W., 2004. Damping and electromechanical energy losses in the piezoelectric polymer PVDF. *El Sevier: Mechanics of Materials,* pp. 1007-1016.

Walpole, S. et al., 2012. The weight of nations: an estimation of adult human biomass. *BMC Public Health,* Volume 12, p. 439.

Wang, Y. et al., 2018. Magnesium Alloy Matching Layer for High-Performance Transducer Applications. *Sensors (Basel),* 8(12), p. 4424.

Wan, X. et al., 2023. A Review on PVDF Nanofibers in Textiles for Flexible Piezoelectric Sensors. *ACS Appl. Nano Mater,* 6(3), p. 1522–1540.

Weerakkody, D. Y. & Morgan, D. M. A., 2005. *Acoustic impedance.* [Online]
Available at: https://radiopaedia.org/articles/acoustic-impedance?lang=gb
[Accessed 17 January 2020].

Wenzheng, C. et al., 2023. Piezoelectric energy harvesting and dissipating behaviors of polymer-based piezoelectric composites for nanogenerators and dampers. *Chemical Engineering Journal,* Volume Volume 465, p. 142755.

Wongmaneerung, R., Yimnirun, R. & Ananta, S., 2007. Effects of sintering condition on phase formation, microstructure and dielectric properties of lead titanate ceramics.. *Applied Physics A: Materials Science & Processing,* pp. 249-255.

Woodford, C., 2015. *Electricity Generators.* [Online]
Available at: http://www.explainthatstuff.com/generators.html

Yang, B., Lee, C., Kee, W. L. & Lim, S. P., 2010. Hybrid energy harvester based on piezoelectric and electromagnetic mechanisms. *J. Micro/Nanolith. MEMS MOEMS,* pp. 1-10.

Yeheskel, O., 2018. *How the density of ceramics material effect the grain size and the conductivity of a material?.* [Online] Available at:
https://www.researchgate.net/post/how_the_density_of_ceramics_material_effect_the_grain_size_and_the_conductivity_of_a_material [Accessed 24 January 2020].

Yu, H. et al., 2014. A hybrid micro vibration energy harvester with power management circuit. *El Sevier: Microelectronic Engineering,* pp. 36-42.

Zhang, Q., Wang, Y. & Kim, E. S., 2014. Power generation from human body motion through magnet and coil arrays with magnetic spring. *Journal of Applied Physics 115,* pp. 1-6.

Zhao, D. et al., 2019. Chapter 1 General introduction to wind turbines. In: *Wind Turbines and Aerodynamics Energy Harvesters.* s.l.:Elsevier, pp. 1-20.